NANYANG TECHNOLOGICAL UNIVERSITY
SINGAPORE

3D PRINTING OF HIGH-VOLUME FLY ASH MIXTURES FOR DIGITAL CONCRETE CONSTRUCTION

BIRANCHI PANDA

School of Mechanical and Aerospace Engineering

2019

3D PRINTING OF HIGH-VOLUME FLY ASH MIXTURES FOR DIGITAL CONCRETE CONSTRUCTION

BIRANCHI PANDA

School of Mechanical and Aerospace Engineering

A thesis submitted to the Nanyang Technological University
in partial fulfilment of the requirements for the degree of
Doctor of Philosophy

2019

Statement of Originality

I hereby certify that the work embodied in this thesis is the result of original research, is free of plagiarised materials, and has not been submitted for a higher degree to any other University or Institution.

20/02/2019
Date

Biranchi Panda
BIRANCHI PANDA

Supervisor Declaration Statement

I have reviewed the content and presentation style of this thesis and declare it is free of plagiarism and of sufficient grammatical clarity to be examined. To the best of my knowledge, the research and writing are those of the candidate except as acknowledged in the Author Attribution Statement. I confirm that the investigations were conducted in accord with the ethics policies and integrity standards of Nanyang Technological University and that the research data are presented honestly and without prejudice.

20/02/2019
Date

Tan Ming Jen

20/02/2019
Date

Cise Unluer

Authorship Attribution Statement

This thesis contains material from 9 papers published in the following peer-reviewed journals where I was the first and/or corresponding author.

Chapter 4 is published as:

Panda, B., & Tan, M. J. (2019). Rheological behavior of high-volume fly ash mixtures containing micro silica for digital construction application. Materials Letters, 237, 348-351.
The contributions of the co-authors are as follows:

- I performed all the experiments and prepared the manuscript drafts.
- A/Prof Ming Jen provided the initial project direction and edited the manuscript drafts.

Panda, B., Ruan, S., Unluer, C., & Tan, M. J. (2019). Improving the 3D printability of high-volume fly ash mixtures via the use of nano attapulgite clay. Composites Part B: Engineering, 165, 75-83.

The contributions of the co-authors are as follows:

- I performed all the experiments and Ruan. S assisted in conducting XRD and FESEM study
- The manuscript was revised by Dr Cise and A/Prof Ming Jen provided the initial project direction

Chapter 5 is published as:

Panda, B., Unluer, C., & Tan, M. J. (2018). Investigation of the rheology and strength of geopolymer mixtures for extrusion-based 3D printing. Cement and Concrete Composites, 94, 307-314.

The contributions of the co-authors are as follows:

- I performed all the experiments and prepared the manuscript drafts.
- The manuscript was revised by Dr Cise and A/Prof Ming Jen provided the initial project direction

Panda, B., & Tan, M. J. (2018). Experimental study on mix proportion and fresh properties of fly ash based geopolymer for 3D concrete printing. Ceramics International, 44(9), 10258-10265.

- I performed all the experiments and prepared the manuscript drafts.
- A/Prof Ming Jen provided the initial project direction and edited the manuscript drafts.

Panda, B., Paul, S. C., Hui, L. J., Tay, Y. W. D., & Tan, M. J. (2017). Additive manufacturing of geopolymer for sustainable built environment. Journal of cleaner production, 167, 281-288.

- I performed the rheology experiments and prepared the manuscript drafts.
- Dr. Paul and Mr. Tay helped me in mechanical testing and 3D printing.
- Mr Hui provided his robot and controller for 3D printing purpose.
- A/Prof Ming Jen provided the initial project direction and edited the manuscript drafts.

Panda, B., GVP Bhagat Singh, Unluer, C., & Tan, M. J. (2018). Synthesis and characterization of one-part geopolymers for extrusion-based 3D concrete printing. Journal of cleaner production, 94, 307-314.

- I performed the rheology and 3D printing experiments and prepared the manuscript drafts.
- Dr. Bhagat assisted in the interpretation of the X-ray absorption spectroscopy data and carried out the spectral interpretation.
- The manuscript was revised by Dr Cise and A/Prof Ming Jen provided the initial project direction.

<u>Chapter 6 is published as:</u>

Panda, B., Paul, S. C., & Tan, M. J. (2017). Anisotropic mechanical performance of 3D printed fiber reinforced sustainable construction material. Materials Letters, 209, 146-149.

- I prepared the materials and performed 3D printing.
- Dr. Paul helped me in mechanical testing and also during the 3D printing.
- A/Prof Ming Jen provided the initial project direction.

Panda, B., Paul, S. C., Mohamed, N. A. N., Tay, Y. W. D., & Tan, M. J. (2018). Measurement of tensile bond strength of 3D printed geopolymer mortar. Measurement, 113, 108-116.

- I prepared the materials for 3D printing.
- Mr. Tay and Mr. Mohamed helped me in 3D printing and parameter setting.
- Dr. Paul conducted the mechanical tests.
- A/Prof Ming Jen provided the initial project direction.

Panda, B., Lim, J. H. & Tan, M. J. (2017). Mechanical properties and deformation behaviour of early age concrete in the context of digital construction. Composites Part B: Engineering, 165, 563-571.

- I designed the structure of this paper and conducted all mechanical tests.
- Mr. Lim assisted me in image analysis of the deformed concrete cylinder.
- A/Prof Ming Jen provided the initial project direction.

20/02/2019
Date

Biranchi Panda
BIRANCHI PANDA

ACKNOWLEDGMENTS

This work was undertaken in the Building and construction Laboratory, Singapore Centre for 3D Printing (SC3DP), School of Mechanical and Aerospace Engineering at Nanyang Technological University, Singapore.

I would like to express my heartfelt gratitude to my supervisors Associate Professor Ming Jen Tan and Dr. Cise Unluer for their guidance and encouragement throughout the PhD study. I appreciate Prof. Tan for leading the exciting research field of 3D concrete printing and making global impacts. He has always devoted his resources to support my research and provided invaluable guidance, whenever I encountered problems. I will also give my sincere thanks to Dr. Cise for her valuable inputs, continuous guidance and patience all through the research and writing phase.

My sincere thanks go to the SC3DP laboratory technicians (Mr. Haer, Mr. Justin, Mr. Daniel) and administration staff (Ms. Suan, Germaine, Ms. Adeline) for their assistance regarding laboratory techniques, equipment and official paperwork.

I would like to thank to our group members Daniel, Jian Hui, Nisar, Andrew, Lu bing, Yewei, Shaoqin, Dr. Mingyang, Dr. Suvash and Dr. Bhagath Singh for experimental assistance and valuable discussions that has contributed to the success of this research work. I would also like to acknowledge Sembcorp Architects & Engineers Pte. Ltd. and National Research Foundation (NRF) Singapore for their funding and support in this research project.

My wife, Karisma, I could never express how lucky I have you in my life. You scarified your valuable time to take care of our family, and I never doubt your love for me. Last but not the least, I am very grateful to my parents who has always encouraged and supported me throughout my studies.

ABSTRACT

Digital concrete construction has recently become the subject of very rapidly growing research activities all over the world. It opens a new horizon and unlimited possibilities for the concrete industry, especially in terms of geometrical flexibility, reduction of manpower and costs, increased productivity, speed of construction, and sustainability. The potential of digital production of concrete is represented by exponentially increasing innovative projects and research, which are often addressed using the generalized term "3D-concrete-printing". Recent advances in concrete printing have mainly focused on developing Portland cement (PC) based binders that are both extrudable and buildable. The production of PC is associated with many environmental challenges including the air pollution and devastation in land and resources. One of the promising measures is the development of sustainable cements, which can be achieved via two main pathways: (i) partial PC replacement with industrial by-products and wastes and (ii) new cement formulations based on different chemistry with lower environmental impacts. This thesis is dedicated to material synthesis of two promising sustainable building materials such as (i) high volume fly ash (HVFA) cement and (ii) geopolymer based cement for extrusion-based 3D printing application.

Rheology of fresh concrete is critically important in 3D printing process, that determines the material ability to be extrudable and buildable. With an aim of utilizing minimum 60-70% fly ash, HVFA cement was formulated while understanding the key parameters influencing yield stress, viscosity and thixotropy properties. Thixotropy was quantified using shear thinning and viscosity recovery protocols. In addition, structural-build up was measured in the dormant period, to control the buildability of printed structures. Considering the rheological requirements of a large-scale concrete printing, nanoclay was added as viscosity modifying agent (VMA) to improve the control mix performance.

The nanoclay was found to improve the thixotropy but had no effect on structural-build up rate which limited the part buildability. To accelerate the build-up rate, micro silica fume was incorporated in the mix design and better buildability was achieved due to significant improvement in the strength development property. The rheology and reaction product of the final mix design were characterized to resolve the underlying mechanisms using laser scattering, isothermal calorimetry, X-ray Powder Diffraction (XRD) and Field Emission Scanning Electron Microscopy (FESEM) techniques.

In the second part of the thesis, fly ash based geopolymer was synthesized with improved rheological properties for 3D printing process. High volume of fly ash was supplemented with blast furnace slag and micro silica fume to provide adequate microstructural packing required for printability. Shape retention, which is related to viscosity recovery was found to be improved with silica fume addition up to 10-15% without much affecting the extrudability. Solution of potassium silicate was used as activator in different concentration (molar ratio) and solution-to-binder ratio to understand the geopolymer rheology based on yield stress and viscosity values. The activator solution was found to reduce the yield stress and enhance the cohesiveness, similar to the use of superplasticizer in conventional PC system. Therefore, nanoclay was again used to improve the printability of geopolymer while minimizing the viscous effect of activator solution. In contrast, powder (potassium) silicate activated system show rheological responses similar to those of HVFA cement system. XRD and FESEM were used to quantify the resultant geopolymer reaction product and relate it to the 28 days mechanical strength.

In the last section, directional properties of both 3D printed HVFA and geopolymer samples were studied in terms of compression, flexural and tensile bond strength. Due to layering effect, 3D printed samples exhibited orthotropic properties with reduced bond strength with increasing inter-layer time gap. Effects of deposition speed and print height were also investigated, which concludes that the material build-up rate plays an important role in determining the final effect along with the printing parameters. Therefore, the

build-up rate was accessed via early age mechanical strength testing, where the fresh concrete was uniaxially deformed to obtain green strength and stiffness. Based on the green strength development and deformation behaviour, print path and speed were optimized to build two large-scale 3D printed structures for demonstrating the proposed criteria and mix designs are suitable in practice.

The contradictory challenge of 3D printing concrete i.e both pumpable as soft fluids and buildable as solid elements were solved in this thesis by understanding the rheology of two promising sustainable materials before, during and after the printing. Based on experimental observations, it is concluded that PC based plain mortars are deemed suitable for concrete printing while geopolymers need significant material tuning based on the printing process.

TABLE OF CONTENTS

LIST OF FIGURES

LIST OF TABLES

LIST OF ACRONYMS

B	
BIM	Building information modelling
BET	Brunauer–Emmett–Teller
C	
CAD	Computer-aided design
CC	Contour crafting
CSH	Calcium-silicate hydrate
D	
3DCP	3D concrete printing
E	
ECC	Engineered cementitious composite
F	
FTIR	Fourier transform infrared spectroscopy
FA	Fly ash
FDM	Fused deposition modelling
FGM	Functionally graded material
FESEM	Field emission scanning electron microscopy
G	
GGBS	Ground granulated blast-furnace slag
H	
HVFA	High volume fly ash
L	
LOI	Loss on ignition
LCA	Life-cycle analysis

M

MDM	Material deposition method
MR	Molar ratio

P

PSD	Particle size distribution
PC	Portland cement
PV	Paste volume
PCE	Polycarboxylate ether superplasticizer

S

SCC	Self-compacting concrete
SSA	Specific surface area
SCM	Supplementary cementitious material
SF	Silica fume
SRF	Shape retention factor
SSD	Saturated surface dry

V

VMA	Viscosity modifying agent

W

WFT	Water film thickness
(w/s) ratio	Water-to-solid ratio

X

XRD	X-ray diffraction

LIST OF PUBLICATIONS

Publications derived from the work in the thesis are listed below:

➢ Journal articles

Chapter 4

- **Panda, B**., & Tan, M. J. (2019). Rheological behavior of high-volume fly ash mixtures containing micro silica for digital construction application. ***Materials Letters***, 237, 348-351.
- **Panda, B**., Ruan, S., Unluer, C., & Tan, M. J. (2019). Improving the 3D printability of high-volume fly ash mixtures via the use of nano attapulgite clay. ***Composites Part B: Engineering***, 165, 75-83.

Chapter 5

- **Panda, B**., Unluer, C., & Tan, M. J. (2018). Investigation of the rheology and strength of geopolymer mixtures for extrusion-based 3D printing. ***Cement and Concrete Composites***, 94, 307-314.
- **Panda, B.,** & Tan, M. J. (2018). Experimental study on mix proportion and fresh properties of fly ash based geopolymer for 3D concrete printing. ***Ceramics International***, 44(9), 10258-10265.
- **Panda, B.,** Paul, S. C., Hui, L. J., Tay, Y. W. D., & Tan, M. J. (2017). Additive manufacturing of geopolymer for sustainable built environment. ***Journal of cleaner production***, 167, 281-288.
- **Panda, B**., GVP Bhagat Singh, Unluer, C., & Tan, M. J. (2018). Synthesis and characterization of one-part geopolymers for extrusion-based 3D concrete printing. ***Journal of cleaner production***, DOI: 10.1016/j.jclepro.2019.02.185

Chapter 6

- **Panda, B.,** Paul, S. C., & Tan, M. J. (2017). Anisotropic mechanical performance of 3D printed fiber reinforced sustainable construction material. ***Materials Letters***, 209, 146-149.
- **Panda, B**., Paul, S. C., Mohamed, N. A. N., Tay, Y. W. D., & Tan, M. J. (2018). Measurement of tensile bond strength of 3D printed geopolymer mortar. ***Measurement,*** 113, 108-116.
- **Panda, B**., Lim, J. H. & Tan, M. J. (2017). Mechanical properties and deformation behaviour of early age concrete in the context of digital construction. ***Composites Part B: Engineering***, 165, 563-571.

Others

- Tay, Y. W. D**., Panda, B**., Paul, S. C., Noor Mohamed, N. A., Tan, M. J., & Leong, K. F. (2017). 3D printing trends in building and construction industry: a review. ***Virtual and Physical Prototyping***, 12(3), 261-276.
- Paul, S. C., Tay, Y. W. D., **Panda, B**., & Tan, M. J. (2018). Fresh and hardened properties of 3D printable cementitious materials for building and construction. ***Archives of Civil and Mechanical Engineering***, 18(1), 311-319.
- Lim, J. H., **Panda, B.,** & Pham, Q. C. (2018). Improving flexural characteristics of 3D printed geopolymer composites with in-process steel cable reinforcement. ***Construction and Building Materials***, 178, 32-41.
- Tay, Y. W. D., Ting, G. H. A., Qian, Y., **Panda, B**., He, L., & Tan, M. J. (2019). Time gap effect on bond strength of 3D-printed concrete. ***Virtual and Physical Prototyping***, 14(1), 104-113.
- Tay, Y. W., **Panda, B**., Paul, S. C., Tan, M. J., Qian, S. Z., Leong, K. F., & Chua, C. K. (2016). Processing and properties of construction materials for 3D printing. ***In Materials Science Forum***. Trans Tech Publications. 861, 177-181

➢ Conference Presentations

- **Panda, B**., Mingyang, L., Tay, Y. W. D., Paul, S. C., & Tan M. J (2017). Modeling Fly Ash Based Geopolymer Flow for 3D Printing Applications. Construction materials and systems, 9. In proceeding of ***71st RILEM International Conference on Advances in Construction Materials and Systems***, September 3 - 8, 2017. IIT Madras, India.
- **Panda, B**., Lim, J. H., Mohamed, N. A. N., Paul, S. C., Tay, Y. W. D., & Tan, M. J. (2017). Automation of robotic concrete printing using feedback control system. In ***ISARC Proceedings of the International Symposium on Automation and Robotics in Construction*** (Vol. 34, pp. 1-5). Vilnius Gediminas Technical University, Department of Construction Economics & Property.
- **Panda, B**., Tay, Y., Paul, S. C., Tan M. J.., Leong, K., & Gibson, I. (2016). Current Challenges and future perspectives of 3D concrete printing. *In Proceeding of 2nd International Conference on Progress in Additive Manufacturing (Pro-AM 2016)*, Nanyang Technological University Singapore.
- **Panda B**., Noor Mohamed N.A., Tay Y.W.D., Tan M.J. (2019) Bond Strength in 3D Printed Geopolymer Mortar. In: Wangler T., Flatt R. (eds) ***First RILEM International Conference on Concrete and Digital Fabrication – Digital Concrete 2018***. DC 2018. RILEM Bookseries, vol 19. Springer, Cham
- **Panda, B**., Mohamed, N. A. N., & Tan, M. J. (2018, April). Effect of 3d printing on mechanical properties of fly ash-based inorganic geopolymer. ***In RILEM International Congress on Polymers in Concrete*** (pp. 509-515). Springer, Cham.

Technical Disclosures

- **Panda, B**., Paul, S. C., Tan M. J. Geopolymer material for 3D Printing and preparation method Thereof. REF NO: PAT/388/16/17/SG PRV

Chapter 1 Introduction

1.1 Research background

Concrete is the most widely used construction material in the world with over six billion tons produced each year. During the last two decades, there has been a rapid advance in adding powder, admixtures, fibers, etc. to conventional concrete in order to improve its workability (pumping, formwork filling, and passing across steel reinforcement) and mechanical strength [1]. A variety of concretes has been developed such as fiber reinforced concrete, polymer concrete and self-compacting concrete (SCC) etc. Each of the developed concretes has its own characteristics to overcome an encountered problem either in its fresh or hardened state.

SCC is highly flowable and gets compacted by itself. It has the advantages of easy placement in densely reinforced structures, high surface quality, durability and low-cost construction. Compared to conventional concrete, the rheological properties of SCC are improved by adding mineral and chemical admixtures [2]. However, creating complex shapes through SCC requires an adapted formwork. This kind of formworks is only used once which increases waste and construction cost. Another main challenge is related to the need of physical labour for erecting molds and reinforcement placement, especially when custom-made geometries are required. This results in various health and occupational hazards that should be avoided as much as possible [3]. To overcome this problem, many techniques have been developed by combining digital fabrication methods and development in construction material science. 3D concrete printing (3DCP) is one of such methods that has recently become the subject of very rapidly growing research over the world. [4]. 3D printing technology has been successfully applied in aviation, metal and other fields [5], however it is now gaining ground in the construction industry. The main feature of this technique is up-scaling a desktop 3D printer to the size of a construction site. The printing system of concrete is usually composed of a material

mixing tank, a material pumping system, an extrusion system (printing head with nozzle), a control box (electronics, positioning and control system) and a safety system. The mix could be a ready-mix or could be directly mixed before the printing process. The material is then pumped, passed through a pipe and injected from a nozzle. Next, the printer deposits layers of continuous concrete-like filaments on top of each other. After the first layer is printed, the next layer must be deposited immediately following the digital model [6].

Compared to other digital fabrication technologies such as computer-aided design (CAD), building information modelling (BIM) and powerful software tools that are well developed, 3DCP has certain additional benefits. On one hand, it can produce concrete elements using digital design and construction data provided by the BIM and on the other hand, it gives an opportunity to create unique elements, which corresponds to the idea of mass customization. Building components manufactured by 3DCP can have different designs and materials will be exactly placed, where there is need of material only. This will optimize the topology of the construction industry, which will lead to reduction in material consumption and consequently the creation of environmentally friendly facilities. The other expected benefits include higher productivity, faster construction processes, minimization of human resources, less waste of material wastes, efficient use of natural resources, higher cost-efficiency, etc. [7,8].

To maximize the benefits of 3D printing, the first step should be to develop a printable material that must be flowable during extrusion and after extrusion, it must retain its shape without significant deformation due to the deposited layers over it [9]. Considering this fact, developments are going on by various universities and industries to realize the potential of 3DCP. Building components can be produced either on site [10] or like Winsun, China pre-fabricated walls can be manufactured off site and later assembled to produce the final structure [11]. The choice of production again can be like regular wall elements or also can be optimized for minimizing the material wastage and construction cost.

1.2 Motivation and objectives

The production of cement is very energy intensive process and it is responsible 5% of global CO_2 output [12]). In order to reduce the environmental impacts of cement industry, approaches have been carried out on finding alternatives to ordinary Portland cement (PC). Among those investigations, fly ash (FA) based sustainable building materials such as geopolymers have attracted great attention and it generate nearly 80% less CO_2 than PC [13]. Moreover, the mechanical properties are generally higher than PC based materials, especially the early strength development [14]. Excellent durability was also reported like better resistance of sulfate and acid attack, improved freeze-thaw resistance due to the refined pore structure, significantly higher fire resistance [15]. Considering the need of rapid hardening material in 3DCP, it would be surely interesting to study and use geopolymer binders since it exhibits rapid (structural) build up property aside from being a sustainable material. The rapid hardening material will allow to easily deposit more layers without the need of any accelerators, however the rheological property still need to be explored as it is not well understood for ensuring printability.

It is well known that thixotropy is one of the important properties in all 3D printing projects. PC has an inherent excellent thixotropy property due to flocculation and literature reveals that in the presence of any foreign materials like FA, sand, fillers it's colloidal network breaks down, thus resulting loss of the thixotropy [16]. One such example is high volume fly ash (HVFA) material which not only possess low thixotropy but also slow hardening rate. Despite sustainability, poor early age mechanical properties limit its application for 3D printing projects. This motivated the author to conduct an extensive study with an aim to improve the printability of HVFA binders.

The main goal of this research is to get a better understanding of these two-3D printable FA based sustainable mixtures such as (1) HVFA cement and (2) geopolymer. The study contains the following objectives:

(1) HVFA material design for 3DCP application

Development of HVFA mortar that can be buildable and has an excellent shape retention after deposition on the print bed. Since rheology is one of the critical parameters affecting 3D printability, the first objective is to optimize the mix design and quantify the rheological parameters such as yield stress, viscosity with more emphasize on thixotropy and structural build-up characteristics.

(2) FA based geopolymer material design for 3DCP application

Unlike PC, geopolymer possess different rheological properties due to polycondensation reaction in the alkaline medium. The second objective is therefore to understand and optimize the rheology parameters of fresh geopolymer mortar such as yield stress, viscosity, thixotropy etc. for extrusion-based 3D printing application.

(3) Mechanical properties of 3D printed concrete

Layer wise deposition are likely to produce anisotropic mechanical properties, and in this regard, the third objective of this research is to evaluate the mechanical performance such as compressive, flexural and tensile strengths of the 3D printed HVFA and geopolymer mortars.

(4) Effects of printing parameters and large-scale printing

Printing parameters such print speed, flow rate, layer height significantly affects the final properties of the filament and depending on the part design, these parameters also need to be adjusted to avoid defects like cracking, cold joints etc. The fourth objective is therefore, to investigate the influence of printing parameters including the part design and conduct a large-scale printing with the knowledge acquired from both material design and parameters settings.

1.3 Scope of the thesis

In this research only two types of sustainable building materials are used (1) HVFA and (2) geopolymer, since the main goal is to maximize the utilization of major industry by-product FA. Fine river sand was used to prepare the mortars due to easy of resource availability in Singapore. There were no chemical admixtures (accelerator, retarder) used in the mix formulation to keep the final product simple and cheap for field application. A very small amount of viscosity modifying agent (VMA) (<1%) was only allowed to improve the 3D printability performance including cheap mineral admixtures like silica fume (SF) and ground granulated blast-furnace slag (GGBS). After hardening, all the mechanical properties were studied up to an age of 28 days, which is the most commonly used curing time in many published and unpublished articles.

1.4 Layout of the thesis

This thesis consists of 7 chapters in total, the details of which are provided below:

Chapter 1 introduces the research and provides background information about the topics investigated under this research and presents the main goals and objectives.

Chapter 2 provides a detailed relevant literature review focusing on the production and properties of 3D printable concrete mixtures, mechanical properties and effect of various printing parameters. A section about different 3D printing systems is also included in addition to large scale concrete printing examples currently explored, both in academia and in construction practices.

Chapter 3 presents the materials used, sample preparation and methodology in all the experiments in this research work.

Chapter 4 focuses on the influence of mix design parameters and quantification of rheological attributes for 3D printing HVFA mortars. The effect of fly ash-to-(total) binder ratio, water/binder ratio, and sand content on performance were discussed along with the mechanical and microstructural study under ambient curing condition. The

effects of different mineral additives and VMA were also explained in this chapter for improving the 3D printability.

Chapter 5 discusses the performance of FA based geopolymer mortar designed for 3D printing application. Effects of activator viscosity, activator-to-binder ratio, water-to-binder ratio were discussed including FA and GGBS replacement ratio. Similar to HVFA, mineral additives and VMA were selected to improve the 3D printability of the geopolymer in terms of shape retention and buildability. Geopolymers made using powder activator was also introduced to envisage the printability performance compared to liquid activator.

Chapter 6 is dedicated on measuring the mechanical performance of 3D printed samples in three orthogonal directions. Compression, flexural and tensile properties were obtained and compared with casted samples. Effects of printing parameters were also explained in this chapter for different part design configurations and finally, with the knowledge of suitable parameters setting and material design, large scale 3D printing was demonstrated for the developed FA based sustainable materials.

Chapter 7 highlights the main findings reached and presents guideline for further related studies.

Figure 1.1 shows the systematic research methodology adopted in this thesis to print sustainable concrete structures. The novelty of this PhD research is the sustainable material design for a new digital manufacturing process, known as 3DCP. This technology offers an opportunity to integrate part design and material digitization to create complex geometrics, inhibited by traditional casting process. The printing technology and material formulation are addressed in the current work.

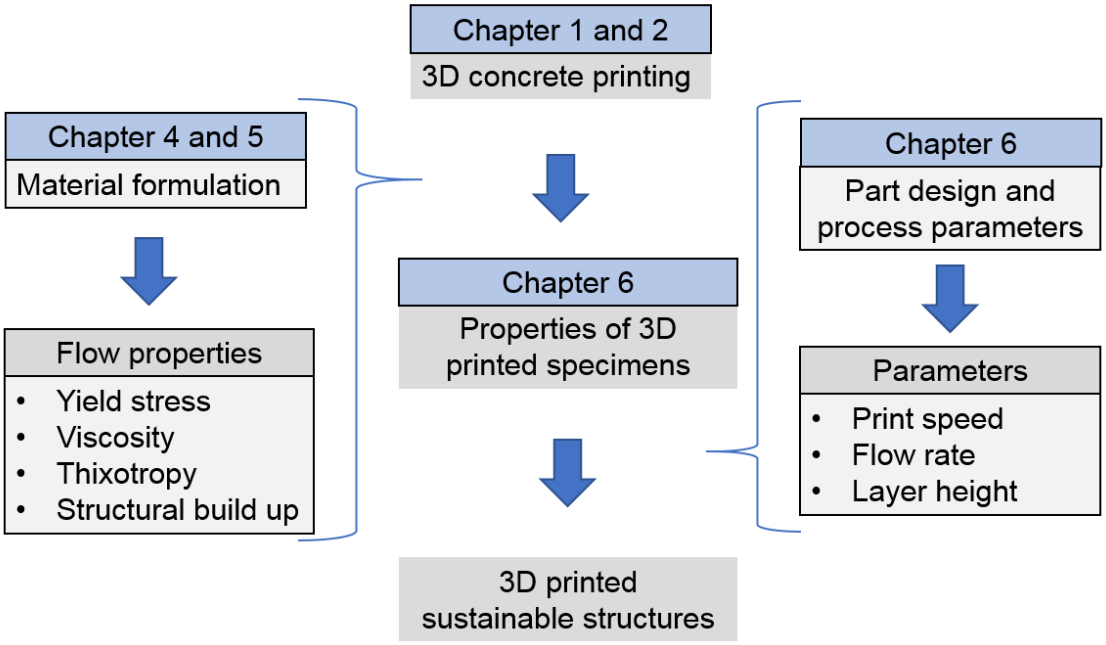

Figure 1.1 Outline of the thesis

Chapter 2 Literature review

In this chapter, fundamental understanding of the 3DCP system is provided, including a comprehensive review of two sustainable building materials. Only extrusion-based concrete printing process is emphasized since this technology has been used to perform all the experiments and accordingly, both materials and process parameters are optimized for a large-scale part design. The merits and disadvantages of the other concrete printing processes are also discussed.

Fresh and hardened properties of the printed concrete are reviewed in terms of rheology and mechanical strength. Additionally, potential applications of the concrete printing technology are explored for building and construction industries.

2.1 Production and properties sustainable binders

2.1.1 High volume fly ash binder

Although there are many studies in the literatures on the properties of concrete containing FA, only publications relevant to the study were reviewed in this section.

FA based concrete in combination with PC has been developed for nearly half a century [17]. FA is a by-product of thermal power plants and it is collected from the combustion residue before they are discharged to the atmosphere. FA, besides being used as an admixture for concrete also finds application as an additive in artificial lightweight aggregate, refractory materials, bricks, and in soil improvement. In general, FA consists of glassy spheres of sizes varying from 1 to 150 μm and based on mineralogical composition, it can be divided into two categories such as Class F and C. Class F FA contains $SiO_2 + Al_2O_3 + Fe_2O_3 > 70\%$, and very less CaO (<5%), whereas Class C contains $SiO_2 + Al_2O_3 + Fe_2O_3 > 50\%$, and more CaO (around 20%) [18].

The higher replacement of PC with 50% or above is termed as HVFA concrete as per CAMNET by Malhotra in 1980 [19]. This aim was to increase the sustainability in

construction industries by reducing the PC usage and thereby reducing the CO_2 emissions associated with PC production. According to life-cycle analysis (LCA) by Griffi [20], there is a possibility to reduce 54% of CO_2 emissions by using a 50% replacement of PC with FA.

The principal hydration product using only PC binder is a colloidal calcium-silicate hydrate (C-S-H) gel and it occupies about 40 to 70% of the hardened cement paste volume. This gel and Ca $(OH)_2$ are responsible for increasing the concrete strength with reaction time. When FA is added to PC, it reacts with Ca $(OH)_2$ produced from hydration of PC to form C-S-H with different Ca/Si ratio [21-25]. The advantage of FA in concrete can be visualized in terms of reduced water demand, heat of hydration, drying shrinkage and reduced permeability, which will reduce the sulphate and chloride ingress. It increases workability, compressive strengths (after 56 days) and gives a better surface finish to concrete due to the spherical shape, which in other hand improves the durability by reducing water requirement [26].

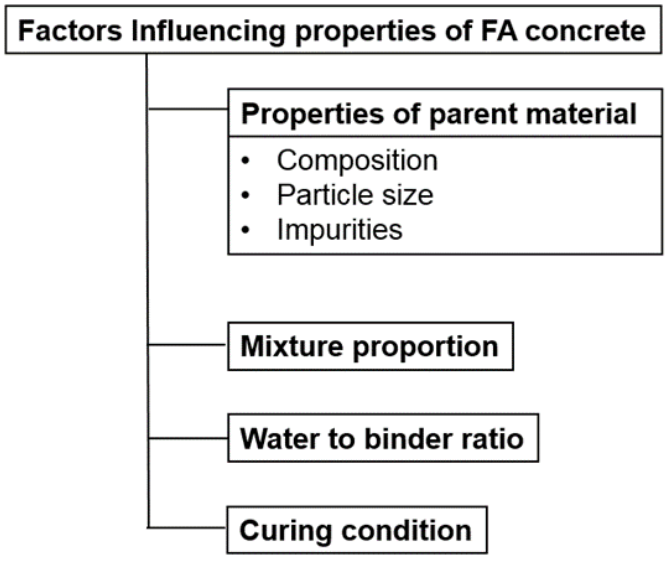

Figure 2.1 Factors influencing the properties and performance of fly ash concrete

FA concretes exhibit different properties depending on the source materials, mix design and curing conditions. The main factors influencing the properties and performance are reactivity, specific surface area (SSA), particle size, pH and morphology [27-29] as shown in Figure 2.1. The SSA determines the reactivity, which also depends on the characteristics of the FA source and the system in which FA is used. The packing and nucleation effect also depend on the size of the FA used in cementitious mix [30]. Chindaprasirt et al. [31,32] conducted an exhaustive study by using different sizes of FA and reported the advantage of finer FA in terms of increased compressive strength, reduced shrinkage and expansion etc. Size of FA can be reduced (by milling processes) for obtaining different PSD and their final properties are widely reported in literature [33-35]. Bentz et al. [36, 37] investigated the rheological properties of blended cement-based materials by varying the PSD and ratio of FA-to-PC in terms of yield stress and viscosity. Based on the conclusion, yield stress was found to be dominated by the particle density of the PC, with the FA mainly acting as a diluent that effectively decreases the PC particle density and thus the yield stress. Viscosities are influenced by both PC and FA particles where a linear relationship was obtained between plastic viscosity values and either total particle surface area or total particle density. In another study [38], use of Class C grade FA revealed higher yield value and plastic viscosity as compared to the neat PC paste. Additional grinding of the high-calcium FA improves the rheological properties of pastes (increase in fluidity) and this effect was negligible for the lowest FA content (20%).

The properties of FA collected from different power plants can be characterized for distinct crystalline and amorphous phases that determines the reactivity of FA [39,40] Most of the FA are made of glassy material (amorphous nature) and usually, the FA with higher amorphous content provides higher strength due to enhanced pozzolanic reaction. The pozzolanic reaction of the FA based material is the chemical reaction between amorphous silica or alumina in the FA and calcium hydroxide formed from cement hydration in the presence of water at normal temperature. Sakai et al. [41] investigated the effect of amorphous content in FA and reported that in an alkaline environment, low

calcium FA is non-reactive and therefore, there is a need of alkali or sulfate activation. The glass phases of FA can be dissolved in alkaline condition to accelerate the reaction at early ages [42,43]. Rather than relying on caustic alkalis, recent studies have attempted to activate the FA based systems through the use of neutral salts such as sulfates and carbonates of sodium and potassium [44]. Addition of Na_2SO_4 increases the pH of the solution, accelerates the pozzolanic reaction between Ca $(OH)_2$ and the FAs [45].

Apart from alkali activation, nano modification and use of different accelerators have been reported in the literature to overcome the slow strength development of HVFA mortars. Among all nano materials, nano silica has been used most widely followed by nano-$CaCO_3$ due to enhanced pozzolanic reaction and improved particle packing of the matrix [46-48]. Calcium hydroxide and a rapid set cement also have been used to mitigate excessive retardation of the FA based concrete. Experimental results measured by both Vicat setting time and rheology evolution indicate a significant reduction of setting time, which further depends on FA grade and dosage amount. The authors highlighted the advantage of using rheological measurement over Vicat penetration test for providing a faster indication of setting time [49-51].

Due to variability in the FA quality, achieving constant mechanical properties is difficult by using high volume of FA and therefore, researchers have attempted to investigate the effects of controllable parameters such as water-to-binder ratio, sand-to-binder ratio and curing conditions (20^0C and 40^0C) to optimize the mix formulation [52-54]. Siddique et al. [55] while replacing PC with class F grade FA in three percentages such as 40%, 45%, and 50% found a significant improvement in strength and abrasion resistance properties at the ages of 91 and 365 days, which was most probably due to the pozzolanic reaction of FA. Similarly, Wang et al. [56] analyzed the strength development by varying the fly ash content and total water content and reported the water-to-binder ratio is most significant parameter affecting the compressive strength for high volume FA mixtures. Despite of other factors considered in the literature, curing/environmental conditions play a significant role [57-59] in achieving potential strength of the FA based concrete. While there are reports about the reduced strength at high temperature curing, few reports

also state the long-term benefit of FA mixtures in improving the mechanical strength [60] at increased curing temperature. Further studies are thus needed in this regard to explore the reaction kinetics in different curing temperatures.

2.1.2 Geopolymer binders

2.1.2.1 Geopolymer Theory

The word ‘‘geopolymer” was coined by Davidovits, where the prefix ‘‘geo” symbolizes the inorganic aluminosilicate materials. Geopolymerization is an exothermic chemical reaction that converts the amorphous aluminosilicates sources into three-dimensional polymeric networks. The chemistry of alkalination depends on the nature of both aluminosilicate sources and the alkali activator used, though the mechanism remains same regardless of the starting materials. Davidovits et al.[61] suggested the geopolymer formation as shown in Figure 2.2.

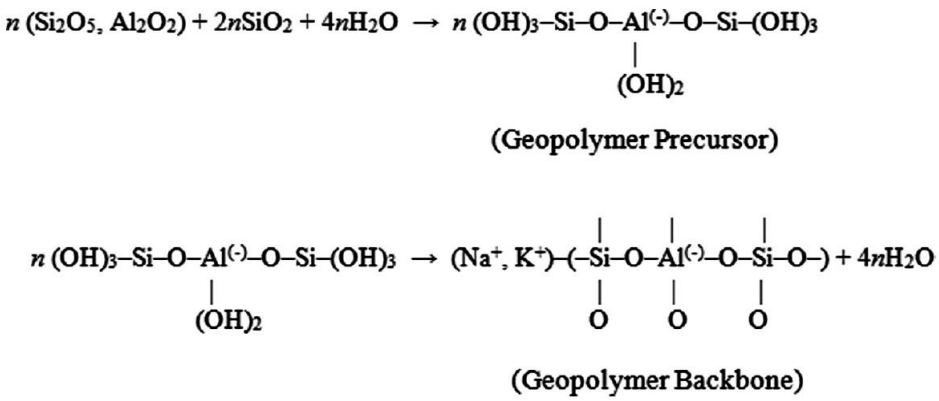

Figure 2.2 Schematic diagram of geopolymerization process [61]

The geopolymerization reaction is suggested occur in multi-step (Figure 2.3) which occurs simultaneously [62-65]:

(a) Dissolution of aluminosilicates;

(b) Reorganization and formation of small oligmers structures;

(c) Polycondensation to form aluminosilicate gel phases; and

(d) Solid state transformation to form hard solid

During geopolymerization, Si and Al units dissolve from precursors and they interact among each other to produce coagulated structure as agreed by most researchers [66-70]. As the reaction progresses, intermediate product (Gel 1) which has high Al content transforms into Gel 2 which has more Si content (Figure 2.4). At last, the gel grows and forms three-dimensional frameworks.

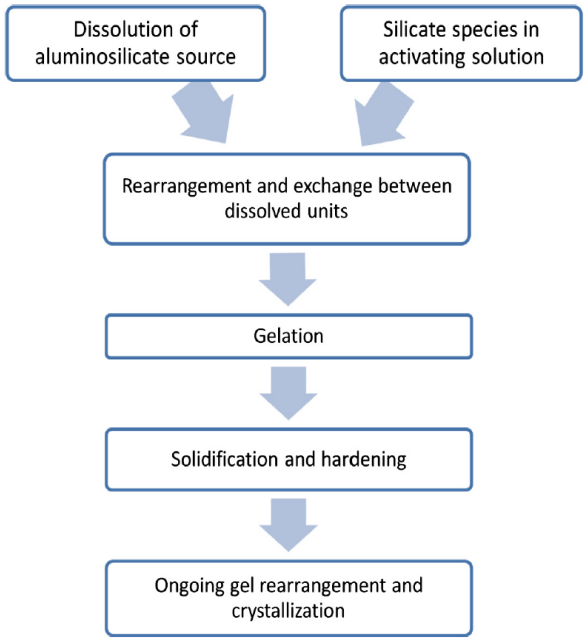

Figure 2.3 Step-by-step geopolymerization process [71]

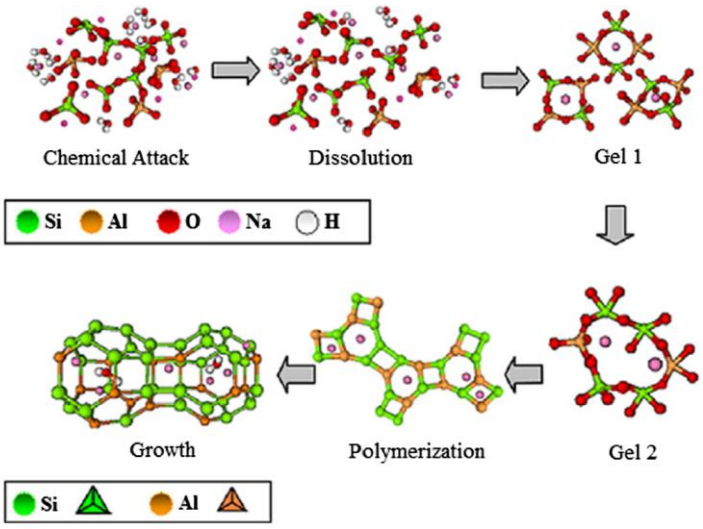

Figure 2.4 Graphic model of alkalination of geopolymers [72]

2.1.2.1 Synthesis and properties of geopolymer

There is a great number of published literatures on the properties of geopolymer derived from different raw materials such as FA, GGBS, metakaolin, red mud etc. However only FA/GGBS based geopolymer is described here due to the importance and relevance to this study.

Aluminosilicates such as FA, rich in alumina (Al_2O_3) and silica (SiO_2) minerals is the most widely used raw material to formulate geopolymer binders along with alkali silicates. The source materials play an important role in the binder formulation, preferably, the Al_2O_3 and SiO_2 compounds that are in reactive amorphous phase [50,51], with total composition of more than 70%. The activation of the FA together with GGBS contribute most significantly in the production of a structurally sound material via geopolymeric process. The GGBS addition helps to harden the binder in room temperture (23 ± 2^oC) without the need of any additional heat source or curing conditions [61]

The most common alkaline activators used in geopolymerization is a combination of sodium hydroxide (NaOH) or potassium hydroxide (KOH) and sodium silicate

($Na_2O{\cdot}nSiO_2$) or potassium silicate ($K_2O{\cdot}nSiO_2$) [73]. Sometimes SF is also used as an alternative to the sodium silicate, which forms part of the reactant solution [74].

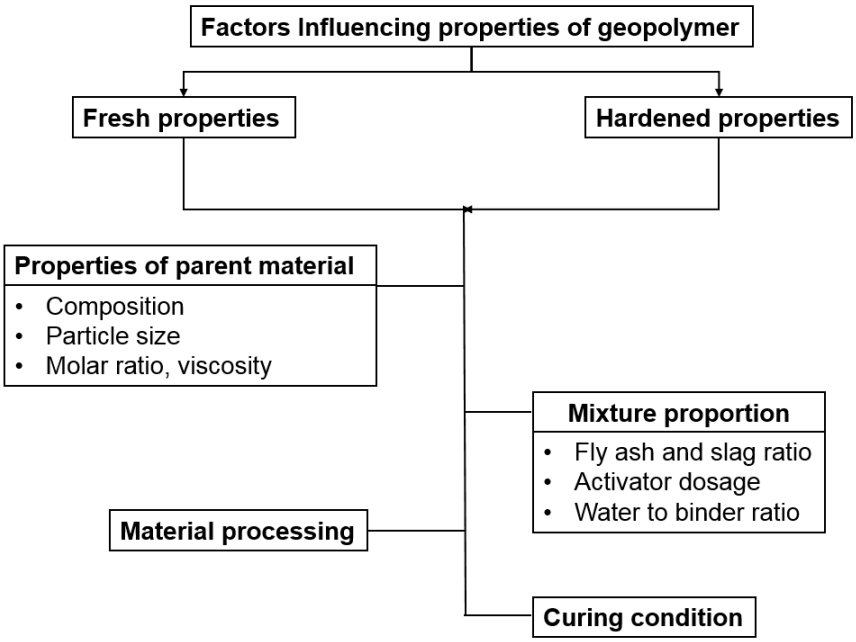

Figure 2.5 Factors influencing the properties and performance of geopolymer

Several factors have been identified as important parameters affecting the properties of geopolymers. Starting from raw material to mix design, each component shown in Figure 2.5 determines the overall fresh (e.g., setting time, flowability) and hardened properties (e.g., compressive, tensile strength) of geopolymers [75-77]. While the fresh properties of PC have been investigated in depth in literature, they have not yet been explored for geopolymers [78-83]. A exhaustive investigation by Vance et al. [84] revealed that viscosity of the activator and it's ratio to the geopolymer binder strongly influences the overall viscosity, where as the yield stress is influenced by the particle (FA) surface charge and alkali ions present in the activator. An increase in activator concentration increases the yield stress and viscosity which is similar to the changes in the activator viscosity. Using NaOH as sole activator, Zhang et al. [85] also observed similar behaviour in the FA/GGBS mixtures due to increase in activator viscosity. Collins and

Sanjayan [86] studied the workability of both solid and liquid silicate activated slag concrete and found better workability as well as longer stting time due to lower (initial) reactivity of solid activator. Laskar & Bhattacharjee [87] studied the rheology of FA-based geopolymer concrete using 1 to 20 M alkali activator. They found a strong influence of molar strength (M) and the ratio of silicate to hydroxide solution on yield stress and viscosity of the geopolymers. The setting time of geopolymer concrete was reported up to 120 minutes. Sathonsaowaphak [88] investigated the workability of lignite bottom ash based geopolymer mortars with respect to activator/ash ratio, Na_2SiO_3/NaOH ratio, NaOH concentration, and water/ash ratio that notably affects the resultant flow properties. Studies conducted on effect of GGBS addition [89,90] concluded that GGBS particles decreases the workabilty of geopolymer due to angular morphology and Huseien et al. [91] observed the similar behaviour when up to 20% GGBS was replaced with the FA. Based on experimental findings, Yan and Sagoe-Crentsil [92] confirmed that the flow behavior of geopolymers can be significantly modified by incorporating dry wastepaper sludge, since plenty of free water in the mix will be absorbed by the sludge, which will ultimately decrease the flow properties. Similarly, silica particles were also found to decreases the flowability due to high surface area and fine particle size.

In terms of setting time, increasing molar ratio (MR) of the activator causes remarkable reduction in the initial setting time due to faster dissolution of Si, Al ions and it can be further accelerated by adding calcium containing materials such as lime and GGBS. Several authors have reported different setting times of geopolymers by varying the activator type, dosage under different curing conditions [93, 94]. Favier et. al [95] investigated the setting process of metakaolin based geopolymer (in terms of early age rheological changes) and concluded that the Al rich gels formation at the grain boundaries are responsible for the initial setting (strength gain) and similar observations have also been idenitfied by Chen et al. [96].

Like rheological properties, mechanical properties of geopolymers are also affected by the activator type, dosages and starting raw materials [97-101]. Literature reveals better mechanical properties of the geopolymer over PC composites [102,103] and it increases

with the activator (NaOH) concentration [104]. Hardjito et al. [105] produced FA-based geopolymer concrete with compressive strength up to 80 MPa and highlighted the importance of water-to-solid ratio, as the strength notably decreases by addition of water. The role of water in geopolymer was found to be analogous to the well known relationship between compressive strength and water-cement ratio for PC concrete and confirmed by several authors [106, 107].

In the light of above discussion, it is clear that mixture design of the geopolymer plays an important role in governing the final mechnical strength. Effects of activator, binder, aggregate, curing methods have been well studied in the literature with their reaction mechanisms and relatively less work was found for the rheological study. The exact nature of rheolgical consequences of geopolymer is still not fully understood and requires additional work.

2.2 3D Concrete printing

2.2.1 Current 3D printing systems

The rapid development of large-scale 3DCP technology in most literatures is categorized into two techniques, namely (1) binder jetting and (2) material deposition method (MDM). The basic principle of both these techniques is to build up any complex structure by adding small layers of material following the CAD model. Like other 3D printing processes, 3DCP begins with the creation of 3D model, which is sliced into several 2D layers and then printed with an assigned material in an incremental manner to obtain the final prototype. The detailed descriptions and main difference between two techniques are highlighted in the following sub sections [108]:

(1) Binder jetting

Binder jetting is a 3D printing process that creates objects by depositing binder layer by layer over a powder bed. Binder is ejected in droplet form onto a thin layer of powder material spread on top of the build tray. This method incrementally glues 2D cross sections of the intended component to each layer of material powder [109]. The cycle repeats until the whole 3D object is complete (Figure 2.6). Any raw material that is not glued by the binder remains inside the constrained build container and is used to support subsequent layers. The unbound material can be removed from the print bed using a vacuum cleaner after the printing, which can be recycled and deployed for another printing task [110]. The advantage of this method is that it allows printing of overhanging designs for producing complex geometries and because of the minimal distance between layers, the part has higher resolution that results in the good surface finish. Currently, Voxeljet and Monolite UK Ltd (D-Shape) are working with this technology to print large-scale components for architecture and building industries. Figure 5b shows an egg-shaped complex sculpture, made by D-shape using a sand-based material; however, this technique can be easily influenced by bad weather, and is difficult to use this process for in situ construction applications [111].

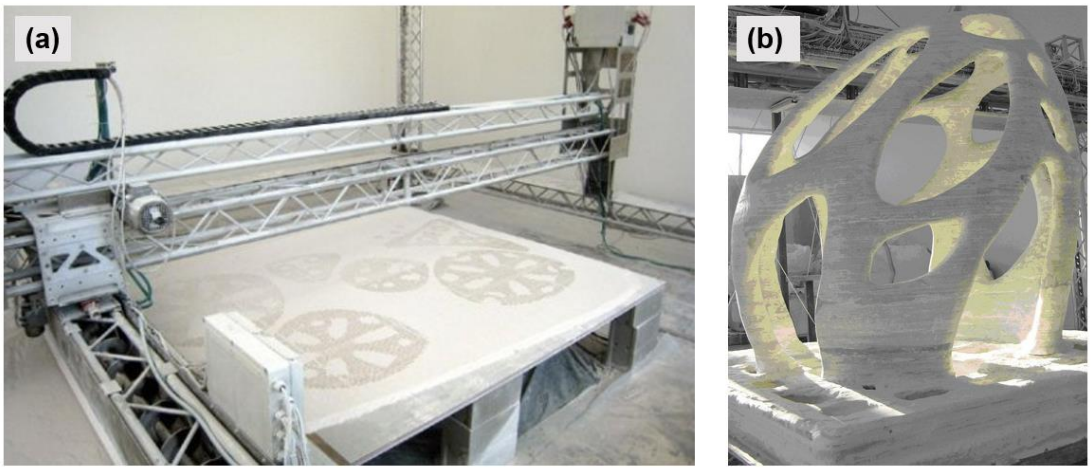

Figure 2.6 a) D-shape printer and (b) final printed component with all the excess raw material removed [111]

(2) Material deposition method (MDM)

Similar to fused deposition modelling (FDM), material deposition method (MDM) is an extrusion-based 3D printing process where the extruded layers are successively deposited as specified in the CAD model [112]. The main challenge is to develop a material that retains its shape after extrusion and hold the loads of multiple layers without significant deformation. Contour crafting (CC) is the first technology to use this MDM process as a core fabrication method and it was introduced by Khoshnevis in the mid-1990s in California, USA [113]. In this approach, the contours of mostly vertical structural elements are produced by extruding concrete filaments (Figure 2.7a) with a width of 2 to 5 cm and a height of generally 1 to 3 cm. These contours establish a permanent, integrated formwork which is eventually filled with flowable concrete in most cases. The key feature of CC is the use of trowels attached to the nozzle. The trowel guides the printed material to create exceptionally smooth and accurate surfaces, as shown in Figure 2.7b.

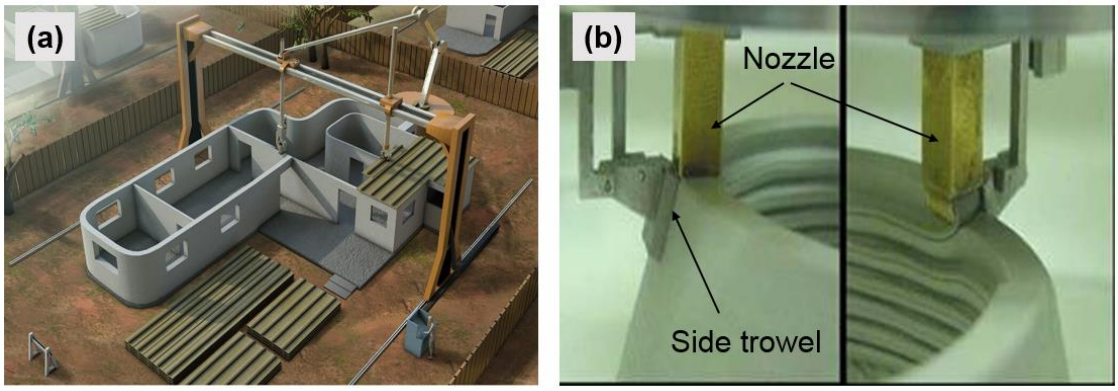

Figure 2.7 (a) Contour crafting process (b) extrusion nozzle with a side trowel [113]

This popular CC approach was introduced into the construction practice by companies like WinSun, TotalKustom and ApisCor and later termed as "3D concrete printing". Researchers at University of Loughborough [114] also followed this approach to print varieties of freeform structures, including channels for reinforcement (rebar) addition. Figure 2.8 shows some noteworthy examples of projects using 3DCP.

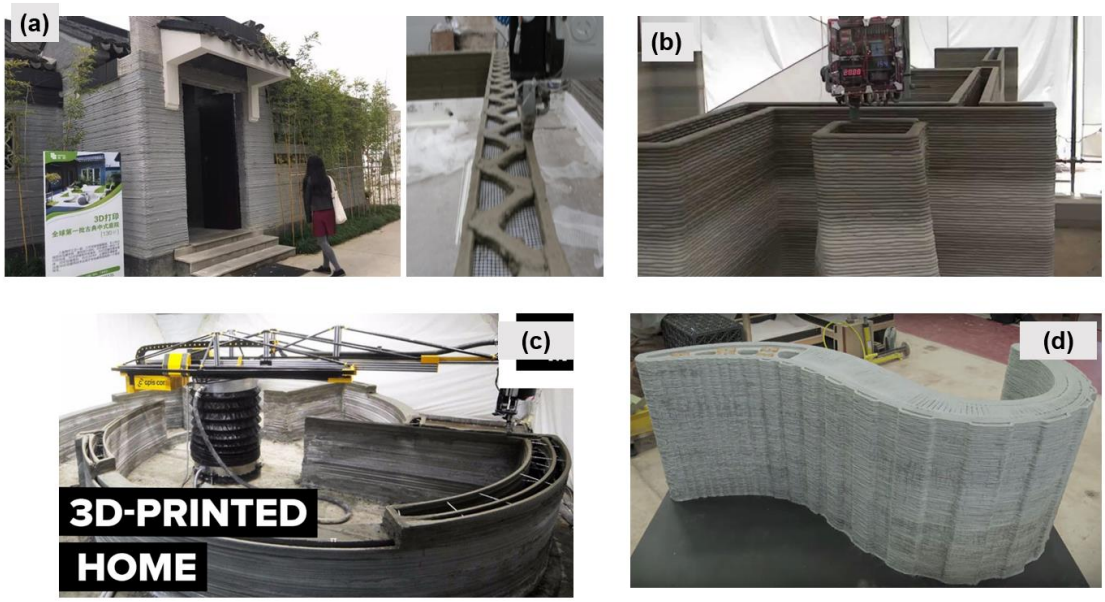

Figure 2.8 Noteworthy examples of projects using 3DCP: (a) Single storey House in China by HuaShang Tengda (b) Hotel suite interior in the Philippines, by Total Kustom (c) Residential house by San Francisco-based 3D printing startup Apis Cors (d) multi-cellular curved bench by Loughborough University, Loughborough, U. K [11, 12,114,115]

The process of 3DCP can be accomplished either by a gantry or robotic system that can hold the extruder (nozzle) and move according to the toolpath specified in the CAD model [116]. Despite having more degree of freedom, robots were found to be less used on construction sites, rather a gantry type printer with an additional axis for nozzle tip rotation. Figure 2.9 shows a typical gantry and robotic printer used for concrete printing application. The advantage of robotic printer can be guaranteed for 3D printing on temporary curved surfaces and any topology optimized structures.

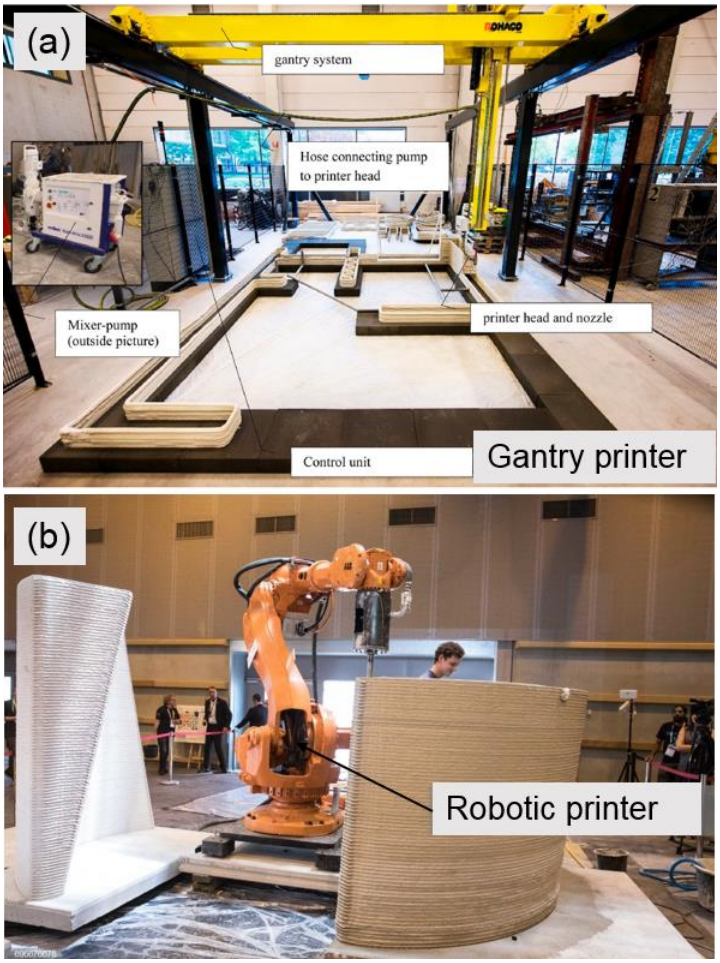

Figure 2.9 The two most used 3D concrete printers (a) gantry (b) robotic [117, 118]

Instead of using single, large robot, the Institute of Advanced Architecture of Catalonia (IAAC) in 2014 introduced a group of small robots that can work together using swarm technology as shown in Figure 2.10a. Similar work has been recently reported by a team of researchers from NTU, Singapore, while demonstrating the ability of large-scale concrete printing by a team of mobile robots (Figure 2.10b).

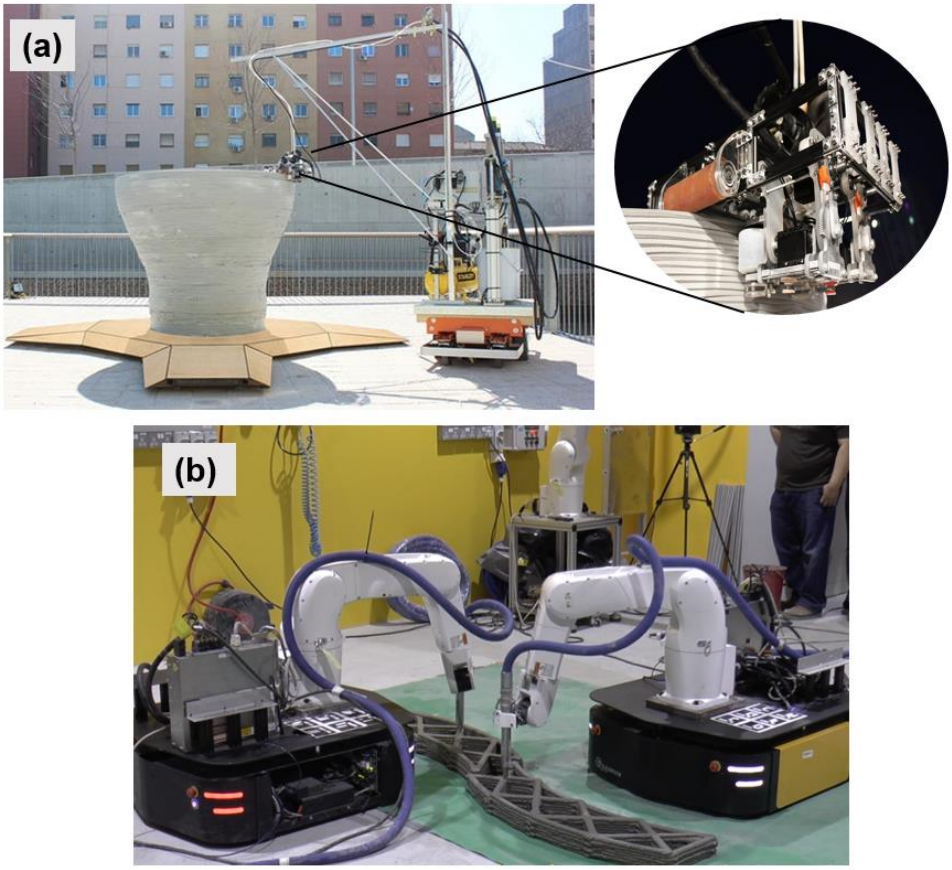

Figure 2.10 Robotic swarm 3D printing (a) Wall-climbing mini-bots mini-bots by Institute of Advanced Architecture of Catalonia, Spain (b) Synchronized 3D printing of concrete by robots at Nanyang Technological University, Singapore [119, 120]

The main limitation of extrusion based concrete printing is to produce some overhanging features without using any support material. In 3D printing of plastic, polymers, meta-materials the deposited layer hardens rapidly, while in 3DCP and other concrete-based methods, the filaments are in an in-between state, depending on the time since deposition and material setting time as mentioned in [121]. The slow hardening of the 3DCP materials results from the slow hydration reactions and which also depends on the target part geometry can be improved with admixtures. Nevertheless, some approaches have been attempted to print support structures on curve bed (Figure 2.11) and in this regard, the use of a robotic printer is helpful that can travel in the tool path lied along the curved print bed.

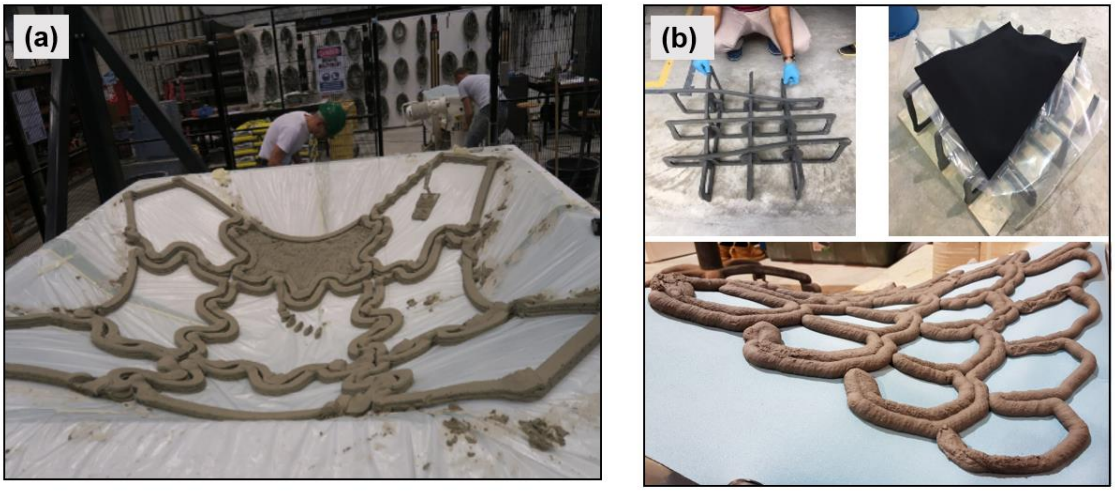

Figure 2.11 Curve bed 3D concrete printing projects at (a) Tu/e, Eindhoven, Netherlands [122] (b) Nanyang Technological University, Singapore

In addition to concrete printers, different material delivery systems were noticed in construction applications which can also affect the 3D printing performance. Progressive cavity pump is mostly used to extrude the fresh concrete, which can be connected to a batch or in-line mixing system. The advantage of in-line mixing will be more pronounced for a rapid setting material, while in batch mixing large-volume of material with long setting time is preferred.

2.2.2 Process parameters

The most striking difference of 3DCP with other 3D print methods is the print size which is very relevant to the way of printing and it affects the final quality, particularly the geometry and stability of the filament. The part design also plays an important role together with the material and printing parameters [123] such as print speed, print time, setting time, and layer interval time. (Figure 2.12).

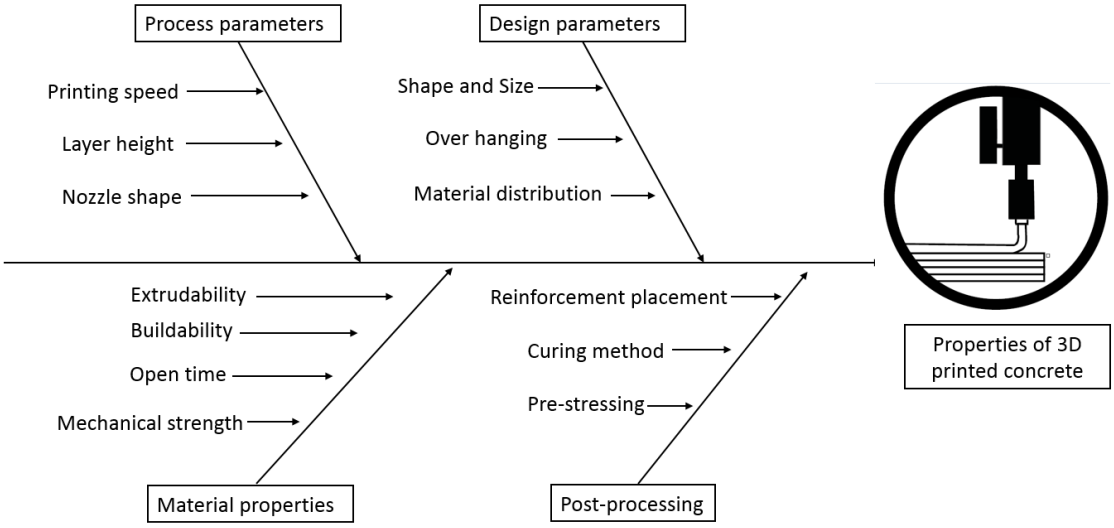

Figure 2.12 Cause and effect diagram of 3D concrete printing process

Research done at Tu/e, Eindhoven [121] describes the effect of tool path on filament shape and reported that the nozzle movement need to be planned in such a way that it should always remain tangent to the tool path, otherwise, filament bending will occur except for circular nozzle. In order to rotate the nozzle, another axis must be added to the gantry system and very few printers around the world are already capable of doing this. Since circular nozzle does not need any rotation, it is the simple and easy way to use it, though there are few demerits using the circular nozzle.

Following the selection of nozzle opening size, the print speed also needs to be precisely determined with respect to flow rate. The dimensions of printed filament not only depend on the material type, but also number of parameters such as flow, print speed, nozzle dimension, inclination of the print bed etc. To determine the optimum print speed, Panda et al. [124] conducted series of experimental study by varying the print speeds at a constant flow rate and for a high-volume slag material, 80 mm/sec was selected as optimum speed since filament dimension was almost equal to the nozzle dimension (Figure 2.13)

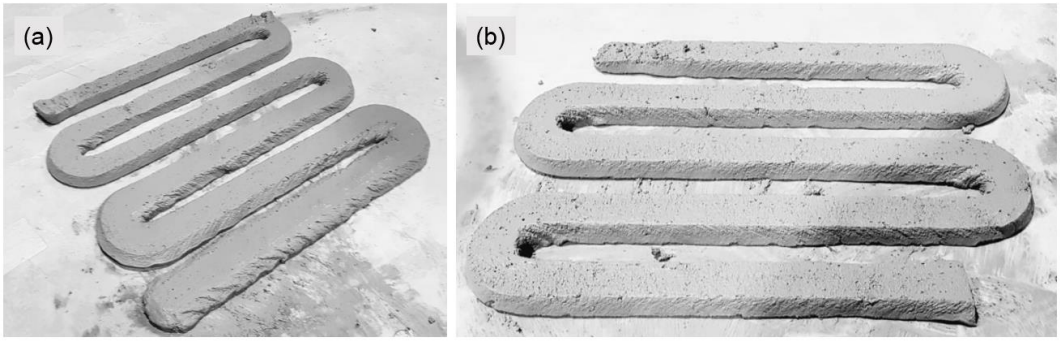

Figure 2.13 (a) Effects of print speed on filament width (b) continuous printing of concrete for a balanced flow and speed [124]

When extruding material in a curve tool path, a difference in deposition rates (between the inside and outside of the filament) was observed by Bos et al. [121] due to lack of minimum radius of curvature. In this research, a similar phenomenon was also observed while printing the geopolymer and HVFA mortars. For a certain nozzle dimension and material, there exist a minimum radius of curvature which currently cannot be estimated using any commercially available CAD/ CAM software. Le et al. [114] discovered the presence of air cavities in between the filaments placed next to each other in 3DCP, however this problem can be avoided by using a square or rectangular nozzle with sufficient flow capacity. In addition, a slight pressing (Figure 2.14) of during layer deposition can minimize the voids by improving the compaction as well as interface adhesion [121].

In the light of above discussion, it is imperative that in concrete printing, material, part design and process parameters are all strongly interdependent with each other. This interdependency is due to slow setting reaction in the concrete that results strong interaction with the process parameters. The following section will discuss more about the fresh property and anisotropic mechanical properties, caused by layering nature of the 3D printing process.

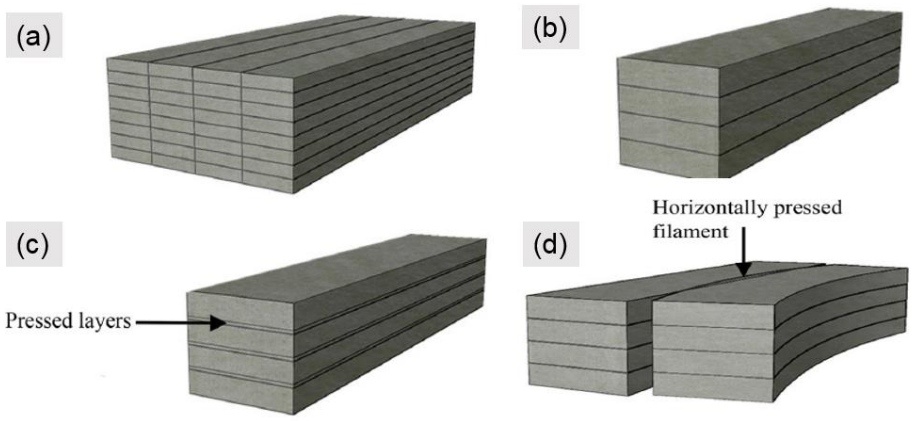

Figure 2.14 Interfaces (a) common in high-resolution 3DCP (b) in usual 3DCP (c) with layers pressed to obtain higher compaction (d) with layer pressed horizontally [121]

2.3 3D printable material design

This section summarizes both fresh and hardened properties of different 3D printable materials developed in the past with respect to extrusion based 3DCP. Due to availability of greater number of research articles, extrusion-based printing is preferred for discussion over other 3D printing processes.

2.3.1 Fresh properties

Fresh property such as rheology and green strength are the backbone of 3D printable materials. Literature reveals conventional rheology indicator: "workability of concrete" is not sufficient to describe the rheological properties required for concrete printing. Le et al. [114] for the first time introduced extrudability and buildability criteria which are significantly influenced by the workability and setting time parameters. Extrudability refers to the ability to transport the fresh concrete to a nozzle where it must be extruded as a continuous filament and buildability is related as the number of layers which could be built up, without noticeable deformation of bottom layers. Shear vane test was used to determine the limit of extrudability, though plastic viscosity yet need to be determined to complete a Bingham fluid model. Following Le et al., several authors [125-129] used yield stress and viscosity as a key parameter to decide the mix proportions suitable for

extrusion-based 3D printing. Bentz et al. [130] demonstrated the formulation of robust binder for 3D printing application by modifying the rheology with limestone and chemical admixtures such as accelerator and retarder. A schematic diagram of their approach is shown in Figure 2.15. Limestone addition affords the opportunity to regulate rheology via water content adjustments and therefore, Sooraj et. al [131,132] used the limestone powder together with metakaolin and SF to tailor the microstructure of cementitious binders for smooth extrusion and better buildability properties.

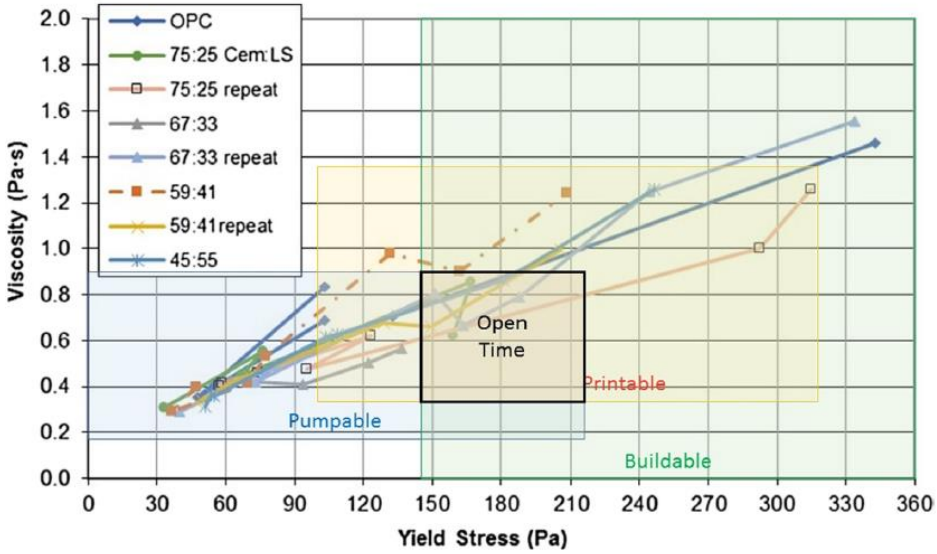

Figure 2.15 Schematic diagram showing hypothetical window for 3D printable materials [130]

Kazemian et al. [133] continuous extruded the mortar mixes to characterize their formulation and according to the authors, a printed layer must be free of surface defects and possess dimension consistency to qualify for the extrudability test. Also, the layers must be able to maintain its shape after extrusion and the edges clearly visible for the square nozzle. Researchers at Tu/e Dresden, Germany used a piston pump to quantify (in-line) the extrudability by measuring the force needed for extrusion. Flow versus pressure graph was plotted (Figure 2.16) and a high flow rate mix at constant pressure was selected for printing experiments [134]. A similar approach was also observed in a recent paper, while using a ram extruder to print alkali activated materials [131]. In order

to improve the extrudability and shape retention of the filaments, several researchers have attempted use different supplementary cementitious materials (SCMs) such as FA and silica fume as well as VMAs such as clay and cellulose. These additives have been explored in the past for their intrinsic property to modify the binder rheology, however in case of 3D printing the effects are more pronounced and worthy of investigation due to the transition in the material processing from casting to printing.

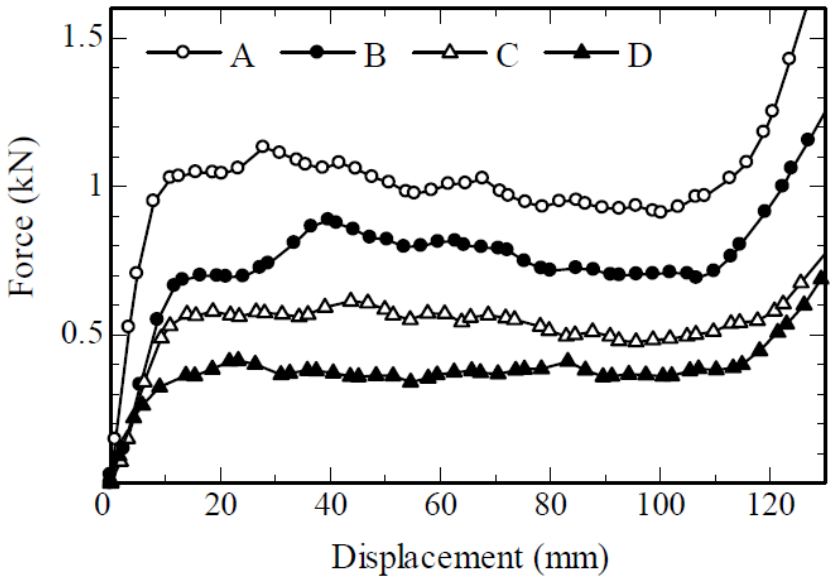

Figure 2.16 Force vs. piston displacement curves obtained for different mixtures from ram-extrusion test [134]

Ma et al. [126] proposed a printable mix design by replacing the river sand with copper tailing, regarded as byproduct of ore extraction process. Due to fine particle size, flowability increases with replacement ratio and finally, 30% replacement was selected considering both extrudability and buildability index. Ketel el al. [135] introduced a printability index to describe how rheological properties (e.g., yield stress, viscosity, storage modulus and crossover energy) affect the printability in terms of geometrical fidelity of the filament as described in the CAD model. This index can be used to identify optimal slurry rheology and develop quality control schemes for 3D-manufacturing

operations. It is well understood that in 3D printing there exist a compromise between extrudability and buildability. Therefore, researchers are trying to optimize both properties by selectively adding the admixtures at different location of printing systems. Figure 2.17 shows an initiative by a France company, XtreeE for adding accelerator only at the nozzle to increase the buildability [116].

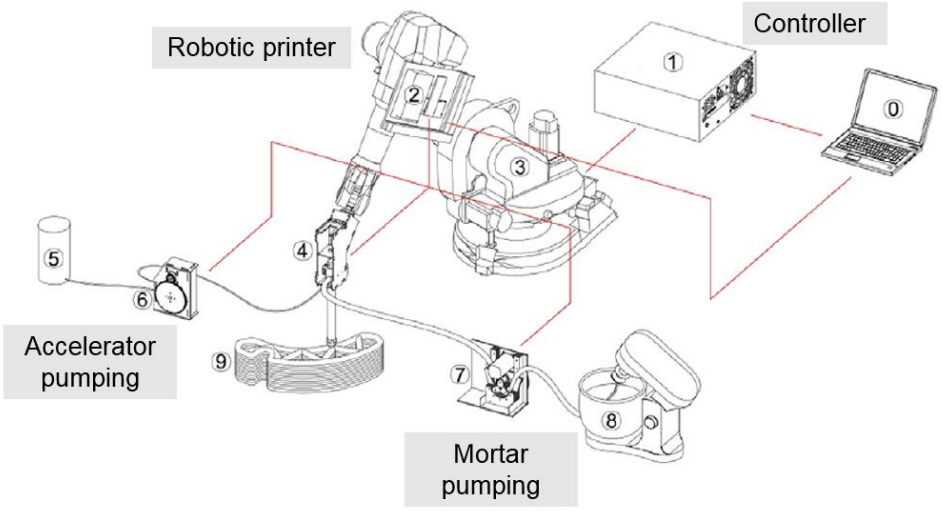

Figure 2.17 3DCP set up by XtreeE, France with in-line accelerator mixing extruder [116]

Thixotropy and structural build-up properties were also explored by the researchers, since thixotropic materials are most suitable in 3D printing projects [136]. Thixotropy is a distinctively rheological phenomenon, associated with changes in rheological properties with time and even when the applied stress or strain rate is kept constant. From a microstructural point of view, cement particle possesses inherent "thixotropy" due to colloidal flocculation [137] and able to build up an internal structure at rest which is a key feature in most printing applications. Therefore, most of the papers and industries have considered PC based binder for concrete printing research and applications. Different protocols have been proposed in the literature to quantify the thixotropy [138-145] and depending on the mix compositions, these protocols can evaluate the thixotropy index which is useful for many digital construction methods including slip layer casting,

3D printing and shotcreting. In a recent review paper Reiter et al. [146] emphasized the importance of controlling the structural build-up and for this, chemically controlling cement hydration was reported as essential step for concrete printing applications. In layered manufacturing process, the bottom layer is always subjected to increasing loading with respect to building rates and therefore, as shown in Figure 2.18a, the concrete yield strength should evolve faster to prevent the structural collapsing. One possibility to solve this challenge is to increase thixotropy of the material or use accelerators that can quickly modify the hydration kinetics to match concrete strength with the increasing stress induced by loading of the layers. In this regard, Marchon et al. [147] have discussed the role of admixtures at different phases to achieve rheological and hydration properties necessary for printable concrete. A schematic representation is shown in Figure 2.18b.

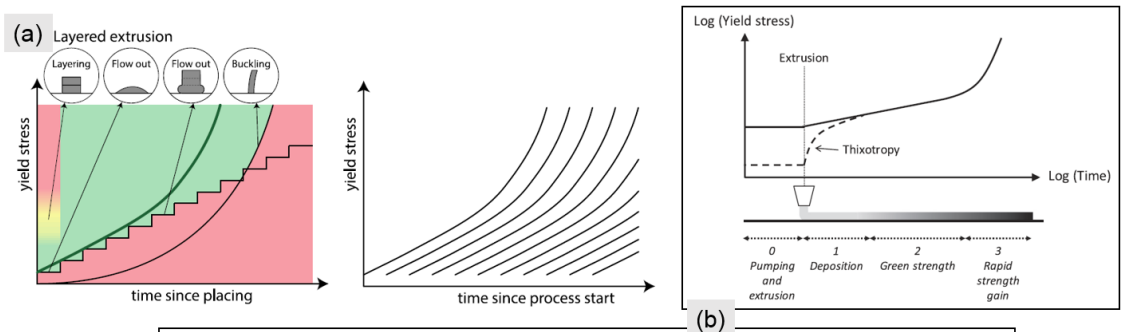

(b)

Stage		Concrete properties	Admixtures	
			Type	Targeted requirements
0	Pumping and extrusion	High fluidity	SPs (PCEs)	Dispersion
		Mix stability	VMAs	Water retention
1	Deposition	Rapid structural build-up to retain its own shape and weight	VMAs	Flocculation of particles
			(Nano-) clays	Flowability during extrusion, "House of cards" effect at rest
			Polymeric fibers	Shear thinning during extrusion, 3D structure at rest
			Entrained air	
2	Green strength	Controlled open time	PCEs	Hydration retardation
			Sugar derivatives	Duration of open time
3	Rapid gain strength	Setting through hydration reactions	Portlandite	Inhibition of retarders action by either sucrose or PCEs uptake
			Clays	Enhanced chemical reactions
			Inorganic salts	Promoted formation of hydrates and development of new surfaces
			PCEs	
			C-S-H seeds	
			Shotcrete accelerator	
	Curing	Concrete hardening	Saturated lightweight aggregates	Reduction of early water loss
			Expansive and shrinkage-reducing admixtures	Minimization of plastic shrinkage cracking

Figure 2.18 (a) Yield stress evolution required for layered extrusion as a function of time [146] (b) summary of potential admixtures for different stages in 3DCP [147]

A proper rheology control is the key success 3DCP process. Thixotropic material with rapid structuration rate is necessary for smooth extrusion and higher build rate even

though part design plays an important role for avoiding structural failure at fresh stage. Research done at Tu/e Eindhoven [148] have confirmed this fact by understanding the (buckling) failure mechanism, while printing a slender layered wall (Figure 2.19). Therefore, part slenderness also needs to be considered for designing printable materials. In fact, for higher slenderness the yield stress must depart more from a linear increase.

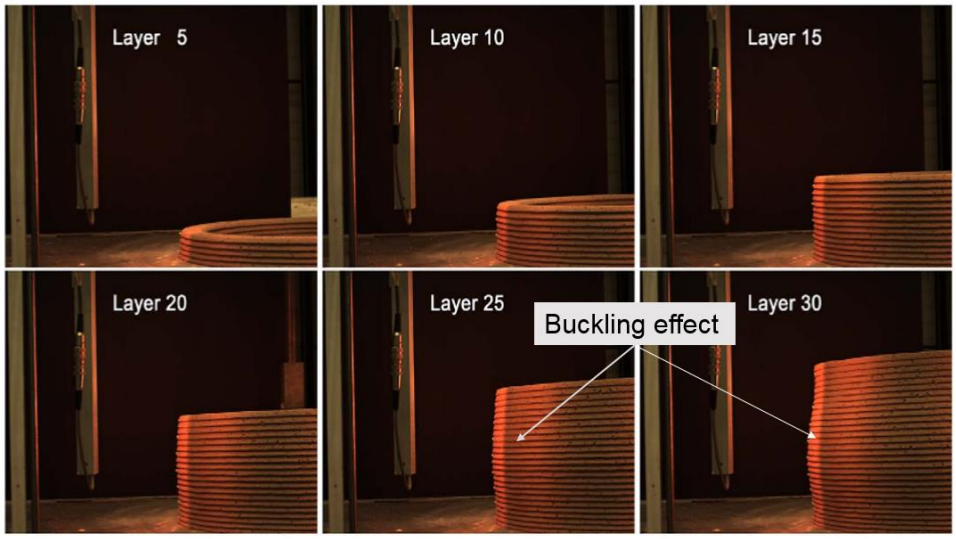

Figure 2.19 Gradual deformation of a cylinder during 3DCP at Tu/e, Eindhoven [148]

2.3.2 Mechanical properties

The mechanical properties such as compression, flexural and tensile strength of 3D printed concrete was first studied by the Loughborough university, U. K. research group for high-performance concrete [149]. Since there are no standards for testing 3D printed samples, 100 mm cube specimens were extracted from 350 × 350 × 120 mm printed slab (S3) and 500 × 350 × 120 mm slab (S5) for directional compression test as shown in Figure 2.20.

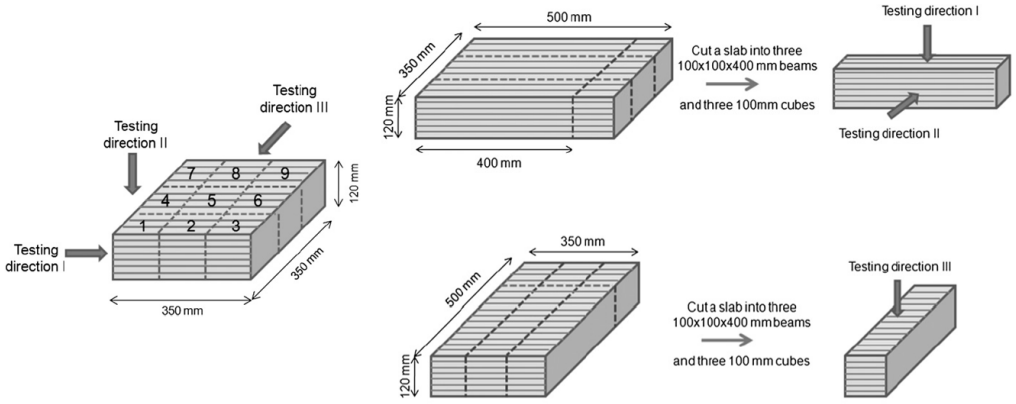

Figure 2.20 Cutting diagram and testing directions of samples in 3DCP process

The average compressive strengths of the cube specimens extracted from S3 slab were 102 MPa in direction I and II, whereas in direction III it was 91 MPa. Compared to standard mold-cast, the printed concretes have similar in directions I and II and 15% lower in direction III. Similarly, the average compressive strength of samples extracted from S5 was of 97 MPa in direction I and 93 MPa in directions II and III. The printed strength was thus 9% lower in direction I and 13% lower in directions II and III, respectively. These results confirmed that properly printed concrete induces relatively little anisotropy, although anisotropy mechanical property is inherent to any 3D printing process.

For flexural strength, 100× 100× 400 mm beams were similarly extracted, and a greater anisotropy was observed with lowest strength in direction III. The strengths in loading directions I and II (16 and 13 MPa respectively), were higher than that of the standard mold cast material (11 MPa) probably because of well-compacted layers in the direction of printing. Feng et al. [150] also found similar behaviour while analyzing the results of flexural test. The authors reported the position of crack exactly at the middle of the beam for direction III, whereas for loading in I direction, the crack was slightly away from the middle. The tensile strengths of 3D printed samples were much lower than mold casted sample and Le et al. [149] found the effect of time delay between the layers as one of the

significant parameters affecting the final strength values. As the time gap increases between the layer, tensile strength was notably decreasing due to poor interlayer bonding. Several authors have investigated this problem of strength loss and argued differently based on surface moisture loss, water transport properties, thixotropy effects, material flow properties etc. [150-155]. However, it is possible to improve the bond strength either by selecting optimum printing parameters or introducing another material in the interface, similar to an approach described in [156]. The result of strength improvement was notably higher compared to control sample, though the final strength was still lower than mold casted sample. Improving the bond strength by increasing surface area contact was another solution proposed by Zareiyan and Khoshnevis. An average of 26% increase in strength was reported by the interlocking profiles generated at the interface with different grove depths as shown in Figure 2.21[157].

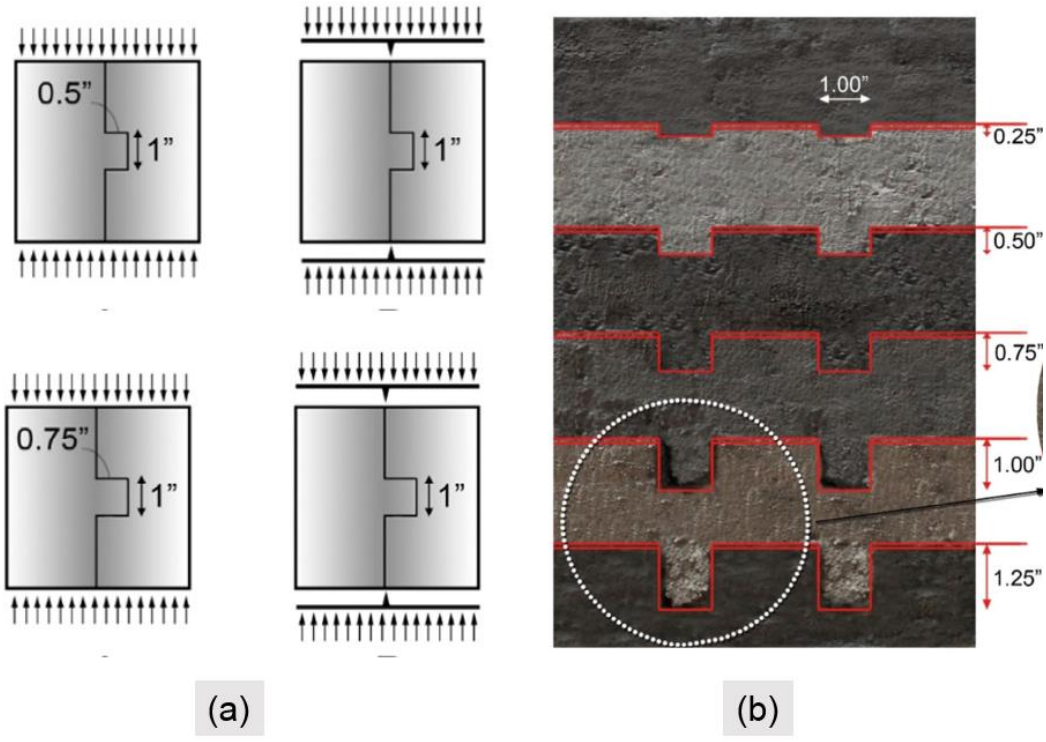

Figure 2.21 Study of interlocking on interlayer adhesion in contour crafting [157]

To improve the tensile properties of 3D printed sample, short fibers (glass, basalt and carbon) were introduced in to the cementitious matrix resulting in novel materials that exhibit high flexural up to 30 MPa [158]. The authors reported excellent fiber alignment in the printing direction, leading to a notable increase of flexural strength. Ma et al. [159] investigated the mechanical performance of basalt fiber reinforced concrete and found 30% improved flexural properties due to fiber alignment in the printing direction as shown in Figure 2.22a. Ogura et al. [160] extruded high-density polyethylene microfibers in two different dosages (1% and 1.5%), which not only improve the shape stability of the extruded layers but also significantly increased the strain capacity, especially for 1.5%. The fibers were oriented in the direction of printing and uniform multiple cracks were observed across the sample. With help of a glue gun, Soltan and Li [161] extruded calcium aluminate binder with 2% PVA fiber to demonstrate the feasibility of 3D printing engineered cementitious composite (ECC) material. Experiential results confirmed tensile strain-hardening behavior of the printed composite, although the set up was regarded very small for on-site applications. Effects of fiber on other building materials such as geopolymer were also documented in literature with indication of improved strength and fiber alignment in the printing direction [162-165].

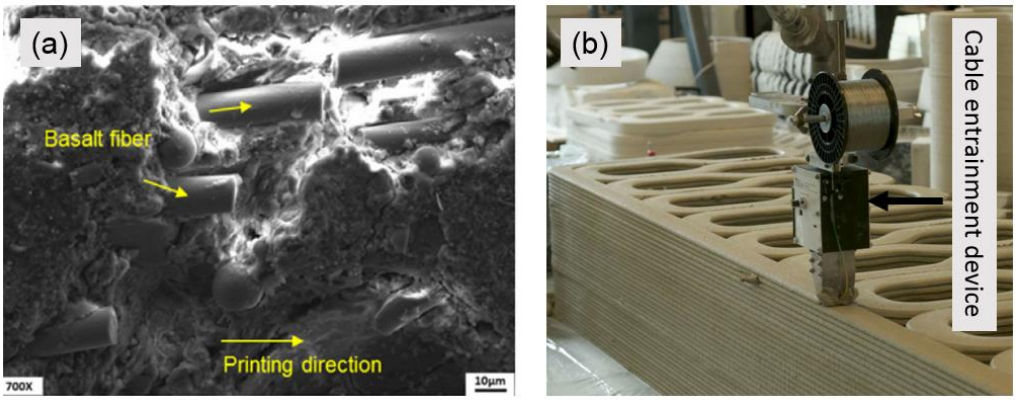

Figure 2.22 (a) Micro fiber [159] and (b) metal cable reinforcement in 3DCP process [166]

More recently, Bos et al. [166] demonstrated the failure behaviour of short steel fibers reinforced printed concrete through several CMOD tests on different scale. Experimental

and numerical research has shown the benefits of fibers not only in terms of increasing the flexural strength, but also the ability to eliminate the strength difference between cast and printed concrete that exists without fibers. The authors of same paper presented an innovative approach of automatically entraining metal cable as reinforcement for 3D-printed concrete [167]. A device was introduced (Figure 2.22b) to entrain these cables directly during printing and results of four-point bending tests shows significant increase in post-crack resistance of the cable reinforced samples, though the final failure was governed by cable slipping which was not to observed in another experiment by Lim et al. [168].

The interest in 3D printing for building and construction has increased drastically in recent years. Figure 2.23 shows the number of publication (conference proceedings and journal articles) available from 1997 to 2016 related to 3D concrete printing only. It is very clear that the rate of publication increases at a faster rate from 2009 onwards, which exemplifies the initiative for more comprehensive and all-rounded work in this discipline. Figure 2.24 shows some noteworthy examples of 3DCP projects to realize the architect potential of this technology, which were never possible by traditional casting methods.

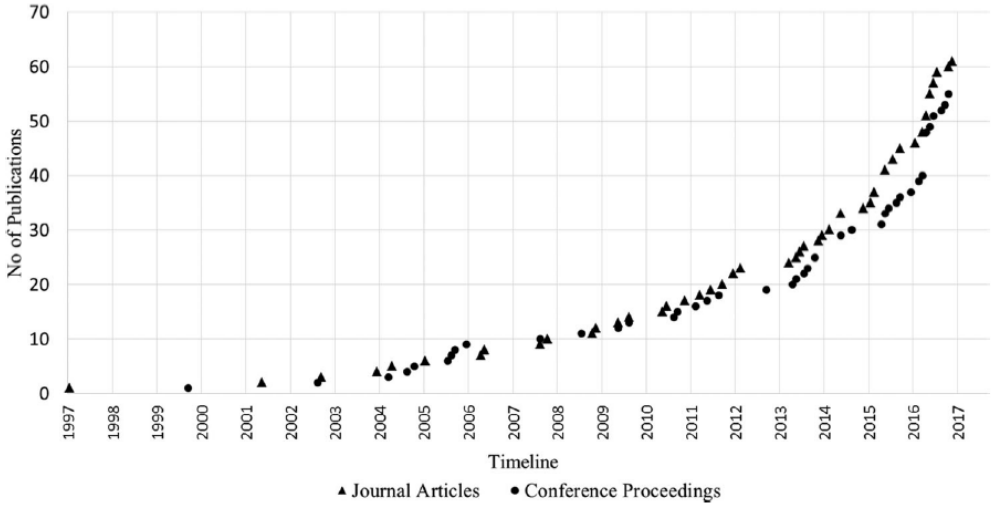

Figure 2.23 Trend of publication over the years related to 3DCP [108]

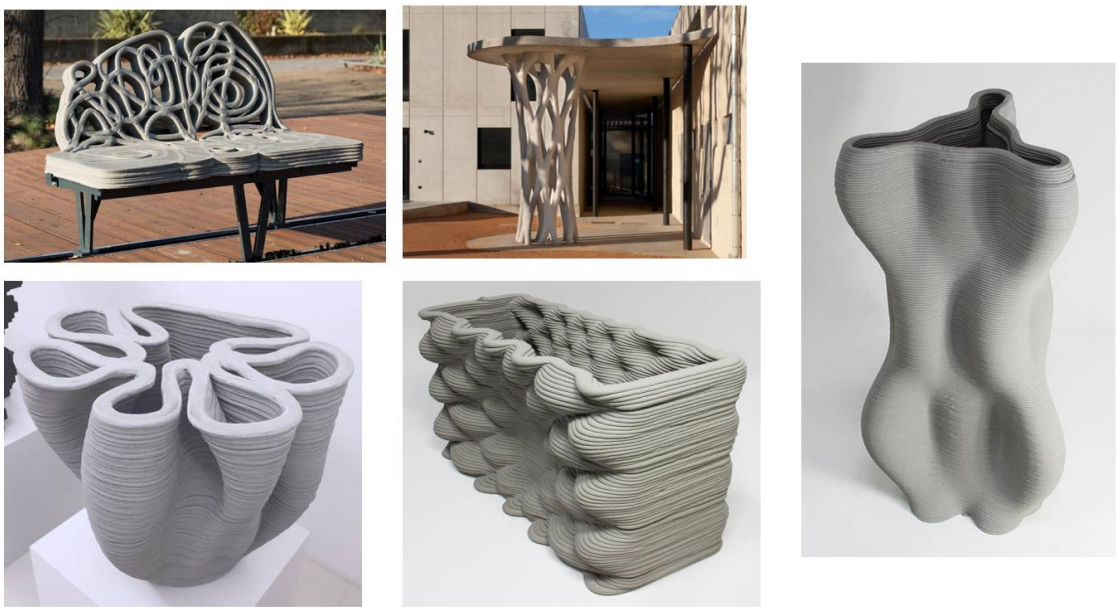

Figure 2.24 Examples of 3D concrete printed complex freeform models by XtreeE, France [169]

Chapter 3 Materials and methods

This chapter presents the materials, test methods and the experimental procedures used to obtain the results.

3.1 Materials

3.1.1 Fly ash

The fly ash (FA) used in sample preparation was supplied by Sembcorp Architects & Engineers Pte. Ltd, India. Chemical composition and physical properties of FA are listed in Table 3.1, as obtained from the supplier. XRD plot showing the crystalline peak (quartz (PDF# 074-3485) and mullite (PDF# 074-4143)) pattern of FA is presented in Figure 3.1. The microstructure of FA (Figure 3.2) consisted of spherical microparticles, which is consistent with those observed in other studies [170, 171].

Table 3.1 Chemical composition and physical properties of FA

Chemical composition (%)	**FA**
SiO_2	51.1
CaO	5.8
Al_2O_3	28.8
Fe_2O_3	6.4
SO_3	1.0
MgO	1.1
Na_2O	0.3
K_2O	1.2
TiO_2	2.5
LOI	1.2
Fineness (%)	11.5
BET Surface area (m^2/g)	0.708

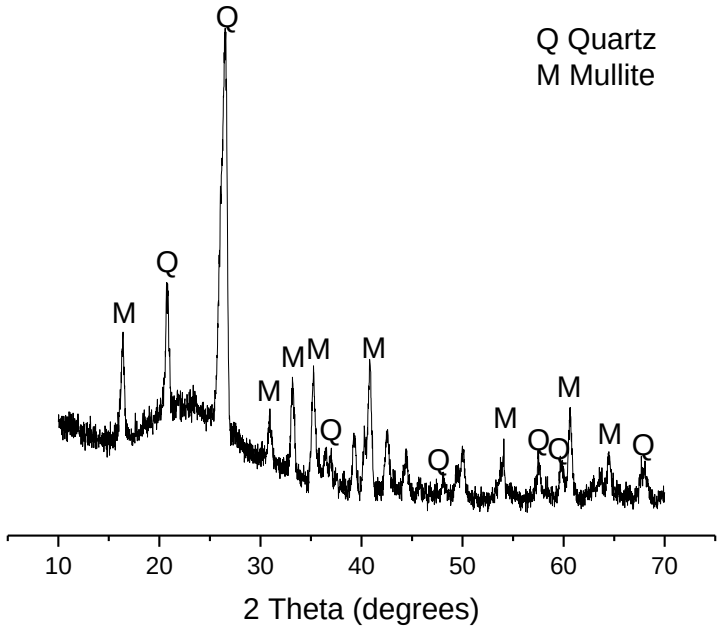

Figure 3.1 XRD plot of FA

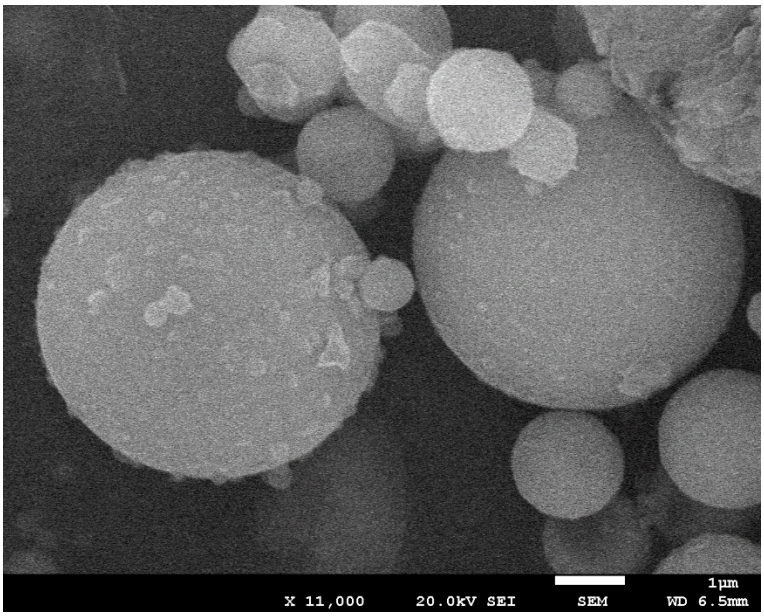

Figure 3.2 FESEM image of FA

The glassy content of FA was determined using an external standard approach, as outlined in [172,173]. Results shown in Table 3.2 revealed that the FA contains a low

amount of reactive phases, which could be due to usage of low grade coal and low ignition temperatures.

Table 3.2 Reactive components of FA and GGBS

Material	Crystalline content (%)						Amorphous content (%)
	Al_2O_3	SiO_2	Fe_2O_3	CaO	K_2O	TiO_2	
FA	10.72	14.28	5.94	2.75	2.17	1.47	38.8
GGBS			2.8				97.2

3.1.2 Slag

The slag (Ground granulated blast-furnace slag, GGBS) used in this study was supplied by Engro Pte. Ltd, Singapore. Chemical composition and physical properties of the GGBS are listed in Table 3.3, as obtained from the supplier. The microstructure of GGBS (Figure 3.4) consisted of mostly angular microparticles, which is consistent with those observed in other studies [174,175]. XRD pattern of the GGBS (Figure 3.3) displays a broad amorphous hump at around 30° 2θ and gehlenite (PDF#0 04-0690), which was present in small amounts.

Table 3.3 Chemical composition and physical properties of GGBS

Chemical composition (%)	**GGBS**
SiO_2	29.6
CaO	39.3
Al_2O_3	15.5
Fe_2O_3	0.3
SO_3	4.3
MgO	7.5
Na_2O	0.4
K_2O	0.5
TiO2	1.7

LOI	1.1
Particle size (%)	
BET Surface area (m^2/g)	0.866

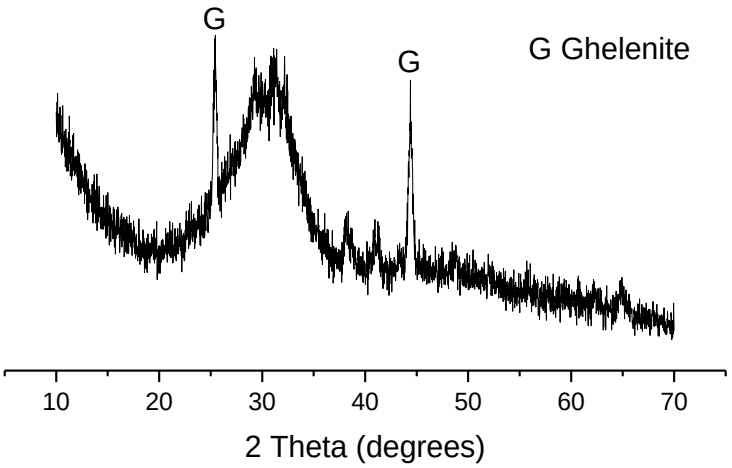

Figure 3.3 XRD plot of GGBS

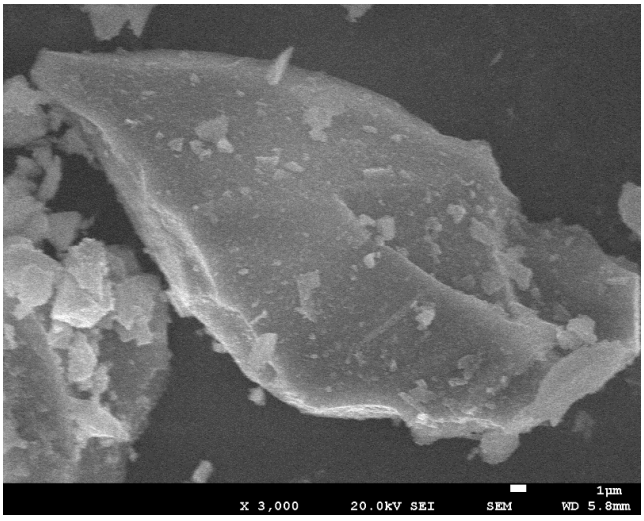

Figure 3.4 FESEM image of GGBS

3.2.2. Micro silica

The micro silica or silica fume (SF) used was 940U (supplied by Elkem Singapore Materials Pte Ltd.). The chemical composition and physical properties of SF reported by the supplier is shown in Table 3.4. The XRD plot for SF is presented in Figure 3.5, showing an amorphous broad band at around 22° 2θ, which is characteristic for amorphous SiO_2. The morphology of SF was composed of spherical SiO_2 particles as shown in Figure 3.6.

Table 3.4 Chemical composition and physical properties of SF

Chemical composition (%)	FA
SiO_2	>90%
CaO	-
TiO_2	-
LOI	<3%
Particle size (%)	>45 μm
BET Surface area (m^2/g)	23.129

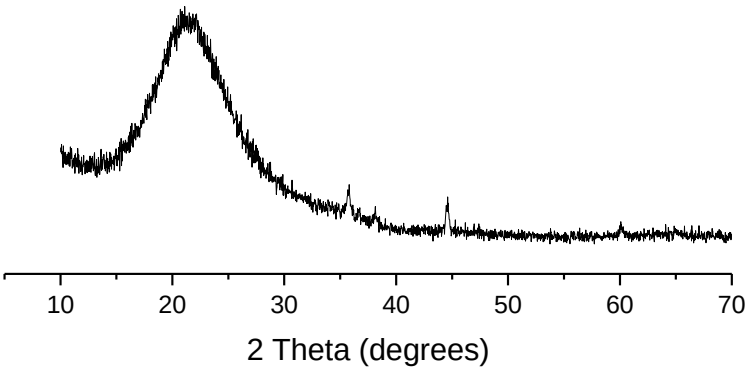

Figure 3.5 XRD plot of SF

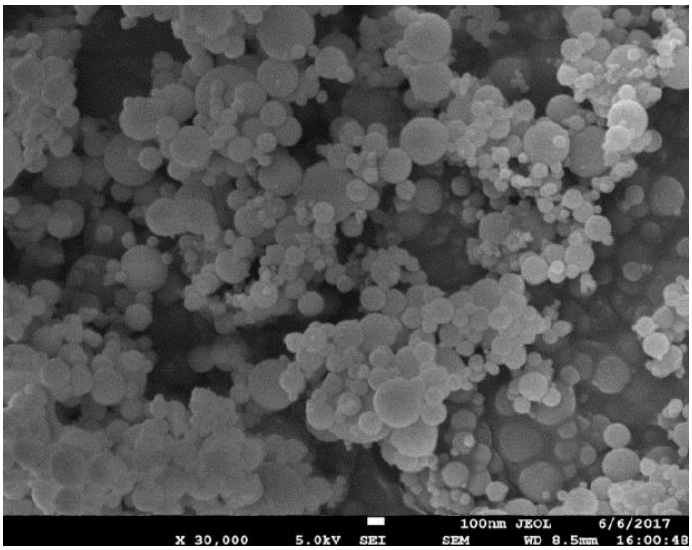

Figure 3.6 FESEM image of SF

3.1.3. Portland cement

Portland cement (PC) used in this thesis was obtained from Lafarge Cement (Singapore). The chemical composition and physical properties of PC as obtained from the supplier are presented in Table 3.5.

Table 3.5 Chemical composition and physical properties of PC

Chemical composition (%)	PC
SiO_2	24.27
CaO	62.2
Al_2O_3	4.56
Fe_2O_3	3.95
SO_3	-
MgO	3.34
Na_2O	0.21
K_2O	0.61
TiO_2	0.55

LOI	1.1
Specific gravity (g/cm^3)	3.1

3.1.4. Alkaline activator

The alkali activator used is this work is a mixture of the potassium hydroxide solution (8M) and commercial grade potassium silicate (K-silicate) solution (supplied by Noble Alchem Pte Ltd., India). The K-silicate solution has a composition of 24.32% SiO_2, 18.71% K_2O and 56.97% H_2O by mass. The desired activator modulus (MR, SiO_2/K_2O molar ratio) was achieved by adding the appropriate amount of potassium hydroxide (KOH) into the K-silicate solution. Instead of sodium (Na), K-silicate was selected in this research, since the Na based silicate is about 10 times more viscous and allows us to add more water to reach the desired workability, and more viscous also leads to a lot of difficulties during the extrusion process.

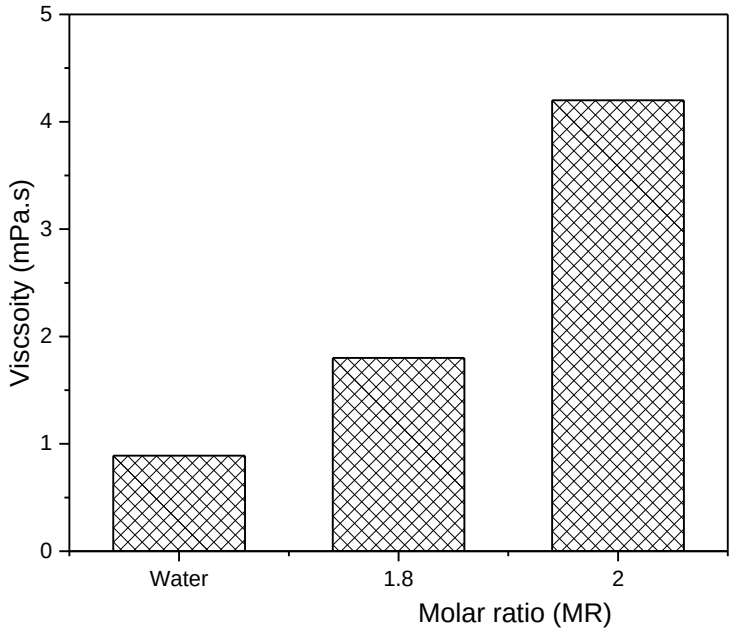

Figure 3.7 Effect of molar ratio (MR) on viscosity of K-silicate liquid activator. Note that a comparison was made with water viscosity for reference purpose.

The rheology of the activators was evaluated in the "normal" shear rate ranging 5–100 s^{-1}. 2.0 and 1.8 MR K-silicate solutions were used to explore the influence of activator modulus/concentration on rheological properties. It is clear from Figure 3.7 that, there is a general increase in viscosity with increasing MR which is in line with find with Vance et al. [84]. NMR studies indicated due to colloidal Si-O-H-K aggregates, the viscosity increases [176] and the size of these colloidal species is likely to increases with MR that affects the final solution viscosity.

An alternative to liquid K-silicate, powder silicate activator (procured from same supplier) was used in this research. Appropriate amount of analytical level KOH pallets (from VWR Singapore Pte Ltd., Singapore) was mixed with powder silicate to reduce the MR, similar to the liquid silicate activator.

3.1.4. Alkali salt activator

Alkali salt, namely sodium sulfate powder (Na_2SiO_4) (reagent grade, VWR Singapore Pte Ltd., Singapore) was used to provide early strength gain of the HVFA mortar. It appears as white crystals and is soluble in water.

3.1.5 Nano clay

Nanoclay (NC), is a magnesium alumino silicate clay with the theoretical formula of $Si_8Mg_8O_20(OH)_2(H_2O)_4.4H_2O$. According to the International Nomenclature Committee (INC), the preferred name is palygorskite, although it is better known as attapulgite commercially. A highly purified form of the attapulgite was chosen in the study, supplied by Active Minerals International (Actigel), USA.

Table 3.6 Chemical composition and physical properties of NC

Chemical composition (%)	NC
SiO_2	52.76
CaO	5.86

Al_2O_3	10.28
Fe_2O_3	3.40
SO_3	0.167
MgO	3.34
Na_2O	0.449
K_2O	0.59
TiO_2	0.55
LOI	16.7
BET Surface area (m^2/g)	125.49

The NC serves the purpose of VMA, is a pure, uniformly sized, rod-shaped mineral particle but spheroidal agglomerates (Figure 3.8) when the particles are dry. Table 3.6 shows the chemical composition and physical properties as obtained from X-ray fluorescence and BET surface area tests.

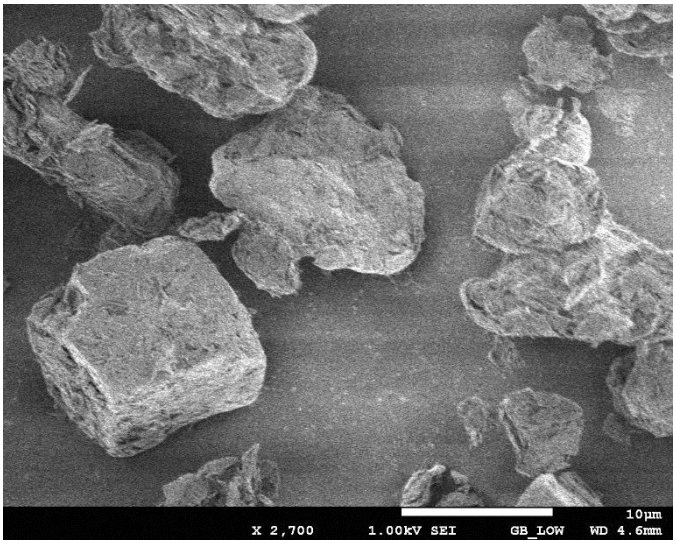

Figure 3.8 FESEM image of NC

3.1.6. Natural fine aggregates

Saturated surface dry (SSD) graded river sand provided by Buildmate (Singapore) with maximum particle size of 1.18 mm and a density of 2.61 kg/m^3 was used to formulate the mortar for 3D printing application. The particle size distribution (PSD) curve as obtained from laser diffraction machine is shown in Figure 3.9. The gradation was maintained to achieve high flow rate with addition of more fines as suggested by Mehdipour and Khayat [177].

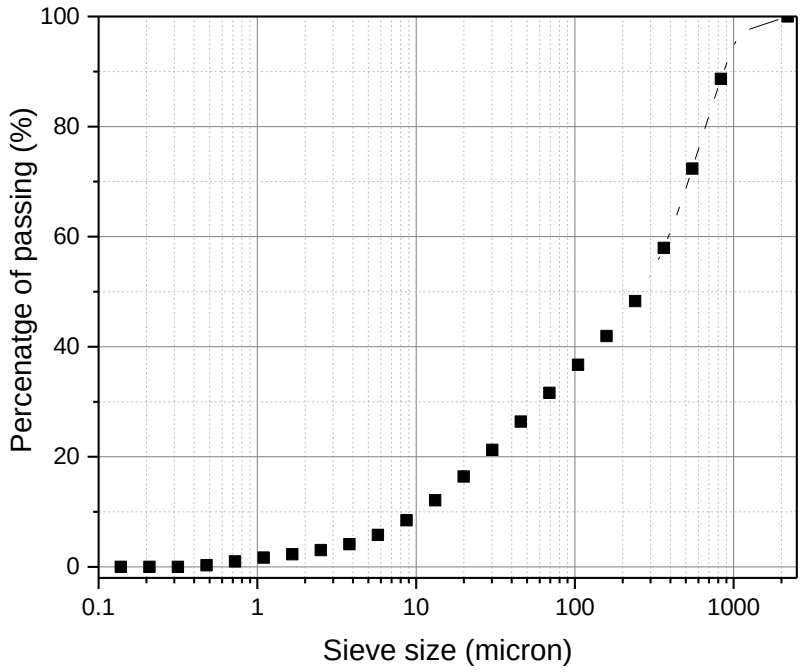

Figure 3.9 Particle size distribution (PSD) curve of river sand

3.2 Mix compositions, sample preparation and curing conditions

3.2.1. High volume fly ash mortar

Sample preparation initiated with dissolving Na_2SO_4 activator in predetermined amount of water, after which FA and PC were slowly added in during mixing. Sand was then gradually introduced into the mix at the determined sand-to-binder ratio. Mixing

continued until a thoroughly mixed and a highly workable paste was obtained. SF was also directly added for altering the rheology, however for NC modified mix, the NC was first dispersed in water using in a Waring blender at a speed of 12,000 rpm for 2 min to produce a clay suspension, which remains stable after 24 h at rest. High speed mixing is effective to disperse the attapulgite clay suspension. The designated water is divided into three parts. 90% of water is mixed with FA and PC mix in the beginning; the remaining 5% and 5% is mixed with activator and NC respectively. The prepared mortar was used for different tests followed by room temperature (23±2^{o}C) curing to mimic the in-situ condition in Singapore. Figure 3.10 shows the prepared NC suspension and mortar mixer set up used in this study for laboratory experiments. Note that for large-scale 3DCP, two 80-liter batch capacity BAMA quick mixer was used.

Figure 3.10 (a) Dispersed NC (b) Hobart laboratory and BAMA mortar mixer

3.2.2 Geopolymer mortar

Geopolymer based binders were used in the preparation of printable mortar where, the binder phase was prepared as explained in section 3.3.1. Liquid activators were prepared and allowed to cool down for a period of 3 to 4h in ambient temperature (23±2^{o}C), prior

to mixing with the binder. A small amount of distilled water was also added to reach the desired workability and this "water" refers to the additionally added water, sometimes being confused with the ones that originally from the K-silicate solution. After a truly homogenized and thoroughly mixed paste was obtained, fine river sand was introduced into the mix to formulate geopolymer mortar. Addition of SF for modifying the rheology was added only after mixing of activator with binder. SF addition step is very important in geopolymer preparation, since it can also act as activator if added together with KOH solution. For NC mixture, similar procedure to HFVA was adopted for uniform dispersion of colloidal clays.

The geopolymer mortar was tested for fresh property followed by hardened property at 28 days under ambient temperature (23±2^{o}C) curing.

3.3 Methods

3.3.1 Yield stress and viscosity

A commercial rotational rheometer (Anton-Paar MCR 102) was used in this study to measure yield stress and viscosity of the mortar by applying deformation at a constant shear rate of 0.1 s^{-1}. During this test, the shear stress progressively developed to a maximum value (Figure 3.11) and then stabilized at an equilibrium value. The static yield stress was defined as the peak shear stress value. Viscosity is a time dependent parameter of thixotropic material and it depends on applied shear rate during the measurement. In this study, the average apparent viscosity was measured by applying constant shear rate of 300 s^{-1} for 30 seconds [178], while mimicking the shear deformation during mortar extrusion.

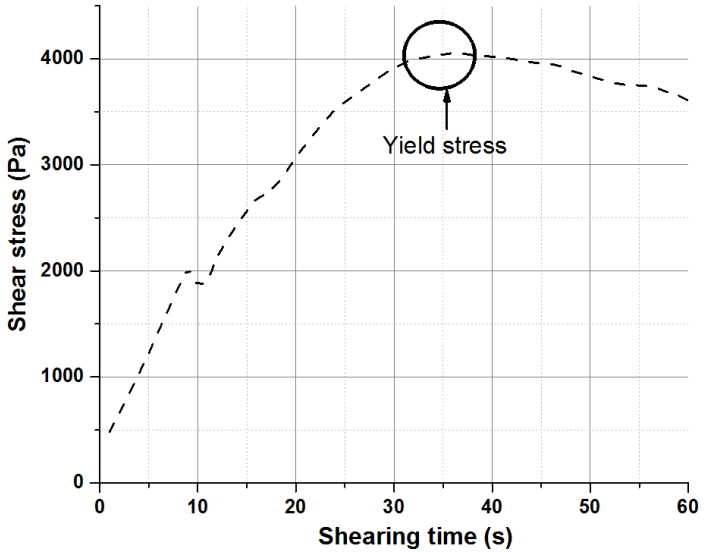

Figure 3.11 Determination of static yield stress from stress growth test

3.3.2 Shear thinning and viscosity recovery (thixotropy)

Thixotropy, which is an important parameter in 3DCP was measured both in terms of break down and recovery in this thesis. Literature reveals shear thinning is the most widely used method to measure the break down thixotropy, however without performing the viscosity recovery, the thixotropy cannot be fully evaluated. Therefore, first shear thinning protocol was employed to calculate a structural parameter (λ) by shearing the mortar at 300 s^{-1} for 120 seconds [179]. In general, the higher the λ, the higher the thixotropy.

$$\lambda = \frac{\tau_0 - \tau_e}{\tau_e} \quad (1)$$

Secondly, viscosity recovery was measured to investigate fresh property of the prepared mortar after the extrusion process. If the original viscosity of the initial deposited layer is not recovered before the deposition of the second layer, it may result in the deformation of the structure. Therefore, in this study, the 3D printing process was mimicked by

applying different shear rates of (i) 0.01 s^{-1} for 60 seconds, (ii) 300 s^{-1} for 30 seconds and (iii) 0.01 s^{-1} for 60 seconds at three different time intervals corresponding to the material state (i) initially at rest, (ii) shearing/extrusion and (iii) again at rest, as used in previous studies [178]. The apparent viscosities were measured during these three intervals to understand the recovery behaviour of the different FA based mortar mixes (Figure 3.12).

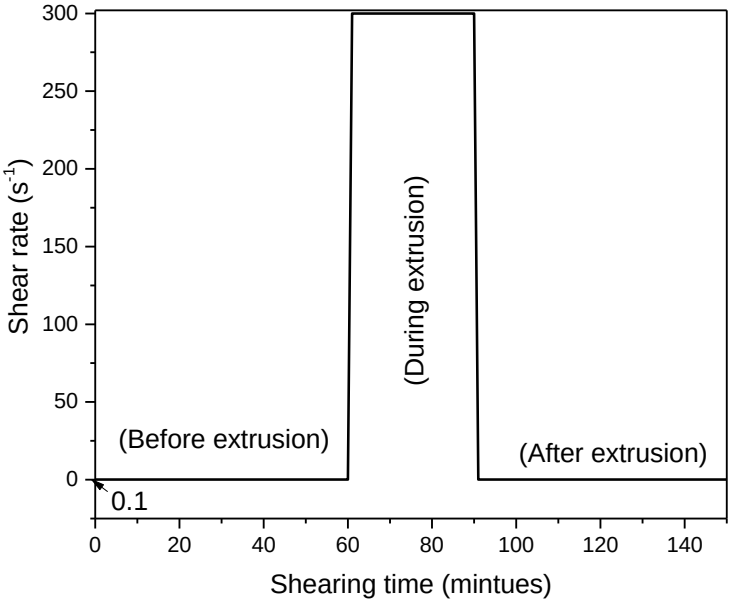

Figure 3.12 Viscosity recovery protocol for quantifying the thixotropy

3.3.3 Structural build-up

In 3DCP the early age strength gain is most important as it directly affects the buildability property and, in this work increase in static yield stress with resting time was used as an indicator of structural build-up similar to a protocol used in [180]. The slope of the curve reflects the A_{thix} index which increases over time due to both physical and chemical reaction in the material. A typical structural build-up example is shown in Figure 3.13, referred from concrete printing study by Perrot et al. [181].

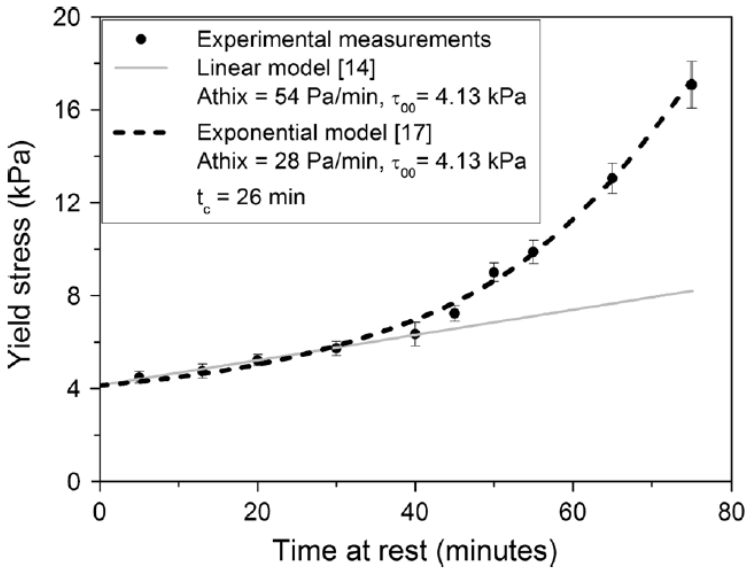

Figure 3.13. Comparison of experimental yield stress evolution with Perrot et al. [181] and Roussel models [137]

3.3.4 Green strength and Young's modulus of fresh concrete

Rheometers are often used in literature to measure early age properties of cementitious mixtures. However, due to maximum torque limitation or high thixotropy of the material, some researchers have preferred slump test to indirectly measure the yield stress. Like slump test, green strength measurement by uniaxial compression test has been recently found to be useful in 3DCP application and therefore, in this thesis an experimental program similar to [148] was adopted to measure green strength development of the HVFA mortar up to 150 mins from addition of the water (with in dormant period).

Uniaxial unconfined compression tests were performed on cylindrical samples with 70 mm diameter and 140 mm height. The dimensions were chosen to avoid impact of particle size and allow a diagonal shear failure [148]. Fresh HVFA mortar was molded in five containers with some compaction and tested after different resting time (5,30,60,120 and 150 mins) as shown in Figure 3.14.

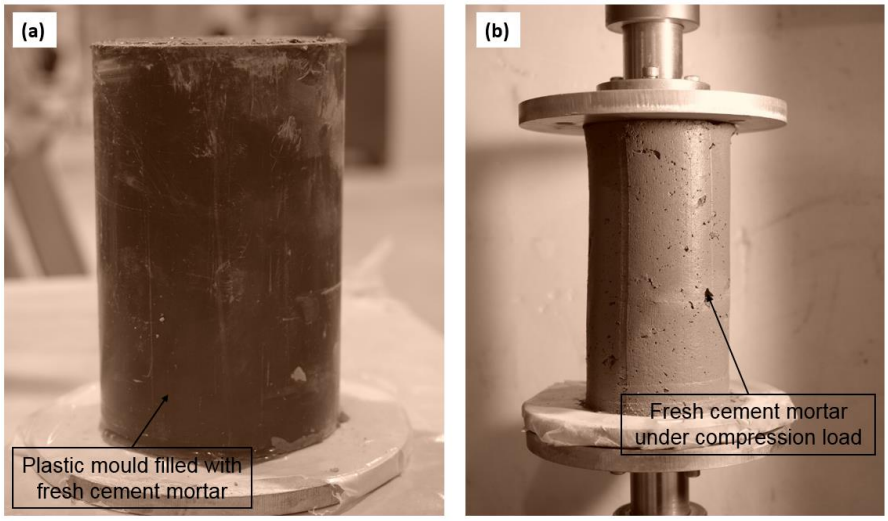

Figure 3.14 (a) Material preparation and (b) uniaxial compression test of fresh cement mortar

INSTRON 5969 test rig equipped with 50KN load cell was used for compression test at a loading rate of 0.6 N/s, chosen to mimic the loading steps in 3D printing test. Each test was conducted close to 60-70 seconds to neglect effects of thixotropic build-up and their average values were presented in terms of force and displacement (F-d) diagram. In addition, the vertical deformations and lateral area of the fresh concrete were measured using 3D optical metrology. This new lateral area was considered for area correction, while deriving stress-strain curve from the F-d diagram.

Optical techniques, based on digital photogrammetry or terrestrial laser scanning, have been found to be very effective and accurate solutions for static load test measurements [182] and therefore, in this study, a relatively inexpensive camera (Kinect V2) was used to capture dynamic measurements of changing cross section area. Figure 3.15 shows the experimental set up with the calibrated Kinect taking a series of point cloud and RGB images during the compression test. Later, the point cloud was processed with a pass-through filter that retains only the region of interest and removes rest of the points in the point cloud. The surface normal of resultant filtered point cloud was estimated using a k-neighbour estimation method. The number of neighbours used in the estimation was scaled in accordance to the density and level of detail required of the input point cloud.

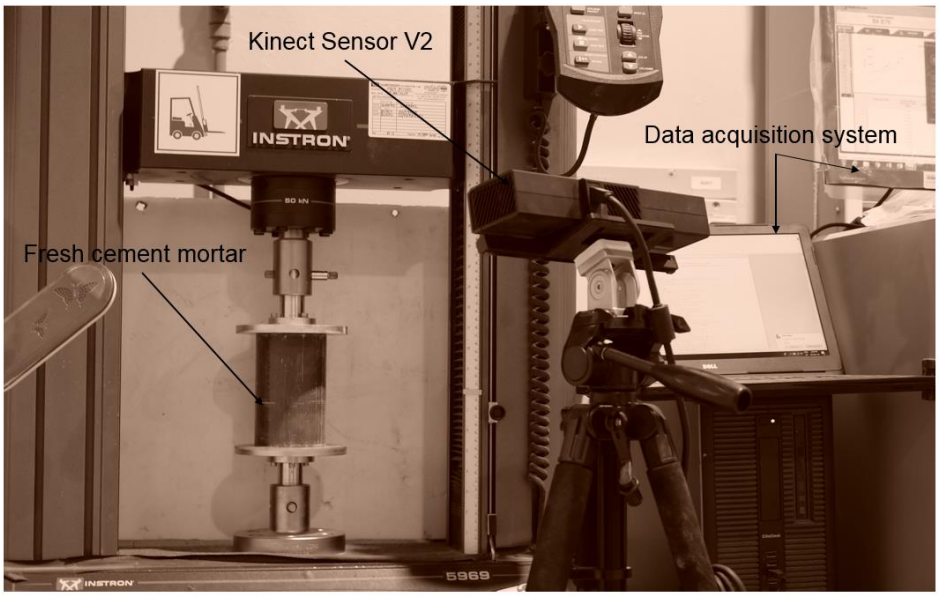

Figure 3.15 Experimental set up for measuring lateral and longitudinal deformation of fresh cement mortar

A *region growing segmentation* algorithm was then applied on the resultant point cloud, to group all the points belonging to the fresh concrete into a single cluster for further processing. This algorithm can selectively merge points that are close together and within a defined smoothness constraint. The region growing segmentation first seed and begins its growth on the point with the minimum curvature value. This initial point was located on a dominant plane, provided intentionally by placing a white Styrofoam board behind the concrete sample during compression testing. By growing the region on the flattest surface, this will greatly reduce the total number of segments. Until every point in the point cloud has been sorted, the algorithm will go through the next point with the new minimum curvature value and start the growth of a new cluster. At every seed point, its neighbouring points were checked for the angle between its normal and the normal of the seed point. If the angle difference is less than the defined smoothness threshold and curvature threshold, it will be added to the cluster. The algorithm then loops through the point cloud and grow the region until the points are exhausted. The output of the

algorithm was a list of clusters of points which describes disjoint regions with homogenous property. The list will be then filtered by checking for a minimum cluster size that removes clusters group which are too small.

The resultant list of clusters was subsequently check for their centroid points and filtered off if their centroid points are outside of the region of interest. This will effectively provide us with the resultant cluster of points that makes up the concrete undergoing compression. A bounding box was then added to the cluster for visualizing purposes (Figure 3.16) and relevant information such as height, maximum diameter and centroid of the fresh concrete were extracted and stored in an excel sheet along with the time the point cloud and RGB image was taken, to correlated with data taken from the compression test.

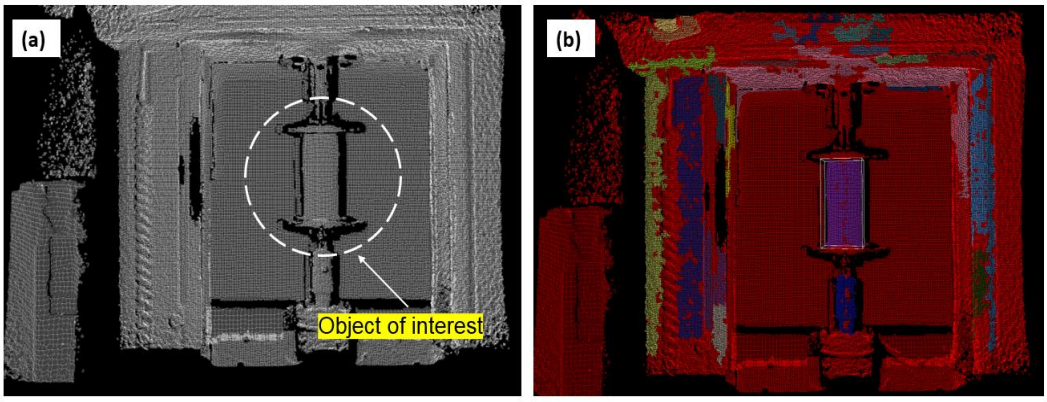

Figure 3.16 (a) Original point cloud and (b) object of interest in a segmented point cloud

3.3.5 Laser particle size distribution

The particle size distribution (PSD) of the raw materials was determined via a Malvern Mastersizer 2000 (Figure 3.17). Before the analysis, the powders were mixed thoroughly in the water to prepare a homogenous solution. A few drops of this solution were used for PSD analysis. The test was conducted once per sample.

Figure 3.17 Malvern Mastersizer 2000 instrument used for PSD analysis of powder samples and flocculated colloidal

3.3.6 Surface area

The specific surface area of the powder samples was measured with a Quantachrome QuadraSorb SI instrument, using the adsorption of N_2 at the temperature of liquid nitrogen (77 K). Prior to measuring, all the samples were degassed at 523 K for 16 hours and finally outgassed to 10-3 Torr. The Brunauer–Emmett–Teller (BET) surface area was calculated using the BET equation from the selected N_2 adsorption data within the range of relative pressure, P/P0.

3.3.7 Zeta potential

A ZetaProbe analyzer (Colloidal Dynamics) was used to measure the zeta potential of geopolymer slurry (3 wt.% suspension) and all calculations were performed using the ZetaProbe Polar software (v. 2.14).

3.3.8 Isothermal calorimetry

The heat flow and cumulative heat released during the hydration and polycondensation reaction were determined under isothermal conditions at by an I-Cal 2000 High Precision Calorimeter (Figure 3.18) in accordance with ASTM C1702−15a (2015) [183]. 50 g of paste was prepared for each composition and was immediately placed into the

measurement chamber within a minute. Readings were recorded for 72 hours under a constant temperature of 26ºC. The test was conducted once per sample.

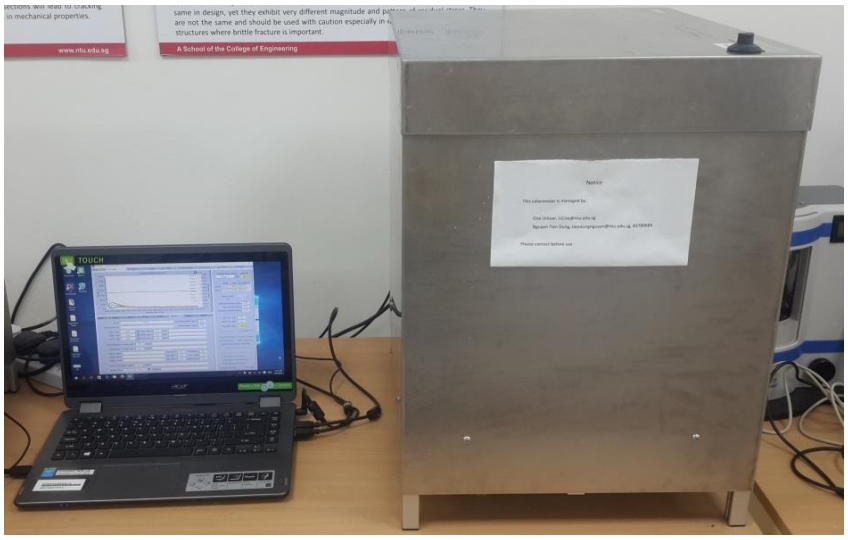

Figure 3.18 Equipment used for isothermal calorimetry analysis of paste samples

3.3.9 pH value measurement

The pH of alkaline activators was measured by using a Mettler Toledo pH meter (Figure 3.19 (a)) with an accuracy of ±0.01. All the measurements were conducted in triplicates and the average values were recorded.

3.3.10 Setting time

The setting time measurement was performed according to ASTM C187-98 via a standard Vicat apparatus supplied by ELE Pte Ltd. (Singapore) as shown in Figure 3.19 (b). The pastes were prepared with different water to solid ratios to determine the exact consistency value corresponding to a needle penetration depth of 10±1 mm as specified by the standard. The test was conducted once per sample.

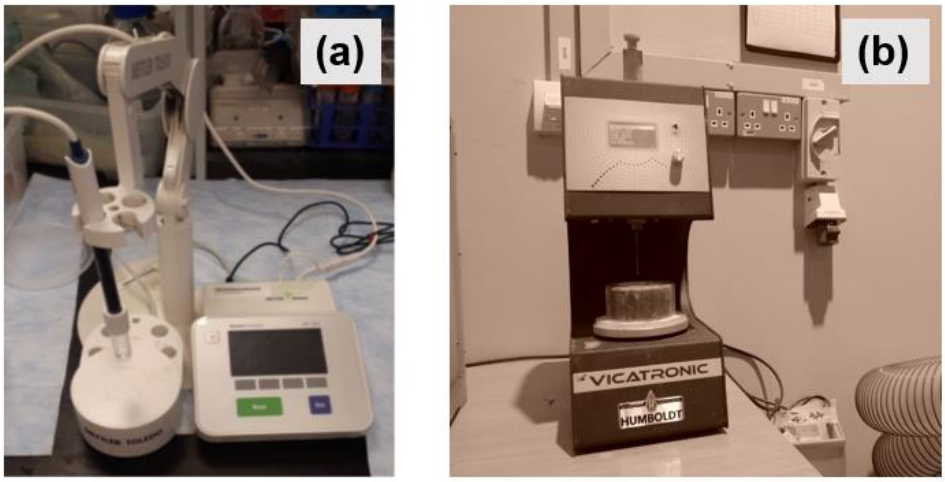

Figure 3.19 (a) Mettler Toledo pH meter (b) Vicat needle setting time instrument

3.3.11 Fourier transform infrared spectroscopy

Fourier Transform Infrared (FTIR) spectroscopy was carried out on the alkali activator solutions. For the powder activator, solutions were prepared by mixing appropriate amounts of silicate and KOH powder and then allowed to rest for 2 h. A small amount of the supernatant solution was spread between two infrared-transparent KBr lenses and the FTIR spectra were obtained in the wavenumber range of 4000–400 cm^{-1}.

3.3.12 X-ray diffraction and scanning electron microscope analyses

X-ray diffraction (XRD) and field emission electron microscopy (FESEM) were used to characterize the raw materials and the reaction products of the prepared mixes. Randomly oriented powder samples were extracted from the selected mixes by grinding the dried samples for XRD analysis. The scan patterns were obtained from 10° to 70° 2θ with a step size of 0.02° by using an Empyrean X-ray Diffractometer with Cu-Kα-radiation (Figure 3.20 (a)). The X-ray tube generator was operated at 40 kV and 40 mA. Corundum was used as the external standard for the quantification of both crystalline and amorphous phases using TOPAS software. The crystalline phases were identified using the powder

diffraction file-2, while known phases were taken from the inorganic crystal structure data base.

For FESEM analysis, a JEOL JSM-7600F electron microscope, equipped with an energy dispersive analyser was used to examine the sample microstructure after 28 days of curing. The equipment used for this purpose (Figure 3.19) are in the Materials Laboratory of the School of Mechanical and Aerospace Engineering.

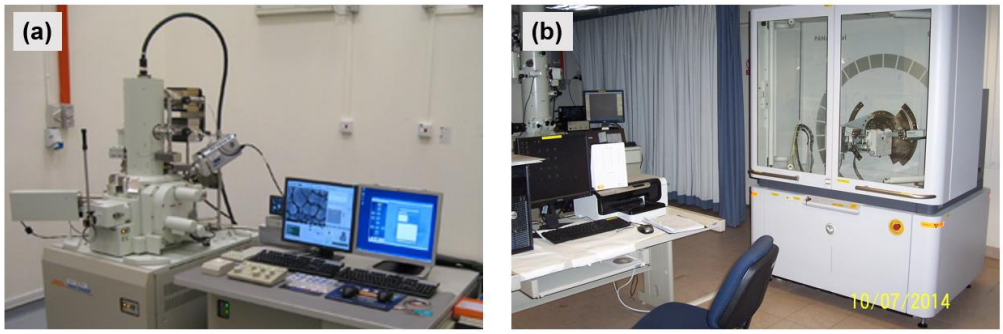

Figure 3.20 (a) FESEM and (B) XRD instrument used for the reaction product analysis

3.3.13 3D printing

Unlike plastic and metal 3D printers, concrete printers are usually large-scale system, and in this work, we have used our custom made four axis gantry printer (Figure 3.2) that can print concrete components of one cubic meter volume. The motion parameters such as maximum speed V_{max} of 4-axis are listed in Table 3.7. The fresh mortar was pumped by a progressive cavity-pump located on the side of the printer. The nozzle is modular set up and it is connected to a hose pipe of 1-inch diameter. The nozzle can rotate 360 degree for maintaining its tangency to the tool path. The first test result with Ø20 mm circular nozzle was found to be unstable for large scale printing and therefore, cross-sectional opening was changed to 30 x 15 mm (Figure 3.22). This resulted in promising buildability, though for 20 x 20 mm square nozzle, buildability was restricted to a certain number of layers. Like the nozzle opening, print speed and pump flow rate (and resultant

pump pressure) setting were optimized to ensure continues flow and good shape retention of the filaments.

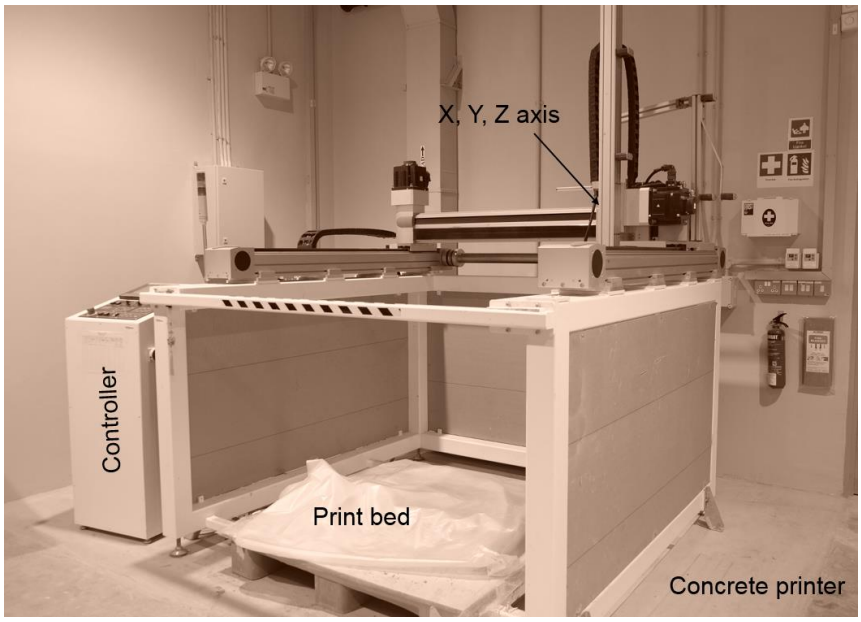

Figure 3.21 4-axis gantry concrete printer at Nanyang Technological University, Singapore

Table 3.7 4-axis Gantry concrete printer motion parameters

Degree of freedom (DOF)	**V_{max}**
Translational X-axis	150 mm/s
Translational Y-axis	150 mm/s
Translational Z-axis	150 mm/s
Rotational X-axis	2 sec/rev

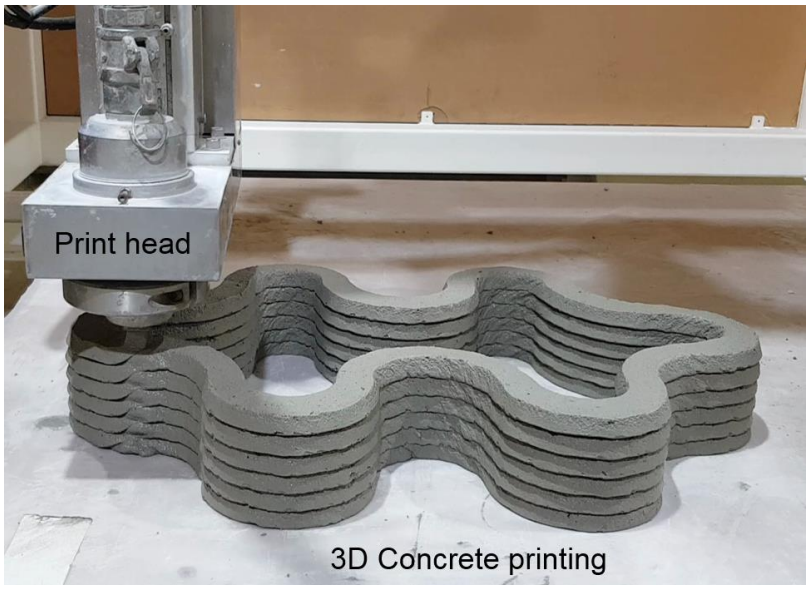

Figure 3.22 Demonstration of 3DCP using the 4-axis gantry printer

3.3.14 Mechanical strength test

The compressive strengths of the prepared samples were measured by uniaxial loading. The equipment used for this purpose was a Toni Technik Baustoffprüfsysteme machine, operated at a loading rate of 100 kN/min. 50 mm cubic samples were casted in the molds and their average value (for 3 samples) and standard deviation were reported following BS EN 196-1:2016 standard [184].

In case of 3D printing, to create samples of these dimensions with the available nozzles it is not possible to do this without printing layers next to each other. Therefore, a block with dimension 300 ×150 × 200 mm was printed as shown in Figure 3.23. Later 50 mm cubic samples are extracted from this block and loaded in different direction (Figure 3.24) for compression strength test. This stepwise creation of the samples is shown in Figure 3.23. The layer orientation of test direction F1 is the same as the print direction while the orientation of test directions F2 and F3 are perpendicular to the print direction.

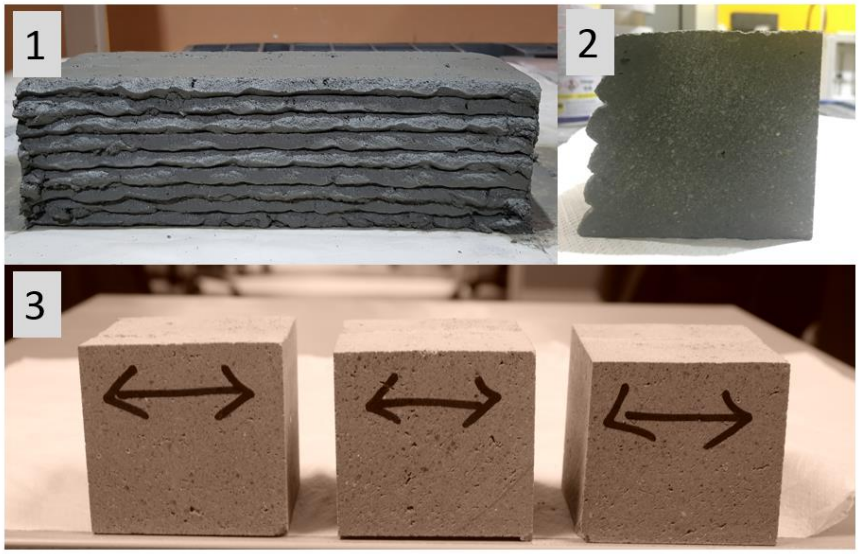

Figure 3.23 Stepwise creation of 3D printed compression test samples

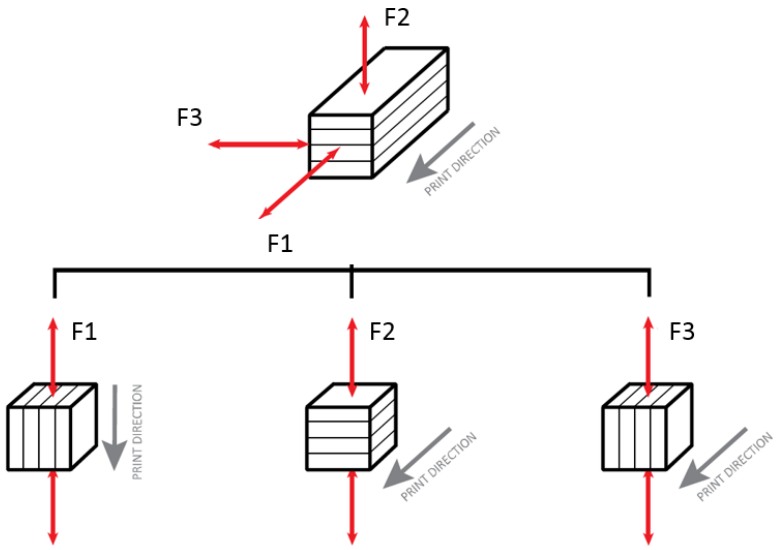

Figure 3.24 Schematic view of 3-directional mechanical testing

Similar to previous studies [2,4], prism samples with dimensions of 40 x 40 x 100 mm were extracted from the printed block and used for uniaxial tension tests. The specimens were glued (HBM X-60 rapid hardening adhesive) at both ends and to get rid of failure

in the glue interface, a small notch was made to reduce the concrete area with less influence of peak stress (Figure 3.25). The uniaxial tension tests were performed in a manner similar to those presented in earlier works [185] in an Instron machine (Instron 5960) with a load capacity of 50kN in a deformation-controlled mode with a displacement rate of 0.1 mm/s. The results of directional tests were averaged for three samples and compared with each other including the control mold casted specimen.

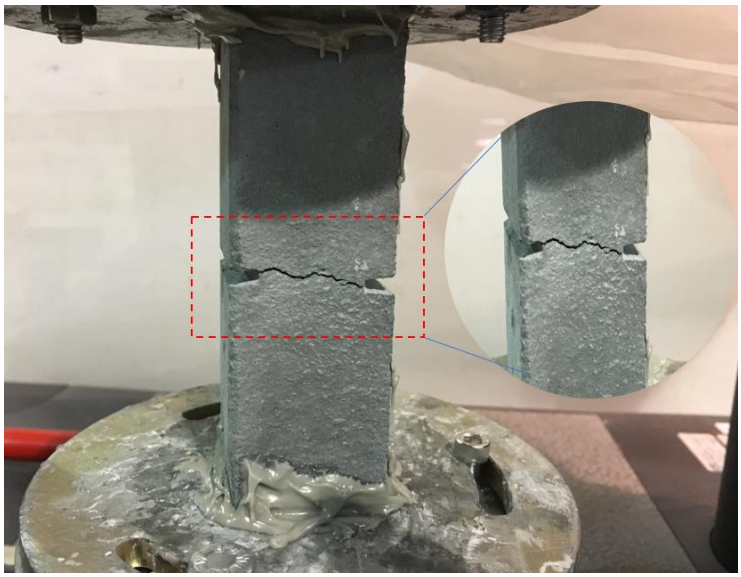

Figure 3.25 Setup for uniaxial tension tests

The flexural (3-point) bending test was conducted in the same Instron testing machine according to the loading configuration shown in Figure 3.26. Similar to casting, nine 160 x 40 x 40 mm samples were collected from the block and tested in different direction for loading rate 10 N/sec.

Inter layer bond strength is a unique property of 3D printed concrete. Two layers of fresh mortar using 20 mm square nozzle were deposited with different time gaps and after 28 days of ambient curing, three specimens of 4 mm length (for each time gap) were saw-cut from it for the tensile bond test. Similar to tensile test, a notch was made and then

the two layers were glued with metal plates using a rapid hardening adhesive (Figure 3.27). The tensile test was carried out at a rate of 0.035 ± 0.015 MPa/s according to ASTM C1583/C1583M-13 [186] and after failure, the effective area of bonding and peak load was then used to calculate the bond strength for each sample.

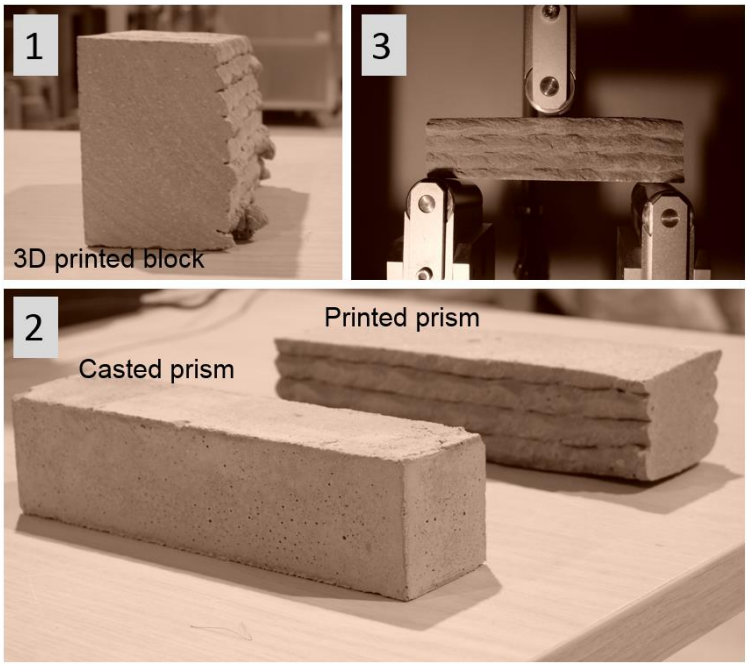

Figure 3.26 Stepwise creation of 3D printed flexural test samples

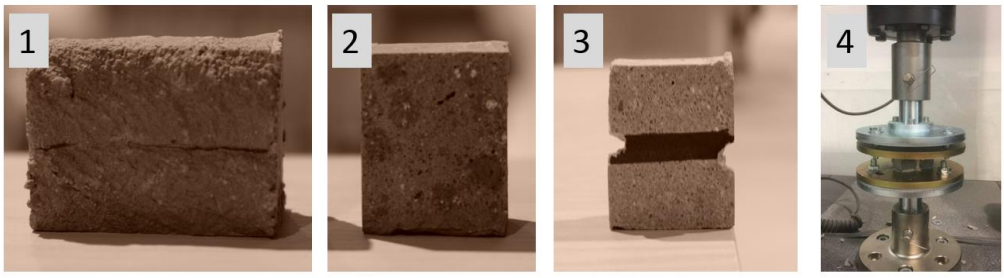

Figure 3.27 Stepwise creation of tensile bond strength test samples

Chapter 4 Influence of material design on 3D Printability of fly ash-cement mortar

4.1 Introduction

In recent years, 3D printing of PC based materials has been at the forefront of construction technologies due to its inherent thixotropic property that enables smooth extrusion and excellent shape retention. However, this research focused on systematic investigation of the effect of various mix design parameters on 3D printability performance of HVFA binder. A yield stress-based mixture design approach was first adopted to obtain a control mix and later, VMA and SCMs were added to modify the rheological properties required for 3DCP. The final modified mix was characterized using strength test, isothermal calorimeter, FESEM and XRD techniques to confirm the suitability of the proposed mix design for a large-scale concrete printing application.

4.2 Material design

The experimental procedure to obtain 3D printable HVFA mortar begins with extrudability and shape retention criteria, followed by buildability test only for few selected mixes. Five mix designs were initially prepared by varying the sand-to-binder ratio from 1.1 to 1.9, while the binder composition was kept constant (FA: PC = 60:40 and 3% sodium sulfate activator by mass of the binder) according to author's previous study [187]. These mix proportions were analyzed based on their paste volume (PV: PC+ FA + water) content to first obtain an extrudable material, so called "control" mix. Table 4.1 shows the detailed composition of five mixes, represented as M42 to M50, where the number preceding M is the respective PVs.

Table 4.1 Mixtures studied for HVFA mortar extrusion (water-to-binder ratio = 0.35)

	PC (kg/m^3)	FA (kg/m^3)	Sand (kg/m^3)	Water (kg/m^3)	PV (%)
M42	246.75	370.13	1168.85	340.91	42
M44	322.87	484.31	968.62	339.01	44
M46	385.65	578.48	803.45	337.45	46
M48	447.86	671.79	639.80	335.89	48
M50	527.88	791.82	429.30	333.90	50

4.3 Results and discussion

4.3.1 Extrudability and shape retention

In this study, extrudability is defined by smooth flow of the mortar from reservoir to nozzle head through one-inch diameter hose pipe connected to a progressive cavity pump. Extrudability, also referred as pumpability, can be characterized by many test methods that have been developed in the past based on concrete rheology, tribology, flow rate and pipe radius [188-190]. However, here the extrudability was confirmed by direct 3D printing the concrete filaments with a 30×15 mm rectangular nozzle similar to [114]. Each filament was ~1500 mm long and the test result was evaluated as YES or NO, when the complete length was deposited successfully without a blockage or discontinuity. Mixes 42 and 44 were difficult to pass through the pipe–pump–nozzle system due to the high sand content and in this regard, extra water was not added that can cause segregation and reduce the concrete compressive strength. However, from mix M46 onwards, all the mortars seem to be suitable to cope with the printing process as shown in Figure 4.1.

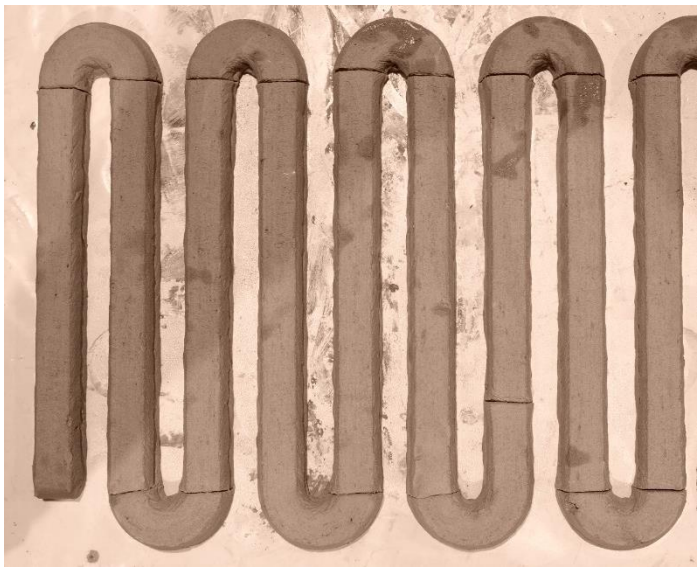

Figure 4.1 Continuous filament extrusion using M46 mix design

The extrudability of the mortars can be explained based on two properties: 1) sufficient PV to create a slip layer, 2) paste consistency and aggregates grading to hinder bleeding due to pump pressure. The decrease in PV increases the solid volumetric fraction in the mix, which results in intensifying the intergranular friction, thus giving rise to a high extrusion force. An interruption in the extrusion was noted at a critical PV equals to 44. For PV below 44%, the mix flow was exclusively frictional during the extrusion and this is related to the insufficient PV that prevents lubricant effect between the sand grains. Therefore, the pump pressure was increased causing paste filtration through the aggregate skeleton. Figure 4.2 shows a schematic diagram of mortar extrusion behaviour with respect to PV content, that explains the role of PV as a lubricant both between sand grains and between the mortar/hose pipe interface. When the PV increased more than 46%, a lower pressure was observed as the intergranular forces become weaker and further increase in PV resulted a colloidal type mix behaviour where the flow is mainly governed by the paste consistency.

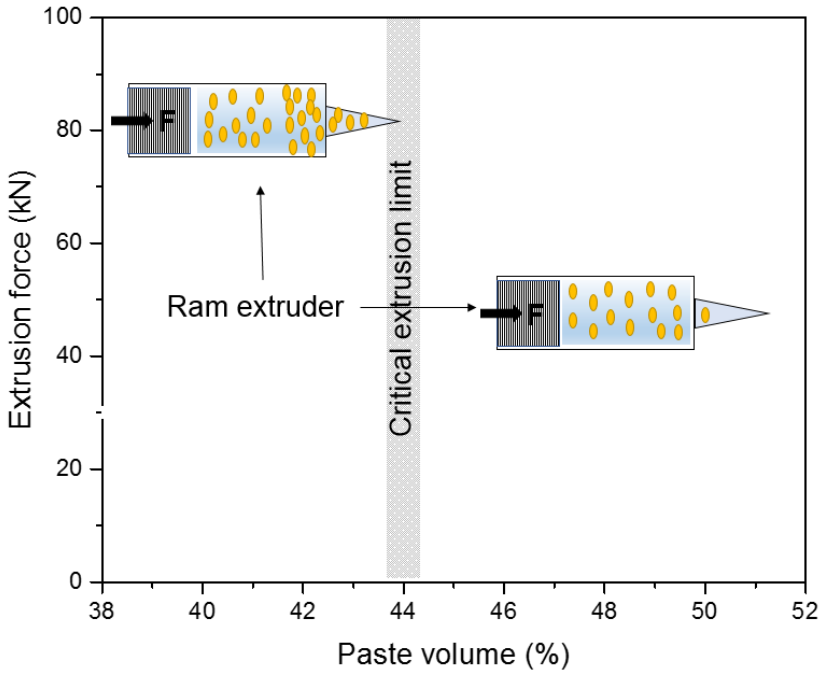

Figure 4.2 Schematic diagram showing relation between extrusion forces and PV

Like PV, the aggregate phase is also important as it typically represents 60–75% of the concrete mixtures. The PSD of aggregates considerably influences the packing density, which in turn determines the voids to be filled with the paste and extra paste to lubricate the aggregates. The total SSA of the aggregates also affects the flowability, since increase in SSA can cause reduction in the thickness of the paste covering aggregates, and consequently the flowability decreases depending on the total paste content. Therefore, PSD should be optimized in such way that both packing density and workability of the mortar can be improved simultaneously. PSD varies according to proportion of fine and coarse aggregate and the fine content for maximum flow rate is reported to be higher than the fine needed for maximum packing density [177]. The difference between the state of maximum packing density and flow rate is depicted in Figure 4.3, where the more fines in Figure 4.3 (b) is not only filing the gaps among the coarse particles but also providing ball-bearing effect, which will alleviate the interlocking and facilitate the movement of coarse particles in the flow direction. Therefore, the gradation of the aggregate used in

this study was selected with more fine contents (see Chapter 3), considering the need of maximum flow condition.

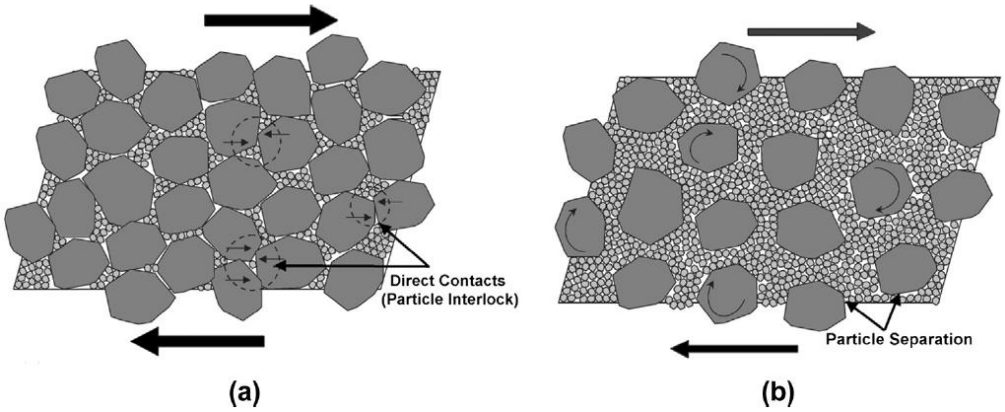

Figure 4.3 Schematic illustration of aggregate structures for: (a) the state of maximum packing density and (b) the state of maximum flow rate [177]

The easy of concrete extrusion in terms of *pumping pressure* or *mass flow rate* can be measured from rheological parameters such as yield stress, which must be exceeded to initiate the flow, and viscosity, which is the resistance in flow velocity. By means of a rheometer, these two parameters were measured for the steady state flow conditions and results were shown in Figure 4.4. It is evident that with increase in PV, the yield stress decreases as expected and this phenomenon can be described using Krieger–Dougherty (K–D) equation [191] which links the rheological properties with solid volume fraction of particles present in a suspension. Hafid et al. [192] also observed similar increase in the yield stress with increasing volume fraction of sand and the rate of increase depends on the particle morphology as shown in Figure 4.5.

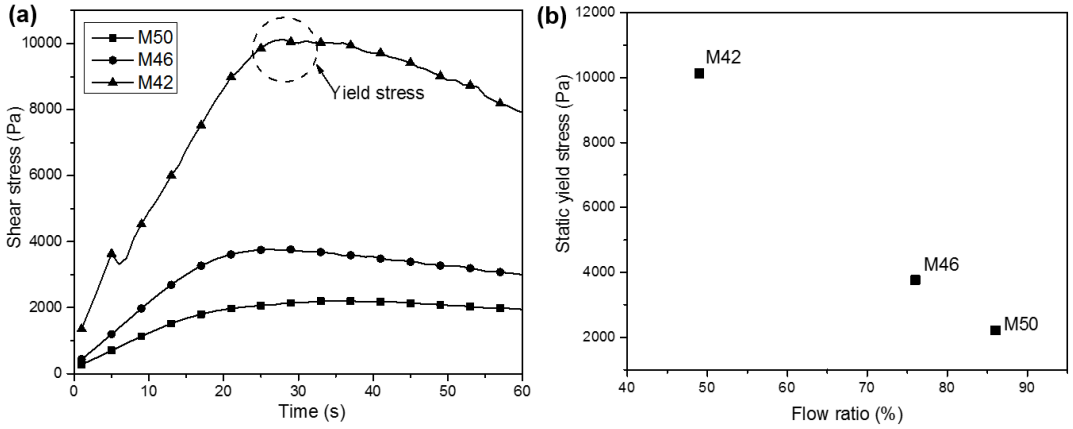

Figure 4.4 Effect of different sand dosage on yield strength and flowability

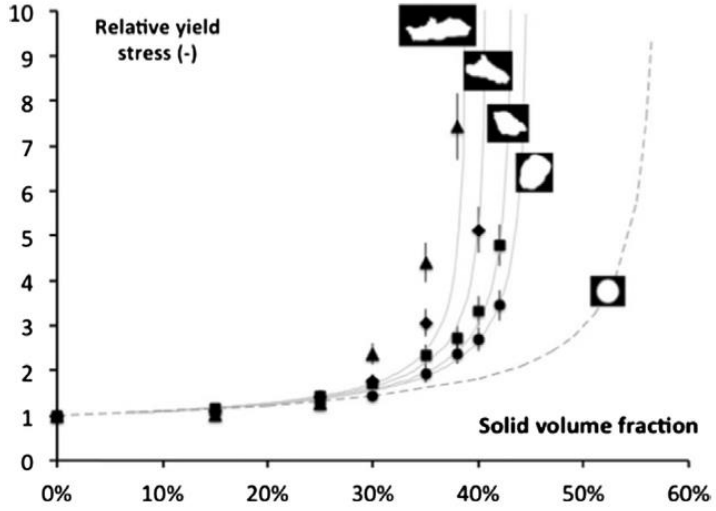

Figure 4.5 Variations in relative yield stress as a function of solid volume fraction [192]

Usually, when the particles like sand, gravels are added to cement paste, the resultant rheology is considered as hydrodynamic, at low volume fractions and when the volume of particle increases, for example in M42 and M44 mixes, the hydrodynamic interaction changes to frictional regime causing considerable solid contacts among the particles. These contact forces increase the yield tress and causes blockage or discontinuity during the mortar extrusion. Yammine et al. [193] found that there exists critical transition

volume fraction, beyond which the frictional contacts begin to dominate the rheological behavior and the material loses its workability (pumpability) property. Therefore, in order to design a pumpable material, the aggregate volume should be kept below the transition value as well as the yield stress need to be adjusted depending on the pump capacity and allowable pressure limit. Since M46 and M50 mixes were able to extrude out smoothly, their flow ratios (refers to viscosity) were plotted in Figure 4.4 (b), out of which the M46 mix was opted for shape retention and buildability investigations due to comparative higher yield stress and low viscosity properties.

The shape retention of M46 was defined by a ratio of area of the extruded filament-to-area of nozzle. The ratio, i.e shape retention factor (SRF) was found to be 0.84 which is reasonably acceptable as there was no visible deformation of the filament after being deposited on the print bed. Effects of binder was also investigated for the M46 mix by changing the FA-to-PC ratio with minimum 50% FA content. It was found that (Figure 4.6) with increase in the FA content, both yield stress and viscosity decreases and many authors have reported similar behaviour in the past [194] due to spherical shape of the FA that improves the workability.

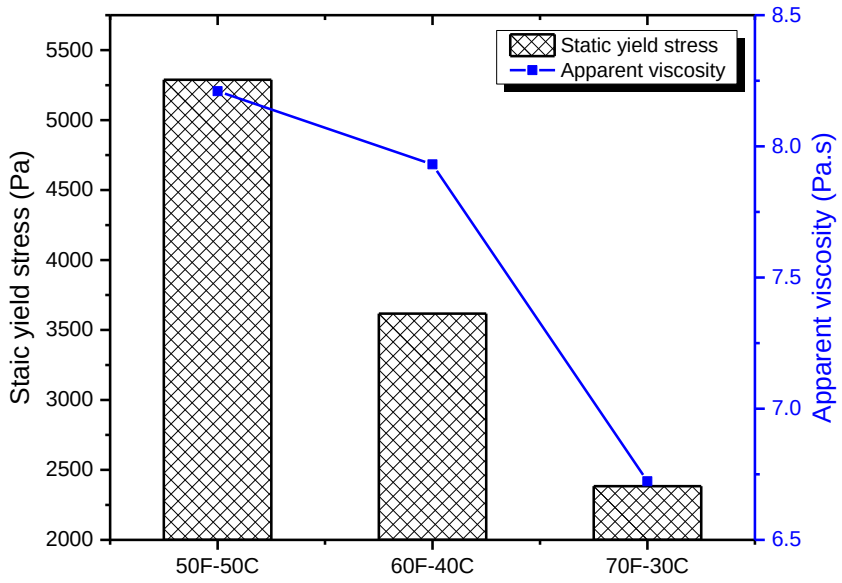

Figure 4.6 Static yield stress and viscosity values of M46 mix

It is interesting to note that though the rheological parameters decrease with FA inclusion, the shape retention was not much affected which contradicts the general understanding that low yield stress/viscosity fluids are more workable. Wangler et. al. [195] proposed an mathematical equation to estimate the stability of a layer based on yield stress and for a layer of height (h) =15 mm, the minimum value was found in between 150 and 1000 Pa, which is easily attained by all the three HVFA mixtures as shown in Figure 4.6. Thus, it is confirmed that despite yield stress variation, shape retention did not change significantly due to fulfillment of required yield stress caused by strong van der Waal force of PC and FA particles.

In 3DCP, shape retention of the extruded filaments is also affected by viscosity recovery property, which is hardly discussed in literature. Viscosity recovery indicates the change in material viscosity before, during and after printing. Due to time and shear dependent behaviour of cementitious materials, it is important to measure the fresh property just after the extrusion and relate it to the SRF. Figure 4.7 shows the recovery graphs of M46 mix with different FA:PC ratio and it is very clear that all the three mixes have comparable recovery behaviour though their viscosities are slightly different. Recovery ability is related to thixotropy property that allows the material to flocculate and de-flocculate at different flow conditions. PC based binders possess an inherent thixotropy property, originates from cement particle flocculation and early age hydration products. However, replacing or adding foreign particles such as FA or aggregates breaks the colloidal flocs and influences the recovery ability of the mixture [17,192]. Considering the effect of thixotropy, it was found that all the three mixes were able to recover 25-35% of their original viscosities within 60 seconds of extrusion. This recovery ability also depends on shearing (pumping) time and applied shear rate, which will be later discussed in this chapter with more details.

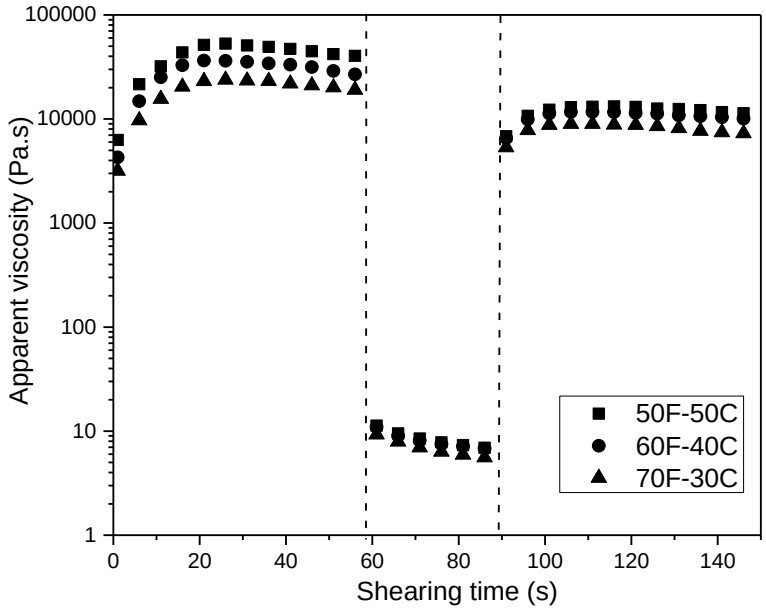

Figure 4.7 Viscosity recovery property of M46 mix with different FA (F) and PC (C) combinations

4.3.2 Buildability

Buildability of 3D printed structures is related to material green strength (compressive yield strength) and stiffness that keep on increasing with hydration reaction and time [196]. Figure 4.8 shows the deformed configurations of a 3D printed cylinder using M46 mix with two different FA-to-PC ratios (FA: PC = 50:50 and 70:30). The cylinder (diameter 30 cm) was printed with 15 mm layer height and 80 mm/sec printing speed and their bottom layer deformations were measured after the printing to compare the load bearing capacities.

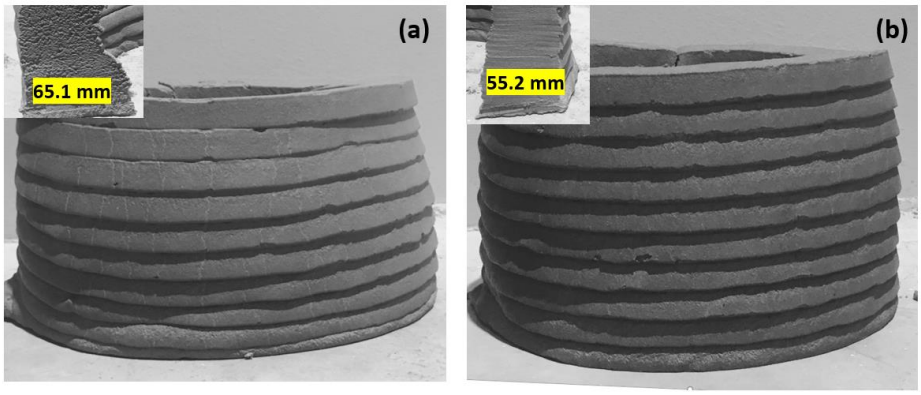

Figure 4.8 Buildability and filament stability of HVFA mixture containing FA: PC (a) 70:30 (b) 50:50 ratio

It is understood from the above figure that increasing the FA content from 50 to 70% notably affected the buildability performance, though in both the cases the bottom layer has completely deformed. High volume of FA leads to early deformation of the structure as seen from "bulging" type failure in the 70% FA mix. However, replacing the FA with PC produced stable layers which is reflected by reduced width of the bottom layer (65 to 55 mm) shown in left-hand corner. Due to low stiffness of the mixtures, the bottom layer deforms quickly with addition of each layer and around 13^{th} layer the whole structure collapsed completely. Rapid structural build-up can improve the buildability and for 3D printing such slender cylinder, the deposited material needs to harden as soon as possible which is addressed in detail in section 4.3.4 and 4.3.5.

4.3.3 Open time and hardened properties

Open time, defined as workable time limit of printable concrete often measured with Vicat apparatus. However, the results of Vicat testing are not directly helpful in characterizing the workability of fresh concrete and it has been reported that open time mostly occur earlier than the usual setting (initial) time of the material. The test results by Vicat setting time device confirmed that addition of FA increased the setting time which is more obvious and reported previously due to low reactivity of the FA particles [44]. An initial setting time of 220 minutes was observed for 70% FA mix, while for 50%

it reduced to 180 minutes indicating an approximate open time of two hours from mixing with water. It is important to note that though the workability of fresh concrete decreases with time due to thixotropy and ongoing hydration, agitation or shearing of the material can extend the workability time by minimizing the effect of thixotropy before setting of the material. Therefore, the material processing [197] has also a significant effect, which must be considered for accurate determination of the open time.

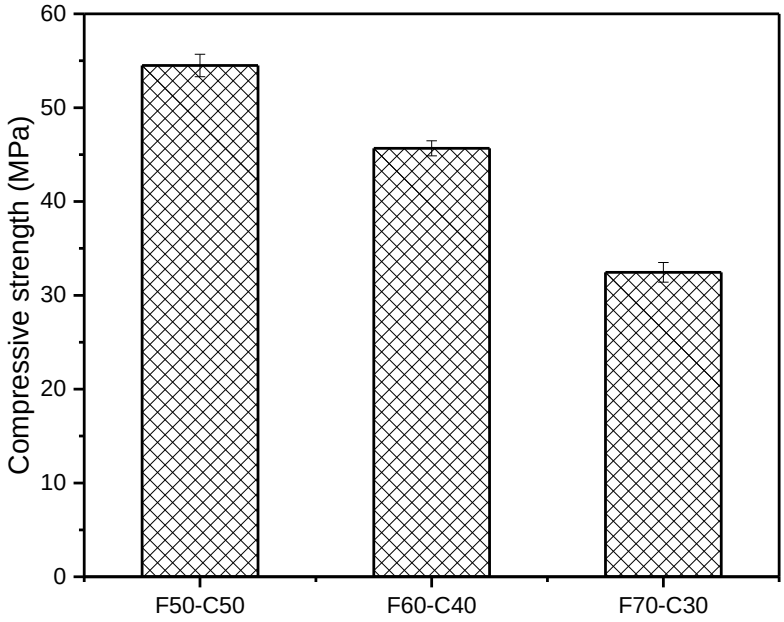

Figure 4.9 Variation of compressive strength of M46 mortars with different FA content

In terms of compressive strength, addition of the FA decreases the 28 days strength (Figure 4.9) due to dilution effect. Partial substitution of PC with FA usually offers later strength development due to slow pozzolanic reaction between portlandite and glassy phases in the FA. So, it is necessary to characterize the FA and only 40% glassy phase was found in the current FA, which is comparatively less with past findings. One way to increase the reactivity of FA is to increase the curing temperature and/or adding a suitable source of alkali such as sodium sulfate used in this study. Sodium sulfate has a positive effect on the activation FA as it can directly react with the Ca $(OH)_2$, increasing the

alkalinity and accelerating FA dissolution. According to the literature, increasing sulfate addition from 3% to 5% has very little impact or no impact on mechanical properties of the HVFA binders [44] and therefore, with an aim for low cost binder we have used 3% sodium sulfate (by mass of the binder) to activate the glassy phase of the FA. Out of three different combinations of FA-PC mortars, 50% FA with 50% PC was found to exhibit highest compressive strength followed by 60-40 and 70-30 combinations. Since the target strength of this study was M30 grade concrete, F70-C30 mix was selected as "control" mix for further fresh property improvement due to acceptable strength and flow properties.

4.3.4 Effect of nanoclay addition

In this section, NC was added to improve buildability of the control mix which is well extrudable and has excellent shape retention property. The effect of NC on flow and thixotropic property were discussed with insights on mechanical and microstructural properties of the optimized mix.

4.3.4.1 Flow properties (yield stress, viscosity and thixotropy)

Figure 4.10 shows the effect of NC dosage on static yield stress and apparent viscosity of the control mix. These results indicated that addition of the NC could help with rapid structural rebuilding at early ages, thus making it an ideal thixotropy modifier. Similar behavior was reported in previous studies [198,199], where it is postulated that at rest, the oppositely charged edges of NC tend to associate with each other via the electrical attraction force, thereby producing a denser microstructure which corresponded to a higher static yield stress. However, during strong shearing the viscosity decreases as the particles progressively separated and aligned in the direction of the flow. This decrease in viscosity is associated with the electrical repulsion between the negatively charged particle surfaces, further enhancing the shear thinning behavior.

Other than surface charge, fineness, dispersion force and the amount of free water were also considered as contributing factors to the increase in thixotropy with the addition of NC [200]. Smaller particle sizes can result in a strong dispersion force which plays an important role in determining the flocculation of particles. As the mix containing 0.5% NC (from here referred as 5NC) led to the highest yield stress, it was selected for further rheological analysis in comparison with the control mix.

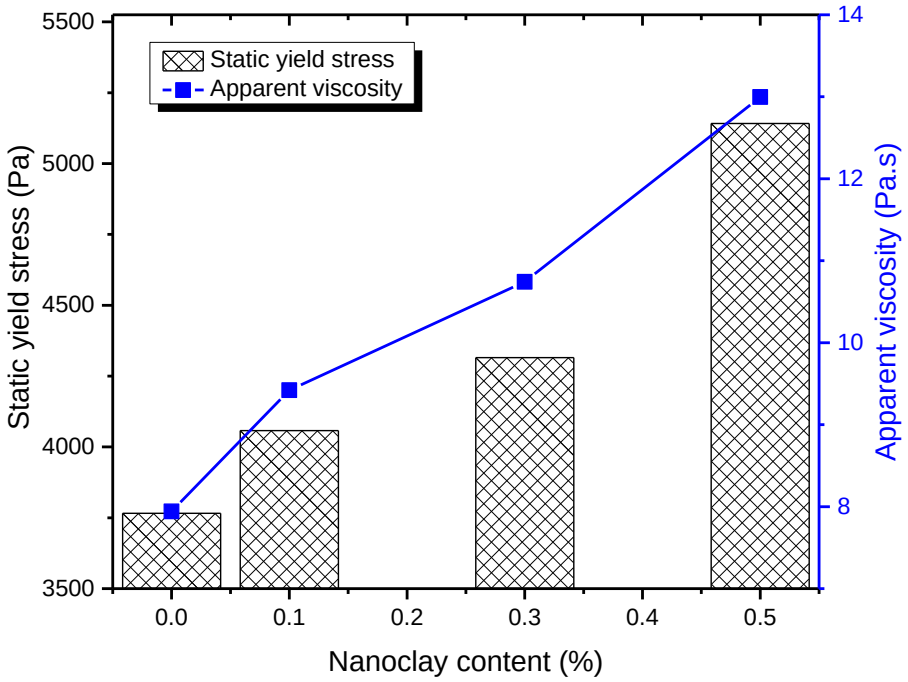

Figure 4.10 Effect of NC dosage on yield stress and viscosity of the control mixture

From Figure 4.10, it can be noticed that a very small amount of NC increased the static yield stress (~48% higher) although during shearing (at constant shear rate 300 s^{-1}), the apparent viscosity went down to <10 Pa·s for both the control and clay modified mixes (Figure 4.11). The effect of NC was therefore observed in terms of improvement in the yield stress without significantly affecting the viscosity. This behavior, so called thixotropy is highly useful in 3DCP applications, where there is a need for high yield stress and low viscosity building materials.

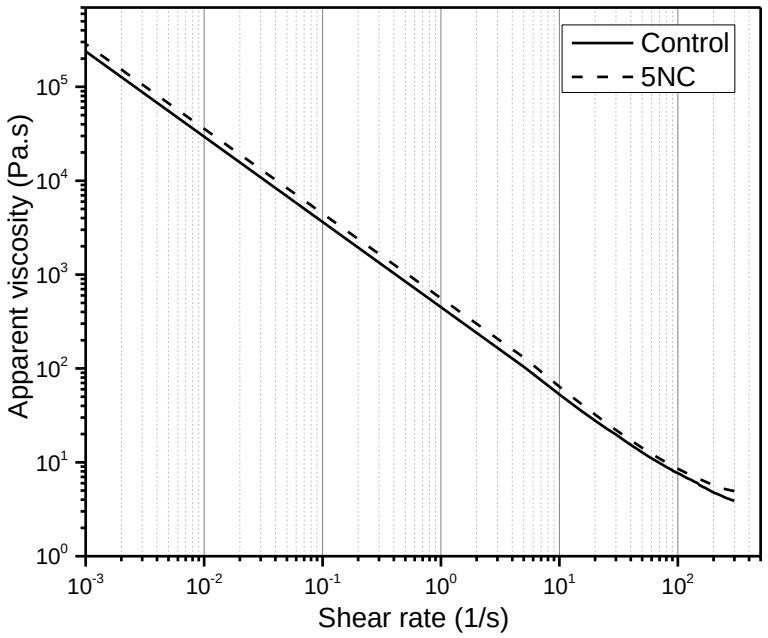

Figure 4.11 Shear thinning properties of control and 5NC mix

Thixotropy performance often characterized in terms of structural break down and recovery is shown in Figure 4.12 and 4.13 respectively. Structural break down indicates the easiness of shearing and how fast the internal structure of a material breaks down during the shearing. It is indicated by a structural parameter (λ), which was found to be substantially higher for the NM mix (0.41) than the control mix (0.27). Higher the (λ), better is the shape stability and higher buildability.

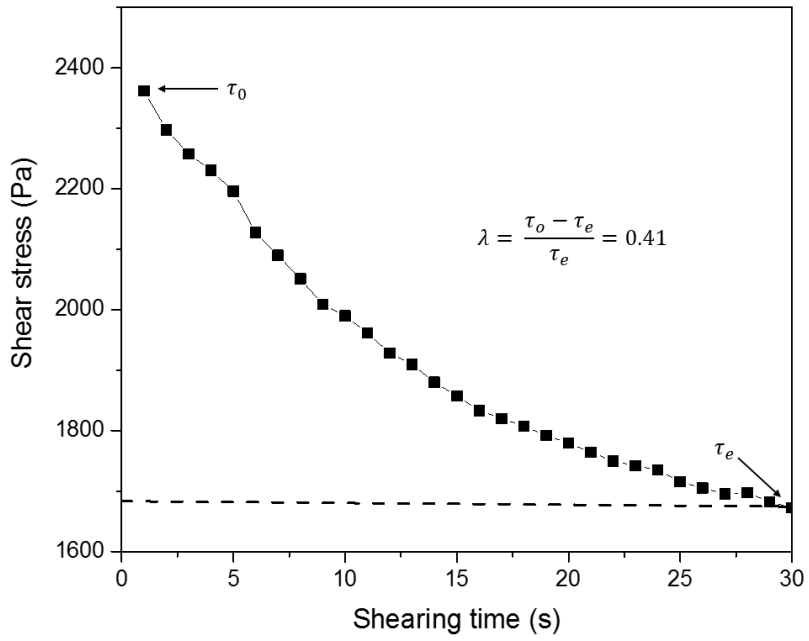

Figure 4.12 Structural break down and λ value of the 5NC mix

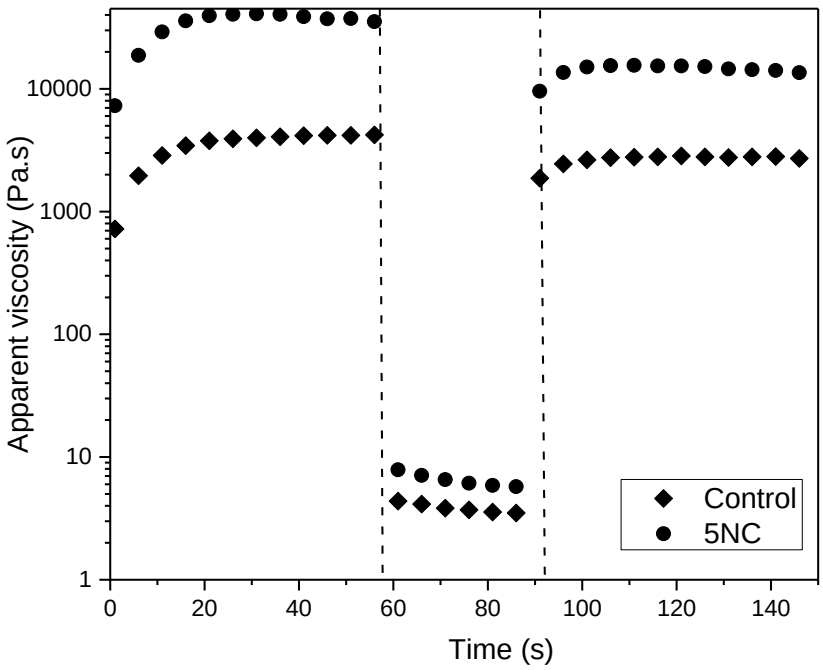

Figure 4.13 Viscosity recovery of the control and 5NC mix

Figure 4.13 shows the viscosity recovery graph of the 5NC mix compared to control mix and it is very clear that a small amount of clay has significantly improved (78.20%) the recovery property due to quick re-flocculation ability after the deposition (static state). However, the recovery behaviour also depends on applied shear history such as shear rate and time. Following section will elucidate these shear effects, while comparing both control and the 5NC mixes.

4.3.4.2 Effect of shear rate and time on thixotropy (viscosity recovery)

Figure 4.14 shows the apparent viscosities of both control and 5NC mixes in three different stages as described earlier in Section 4.3.2.2. The recovery percentage was assessed by the percentage of original viscosity (in stage (i)) recovered in stage (iii). Compared to the control mix, recovery ability of 5NC was found to be more prominent irrespective of the applied shear rates and accordingly, 5NC300 mix recovered 44% more viscosity than the control mix at highest shear rate i.e. 300 s^{-1}. This rapid recovery was akin with a jammed system, where the thixotropy effect of both the NC and PC particles built up a network that quickly increased the viscosity of the mixture. The recovery kinetics after shearing is completely different from the breakdown kinetics during shearing. The van der Waals force of attraction that agglomerates the PC particles are generally weak physical bonds and can breakdown easily by the shearing action of the pump. This process of break down and recovery after the shearing is reversible in nature before initial setting of the mortar and addition of NC to this system further increased the flocculation strength due to their inherent charged edges. Therefore, in the case of 5NC100 and 5NC200 the recovery percentages remained almost the same as 5NC300, except slight increase in the viscosity in stage (ii), which is related to the shear rates.

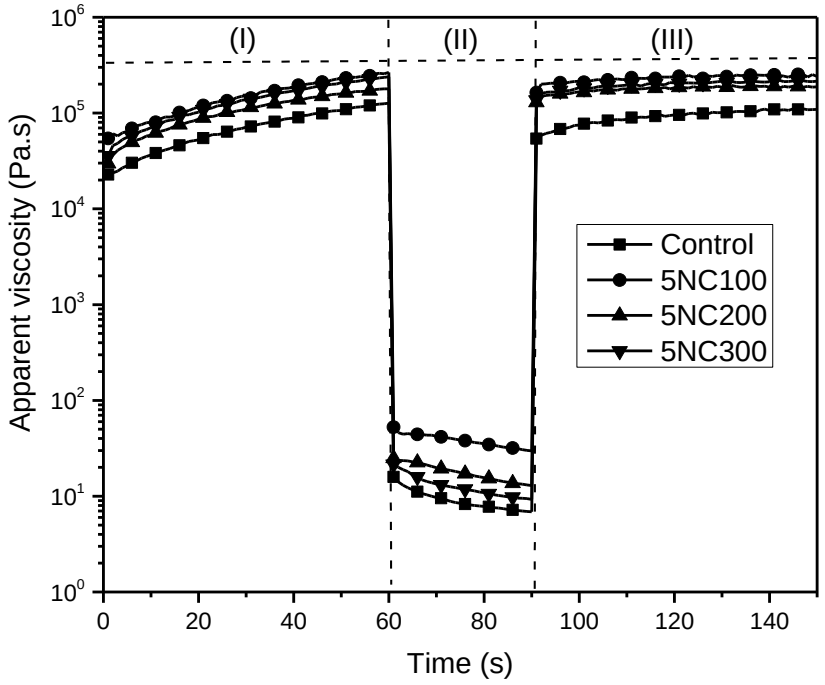

Figure 4.14 Effect of shear rate on viscosity recovery of 5NC mix. Note that the number preceding 5NC denotes the applied shear rate in s^{-1}.

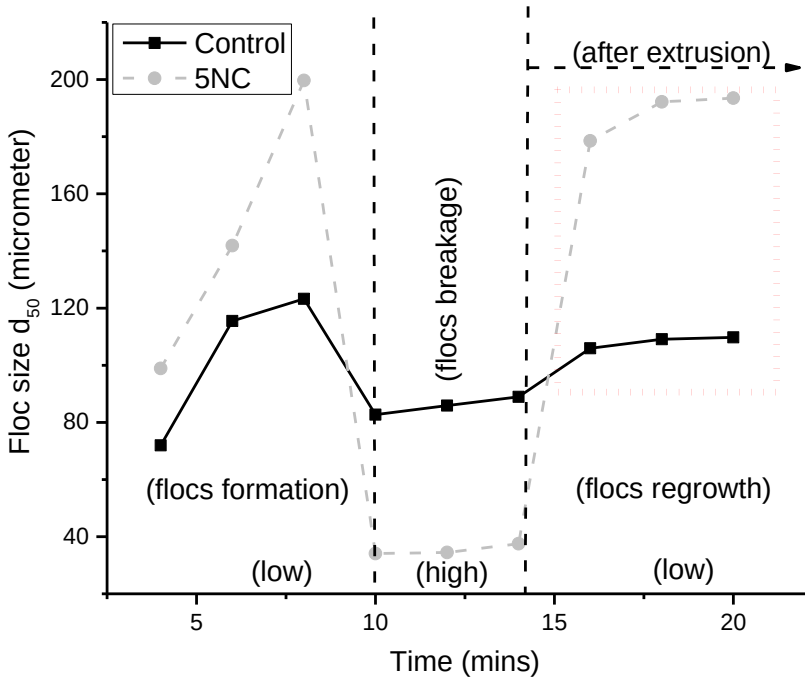

Figure 4.15 Floc size evolution under different shearing conditions

In order to have a better understanding of the behaviour of mixtures under structural buildup and recovery, floc size measurements were performed via laser diffraction analysis. The average floc sizes of both the control and 5NC mix at different alternating cycles of low (60 rpm), high (600 rpm) and low (60 rpm) was shown in Figure 4.15. It is evident from the floc size variation that the microstructure of 5NC is in a condition that is more agglomerated than the control mix at low rpm, however during high rpm the floc size decreases, similar to the findings by focused beam reflectance measurement device [201]. Such agglomeration effect of NC is at origin of thixotropy and it's consequence is demonstrated in this thesis for 3DCP application.

In 3DCP, shearing of the material (time) depends on the distance between the delivery system (i.e pump) and printer, connected by the hose pipe. The obtained result shows that the thixotropic recovery properties of 5NC mix is hardly affected by different shearing time. However, without NC long shearing time led to delayed in viscosity recovery as shown in Figure 4.16. Two scenarios involving shearing of the control and 5NC mixes were observed for 60 and 120 seconds at constant shear rate (300 s^{-1}). Increasing the shearing time from 60 to 120 seconds did not cause any major influence over the 5NC mortar. However, in the case of the control sample despite quick recovery in 60 seconds, the recovery time was delayed for 120 seconds shearing. This delay in viscosity recovery is attributed to breakdown and re-growth of the internal structure in the absence of sufficient networking elements such as NC or PC. Based on these observations, it can be envisaged that for longer shearing FA based mixtures need more time gap between the layers to avoid any early age deformation whereas addition of small amount of NC can improve the buildability by enabling faster microstructure recovery. Note that, in 3DCP a second layer is usually deposited after the first layer recovers the initial viscosity.

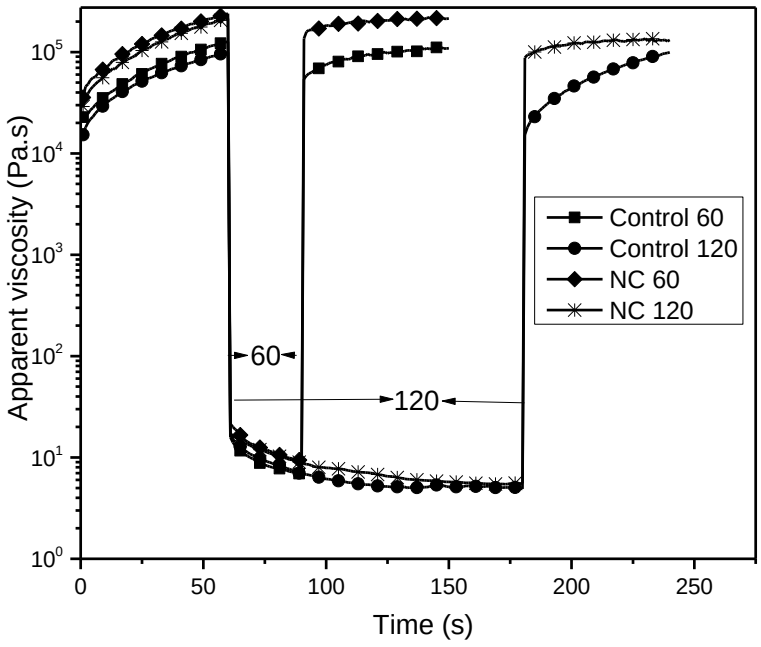

Figure 4.16 Effect of shearing time on viscosity recovery of NC modified mix. Note that the number preceding Control or NC denotes the shearing time in second.

4.3.4.3 Buildability (Structural build-up)

Both control and 5NC were 3D printed to assess their buildability as shown in Figure 4.17. It was clearly observed that the control sample started to deform after the placement of 10^{th} layer and width of the bottom layer expanded from 30 to 65.1 mm as printing progressed. On the other hand, the 5NC mix was able to hold 20 layers without any issues of shape stability. The bottom layer expansion was also found to be limited even after the deposition of 20 layers. This behavior was attributed to the improved thixotropy of 5NC mix.

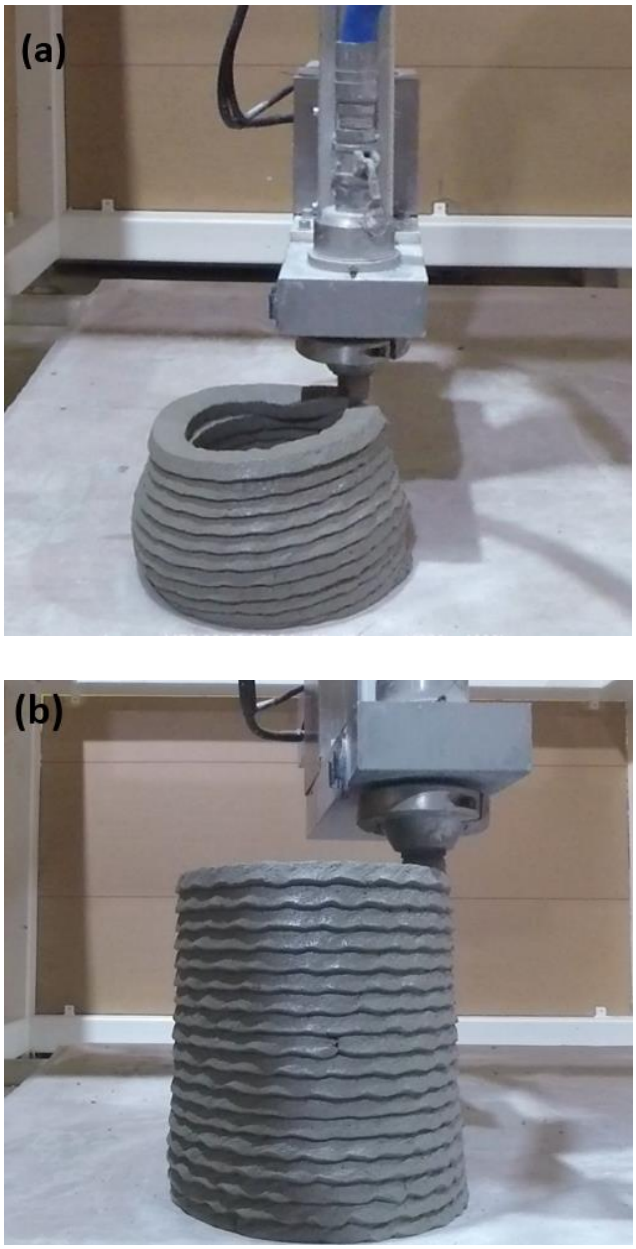

Figure 4.17 Structural build up properties of (a) control and (b) 5NC mix

The evolution of the static yield stress (structural build-up) of both the control and 5NC mix is shown in Figure 4.18 and their relevant parameters (A_{thix}) are summarized in Table 4.2. The A_{thix} index is an indication of the rate of change of material stiffness related to load carrying capacity of the extruded layers. It is apparent from Figure 4.18 that the

yield stress of the prepared mixes increased linearly with time, though the 5NC mix has higher yield stress than control mix due to NC thixotropy effects. These nano-sized clay particles increased the yield stress by minimizing the space between cement grains, leading to a stronger flocculating network that increased the material buildability.

It was pointed out in a previous study [202] that the yield stress of thixotropic fluids is a function of structure and time, gradually increasing in two folds. The first one of these is the dormant period, during which the yield stress increases slowly; and the second one is the accelerating stage, where it increases rapidly. However, in this study the measurements were only performed in the first 20 minutes of dormant period, where the A_{thix} indexes were found to be similar for both control and 5NC mixes, thus indicating similar structural rebuilding rate. This agrees with previous findings [199], where NC was shown to have an immediate effect on thixotropy and little influence over time.

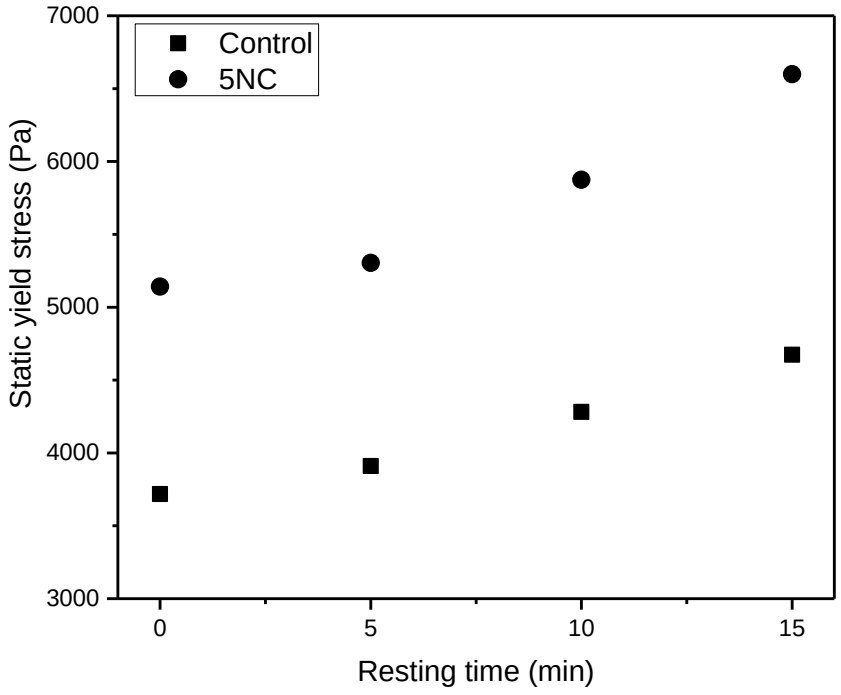

Figure 4.18 Buildability performance of (a) control and (b) 5NC mixes

Table 4.2 Build-up indices (A_{thix}, Pa/s) of the control and NC modified mixes

Sample	Resting time (min)		
	0-5	5-10	10-15
Control	0.63	1.23	1.64
5NC	0.74	1.27	1.54

4.3.4.4 Mechanical strength and isothermal calorimetry

The 28-day compressive strengths of the control and clay added mixtures (5NC) are shown in Figure 4.19. 48.5 MPa compressive strength was recorded in 28 days for the control mix, whereas the addition of NC led to a slight increase in strength.

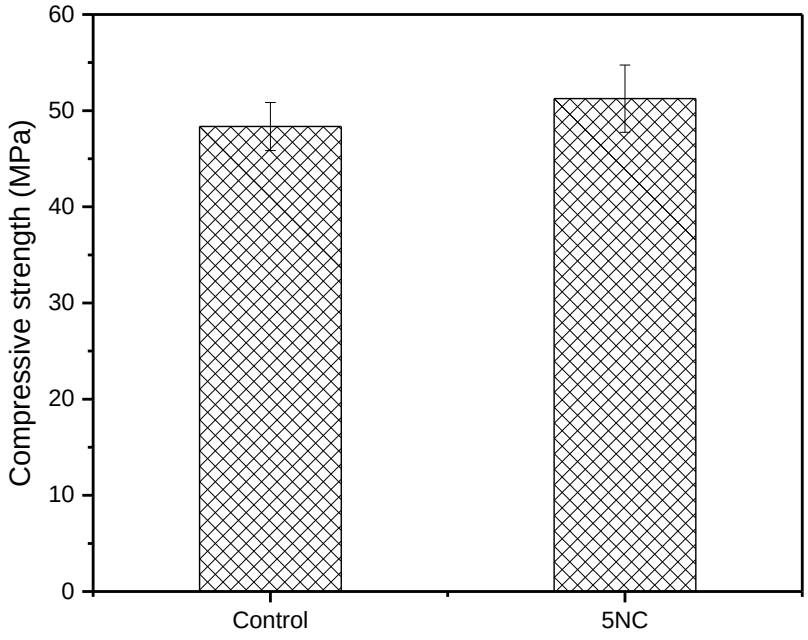

Figure 4.19 28 days compressive strengths of the control and 5NC mixes

Figure 4.20 shows the hydration kinetics of the paste samples with and without NC. Compared with the control sample, the amount of heat released by 5NC mix was higher, as evident by the higher intensity of the initial hydration peak. This increased heat was an indication of the improved hydration mechanism in the presence of NC, which was associated with the nucleating effects of nanomaterials that have large specific surface areas [198]. Accordingly, the addition of NC increased the number of nucleation sites and thereby enhanced the hydration process. An opposite effect can be observed in the presence of high contents of NC, in which hydration can be negatively influenced via the agglomeration of NC particles, thereby hindering mobility inside the matrix [198]. Therefore, adjusting the NC content within HVFA mixes is important for achieving improved hydration without leading to the agglomeration of particles within the matrix.

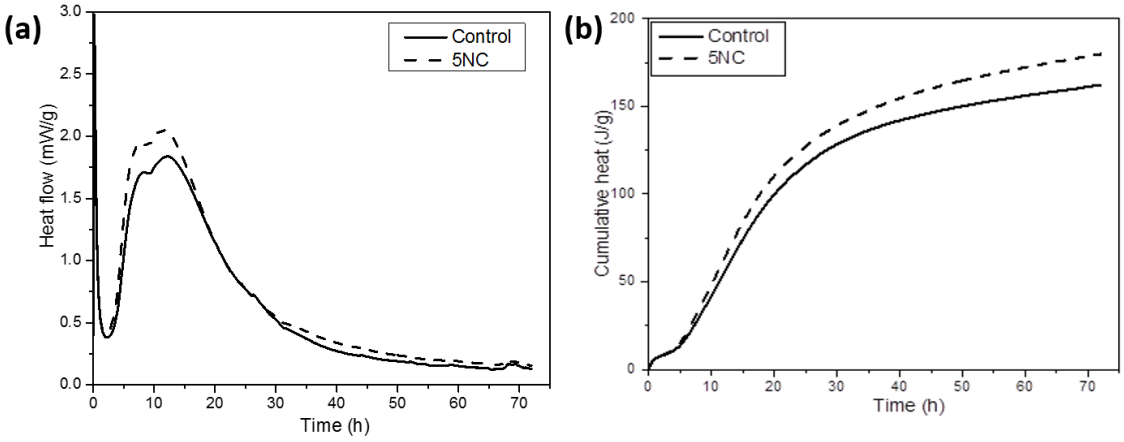

Figure 4.20 (a) Heat flow (b) cumulative heat flow curves of control and clay modified mixes

4.3.4.5 Microstructure and XRD Quantification

The XRD patterns of the control and 5NC samples at different curing ages are shown in Figure 4.21. All the patterns indicated the presence of C-(A)-S-H (2θ = ~29°; PDF #00-033-0306), as Al_2O_3 from FA was also involved in the hydration process. Other than C-(A)-S-H, hydrate phases such as ettringite (2θ= ~16°; PDF #41-1451) and portlandite ($Ca(OH)_2$, 2θ= ~17° and ~47°; PDF #04-0733) were also observed in the XRD patterns.

The presence of calcite (2θ = ~30°, ~38°, ~48°; PDF #02-0623) was also confirmed due to the carbonation of Ca-based hydrates (e.g. portlandite and C-S-H) over time. These were in line with the findings reported in [18, 38]. When mixes with and without NC were compared, it was seen that the incorporation of NC did not change the composition of the final mix by mainly acting as a filler, which could be associated with its low content (i.e. 0.5% of the binder) within the prepared mixes. For both mixes, most of the hydration took place within the first 7 days, as evident by the early formation of the hydrate phases, after which the composition did not drastically change at 14 or 28 days.

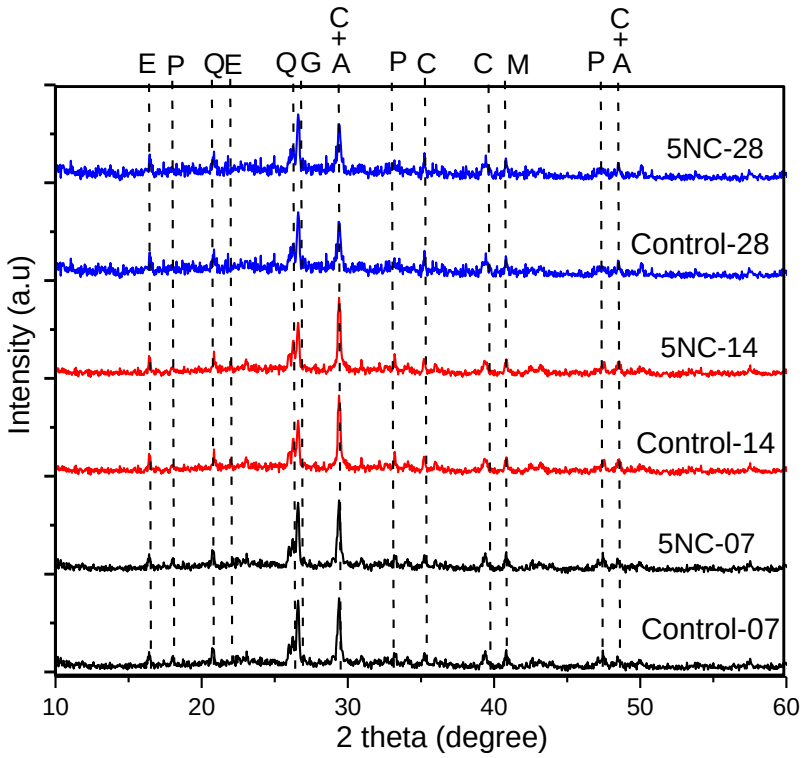

Figure 4.21 X-ray diffractograms of the control and clay modified pastes at 7, 14 and 28 days of curing (E: Ettringite, P: Portlandite, Q: Quartz, G: Gaylussite, C: Calcite, A: C-(A)-S-H, M: Mullite)

In line with the XRD patterns presented earlier, the SEM image of the 5NC mix at 28 days, shown in Figure 4.22(a), indicated the presence of portlandite ($Ca(OH)_2$), ettringite ($Ca_6Al_2(SO_4)_3(OH)_{12}\cdot 26H_2O$) and C-(A)-S-H. Along with these hydrate phases,

spherical unreacted FA particles were also observed among the matrix. The selected area (black frame) was selected for EDX analysis, at the end of which the elemental spectra displayed in Figure 4.22(b) was obtained. The spectra showed the presence of C due to the formation of calcite ($CaCO_3$). Within these mixes, calcite was intermixed with C-S-H, showing that C-S-H was partially carbonated over time. The element Al was also observed in the spectra, indicating the formation of C-A-S-H with a Ca/Si ratio of 1.53, which is within the Ca/Si ratio of C-S-H (1.2-2.3) [203]. Besides these phases, the spectra also reported the presence of element S, confirming the identification of the fibrous phases shown in the SEM images as ettringite.

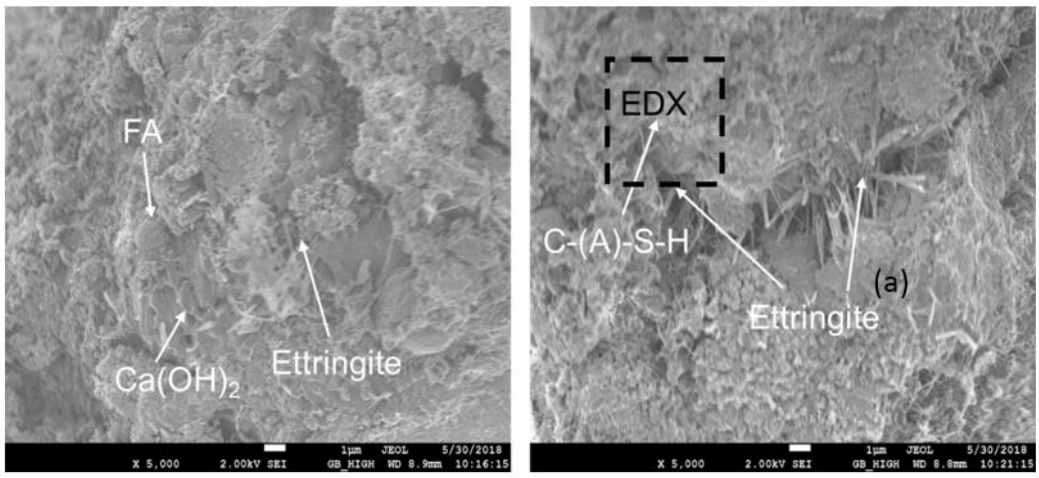

(a)

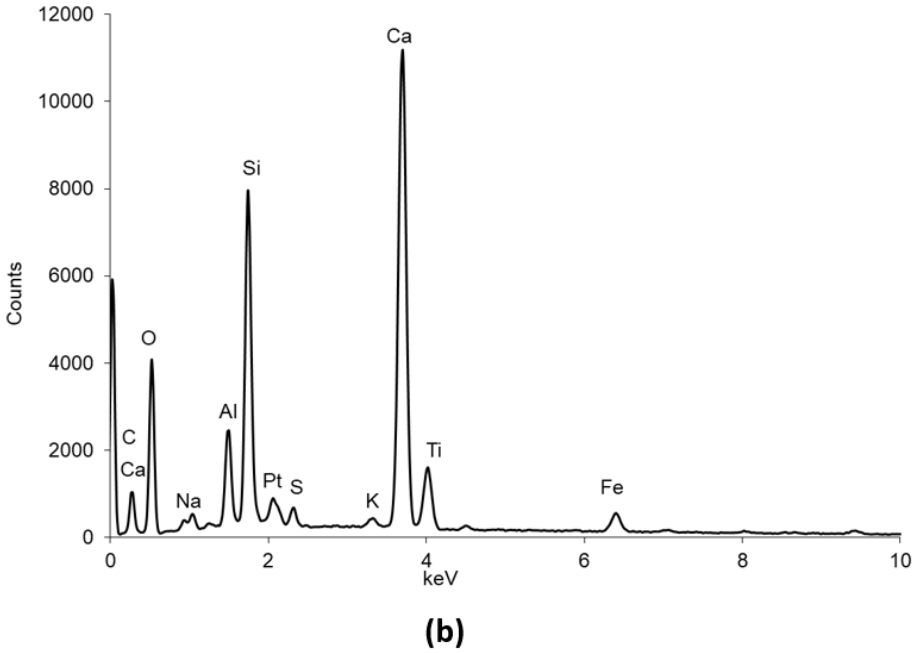

Figure 4.22 Microstructural analysis showing the (a) SEM micrograph and (b) EDX results (selected area) of the 5NC mix

4.3.5 Effect of partial replacement of fly ash with silica fume

In this section, the FA was partially replaced with SF to further enhance buildability of the 5NC mix for large-scale 3DCP application. Effect of SF on both rheological and mechanical properties were investigated while replacing the FA up to 5% (by mass of binder) without changing the water-to-binder ratio.

4.3.5.1 Flow properties (yield stress, viscosity and thixotropy)

Figure 4.23 presents the relationship between yield stress and flow ratio as a function of different SF dosage added to the 5NC mix. Both the flow parameters were noted to increase with increase in SF content which is in agreement with effects produced by SF due to very high surface area and propensity of silica fines to agglomerate [204].

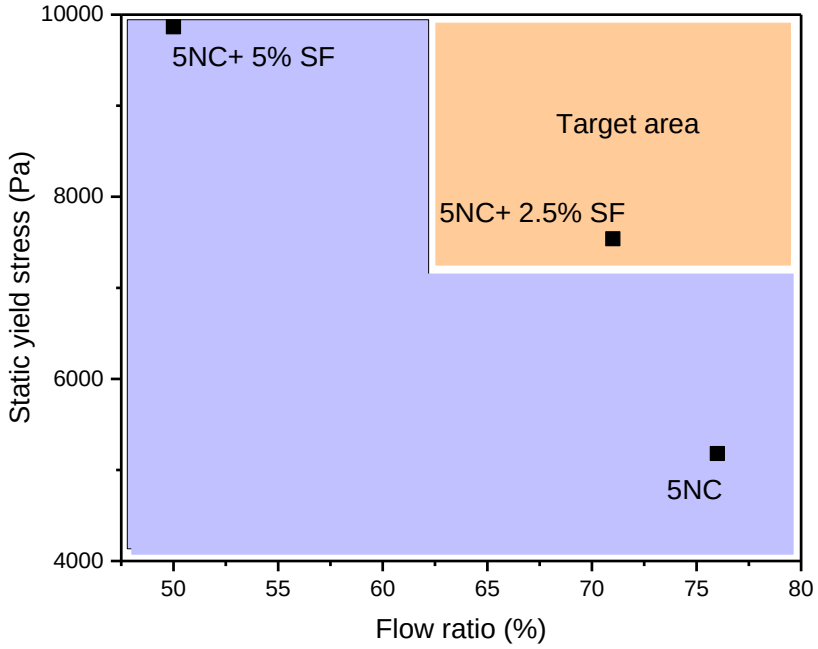

Figure 4.23 Flowability and yield strength for SF modified HVFA mixtures

The effects of increases in SSA on yield stress can be easily explained based on two major effects: (i) packing density and (ii) interparticle interactions. As the SSA increases, the interparticle spacing decreases and there is an increase in number of interparticle contacts and interparticle friction, which results in elevations in the yield stress [205]. Figure 4.24 shows the increasing surface areas by inclusion of SF at different percentages, which confirms the direct relationship between yield stress and SSA caused due to increased agglomeration at constant water-to-binder ratio. The influence of the calculated water film thickness (WFT) on the yield stress is shown in Figure 4.25. Since the WFF is inversely related to the SSA, the observed relationships of yield stress as a function of the film thickness are expected. An increasing thickness of water films around the particles then decreases the packing density and increases the interparticle spacing helping reduce the yield stress and increase the flow ratio.

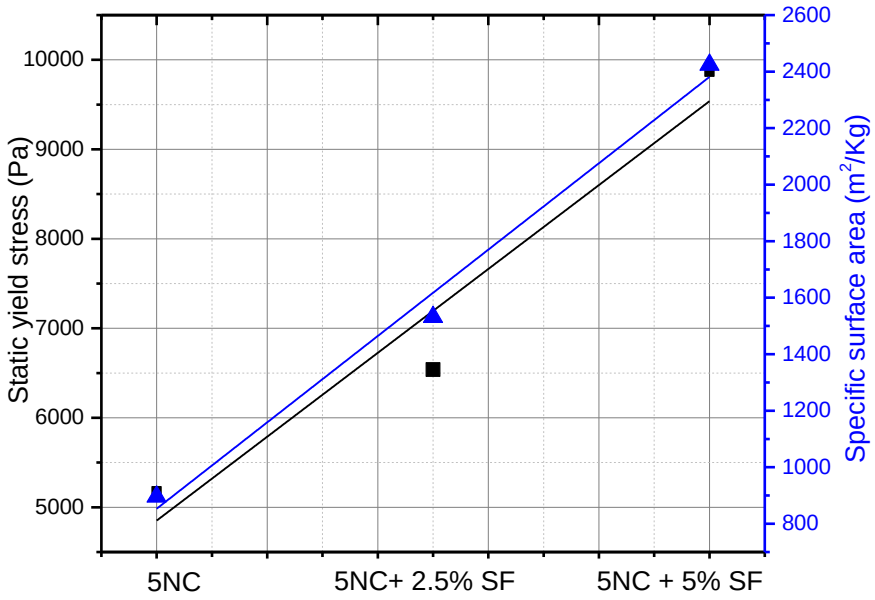

Figure 4.24 The influence of the specific surface area on the rheological properties of SF added HVFA mortars

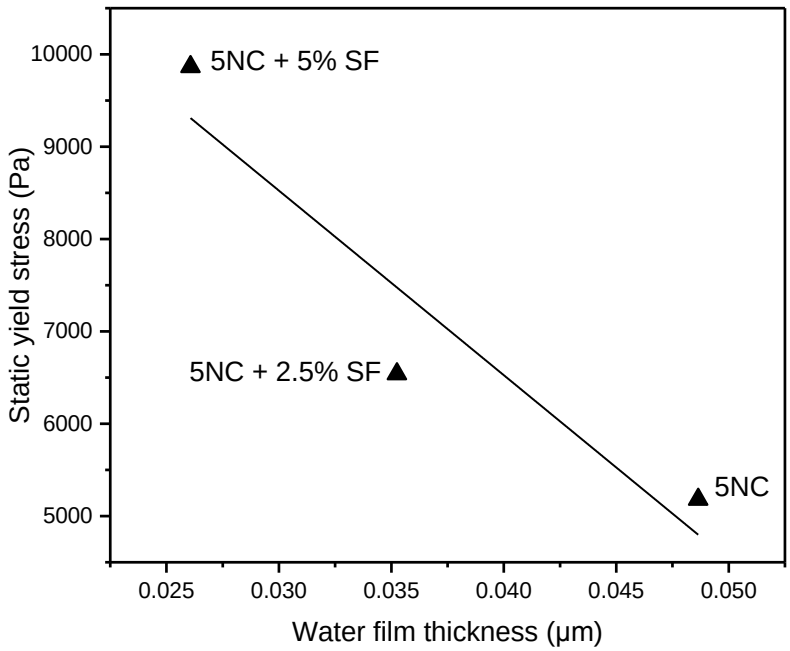

Figure 4.25 The influence of a calculated water film thickness on the rheological properties of cement pastes with 0, 2.5 and 5% added silica fume

Based on the above rheological observations, 2.5% added SF mortar was only considered for further rheology investigation, since 5% SF caused high pumping pressure and discontinuity in the filament during extrusion process. A shear thinning behaviour was observed for both the mixes, where apparent viscosity notably increases with SF inclusion and decreases with shear rate as shown in Figure 4.26. This is the most common behavior of non-Newtonian fluid that indicates smooth extrudability of SF added mixture with better rheological property than the 5NC mix.

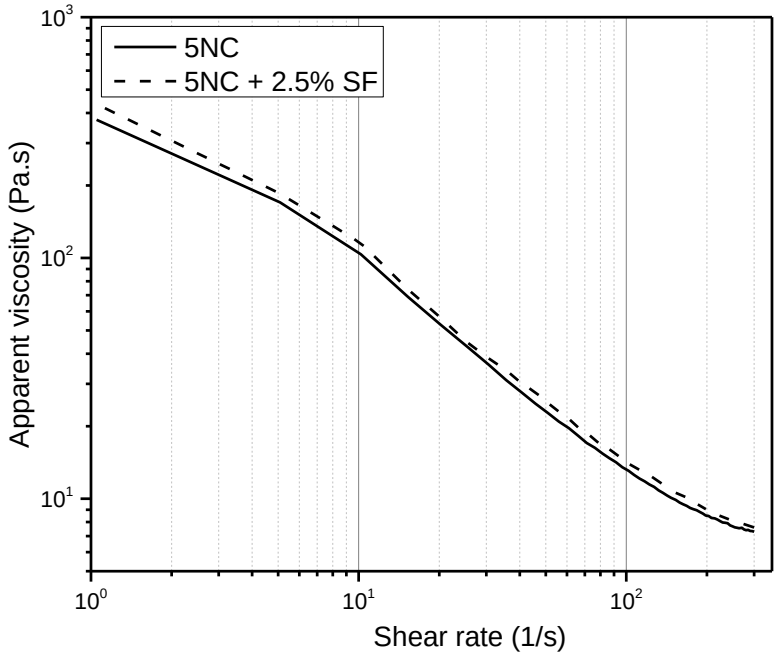

Figure 4.26 Shear thinning properties of control and SF modified mixes

Similar to NC, both structural break down and recovery protocol was applied to investigate thixotropy of the SF added mortar and obtained results are shown in Figure 4.27. The structural parameter (λ) obtained from break down curves indicates an increase in thixotropy, though the recovery ability (Figure 4.28) was not significant like the NC. Such observations can be understood as saturation effect and lack of free water for effective flocculation. Due to high surface area of SF, water can easily absorb on its surface and the mix moves out of proper viscosity zone, that hinders the flocculation and

thus the thixotropy. Addition of extra water may enhance the performance, or alternatively, PCE based plasticizer can prevent this excessive loss of workability.

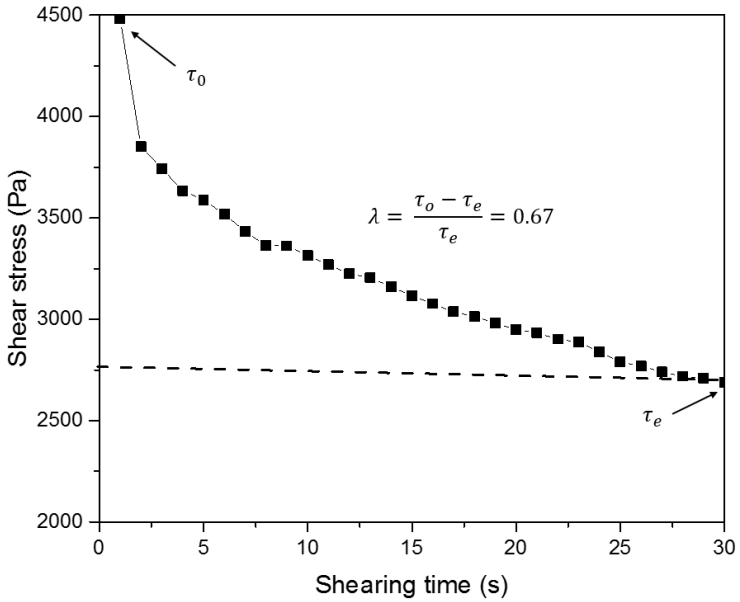

Figure 4.27 Structural build up property of NC and SF modified optimum mix

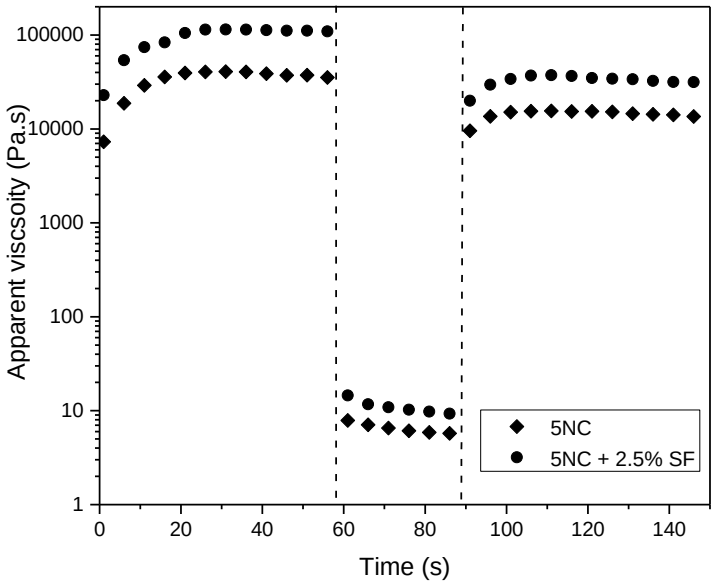

Figure 4.28 Viscosity recovery property of NC and SF modified optimum mix

4.3.5.2 Buildability

The effect of SF on buildability is shown in Figure 4.29 and it is very clear that addition of SF increased the stability of layers and the bottom layer deformation has been reduced compared to the 5NC mix. These observations are attributed to: higher yield stress and improved particle packing which are quantitatively described in the above sections.

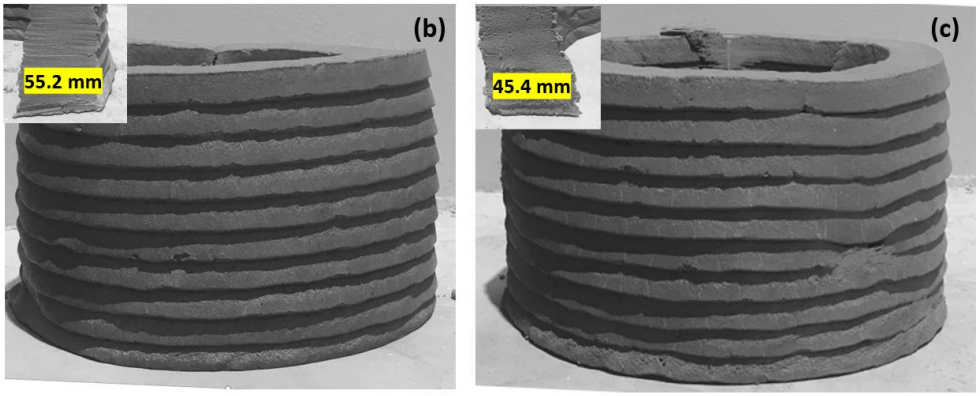

Figure 4.29 Buildability and layer deformation property of (a) 5NC (b) 5NC +2.5% SF mix

It is interesting to note that structural build up rate was increased with SF addition, unlike the NC. This increasing structuration rate can be reckoned by the accelerating effect of the SF on cement hydration [206]. It was found that the dissolution and precipitation processes of cement particles and hydrates were accelerated at the beginning of reaction by the silica particles, and thus the hardening rate was enhanced. The effect of this accelerated structural build up will be realized during a large-scale concrete printing test in Chapter 6 to demonstrate the improved fresh properties are suitable in practice.

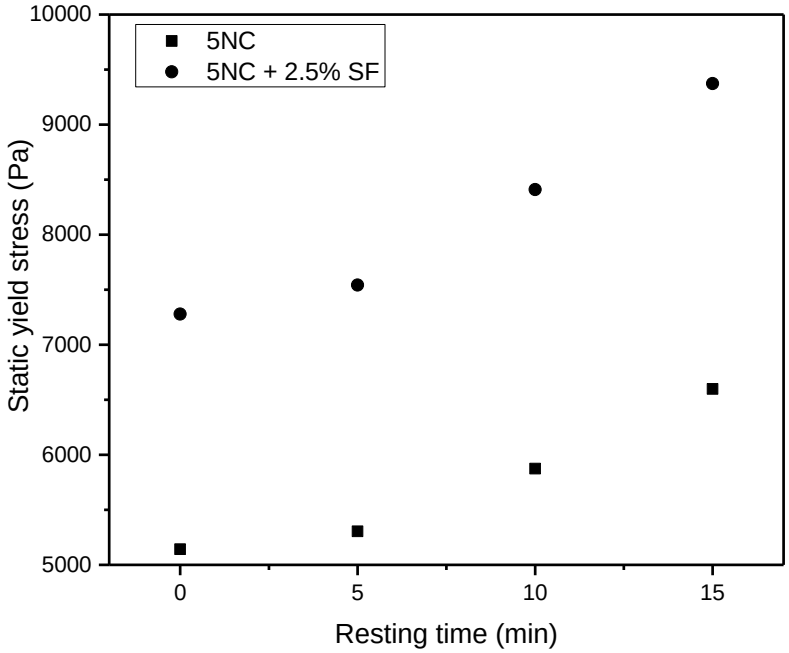

Figure 4.30 The effects of SF on structural build up properties

4.3.5.3 Mechanical strength and isothermal calorimetry

The effect of SF inclusion on 28 days mechanical performance is shown in Figure 4.31. It is evident that the compressive strength development of the 5NC mixture containing SF 2.5% and 5% have increased 8% and 13% respectively. The difference in strength is attributed to the pozzolanic activity of SF, that react chemically with calcium hydroxide (CH) to form space-filling C-S-H gel. Such formation of C–S–H improves the paste's microstructure, which in turn manifests as improvement in mechanical properties [207-209].

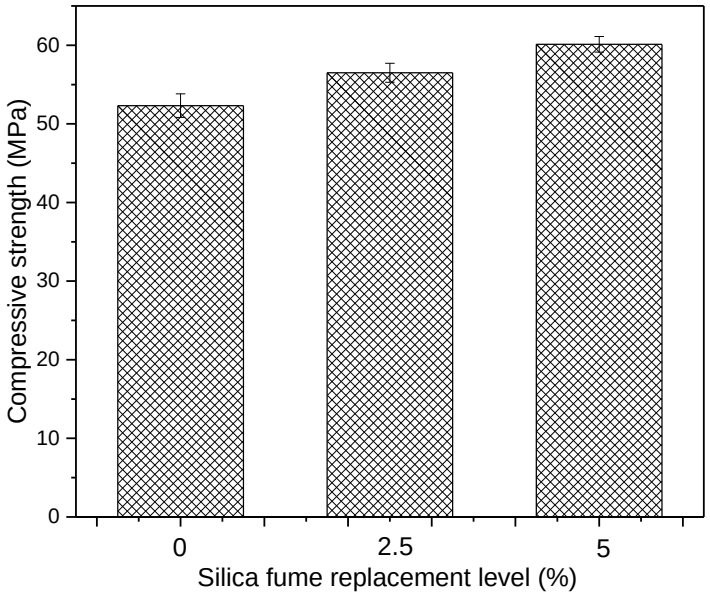

Figure 4.31 The effect of SF on compressive strength of HVFA mortar

SF contains of more than 90% amorphous silicon dioxide which is typically used to bolster the performance of cementitious materials. Literature reveals that SF enhances the cement hydration, by offering preferential nucleation sites at very early age (i.e., within a few hours of hydration) of the reaction. This is also known as filler effect, where the PC hydration product grows heterogeneously on the extra surfaces provided by the SF to form C-S-H and then it acts as seed to further enhance the hydration reaction. Figure 4.32 shows the heat evolution profiles and calorimetric parameter, which indicates the enhancement in early age hydration rates by the SF (2.5%) compared to 5NC paste. The length of the induction period and the time of the main hydration peak found to decrease significantly with SF replacement level, thus confirming the SF accelerating nature, as reported in various previous studies [208]. Out of filler/seeding and pozzolanic effect, the latter is expected to be a secondary effect on early ages properties because of the slow dissolution of SF in the low alkaline condition of HVFA system. The early age improvements are most likely related to the provision of extra nucleation sites by the SF particles.

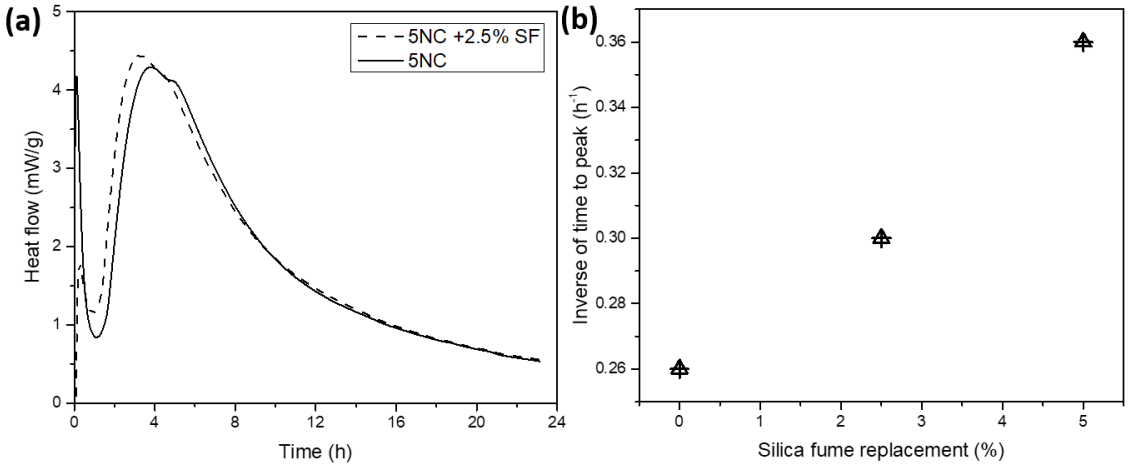

Figure 4.32 (a) Calorimeter heat flow curve (b) inverse of the time to the main hydration peak parameter from the calorimetry profiles

4.3.5.4 Microstructure and XRD Quantification

To gain quantitative information on the hydration product of NC and SF modified HVFA mortar (5NC +2.5% SF), XRD phase quantification was carried out at the age of 3 and 28 days (Figure 4.33). Figure 4.34 illustrates the quantitative phase analysis of the compositions, which was done by the Rietveld method.

The results show different crystalline phases associated with the mainly calcium silicates (C_3S and C_2S), portlandite, calcite, quartz, mullite along with the broad amorphous hump over the 2θ angle range. A broad hump was observed in the diffractogram between 2θ angles equal to 15^o and 38^o, which is the combination of the glassy phase of FA and the amorphous hydration product products in the FA-PC blended system. From 3 to 28 days, the depression in the amorphous hump at lower 2θ angles and a rightward shift of the entire hump in the diffraction pattern of the blended system, indicates a decrease in the glassy content of FA (centered on lower 2θ angles) and the formation of amorphous hydration products (centered on higher 2θ angles).

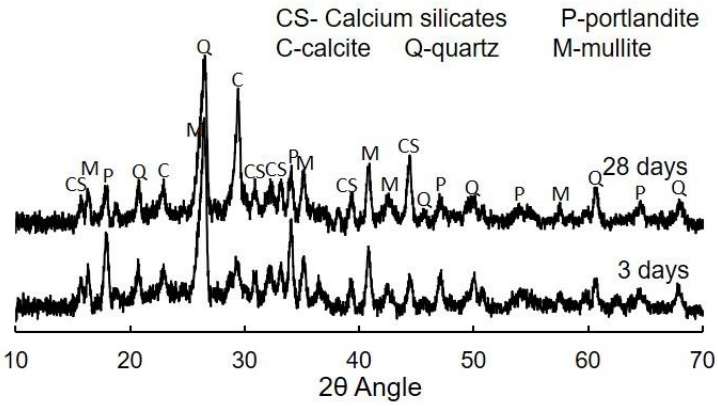

Figure 4.33 XRD signature of 5NC +2.5% SF paste at 3 and 28 days

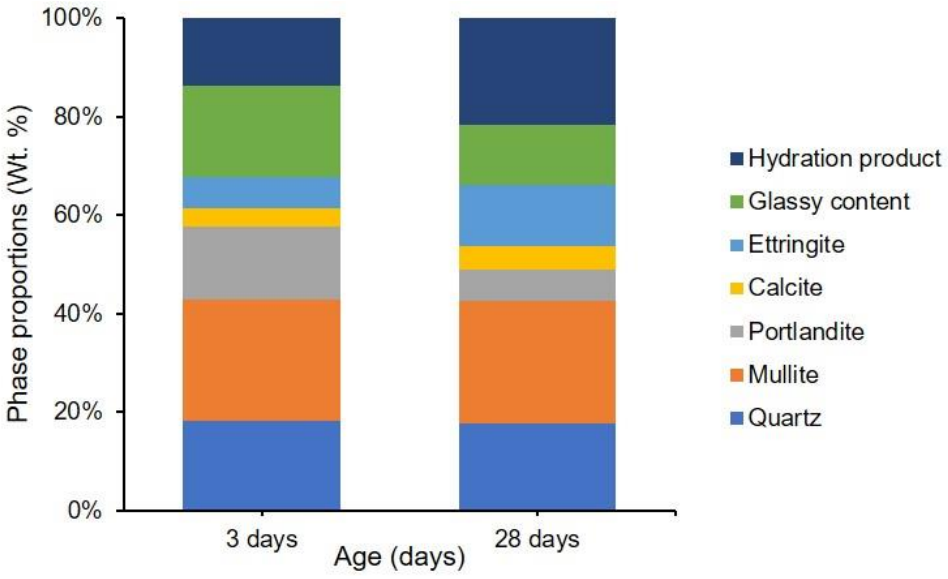

Figure 4.34 The different quantified phases of the 5NC +2.5% SF mix at the age of 3 and 28 days

Based on the relative proportions (Figure 4.34), it can be proven that the amount of portlandite and glassy content decreases during the reaction and similarly the hydration product increases due to the pozzolanic effect of FA, especially in the later stage of reaction. The reduction of these contents is an indication of pozzolanic reaction and

related to the material strength development, depending on the amount of hydration product formed via the synergistic effect of binary cementitious materials [210]. The mullite and quartz content was not changed with age as these phases are contributed by the FA and inert in nature. The ettringite content was changing during the hydration reaction, which originate from the consumption of gypsum.

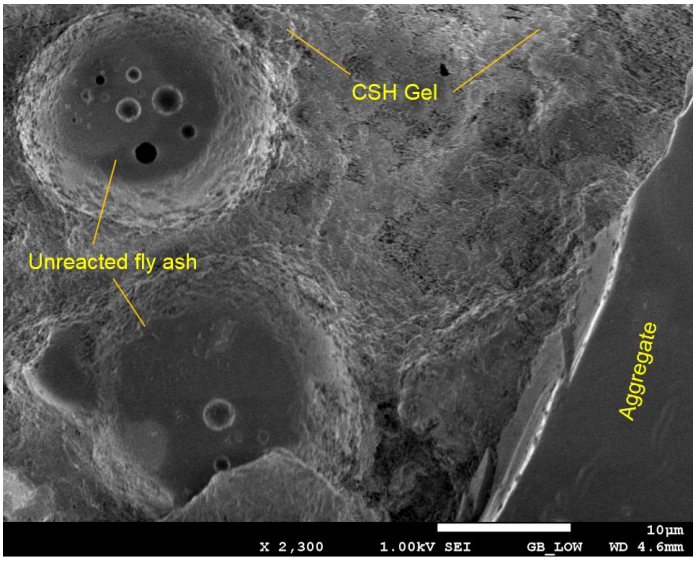

Figure 4.35 SEM image of the optimum NC and SF modified HVFA mortar at 28 days

Figure 4.35 shows the FESEM image of the hardened 5NC +2.5% SF mortar after 28 days of reaction and from the smooth surface of FA, it can be deduced that some of the FA particles did not react during the hydration process and only serve as an inert filler. However, presence of sodium sulfate promoted pozzolanic reaction of the FA and therefore, dense amorphous gel was observed with much lower trace of CH crystals. It is considered that majority of CH content might have reacted with the amorphous silica of the FA to produce secondary C-S-H gel. The denser microstructure is most likely to be associated with these C-S-H gel and/or filler effect of the nano particles [210].

4.4 Conclusions

This study investigated the material design of 3D printable HVFA binder systems. The key findings are as follows:

1. HVFA mortar is a printable material that is easily extrudable and retains the shape of the filament. The addition of spherical FA particles increases the flowability without the need of superplasticizer. Due to the reduction in the amount of PC, the early age strength development is very slow, thereby limiting the buildability property. Higher PC contents improve the shape stability and provide higher buildability.

2. During 3D printing, gradual deformation was observed due to the low green strength and stiffness of the extruded filament, which is reckoned as strength-based failure unlike structural (stability) failure. NC was added to improve the green strength via flocculation, which led to the printing of additional layers using the clay modified mix. Addition of small amount of NC significantly improved the thixotropy of the control mix, which was verified using both break down and recovery protocols. The recovery property was also found to be improved despite of the long time shearing and higher shear rate.

3. The use of NC did not have a notable influence on the structural build-up property. Therefore, SF and sodium sulfate salt was further incorporated to enhance the buildup rate. SF reduced the open time and increased the compressive strength due to its filler effect. Presence of sodium salt also enhanced the reaction rate, which was illustrated in Chapter 6 in the large-scale concrete printing case study.

4. In order to ensure a reliable long-term performance, the modified mix designs were characterized for their microstructure and reaction products, which were found to be similar to the conventional cement-based materials using FESEM and XRD techniques.

Chapter 5 Influence of material design on 3D Printability of fly ash based geopolymer mortar

5.1 Introduction

Advances in 3DCP rely heavily on the development of new cementitious binders that are both extrudable and buildable. High-performance concrete mixtures for 3D printing have been developed in the past while utilizing the PC as binder material. Due to negative environment impact of the PC, FA based geopolymer printing could be a sustainable option, especially in areas where waste/by-products are abundantly available. Previous studies [23,30,31] have elucidated some of the characteristics of powder bed geopolymer printing however, extrusion based geopolymer printing with detailed understanding of rheological property is still missing. Therefore, this chapter discusses the material design of ambient temperature cured geopolymer binder required for extrusion-based 3D printing. Special focus is given to: (1) characterizing the flow properties such as thixotropy, structural build-up in the dormant period, and (2) the use of SCMs and VMA including NC, SF that contributes to improved microstructural packing and flocculation. The influence of activator properties such as molar ratio (MR), viscosity and state (powder or solution) was also studied for 3DCP application.

Due to different conclusions about the geopolymer binding mechanisms and their consequences, a systematic study was conducted to first formulate an ambient temperature cured geopolymer mortar (control specimen), considering the effects of raw materials and activators. Later, the control mix was improved with different additives and their flow properties were characterized using a rotational rheometer. Mechanical strength and microstructures of the modified geopolymers were also analyzed using XRD, FESEM and calorimetry techniques.

5.2 Material design

The experimental procedure for printable geopolymer mortar starts with understanding the binder rheological behaviour that affects extrudability, shape retention and buildability properties. Following a traditional ambient temperature cured geopolymer mix design, FA and GGBS were used to formulate mixture proportions with reagent grade K-silicate solution. The FA was replaced with three different percentages of GGBS (Table 5.1), while the activator dosage and MR (1.8) kept constant according to the author's previous findings [211]. The three geopolymer mixes were first tested for both rheological and mechanical performances and based on required properties for 3DCP further modification was carried out using different SCMs and VMA.

Table 5.1 Geopolymer mortar mixture design

	Binder		Activator	Aggregate	Water
	FA	GGBS	activator/ binder	sand/ binder	water/binder
F90G10	90	10	0.35	1.5	0.30
F80G20	80	20	0.35	1.5	0.30
F70G30	70	30	0.35	1.5	0.30

In this mix design study, the selection of sand-to-binder ratio was confirmed by a preliminary investigation similar to the yield strength-based criteria described in chapter 4. As expected, addition of more sand increases the maximum torque (Figure 5.1) and therefore, 1.5 ratio was selected to produce extrudable geopolymer mortar.

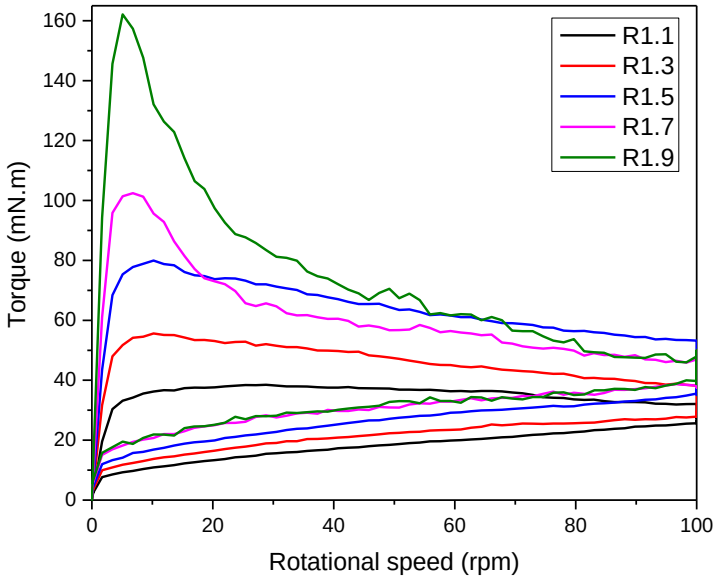

Figure 5.1 Effect of sand-to-binder ratio on Torque-speed relationship. Note that the number preceding R denotes the ratio.

5.3 Result and discussion

In this section, the general flow behaviour of FA based geopolymer was described followed by series of improvements in the rheological property (thixotropy) as required for 3DCP application. NC and SF were introduced to modify the rheology as well as powder (one-part) geopolymer was investigated for print-in-situ applications.

5.3.1 3D printability (Extrudability and buildability)

5.3.1.1 Effects of binder

Figure 5.2 presents the yield stress as a function of the GGBS content for the geopolymer mortars evaluated in this study. The yield stresses were found to increase with addition of GGBS, which is attributed to accelerated reaction and angular shape of the GGBS compared to spherical shape of FA particles [212]. The consequent effect of GGBS also depends on particle size and MR of the activator used to make the binder. However, the

activator was remained fixed during the experiment and the effect of GGBS for 20% replacement was appeared to be more pronounced compared to 30%.

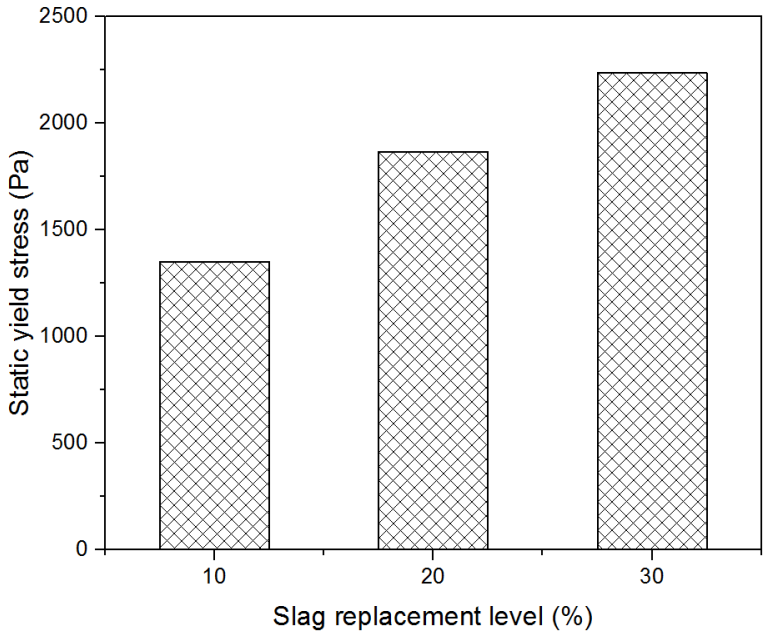

Figure 5.2 The effects of GGBS on yield stress of geopolymer mortar

In terms of 3D printing, the increased yield stress by GGBS particle was found to be nominal as the maximum yield stress is still low for maintaining the shape of the extruded filaments according to [195]. As shown in Figure 5.3, none of the extruded geopolymers have excellent shape retention like HVFA mortars and these observations could be due to lack of thixotropy that stabilize the layers. The recovery graph (Figure 5.3) confirms this fact (low thixotropy: 20-35%) for the geopolymers used in 3DCP.

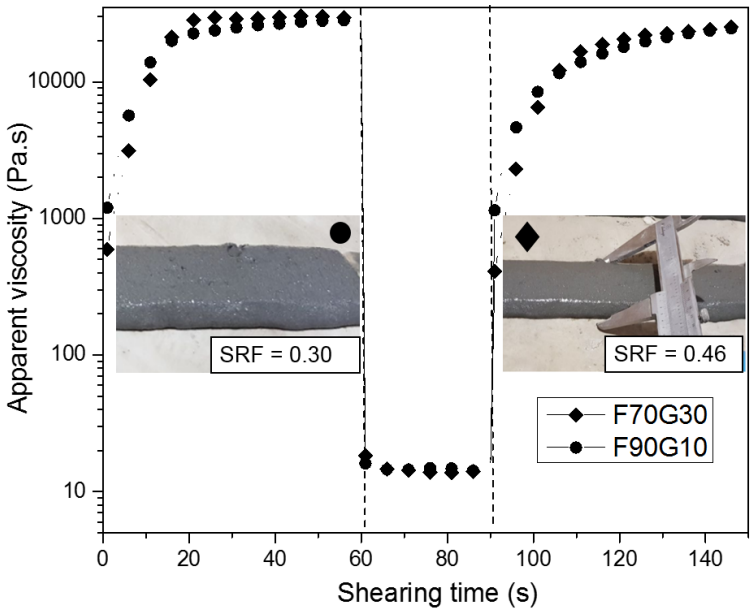

Figure 5.3 The effects of GGBS on viscosity recovery and shape retention of filaments

5.3.1.2 Effects of activator molar ratio and (w/s) ratio

Rheological studies of geopolymer mortars (FA: GGBS = 85: 15) were performed by varying the MRs of activator with 0.30 and 0.35 (w/s) ratio. K-silicate solution of MR 2 was originally used and later modified to MR 1.8 by adding appropriate amount of KOH solution. Figure 5.4 (a) and (b) show the influence of MR and (w/s) ratio on the yield stress and apparent viscosity of geopolymer mortars respectively. It can be noticed that increase in (w/s) ratio results in drastic decrease in the yield stress and plastic viscosity as would be expected. Increasing the amount of suspending fluid in a suspension increases the particle spacing, thereby increasing the fluid film thickness around the particles, thus decreasing yield stress and plastic viscosity. Increasing the water content also reduces the alkali ion concentration in the solution which reduces the viscosity of the activation solution, further contributing to a decrease in the values of the rheological parameters. However, increasing the MR of silicate increases the yield stress and apparent viscosity as observed. This observation is partially attributed to change in

activator solution viscosity with MR. Higher the MR, higher is the viscosity and this higher viscosity results in viscous geopolymer.

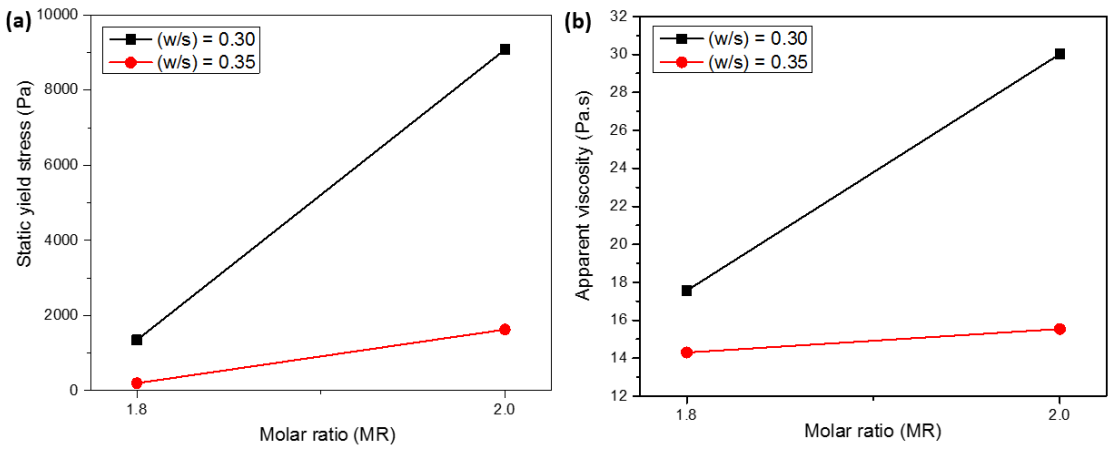

Figure 5.4 The effect of MR and water-to-solid ratio on (a) yield stress and (b) viscosity of geopolymer mortar

5.3.1.3 Effects of activator-to-binder

Activator solution-to-binder ratio is a mass-based ratio of the activation solution to the binder, which is an appropriate proportioning parameter for practical application. Depending upon the volume of activating solution and its viscosity, rheology of the geopolymer mortar varies as previously reported by many authors [31,32]. In this study, Figure 5.5 (a) and (b) illustrates the influence of activator solution-to-binder ratio on yield stress and viscosity of geopolymer mortars at a constant (w/s) ratio of 0.30 respectively. In general, as expected the yield stress and the apparent viscosity decreases for all the mixtures when the solution-to-binder ratio increases, due to the reduction in particle concentration. It is further noticed that, with constant solution-to-binder ratio both the yield stress and plastic viscosity increases with increase in MR, as attributed to the increase in viscosity of activator solution as shown in Figure 5.6. While using the activating solution of MR 2.0, the decreases in yield stress and viscosity values were found to be more significant (compared to MR1.8), when solution-to-binder ratio increased from 0.35 to 0.40. The yield stress reduced to 70% of the original value and

the viscosities for both MR 2.0 and 1.8 merged into a single value when the solution-to-binder ratio became 0.40. It indicates that the viscosity of the activating solution has dominant influence on the geopolymer viscosity whereas yield stress is more dominant by particle interaction and solid loading similar to findings of [84].

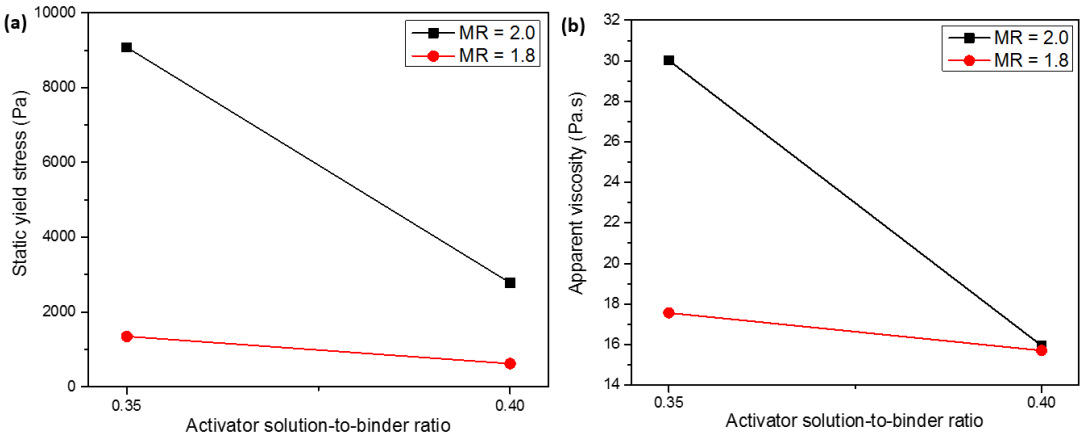

Figure 5.5 The effect of activator-to-binder ratio on (a) yield stress and (b) viscosity of geopolymer mortar

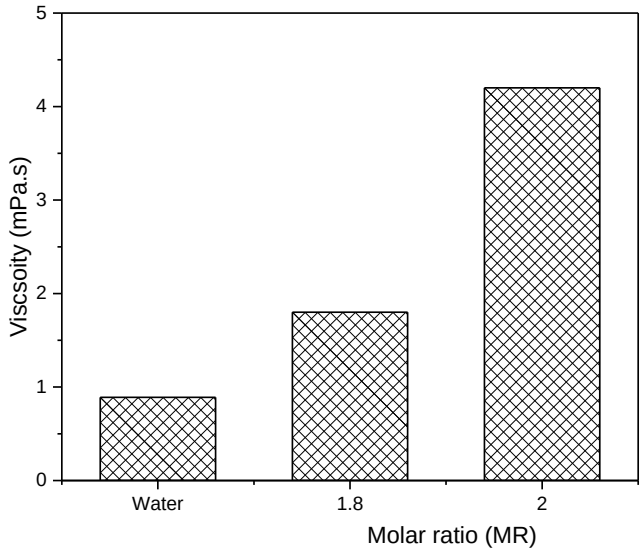

Figure 5.6 Influence of MR of K-silicate solutions on its viscosity in comparison with water

Figure 5.7 (a) and (b) shows the shape retention ability of the geopolymer made using MR 2 and 1.8 activator respectively. It is apparent that due to higher viscosity of MR 2 silicate (Figure 5.6) better shape retention property was observed than MR 1.8. However, as the printability of geopolymers could not be accurately concluded based on a single line extrusion, which only revealed the extrudability aspect, the 3D printing of a cylinder structure was also carried out to assess the buildability of this binder at a MR of 2, as shown in Figure 5.8.

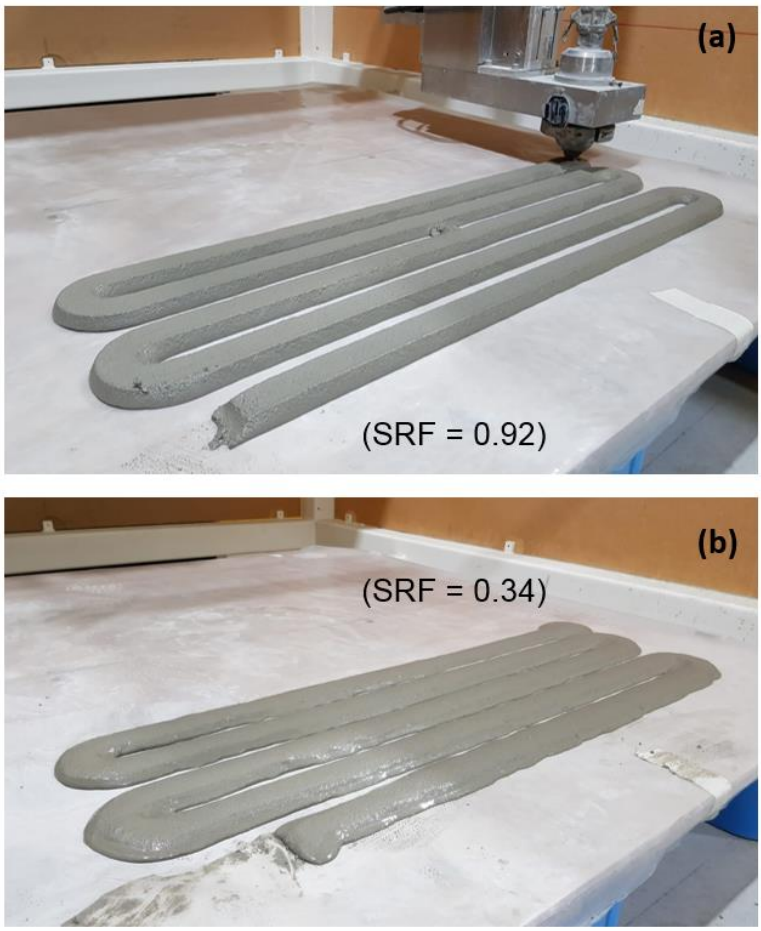

Figure 5.7 Demonstration of shape stability of extruded filaments made with MR (a) 2.0 (b) 1.80

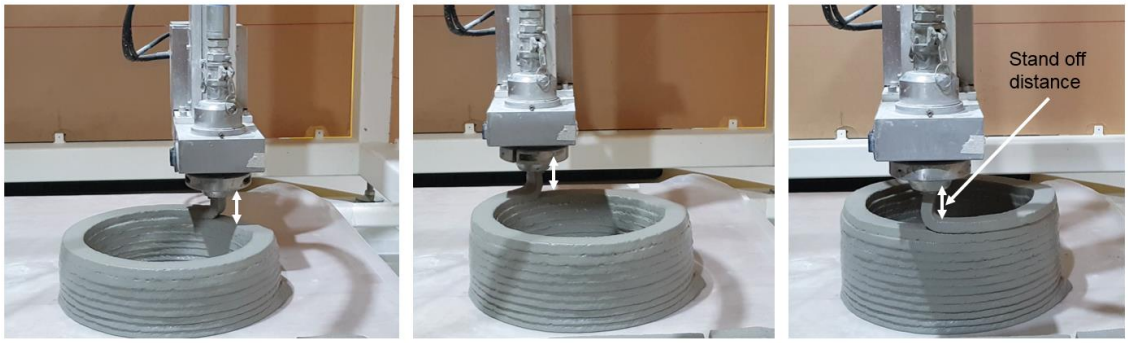

Figure 5.8 Buildability of the geopolymer mortar using MR 2.0 activator

Within this demonstration, an increase in the slump value was observed with additional layers which is reflected by the large standoff distance. This standoff distance signifies the low yield stress (stiffness) of the geopolymer, which could easily collapse under the loading imposed by the subsequent layers. Thus, it is confirmed that 3D printing of geopolymer is a challenging task due to very low yield stress caused by viscosity of the alkaline activator. Following sections will therefore focus on improving rheological properties of the geopolymers (based on a control mix) with an acceptable strength for non-structural application.

5.3.2 Mechanical strength, setting and isothermal calorimetry

Over rheology, strength and setting are the two most commonly known properties of any building materials. For many practical application, good workability related to rheology evolution and high compressive strength are desirable to produce reliable building components. Figure 5.9 shows the 28 days strength and setting time of geopolymer mixtures and it was noticed that with GGBS inclusion the setting time decreases, and the strength increases. Secondly, higher MR silicate improved the strength, which is in accordance with the previous findings that describes positive effect of high activator MR on effective dissolution of silicon, aluminum, calcium ions and formation of aluminosilicate gels [90]. Out of FA and GGBS, glassy phases of the GGBS is more vulnerable to alkaline attack under room temperature and it has a higher content of

reactive phase than FA. Thus, for high GGBS content higher amount of Si and Ca will dissolve, and more amorphous gels will be formed which explains the increase in compressive strength. In addition to higher compressive strength, GGBS also decreases the setting time due to its faster reaction in alkaline medium to form the reaction products. Similar results are also reported in the literature relating the role of GGBS in the hardening behaviour of geopolymers [213].

The results of the isothermal calorimetric analysis (Figure 5.10) shows higher content of GGBS resulted in higher dissolution heat flow, which demonstrates the fact that GGBS is easier to dissolve than FA. It was also noticed that as the activator MR decreases, the induction period decreases (curves representing induction period become narrower and sharper), resulting shorter setting time geopolymer samples. Literature reveals decrease in MR leads to a higher alkali concentration, that enhances the dissolution rate and reaction degree [214]. It should be noted that the rate of reaction also depends on binder formulation, for e.g. GGBS-to-binder ratio that possess a synergetic influence on setting time. Setting in geopolymer occurs when the silicate ions begin to attach with the previously released 4-to-6 coordinated aluminum to form aluminosilicate oligomers that further grows in the process of polycondensation. This release of aluminum ion and condensation speed are mostly controlled by binder as well as the activator characteristics. Thus, in order to achieve a desired setting time these two parameters (MR and binder mix design) need to be considered simultaneously.

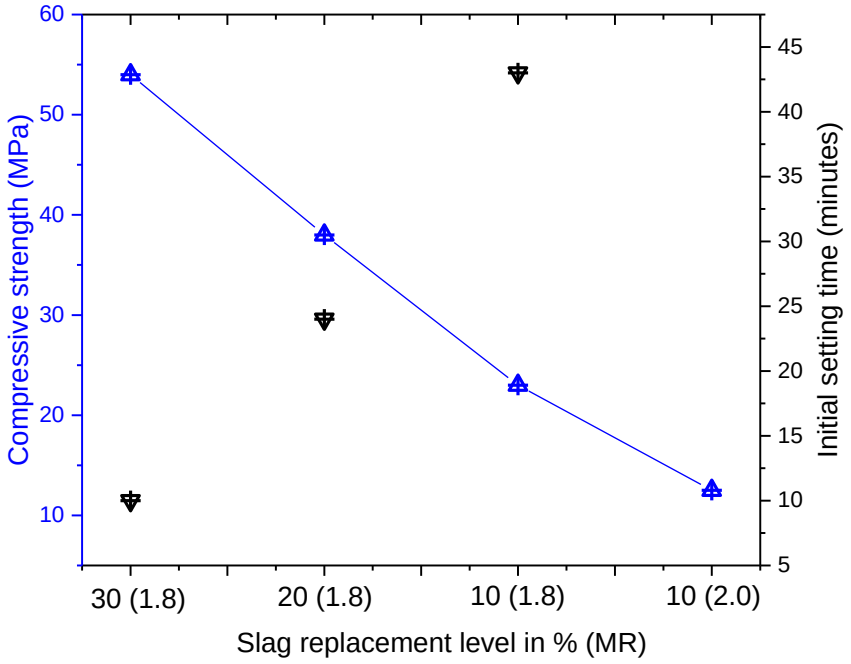

Figure 5.9 The effects of slag replacement on compressive strength and setting time of geopolymers

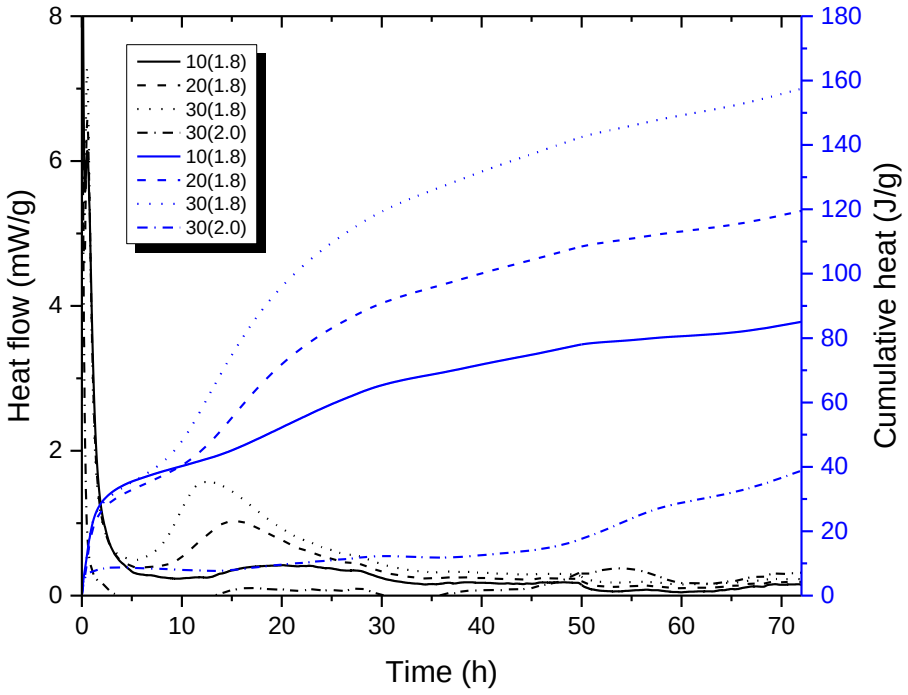

Figure 5.10 The effects of slag and activator MR on heat flow curves of geopolymer paste

In the light of above discussion, FA85G15 mix design was finally selected as "control" mix for further rheological improvement due to satisfactory strength (> 30 MPa) and setting time. Despite higher strength, G20 and G30 mixes were not opted for their lack of acceptable setting time (min 30 minutes) needed for 3DCP. The activator MR was also fixed at 1.8, whereas the activator-to-binder ratio was remained as variable since during material design the PV need to be adjusted depending on additives dosages and their physical properties. The following sections will focus on improving the geopolymer shape retention and buildability properties using potential admixtures, necessary for 3D printable concrete.

5.3.3 Effect of nanoclay as thixotropy modifier

The importance of NC originates from the low yield stress property of geopolymer which need to be improved for 3DCP application. NC has been found to be an effective additive for improving 3D printability of various cementitious materials and in this study, for the first time NC was added in the geopolymer binder and results were discussed in terms of both fresh and hardened properties.

5.3.3.1 Flow properties (yield stress, viscosity)

Like HVFA mixture, different amount of NC was added to the control geopolymer mortar and their respective flow properties were displayed in Figure 5.11. Since 0.5% NC exhibited highest yield strength, this dosage was used to investigate the geopolymer performance with different activator-to-binder ratio and water-to-solid (w/s) ratio.

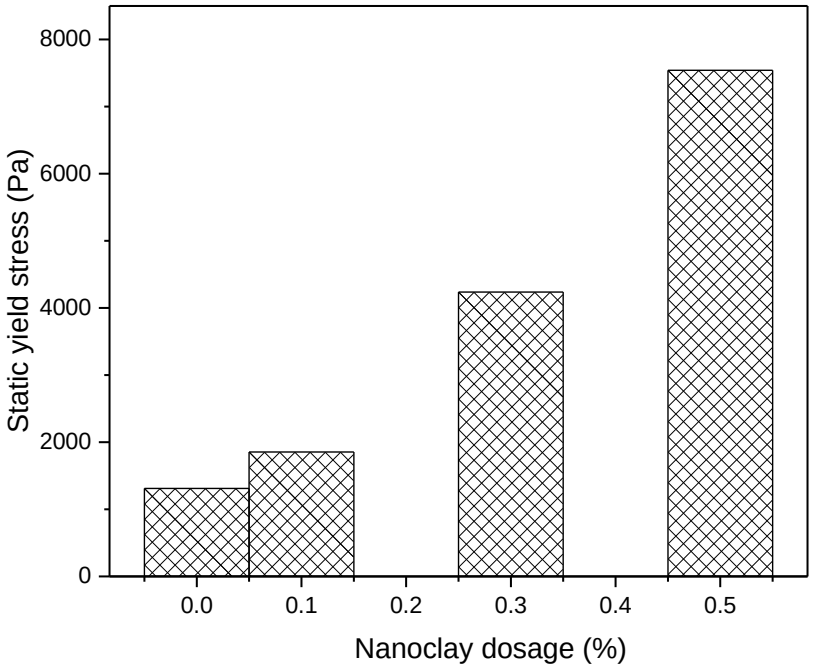

Figure 5.11 The effect of NC dosage on yield stress of control geopolymer for 0.35 activator-to-binder ratio

Figure 5.12 (a) and (b) shows yield stress and viscosity of geopolymer mortars with two (w/s) ratios of 0.30 and 0.35 respectively at constant activator-to-binder of 0.35. It can be noted from figure 5.12 (a) that a small amount of clay addition can significantly improve the yield stress of geopolymer, though the yield stress decreased to 82% with increase in (w/s) ratio. The NC used in this research are opposite charged ends and they flocculate to form a colloidal network [199]. This flocculation is at origin of increased yield stress and it is believed that the flocculation is more effective when there is some extra free water available in mix design, otherwise the clay cannot disperse properly in low (w/s) ratio. Unlike PC, the viscosity and pH of silicate activator can affect the performance of NC dispersion as previously reported in few scientific studies [215], however such insight mechanism is not covered in the scope of this thesis.

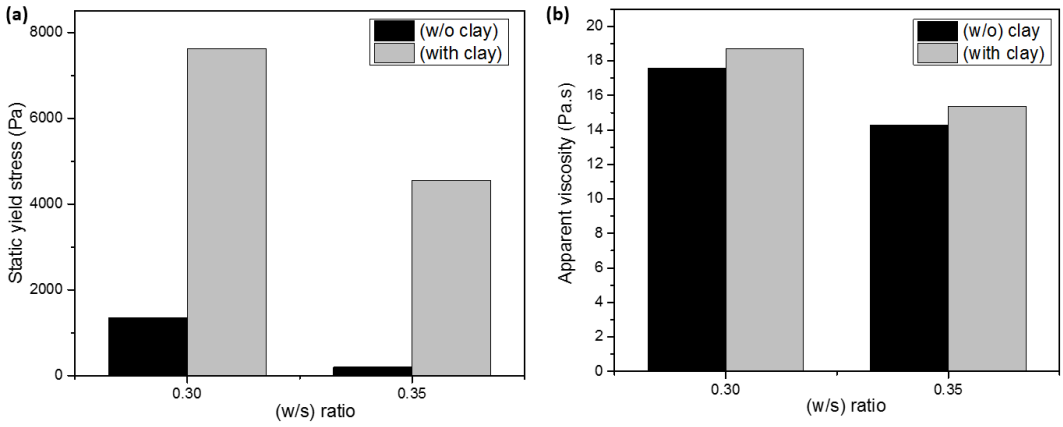

Figure 5.12 Influence of (w/s) ratio and NC on (a) yield stress (b) viscosity of geopolymer mortar. Note that the activator molar ratio was kept constant at 1.8. (w/o = without)

Figure 5.13 (a) and (b) illustrates the effect of clay on yield strength and viscosity of geopolymer mortar for different activator-to-binder ratios respectively while (w/s) ratio was fixed at 0.30. As expected, both yield stress and viscosity decrease with increase in activator dosages, even in the presence of NC. The activator dosages and viscosity seem to dominate the overall yield stress, when the dosage increased from 0.35 to 0.40. An interesting fact to be noted that the clay has minimal impact on viscosity of the geopolymer compared to the effect on yield stress. This is attributed to a fact that yield stress is more controlled by particle-to-particle interaction, whereas the viscosity is mainly regulated by the activator viscosity.

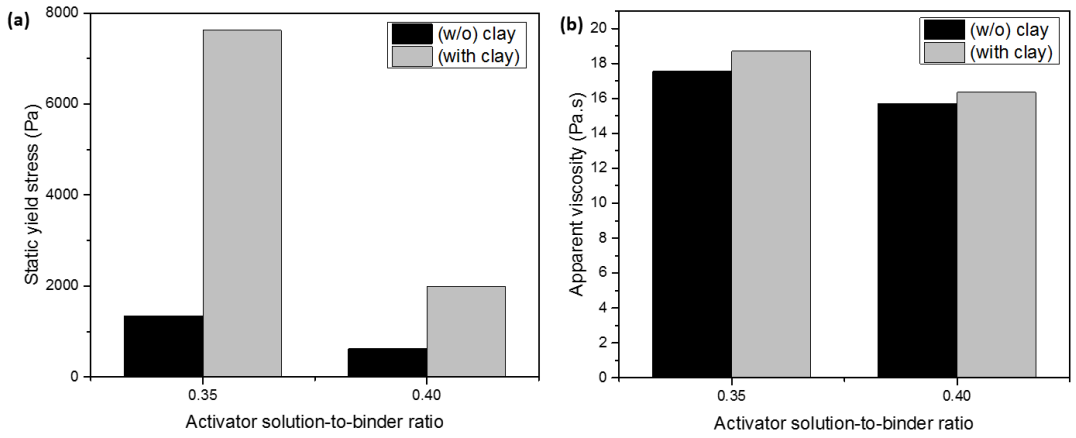

Figure 5.13 Influence of activator-to-binder ratio and NC on (a) yield stress (b) viscosity of geopolymer mortar. Note that the activator molar ratio was kept constant at 1.8. (w/o = without)

5.3.3.2 Shape retention and buildability

The effect of improved yield stress of clay modified geopolymer can be seen in Figure 5.14 where the extruded layers of geopolymer ((w/s) ratio = 0.30 and activator-to-binder ratio = 0.35) are more stable after continuous loading of 18 layers. The printed layers led to no visible standoff distance during the printing process. This was an indication of the zero-slump behaviour of the designed geopolymer mix, thus confirming it as an ideal material to be used in 3DCP applications.

Figure 5.14 3D printing of clay modified geopolymer showing excellent buildability (no visible standoff distance)

The stability of the extruded geopolymer filament also depends on viscosity recovery property that determines the material rheology before and after the printing. Figure 5.15 compares recovery ability of the geopolymers made using two different MRs i.e. 2.0 and 1.8 (represented as GEO 2.0 and 1.8) along with the clay added formulation (GEO 1.8+0.5% clay). Two important observations can be marked from this graph: (1) none of the mix is able to recover 100% of their initial viscosity after printing (2) addition of clay improved the yield stress and recover ability, within 60 seconds of extrusion. Due to high viscosity of MR 2 activator, GEO 2.0 exhibited higher viscosity than GEO 1.8 and with NC addition, the buildability improvement of GEO 1.80 is believed due to flocculation effect, similar to the findings of [187].

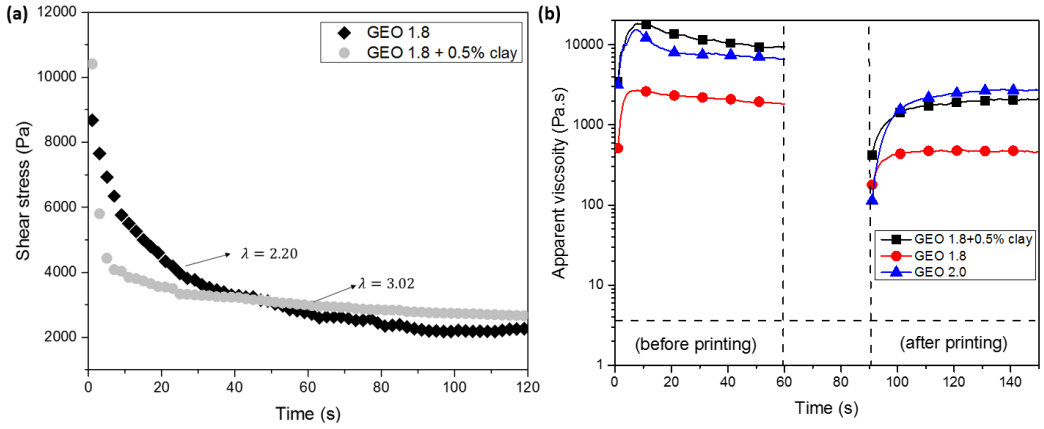

Figure 5.15 Comparison of (a) structural break down and (b) viscosity recovery properties of geopolymer mortars

Unlike PC, geopolymer lacks thixotropy property and therefore, despite high initial viscosity final viscosity after extrusion is too low for shape stability of the layers [216]. Therefore, in this research, NC was used to enhance the thixotropy which is now confirmed from the viscosity recovery plot. Moreover, the structural parameter (λ) displayed in figure 5.15 (a) also supports the fact that the clay can modify the shear thinning behaviour of geopolymer, indicated by higher λ value. This is probably because the stiffening mechanism of NC that makes the microstructure bonding stronger leading to higher equilibrium stress and thus higher the λ value.

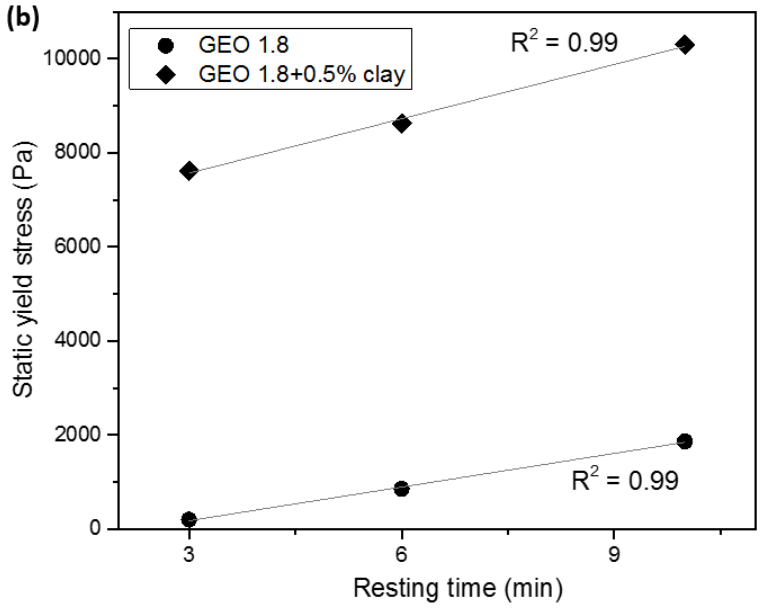

Figure 5.16 Influence of nanoclay on (a) setting and (b) green strength development behaviour of printable geopolymer mortar

Like structural recovery, structural build-up is an important parameter of 3DCP process that characterize the material behaviour before its initial setting and represents the early-age load bearing capacity. It is well understood from Figure 5.16 that both the geopolymer mixtures are gaining strength with time, though the clay added mix has a higher initial yield stress. A close look into the graph reveals that the clay has minimal effect on the strength development rate, rather the rate is more controlled by the

geopolymer reaction. Thus, the presence of NC seems to be not effective for accelerating the strength development rate, which is also in line with findings of past studies [187,199].

5.3.3.3 Mechanical properties and microstructure analysis

Figure 5.17(a) shows notably reduction in compressive strength of the geopolymer mortar, when NC was added to improve the thixotropy. Past studies have found an improvement in mechanical properties (i.e flexural strength) with different NCs due to the space filling ability of the nano size clay that densifies the geopolymer microstructure [217]. In another study, Joshi et al. [218] used NC to improve the rheology of geopolymer, by coating FA microparticles which in return decreased the compressive strength similar to findings of the present study. The clay used in this study is hydrophilic in nature, so there might be some water adsorption by the clay, which slow down the geopolymer reaction as reported earlier in [219]. Since geopolymer is not a water-based reaction, presence of too much water can cause poor mechanical strength by increasing the porosity level which may or may not be fulfilled by small amount of NC. However, the difference in strength was not reflected in the heat release responses as observed in Figure 5.17(b).

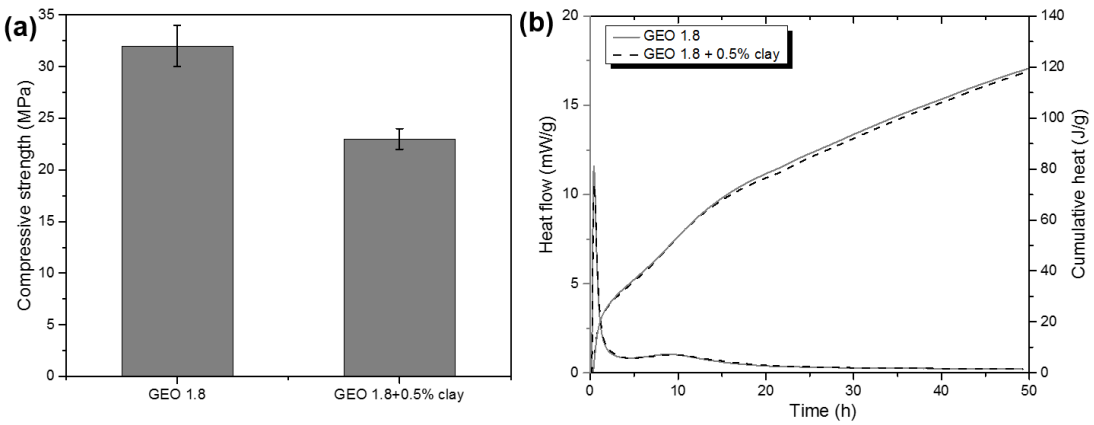

Figure 5.17 Influence of NC on (a) compressive strength (b) calorimetry curves of geopolymer

To further investigate the influence of NC, the FESEM images of the geopolymer samples taken at the age of 28 days are displayed in Figure 5.18. A heterogeneous aluminosilicate gel matrix accompanied with unreacted or partially reacted FA particles was observed in the geopolymer mix containing NC. These unreacted FA particles were separated from the geopolymer binder, thus indicating a weak adhesion between them and the surrounding gel, and this could be linked with the reduction in the compressive strength of this sample, as observed in Figure 5.17(a). Further study is therefore needed to explore the exact mechanism of the clay modified geopolymer.

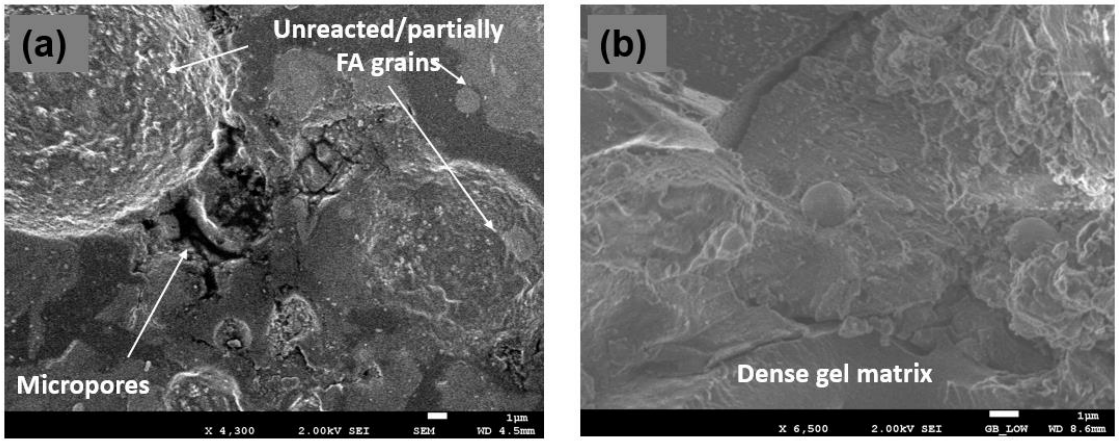

Figure 5.18 FESEM images geopolymer paste samples of (a) 1.8 GEO+0.5% clay (b) 1.8 Geo

5.3.4 Effect of silica fume as alternative thixotropy modifier

In this section, SF was incorporated in to the geopolymer mix design ((w/s) ratio = 0.30 and activator-to-binder ratio = 0.35) to enhance the rheological properties required for 3DCP. Yield stress, viscosity, structural break down, recovery and build-up properties were characterized with different SF replacement percentages. Effects of the optimum SF dosage in terms of strength and microstructure were also described in the end of this section.

5.3.4.1 Flow properties (yield stress and extrudability)

Figure 5.19 shows the effect of SF addition on the yield stress of geopolymer mortar and for a fixed binder content, addition of SF was noticed to increase the static yield stress significantly. The evolution of the yield stress follows the same trends noted in the case of HVFA mixtures in Chapter 4. Since the SF particles have large effective surface area [209], they can rapidly absorb water and thus reduce the workability of the geopolymer mortar, which has been reported in the literature, similar to the perceived effects of SF in this experiment.

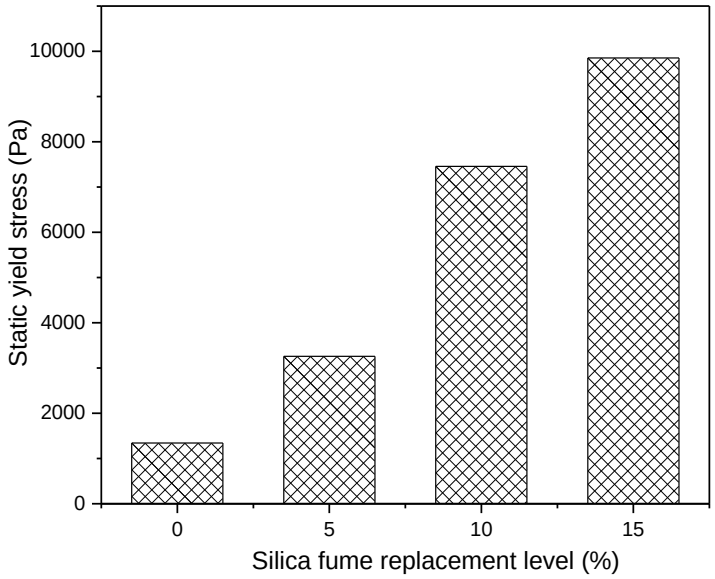

Figure 5.19 The effect of SF replacement on yield strength of geopolymer mortar

Figure 5.20 represents the increasing yield stress as a function of the SSA and as the surface area increases (by the addition of SF), the interparticle spacing decreases and there is an increase in the number of interparticle contacts and friction, that results increase in yield stress. Increase in packing density by the micro SF particles can also be regarded as one of the reasons, that explain the gradual increase in the yield stress of geopolymer mortars. To facilitate a better understanding of the SF influence, paste film thickness was used similar to an approach described in [220]. The influence of the calculated film thickness on the yield stress is shown in Figure 5.21. Since the film thickness is inversely related to the SSA, the observed relationships of yield stress as a function of the film thickness are expected. A decrease in film thickness around the particles increases the packing density and decrease the interparticle spacing that ultimately helps to increase the respective yield stresses.

Based on required rheological properties for 3DCP, a favorable limit diagram is shown in Figure 5.22 considering yield stress based extrudability criteria. It is noted that only 10% SF mix fits in to the target zone, whereas other combinations either due to lack of minimum yield strength or too high yield strength are not suitable for extrusion based 3DCP. The selection of mix design also depends on the pump type and its pressure limit which can be subject of future research to determine the most appropriate method for quantifying the 3D printable mortars.

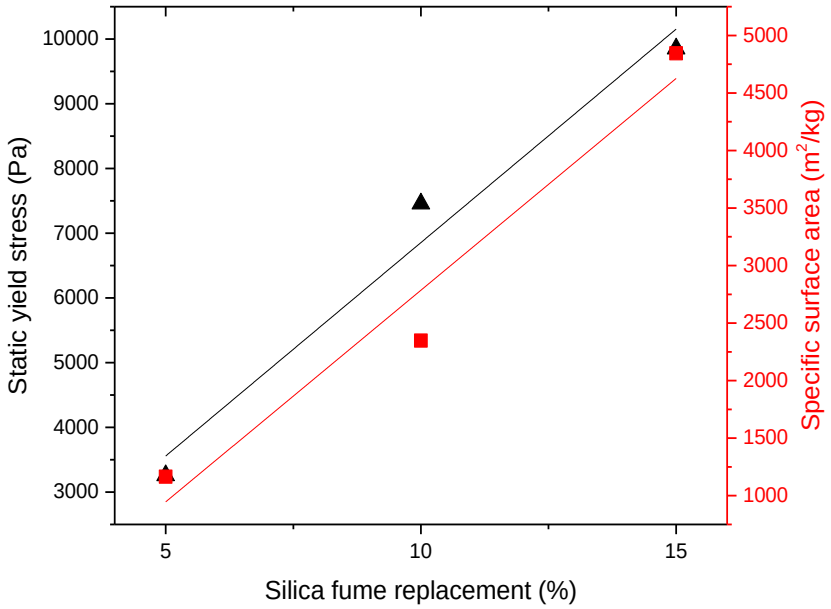

Figure 5.20 The influence of the specific surface area on the rheological properties of pastes with different silica fume replacement percentages

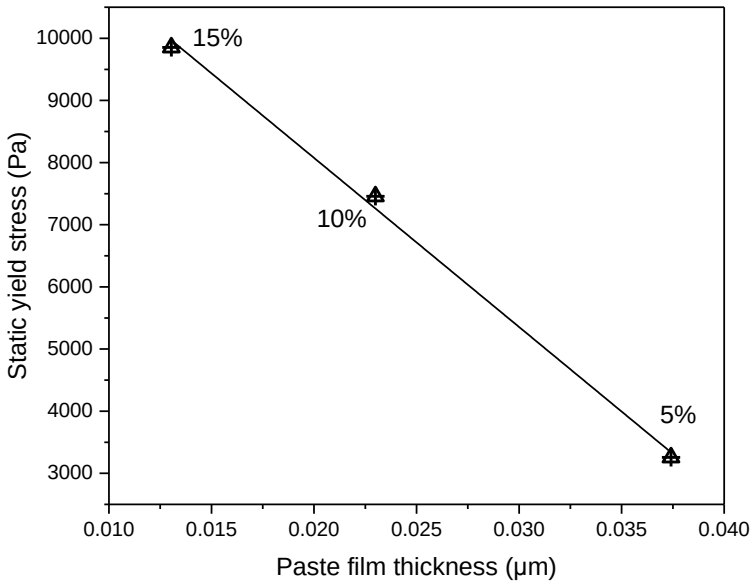

Figure 5.21 The influence of a paste film thickness on the rheological properties of cement pastes

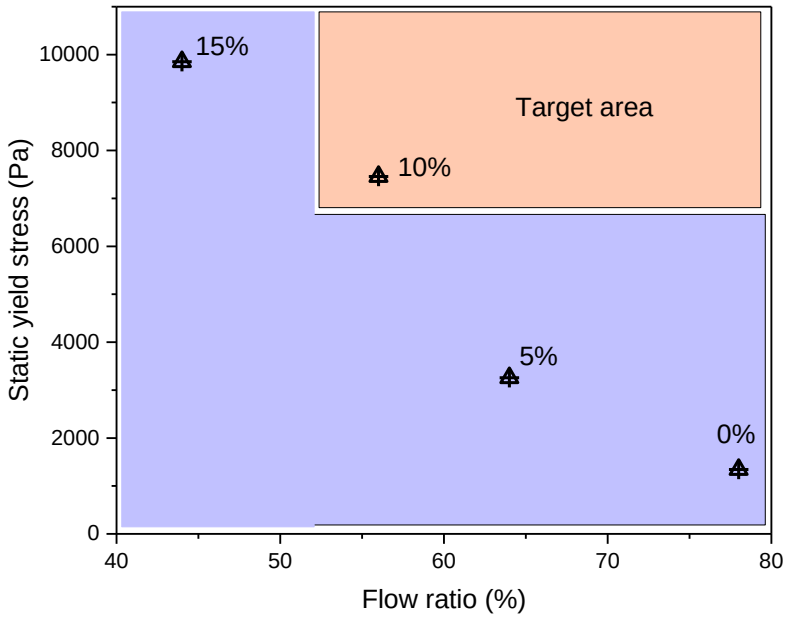

Figure 5.22 Flowability and yield strength of geopolymer mortars modified with silica fume

The effect of improved yield stress by the SF particles is shown in Figure 5.23, where the conventional geopolymer due to lack thixotropy property exhibited too low SRF for addition of a second layer. However, addition of 10% SF found to be an effective alternative by increasing the yield stress 36% higher and the extruded filament has better SRF.

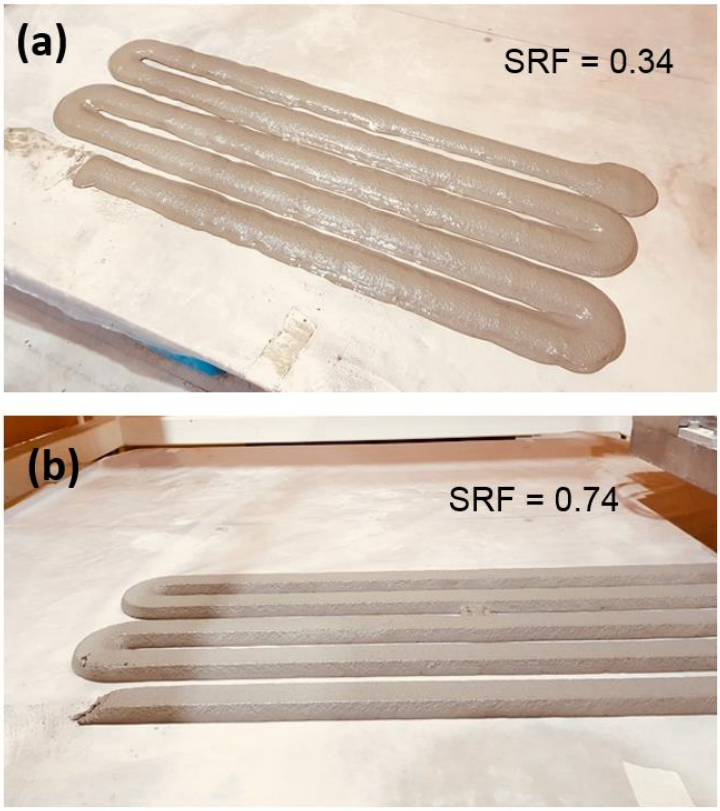

Figure 5.23 Extrudability and shape stability of geopolymer mortars (a) without and (b) with SF (10%)

5.3.4.2 Shape retention and buildability

This section harmonizes the thixotropy property of SF added geopolymer mortar responsible for the shape retention and buildability attributes. The SF addition increased the SRF of the geopolymer mixes which is evident from Figure 5.23. The shape retention as discussed before depends on yield stress and viscosity recovery ability of the material and as seen from Figure 5.25, the influence of increasing SF content on original viscosity at rest is obviously visible, however after shearing the rise in the viscosity is still limited to certain extent. Compared to the control sample, 10 and 15% SF added geopolymer exhibit a little higher recovery which is reflected in the deformation images of the cross-section area shown in Figure 5.24.

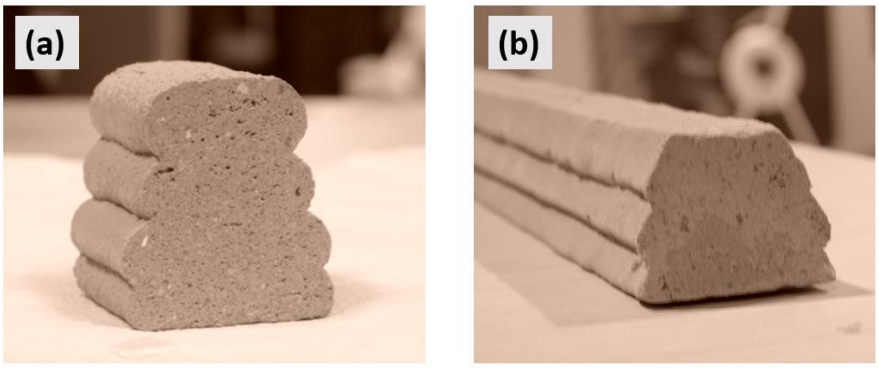

Figure 5.24 Deformation images of cross section area of geopolymer (a) without SF (b) with SF (10%)

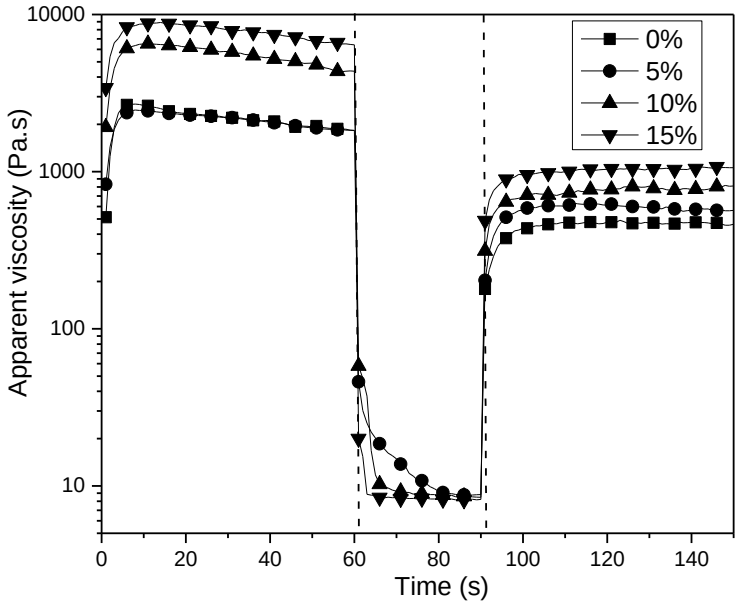

Figure 5.25 The effects of SF on viscosity recovery of geopolymer mortars

Considering the structural break down curves shown in Figure 5.26, a higher value structural parameter (λ) was obtained for 5 and 10% SF addition which confirms easiness of breakdown of the SF modified mix due to improved thixotropy property. SF has been used in the past studies as a promising thixotropy modifier for cementitious material application and as cited by Mehdipour and Khayat [221], particle packing and

interparticle links are responsible for flocculation, that affect thixotropy in cement-based system. However, the flocculation force also depends on the properties of suspending medium viscosity, pH, consistency etc. and in this study, the effect of viscous activator seems to worthy of investigation since the recovery property of SF added geopolymer was not as expected.

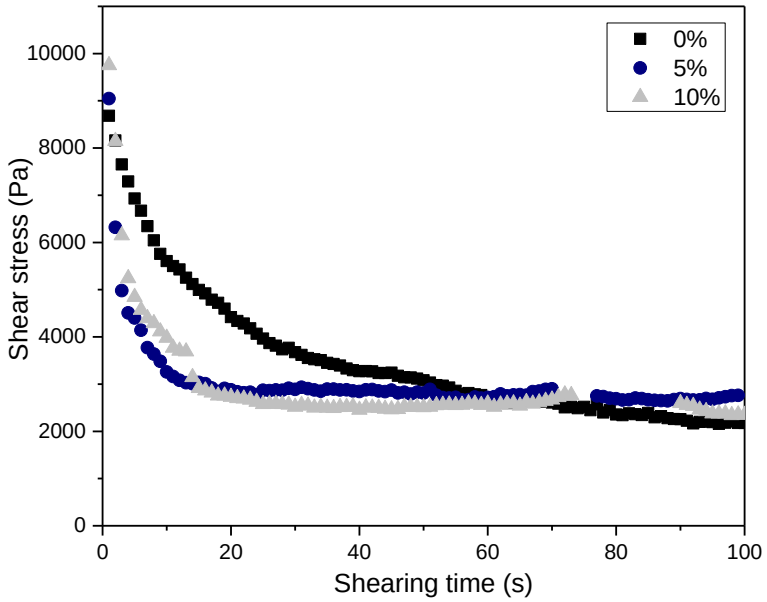

Figure 5.26 Structural break down curves of SF modified geopolymers

To further investigate these mixtures, only tap water was used to make geopolymer mortar instead of the silicate activator and thereby, disconnecting the influence of activator on the rheological parameters. The viscosity recovery results shown in Figure 5.27 confirms the slight improvement in the recovery properties of SF, which was missing in silicate based geopolymer (named as Control) probably due to viscous and higher pH effect of the K-silicate activator. The flocculation state of thixotropy suspensions are highly sensitive to pH values, and in this study pH of the activator may be thought of one possible reason to modify the SF behaviour by dissolution mechanism at early stage of geopolymer reaction. Comparing recovery performance of the water

based control geopolymer, liquid activator is thus confirmed to be responsible for significantly affecting the thixotropy of the FA based geopolymers.

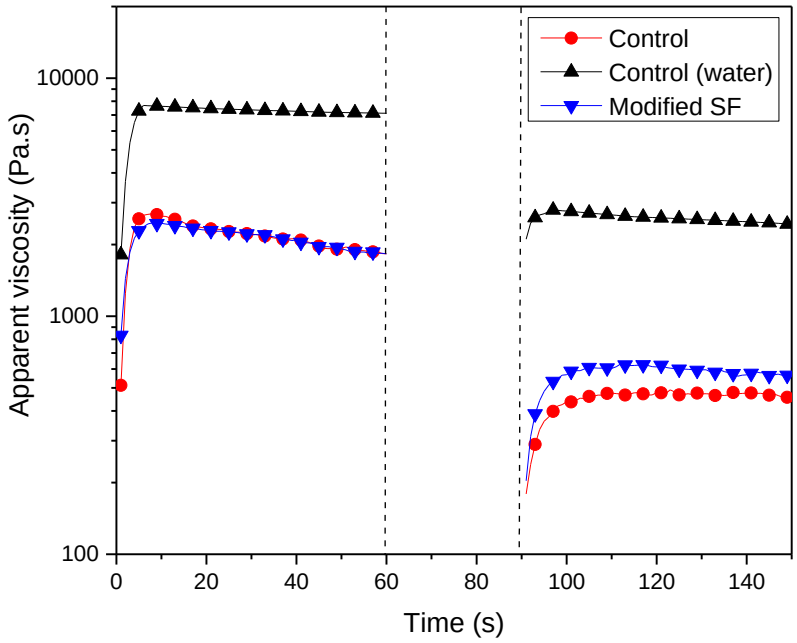

Figure 5.27 The effect of SF (10%) on viscosity recovery properties of geopolymer mortars

In an attempt to compare the effect two rheology modifiers i.e SF and NC for a longer shearing period scenario, the stage (II) of structural recovery test was extended to 120 seconds from 30 seconds. It is quite evident from Figure 5.28 that NC performed better than the SF, which can recover 27% of original viscosity within 60 seconds of deposition. In contrast, the SF modified geopolymer is not able to recover the original viscosity (only 14%) despite having higher yield strength. Consumption of the SF during early age geopolymer reaction may be reasoned for this, which corresponds to the loss of thixotropy in a highly alkaline medium.

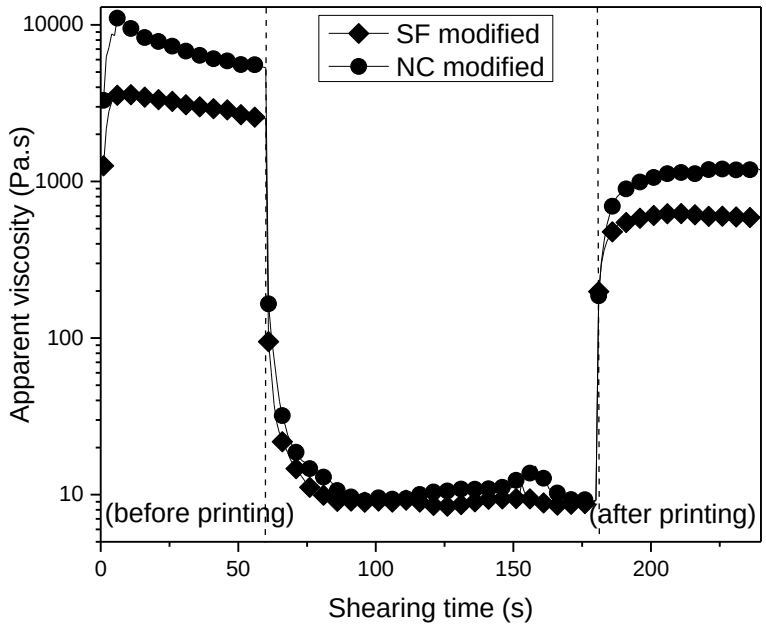

Figure 5.28 Comparison of viscosity recovery properties of geopolymer modified with SF (10%) and NC (0.05%)

In addition to thixotropy, the chemical reaction of geopolymer also plays an important role in determining the buildability since it controls the stiffening/structural build-up rate of the extruded filaments. Figure 5.29 shows the structural build-up rate of the geopolymer mortar modified with SF. It can be observed that compared to conventional geopolymer, addition of SF accelerates the hardening behaviour of geopolymer and the resultant material became no more workable after 25 minutes of mixing with activator. In geopolymer the setting mechanism is controlled by the rate of formation of aluminosilicate gel and this is linked to Si/Al ratio as well as (if any) presence of calcium containing compound in the mix design [94]. Calcium interacts with Si to form C-A-S-H and in this study, increase in Si concentration by adding the SF, might provide an insight of the acceleration effects compared to the control mix. The exact nature of this correlation is not fully understood and probably requires additional work due to rich in significance.

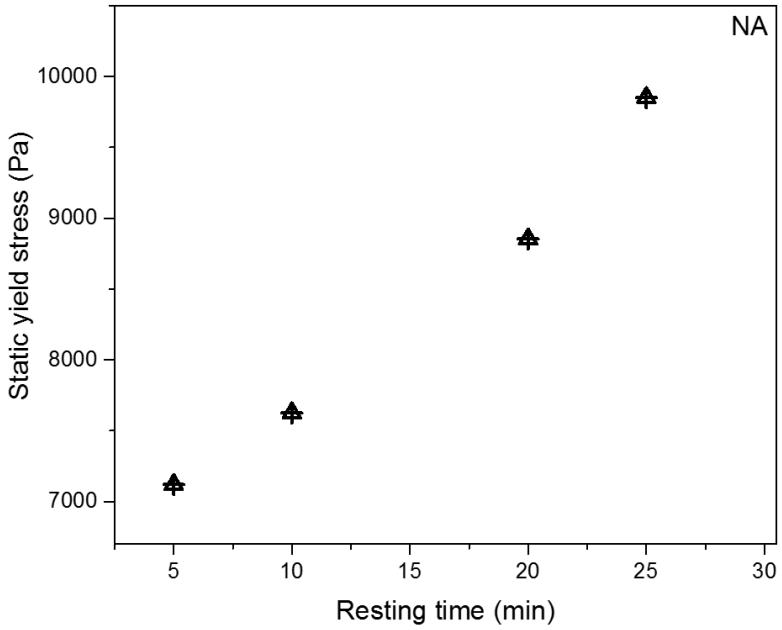

Figure 5.29 Structural build up properties of SF (10%) modified geopolymer mix

5.3.4.3 Mechanical properties and microstructure analysis

Figure 5.30 demonstrates that the SF addition accelerated geopolymer reactions by shifting the heat release curves to earlier times. The calorimetric response of the paste incorporating SF also demonstrates increasing the magnitude of initial heat release peak which may be due to the dissolution of fine particle size and high surface area of SF. However, the total cumulative heat was found to be lower for the SF added mix and it's influence was noticed on 28 days compressive strength as shown in Table 5.2. The decrease (6%) in compresive strength can be related to some observations found in nano silica containing geopolymer system [222]. Early age dissolution of SF possibly lead to an increment of the initial silica content in the solution, which delays the reaction of GGBS and FA by retarding the dissolution of Si from FA-GGBS to some extent. This can be indirectly noted during in the heat flow pattern from 10 to 30 hours of the reaction.

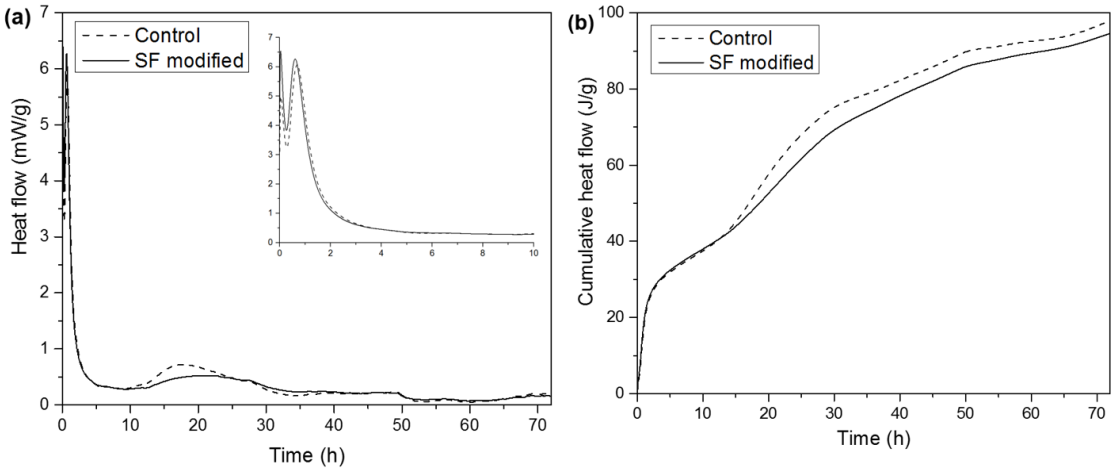

Figure 5.30 Influence of SF on (a) heat flow and (b) cumulative heat release rate

Table 5.2 Quantities of phases within unreacted and reacted geopolymer mix with and without SF at 28 days

	(a) Unreacted Without SF	(b) Reacted without SF	(C) Unreacted with SF	(d) Reacted with SF
Quartz	16.68	14.14	14.15	12.34
Mullite	29.64	23.13	23.65	19.85
Hematite	0.41	0.58	0.65	0.26
Magnetite	0.42	0.71	1.41	0.5
Calcite	0.52	0.42	0.35	0.24
Gehlenite	0.93	1.62	1.16	1.15
Glassy Content/ Reaction Product	51.4	59.4	58.63	65.66
Avg. compressive strength		32.45		28.32

The retarding effect of SF in terms of delayed reaction product formation was also noticed by the quantities of the different phases listed in Table 5.2 (obtained from XRD signatures, Figure 5.31). The combined amorphous reaction products and unreacted glassy content present in the SF system was slightly lower in content than the one without SF. The incorporation of SF leads to a decrease of effective slag content in the system,

which leads to the decrease of the reaction intensity. Further in-depth analysis are needed to be carried out to clarify the actual mechanism of SF in detail.

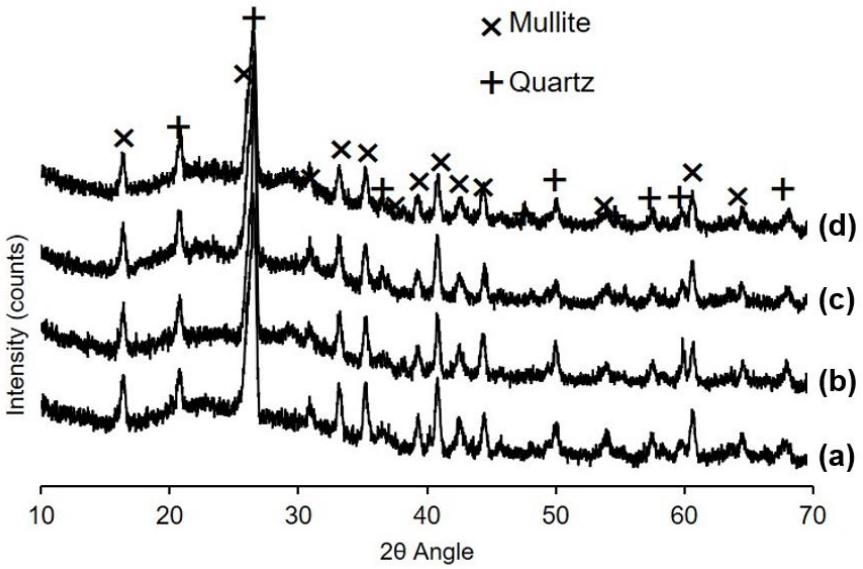

Figure 5.31 XRD patterns of unreacted and reacted geopolymer mix with and without SF at 28 days

5.3.5 Effect of powder activator

Processing conventional geopolymer mixes, in which alkaline solutions are used for activation could be troublesome in 3DCP due to the high viscosity of the alkaline solution. One-part geopolymers offer one possible solution to this challenge as they involve the use of a powder activator with solid aluminosilicates precursors [223]. Therefore, in this work a printable one-part geopolymer mix was developed using powder silicates, while comparing rheological and mechanical performances with the geopolymers activated by liquid silicate.

5.3.3.1 Material design

Five geopolymer mortars with a constant (w/s) (i.e. solid component (s) consisting of FA (F), GGBS (G) and anhydrous activator (A)) ratio of 0.35 were prepared by varying the GGBS and activator (MR =1.80) contents, as shown in Table 5.3. Accordingly, the GGBS ranged between 15-40% of the overall source materials content within samples F85G15A15, F70G30A15 and F60G40A15, in which the activator content was kept constant at 15% (i.e. by mass) of the binder. Furthermore, the FA and GGBS contents remained constant, whereas the activator dosage varied at 10, 15 and 20% in samples F70G30A10, F70G30A15 and F70G30A20, respectively. These activator dosages in the powder form were selected to maintain the same K_2O-to-binder ratio used in liquid activator.

Table 5.3 One-part geopolymer mortar mixture design

Mix name	Binder composition (wt.%)		Activator content (%)
	FA	GGBS	
F85G15A15	85	15	15
F70G30A15	70	30	
F60G40A15	60	40	
F70G30A10	70	30	10
F70G30A20	70	30	20

5.3.3.2 Extrudability, shape retention and buildability

Figure 5.32 shows the static yield stress and apparent viscosity of the five mixes containing different GGBS and activator contents. An increase in the GGBS content led to an increase in both the yield stress and viscosity, which could be due to the chemical composition (i.e. presence of calcium) in GGBS and its angular particle shape. Angular particles can provide an interlocking effect, which can increase the yield stress. A similar

outcome on the effect of the angular morphology of GGBS on concrete workability was reported in previous studies [86, 224]. Therefore, the partial replacement of 40% of FA with GGBS resulted in 125% increment in the yield stress, which can be useful in the shape fidelity and buildability of the printed layers. As the addition of GGBS was reported to decrease the setting time of alkali-activated materials, it can significantly affect the workability time (i.e. open time) by changing the flow properties. Therefore, the amount of GGBS included in these mixes are carefully controlled with proper activator dosage for the 3DCP. Similarly, increasing the activator content from 10 to 20% in mix F70G30A20 led to a higher yield stress, in line with the findings of [225]. Accordingly, a higher dosage of the activator induced higher pH and ionic strength of surface charges, which can be related to the increase in the yield stress. The viscosities of geopolymer mortars, irrespective of different slag and activator contents was found to be substantially low (< 10 Pa·s) under high shearing rate of 300 s^{-1}. This decrease in viscosity can be attributed to deflocculating phenomena in the early stages of the alkali-activation process and due to high yield stress combined with low viscosity property, it can be directly used in the 3DCP application with some additional attention on thixotropy and structural build-up.

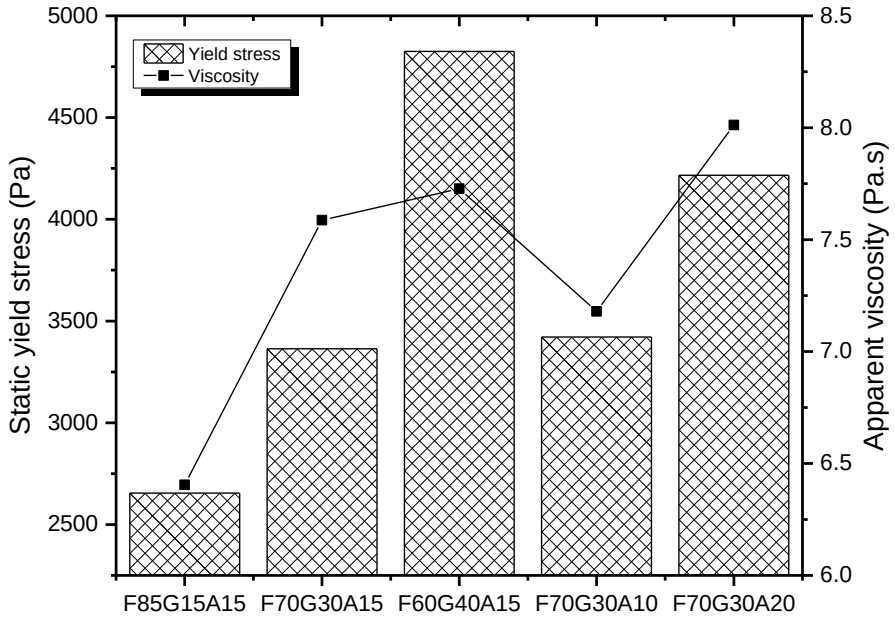

Figure 5.32 The effect of mix design on yield stress and viscosity of geopolymer mortars

Figure 5.33 Extrudability test of one-part geopolymer mixture

The impact of improved yield stress on extrudability and shape retention is clearly visible in Figure 5.33 in terms of continues filament and excellent shape retention property. However, thixotropy is believed to affect these properties similar to the previous rheological investigations and therefore, thixotropy, referring to the reversible structural breakdown and build-up was again studied for one-part geopolymers.

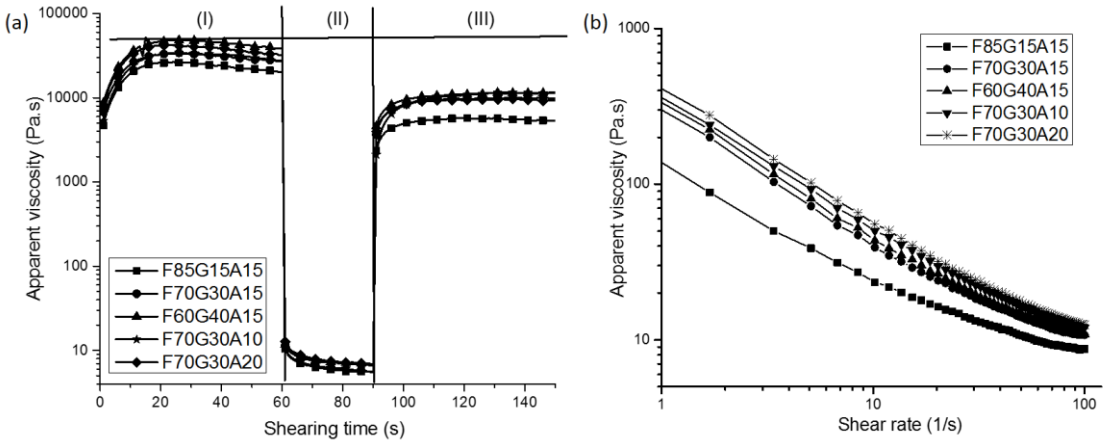

Figure 5.34 The effects of mix design on (a) viscosity recovery and (b) structural break down performance

From the above recovery graph (Figure 5.34), it is clearly observed that the one-part geopolymers can recover 50-60% of their initial viscosities, unlike liquid silicate activated geopolymers. To gain more insights on the rheological effects of the two activators (liquid and powder), a comparison study of yield stress, break down and recovery properties was conducted, including a plain mix without any activator. Tap water was only used in the plain mix to reveal the activator impact, while binder (FA + GGBS) formulation was remaining the same. Similar activator-to-binder ratios (0.30; 0.35) and water-to-binder ratios (0.35, 0.40) were used to formulate one-part geopolymers and their yield stress analysis were presented in Figure 5.35. It is important to note that the activating solution-to-binder ratio 0.30 and 0.35 corresponds to 15 and 17% powder activator-to-binder ratio used in this one-part geopolymer study.

As seen in Figure 5.35, for any water-to-binder ratio the yield stress of liquid geopolymer is much lower than the one-part geopolymers and by replacing the activator with pure water the yield stress was found to be similar to one-part system. This indicates the important role of activator physical state i.e powder (dry) or liquid in determining flow properties of the geopolymer binders. To corroborate this effect, zeta potential

measurement was used to monitor the changes in electric double layer forces under different activator environments, which determine their resultant yield stresses [28].

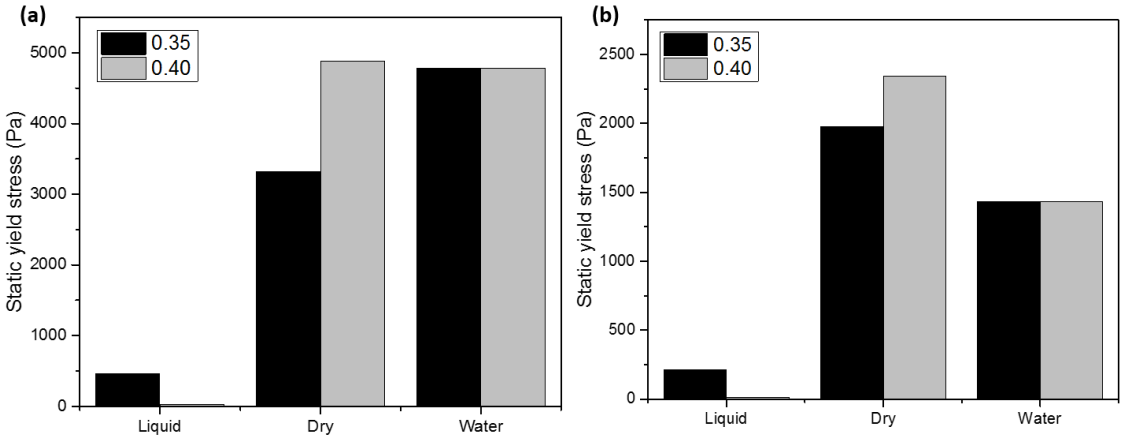

Figure 5.35 The effects of physical state of suspension medium on yield stress of geopolymers at (w/s) ratio of (a) 0.30 (b) 0.35

Figure 5.36 shows the zeta potential of geopolymers for both the activators while using two different dosages. Addition of liquid silicate resulted in negative zeta potential, as negatively charged silicate species from the suspension can adsorb or precipitate on the slag surfaces, which results in more negative values of zeta potential with higher dosage of silicate. Such higher value of zeta potential signifies the increase in repulsive force, that resulted particle separation and therefore lower yield stress [224]. Conversely, for one-part geopolymer, although the increase in zeta potential is a sign of repulsive electric double layer forces which could reduce the yield stress, the fast geopolymer reaction (see calorimeter curves) seem to be more influential in determining yield stress changes.

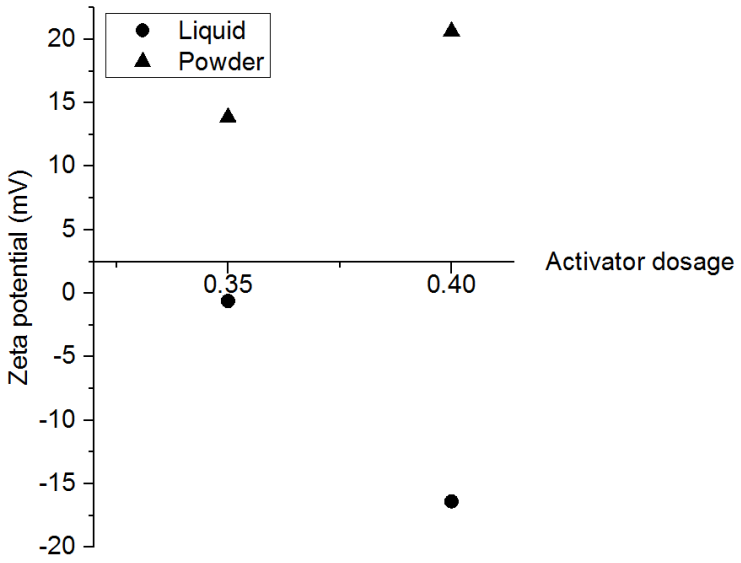

Figure 5.36 The effects of activator type and dosage on Zeta potential

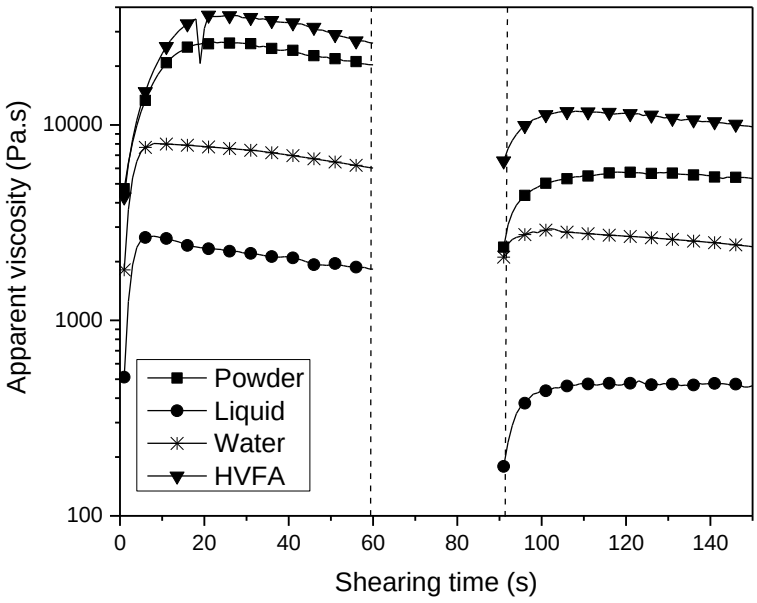

Figure 5.37 Effects of activator type on viscosity recovery properties of geopolymer mortar. Note that 0.30 activator solution-to-binder ratio and 0.35 (w/s) ratio used here for all the mixes.

Following the yield stress, viscosity recovery (Figure 5.37) was also found to follow the same trend, as the recover ability for one-part geopolymer was around 20-25% higher than liquid silicate activated geopolymers. The benefit of higher recovery is represented by excellent shape retention of the extruded geopolymer filaments (Figure 5.30) and it is interesting to note that the SRF was similar to HVFA mortars, developed in Chapter 4. Similar recovery behaviour also observed between the HVFA and one-part geopolymer, which confirms the shape retention observations due to strong vender wall attraction force and higher thixotropy. In contrast, the liquid silicate activated geopolymer lacks thixotropy property and is not suitable in it's current form for 3DCP application.

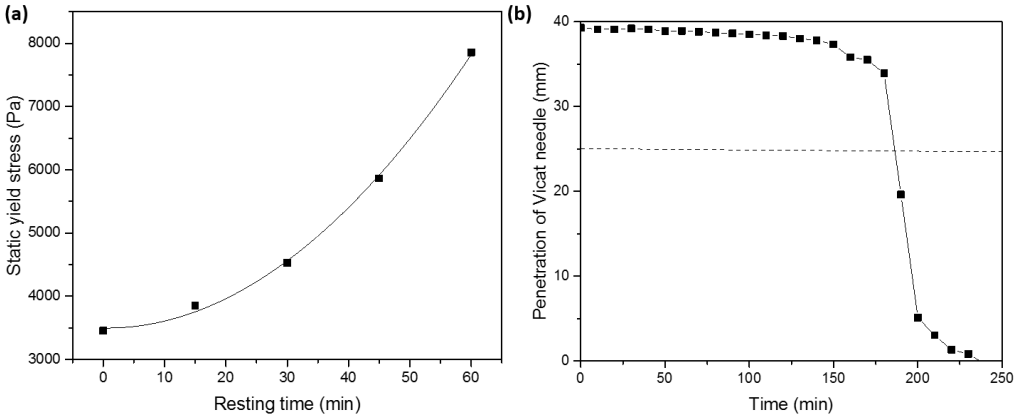

Figure 5.38 (a) Structural build up and (b) setting time of one-part geopolymer mixture using 0.30 activator-to binder ratio and 0.35 (w/s) ratio which corresponds to 15% powder activator

Figure 5.38 shows the structural build-up of one-part geopolymer mortar which describes the time-dependent hardening behaviour starting from mixing to initial setting. Unlike conventional geopolymer, one-part mixture has a longer open time which is also confirmed from vicat setting time measurement. The open time is around 60-90 minutes and it is much earlier than the setting time of geopolymer paste. Due to minimum strength requirement (i.e 30 MPa), only the selected mix was evaluated for structural build-up test.

5.3.3.3 Mechanical strength and isothermal calorimetry

The 28 days compressive strengths of one-part geopolymer mortars were shown in Figure 5.39, which reveals highest activator dosage led to highest compressive strength. This increase in strength could be due to the early formation of C–(A)-S–H gel in the matrix and presence of a higher amount of Si ions available for geopolymerisation reaction [226,227]. GGBS addition also increases the strength, which is attribute to the early formation of C–S–H gel like conventional geopolymer. However, comparing the strength of liquid silicate based geopolymer (for same binder: F85G15), powder silicate exhibited 20% less compressive strength in line with findings of [229]. To explain this observation, both activators characteristics were accessed using FTIR analysis and results were shown in Figure 5.40. The plots labeled "liquid" and "powder" show the spectra of the supernatant solutions and both these spectra look identical irrespective of the difference in activator type. Bands that appear in these spectra are the stretching and bending modes of OH^- in water at around 3450–3500 cm^{-1} and around 1600 cm^{-1} respectively. A quick comparison between the two spectra, reveals that the dominant Si-O-Si peak (that typically appears in the 970–1050 cm^{-1} range [228]) is missing in the powder activator and it indicates that the silica from the powder silicate is unable to dissolve in water, thus resulting low strength geopolymer products. The contribution of powder activator seems to have same effect as NaOH or KOH activated slag system, where the high concentration of OH^- ions present aids in the breaking of Si-O and Al-O bonds in addition to the Ca-O bonds. Release of CaO occurs very fast and stops quickly after an early reaction resulting in a single-peak calorimetric curve (see Figure 5.41). In contrary, the CaO continues to release for much longer time in case of liquid activator [229], resulting in an extended induction period and a two-peak calorimetric curve.

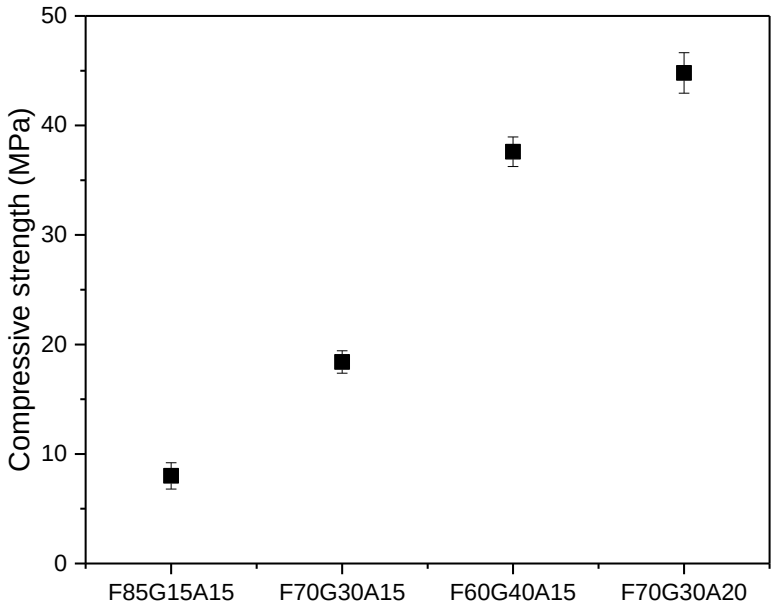

Figure 5.39 The effects of mix design on compressive strength of one-part geopolymers

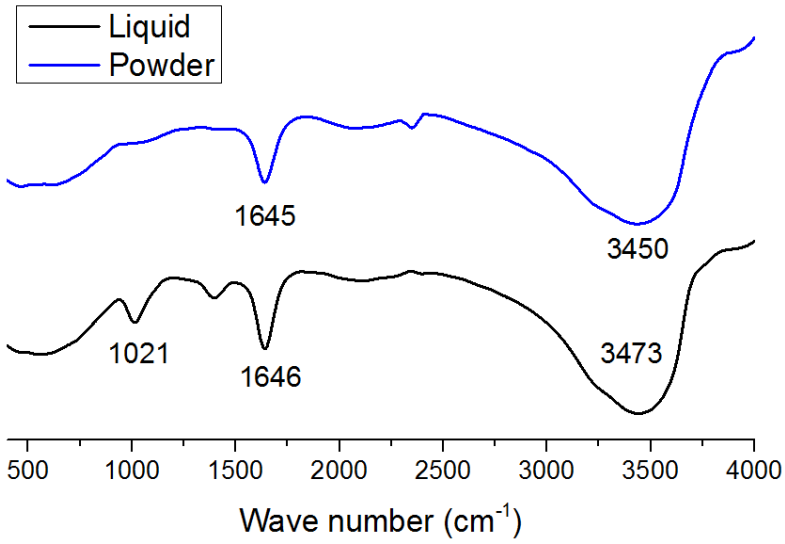

Figure 5.40 FTIR spectra of dry and liquid activator solutions

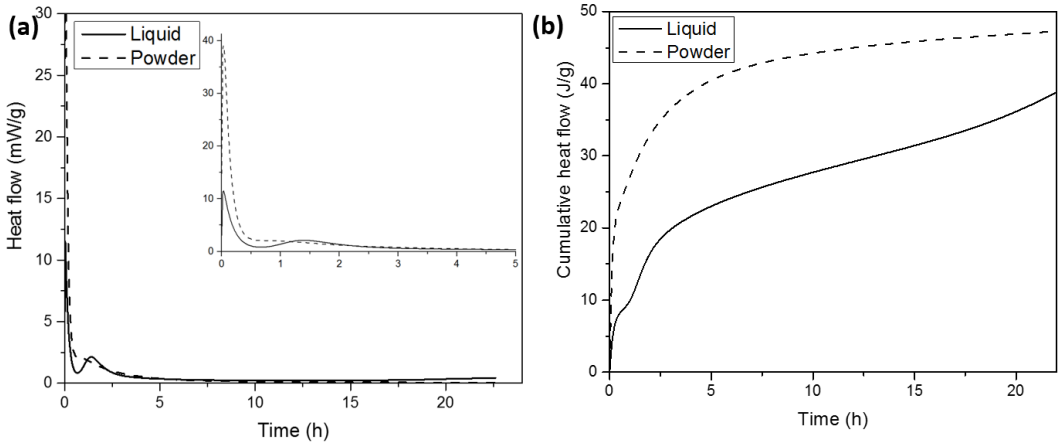

Figure 5.41 The effects of powder and liquid activator on (a) heat flow and (b) cumulative heat flow curves

5.3.3.4 Microstructure and X-ray diffraction quantification

The microstructural analysis of mix F70G30A10 after 28 days of curing revealed the presence of aluminosilicate gel and unreacted FA and GGBS particles, as shown in Figure 5.42. In both cured and uncured systems, a broad hump was observed. In the unreacted system, the hump located at around 15-40° 2θ represented the glassy portion contributed by FA and GGBS. Alternatively, in the case of the reacted sample, the position of the hump slightly moved from lower to higher 2θ angles, as shown in Figure 4.33. This change in the location of the hump indicated the formation of amorphous reaction products and presence of unreacted glassy content. The amorphous reaction products partially overlapped with the unreacted glassy content at higher 2θ angles. As shown in previous studies [230], the amorphous reaction product usually formed at higher 2θ angles (e.g. 29^{o}), which could be attributed to potassium alumino-silicate gel (K-A-S-H), when potassium was used as an alkaline activator. As shown by the quantities of the different phases listed in Table 5.4, the presence of amorphous reaction products directly influenced the mechanical performance of the prepared mixes. The combined amorphous reaction products and unreacted glassy content present in the reacted system (F70G30A10) was slightly lower in content than the glassy content present in the

unreacted FA-GGBS system. This could be because the glassy content involved the formation of zeolites in the system.

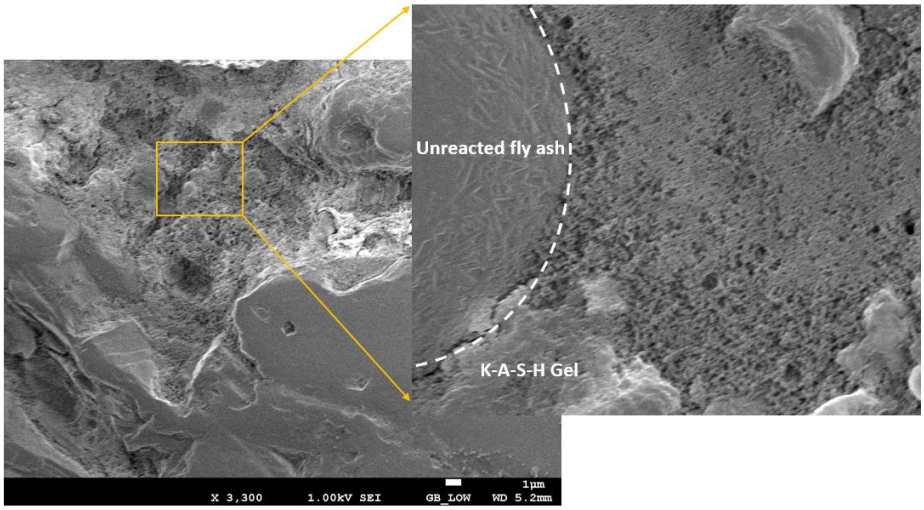

Figure 5.42 FESEM image of one-part geopolymer sample at 28 days

Zeolites K (PDF# 022-0793) and G (PDF# 019-0092) were identified as the secondary reaction products in mix F70G30A10, along with major crystalline phases such as quartz, mullite and gehlenite. The formation of zeolites could explain the initial hardening of geopolymer mixes, which can be linked with the buildability property of 3DCP process.

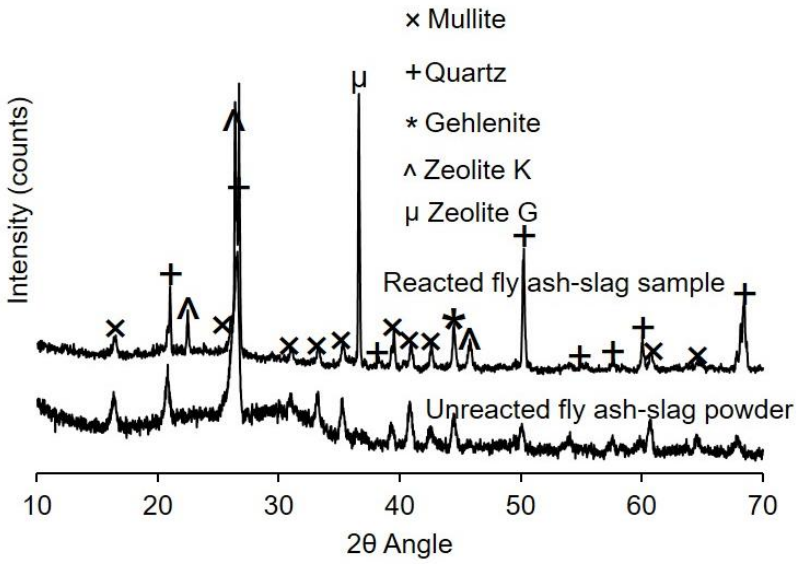

Figure 5.43 XRD patterns of unreacted binder and one-part geopolymer sample

Table 5.4 Quantities of phases within unreacted binder and one-part geopolymer at 28 days

Compound	Unreacted FA-GGBS	Reacted FA-GGBS (F70G30A10)
Quartz	13.3	11.2
Mullite	25.0	10.2
Hematite	0.4	0.9
Magnetite	0.2	0.9
Rutile	0.2	0.2
Calcite	0.2	0.6
Gehlenite	1.2	0.1
Zeolite K	-	9.9
Zeolite G	-	13.9
Amorphous reaction product / unreacted glassy content	59.6	52.1

5.4 Conclusions

This study investigated the material design and evaluation of 3D-printable binders based on fly ash-based geopolymers. The key findings are as follows:

- Using FA as the major ingredient, geopolymer mixtures were proportioned to be extrudable and buildable for extrusion based 3DCP application. When alkaline activators were used in lieu of water, the yield stress of the fresh pastes decreased, and the cohesiveness increased, similar to the effect of superplasticizers in conventional PC systems.

- Structural break down and recovery tests were used to characterize the thixotropy of geopolymer mixtures. Due to the lack of shape stability, NC was used to improve the printability of the geopolymer mortars. Despite of the alkaline environment, the NC was able to flocculate when the activators were used in an appropriate amount together with extra water. NC modified geopolymers demonstrated an improved buildability, though 20% reduction in strength was observed due to the higher content of unreacted FA and less dense microstructure. XRD, FESEM and calorimetry tests confirmed the mechanical consequence of the modified geopolymer.

- SF was also used to improve the rheological properties of geopolymer. Inclusion of 10% SF led to improved extrudability and shape stability without significantly affecting the mechanical strength. The structural build-up was accelerated, which could increase the buildability, if the layer deposition speed and build-up rate were optimized together. When compared to the performance of samples containing SF, NC modified geopolymers exhibited better thixotropy properties, although their strength development rate was similar to the control.

- The influence of powder potassium silicate activator, instead of liquid silicate was investigated in terms of yield stress and thixotropy properties of the geopolymer. Powder activators caused a significant increase in the yield stress and better recovery properties reflected by improved buildability, like HVFA mortars. However, the compressive strength of powder geopolymers were not as strong as liquid silicate based geopolymers due to the lack of silica released in the reaction. FTIR spectra and calorimetry results were used to confirm these observations.

In light of above results, it can be concluded that 3D printing of geopolymer mortars requires very careful material design to ensure robust rheological and mechanical performances. Since out of the three different approaches, powder silicate activated geopolymers exhibited excellent thixotropy and acceptable strength characteristics, further directional mechanical tests will be carried out to realise the suitability of the proposed mix design for a large-scale printing case study.

Chapter 6 Mechanical properties of 3D Printed mortars

6.1 Introduction

This chapter will discuss the mechanical performance of 3D printed mortars in addition to the influence of process parameter related to design of printable structures. Process parameters such as print speed, flow rate, time gap etc. were studied to understand their effects on printability using a custom made 4-axis gantry printer. The whole process of 3DCP depends on various tangible and intangible parameters which defines the dimensions of the printed filament, curvature of the printed geometry, buildability and so on. In this regard, before investigating mechanical properties of 3D printed parts, the effect of printing parameters are described in sub-sections 6.2 and 6.3 followed by a case study of large-scale 3DCP.

6.2 Effect of printing parameters on mechanical properties of fly ash-cement mortar

6.2.1 Understanding and selection of optimum printing parameter

Figure 6.1 displays the important machine parameters of 3DCP process. These parameters are interrelated with each other and therefore, their individual effects were studied in this section using a slow hardening material to eliminate the material stiffening behaviour on the final decision.

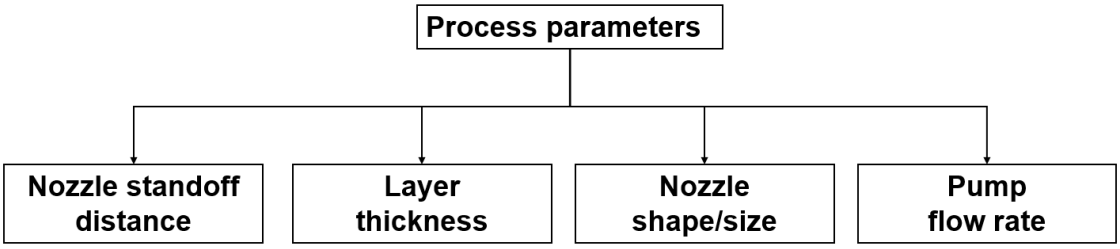

Figure 6.1 Process key parameters of 3DCP

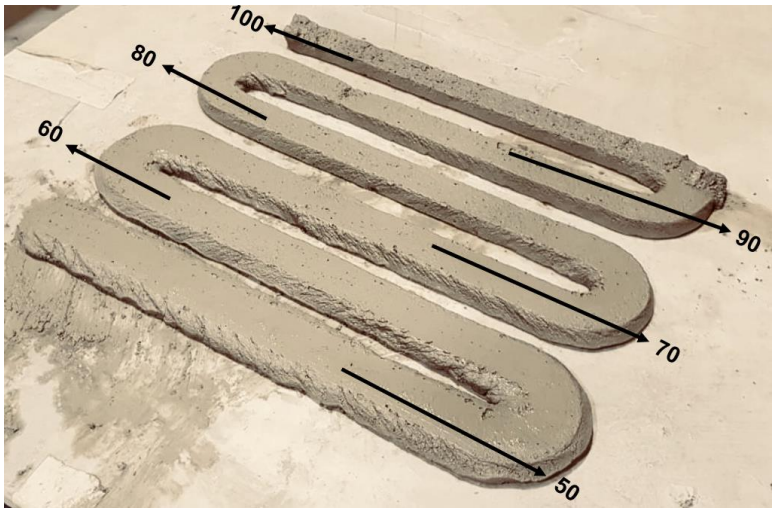

Figure 6.2 The effects of print speed on filament thickness at constant flow rate (arrow indicates the speed in mm/s)

The effect of different printing speeds (50-100 mm/sec) on the extruded filament width is shown in Figure 6.2 and its evident that the width is getting thinner with increasing speed, while the flow rate was constant. The flow rate of concrete in conjunction with the print speed controls the diameter of the deposited filaments. The diameter is directly proportional to the flow rate of the deposition at a constant velocity and indirectly proportional to the print speed at a constant flow rate deposition. However, there is an optimum velocity range where the filament width can be equals to the nozzle diameter. The print speed (V) can be approximately determined based on the deposition volume equality according to Eq. (2).

$$V = \frac{4Q}{\pi D^2} \tag{2}$$

Where Q is material flow rate and D is nozzle diameter

The experimental observations revealed that if the print speed is greater than V then the width is usually smaller than the nozzle diameter (case I), and if the print speed is smaller

than V, the width is usually larger than the nozzle diameter (Case III). This relationship is schematically illustrated in Figure 6.3.

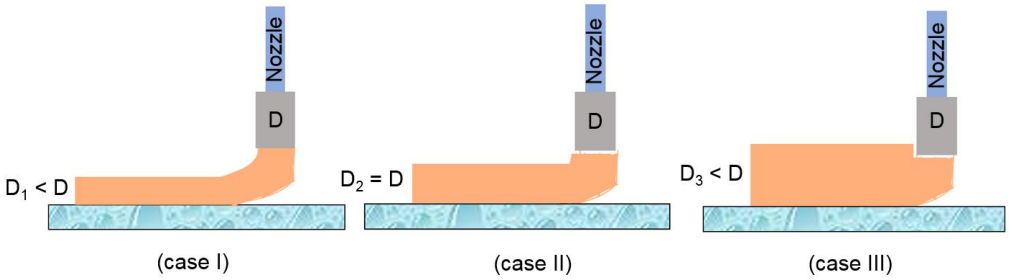

Figure 6.3 Schematic of the printing speed effect on extruded filament diameter

Considering the effect of print speed, it is understood that there exists a favorable velocity range for extruding filaments with their width equals to the nozzle diameter. This is highlighted (blue colour) in the following figure, whereas the red areas are not suggested due to lack of filament continuity, voids and weak mechanical properties. Based on obtained experimental results, 80 mm/sec was selected as optimum speed for further investigating the effect of part design in 3DCP.

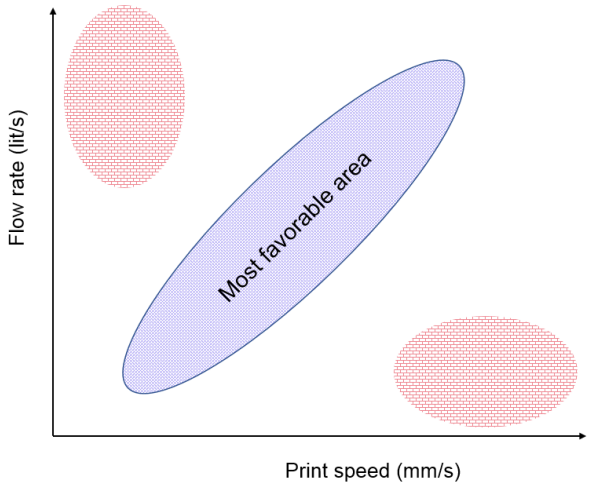

Figure 6.4 The relationship between flow rate and printing speed in 3DCP

Figure 6.5 shows one of the corner designs of the large-scale printing (described in section 6.5) and different radius of curvatures were attempted to find the best combination with 80 mm/sec printing speed. Keeping the print speed constant with flow rate, 40 to 80 mm radius was printed to see the effect of curvature on filament properties.

Figure 6.5 The effect of radius of curvature on filament surface property

As depicted in Figure 6.5, for a 40 mm radius there is a tearing and/or cracking of outer edge and this effect seems to be similar on many aspects to the "sharkskin" instability as described in [136]. The speed at the exit of the extruder is reported to cause a such cracking by inducing tensile stresses and this can be avoided by using a thicker nozzle with reduced print speed [136]. Alternatively, if the radius can be made bigger a smooth surface will be observed as seen for 60, 70 and 80 mm radius. Such effect also depends in layer height, material thixotropy and speed of the nozzle when passing through the corner. Sometimes, if the curvature of the toolpath is too steep the rotational axis of the printer cannot keep up with the translational axes and it causes jerky movements that

likely to affect the filament quality. Figure 6.6 shows the consequence of printing a sharp 90-degree corner of a regular square pattern using 40×10 mm nozzle. It is clearly visible that the material deposited in the smaller inner curve tend to pile up, while on the outer curve tends to expand which caused tilting of the filaments and with addition of more layers, it can cause failure of the printed elements. These problems can be solved by reducing the linear print speed, preferably in combination with scaling down the dimensions of the printed filament as done by University of Loughborough, U.K. [114].

Figure 6.6 Example of layer stacking at the corner due to sharp turn curvature and small layer width

6.2.2 Effect of printing direction

In the light of process parameters effect in 3DCP, mechanical strengths were conducted on the 3D printed mortars in different loading directions and the obtained results are discussed below.

Figure 6.7 shows the average compressive strengths of 3D printed HVFA mortar (NC and SF modified) and from this graph it can be concluded that the layer direction has almost no influence on the compressive strength. The only noticeably difference is that if the layer direction is parallel to the print direction (F1) is approximately 8-10% stronger than the other two-layer directions at 28 days after printing. It is not possible to state that this effect is due to the layer direction because the layer direction in test

direction F1 and F3 is the same. The difference in strength could be imposed to the way of motion of the material through the print system. The movement of the material through the system is in the direction of test direction F1. It could be possible that in the direction of movement the particles are placed and compacted better than the other directions and provides a higher compressive strength. Comparing the results of the printed samples with the casted control samples, there is a larger difference visible. The maximum compressive strength of printed concrete is 35.15 MPa and is only 16% higher than the average strength of the casted control samples. The fractured images of 3D printed samples are shown in Figure 6.8.

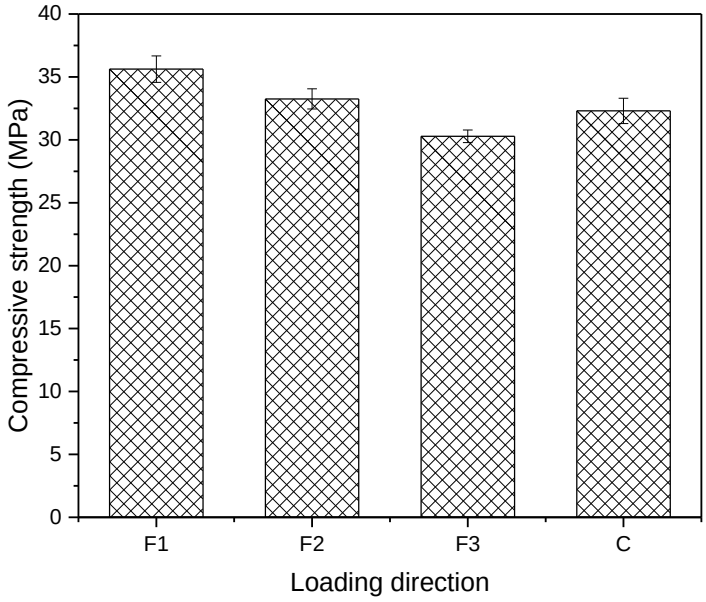

Figure 6.7 Directional compressive strength of 3D printed HVFA mortar

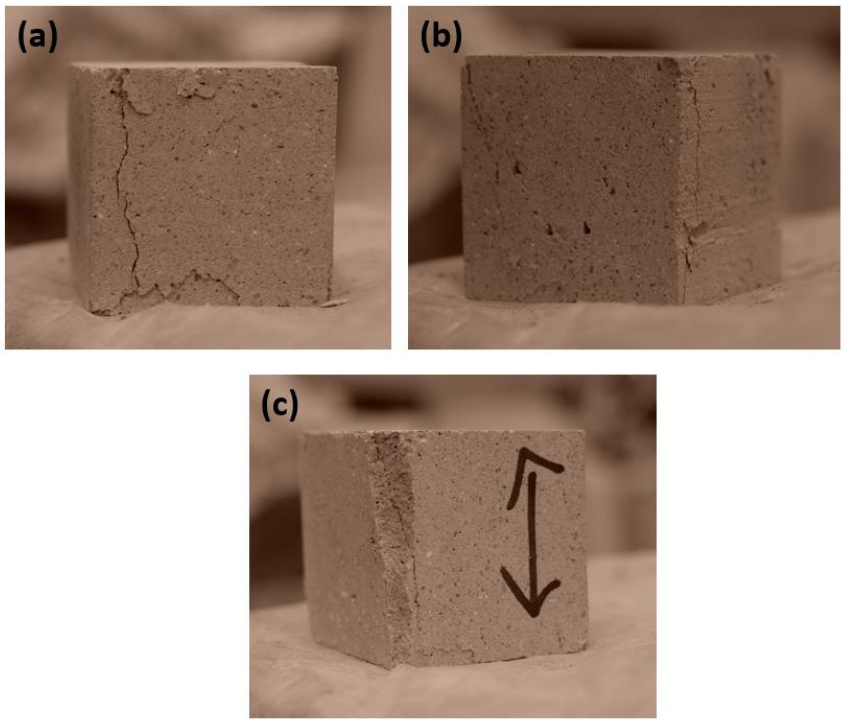

Figure 6.8 Failure pattern of 3D printed sample (a) F2, (b) F3, (c) F1 after compression

The results of directional flexural strength test were shown in Figure 6.9. The printed specimens showed the weakest bending resistance F1 loading direction, which is similar to the results obtained by Feng et al. [150]. The flexural strengths corresponding to samples F2 and F3 are 56.1% and 20.6% higher respectively than the mold cast samples. The anisotropic flexural bending behavior of printed samples may be explained on basis of laminate theory of the composite material i.e when the printed sample was loaded in F1 direction, the tensile stress at the bottom occurs directly perpendicular to the weak interface layer joints and so, the cracks initiated easily causing the premature failure. Therefore, the samples exposed to F1 loading direction performs the worst bending capacity. However, it may be appreciated that the samples F2 and F3 show higher flexural strength than the mold cast samples, even though the layer wise nature of 3DCP likely to weaken the integrity of printed samples.

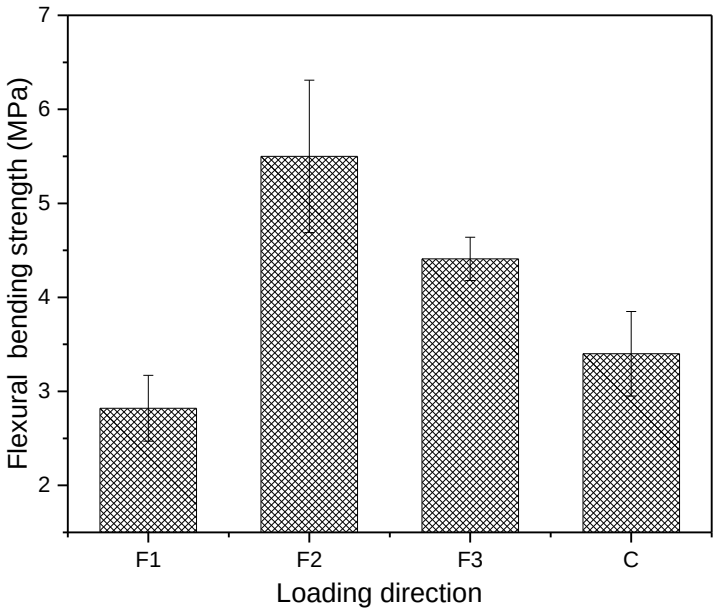

Figure 6.9 Directional flexural strength of 3D printed HVFA mortar

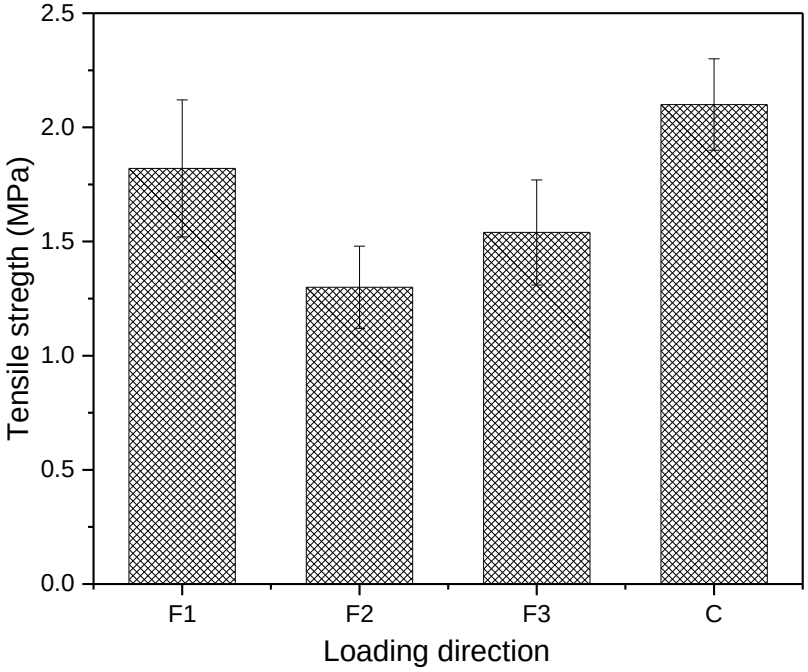

Figure 6.10 Directional tensile strength of HVFA mortar

The results of directional tensile strength test were shown in Figure 6.10. Test direction F2 is the weakest, because in this direction the layers are pulled off each other and the samples failed on the interface. The other two directions are loaded parallel to layer direction, so the samples failed in the concrete. The deviation in the results could also be caused by inclination in the top or bottom where there is not only tensile load in the samples but also a bending moment. These bending moments could have provided addition stresses causing the sample to fail at lower load.

6.2.3 Effect of time gap between layers

Besides layer direction, time interval is also a test variable that can significantly affect the hardened property especially, the tensile bond strength. In the first attempt, the control HVFA (without NC) mix was used to envisage the effect of delay time between the layers. 0, 5, 10- and 15-minutes time gap was allowed in between two layers of the extruded mortar followed by their tensile tests as described in the methodology section. As shown in Figure 6.11, the bond strength decreases with increase in time gap which can be explained based on material structural build-up properties.

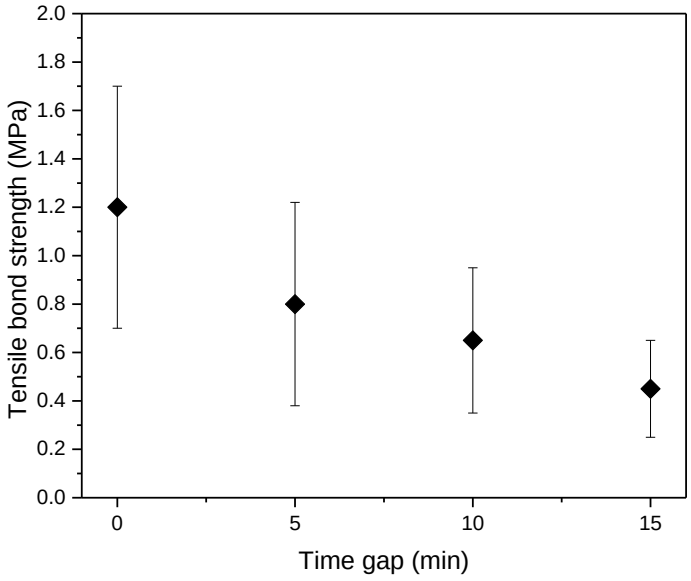

Figure 6.11 The effects of time gap on bond strength of HVFA mortar

When the filament is extruded, it's yield stress increases with time due to thixotropy property as shown in Figure 4.18. This behaviour is known as structural build up at rest, which incurs high stiffness in the material and could be the cause of loss of bond strength with longer time gap. Only the first deposited layer structural evolution is responsible for such phenomena as it is accepted that the second layer build up can be destroyed during pumping and it will be always in the flowable condition before its initial setting. Therefore, it can be concluded that structural build-up of the first layer is one of the main causes of poor bond strength and the experimental results were in agreement with findings of Le et al. [114], that describes the similar effect. According to Sanjayan et. al. [153], loss of surface moisture is one of the major factors affecting the inter-layer strength, in addition to process parameters, evaporation rate and bleeding rate. Nicolas Roussel [136] also confirmed this effect of moisture while comparing the bond strength for an interface protected from drying and exposed to drying. The interface strength was found to be 90% higher than the reference strength, when the material was protected from drying.

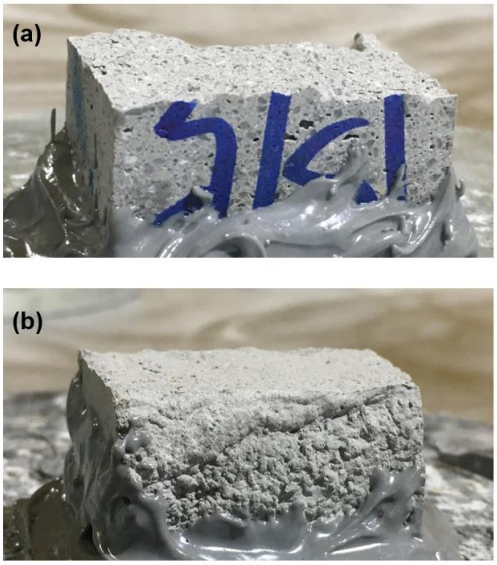

Figure 6.12 The fracture surface of tensile bond strength samples whereby (a) specimen failed on the bulk material and interface (b) specimen failed on the interface

The fractured surface of printed HVFA mortar with two different time gaps (0 and 15 min) is shown in Figure 6.12 and it is very clear that the delay in deposition has caused failure at the interface, while in time deposition resulted a mixed (adhesive+ cohesive) failure.

Since material structural build-up is found to be the main cause of weak interface bond strength, it is thus important to measure the bond strength of the NC modified HVFA mixture (5NC +2.5% SF) designed for large scale 3DCP. As seen in Figure 6.13, the modified mix has 20% lower bond strength compared to the control mix for 15 mins time gap. This behaviour can be explained based on higher thixotropy and yield stress of the mix caused by addition of NC (Figure 4.18). Due to higher yield stress, the interface became too stiff to mix well with the subsequent layer. This is an interesting challenge in 3DCP, where there is a need of thixotropic material and with rise in thixotropy (with time) the bond strength found to be weaker in the printed structure.

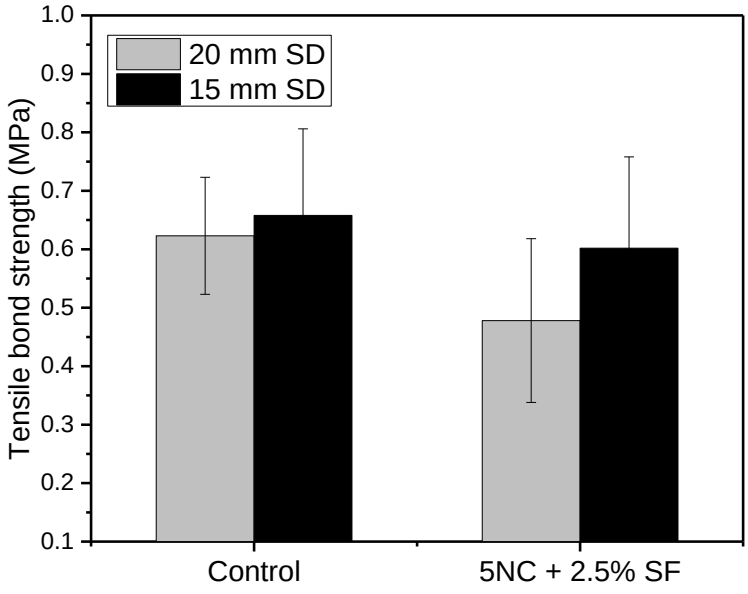

Figure 6.13 Effect of standoff distance on tensile bond strength of control and modified HVFA mortar (5NC +2.5% SF)

In order to overcome this issue, the nozzle height or standoff distance (SD) was reduced during printing as shown in Figure 6.14 and after 28 days of curing, the strength was measured following the similar tensile strength test protocol. The SD is defined as the distance from tip of the nozzle to the build plate.

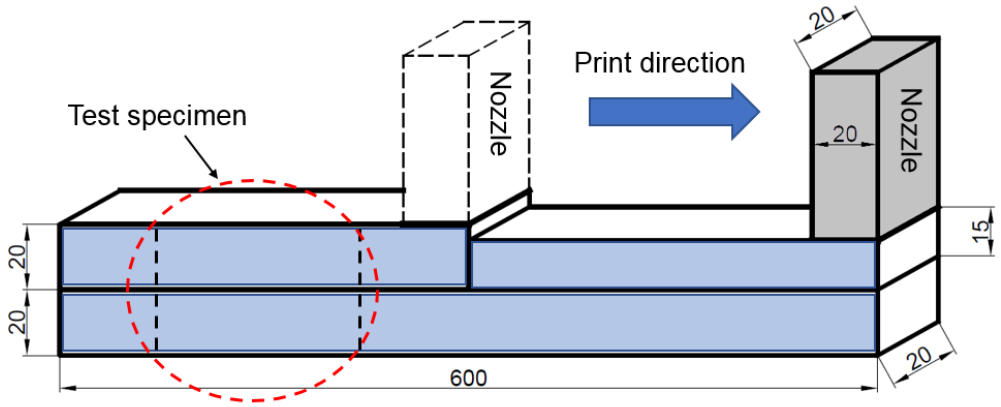

Figure 6.14 Experimental plan for tensile bond strength with different standoff distances

It is well notable from the Figure 6.13 that the two SDs, i.e. 20 and 15 mm have a little or negligible effect on bond strengths of the control mix, however for 15 mm SD notably increased in the bond strength of modified mix was observed compared to 20 mm. A close look at the interface conditions revealed that, presence of micro pores resulted the strength loss which is clearly visible in the interface zone, as shown in Figure 6.15 (a). The bond strength of the concrete-to-concrete interface is mostly influenced by adhesion including substrate condition, overlay compaction and curing procedures [231-233]. Overlay compaction, which was achieved by decreasing the SD from 20 to 15 mm, was found to be improve 33% bond strength for the higher yield stress and thixotropic material i.e. the modified mix. The improved bond strength of the modified mix can be explained in terms of reduced micro-pores as shown in Figure 6.15 (b). It is also believed that the stresses generated by the flow of the overlay layer was sufficient to initiate flow in substrate layer, that allows the two layers to intermix together more or less, as no sharp interface was spotted between the layers. On the other hand, we did not notice any

notably impact of SDs in case of the control mix, which is attributed to its low yield stress property. Moreover, there was no visible difference in the micro images (Figure 6.15(c) and (d)) of control mix interface, when printed with lower SD.

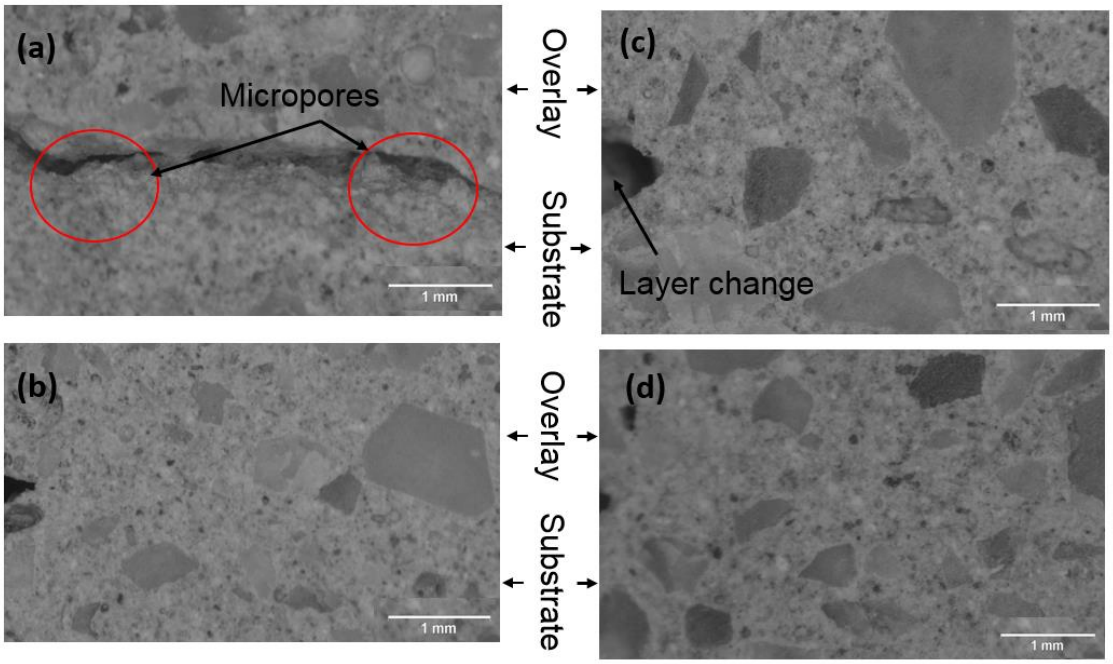

Figure 6.15 Interface microstructure of modified mix printed with (a) 20 mm SD (b) 15 mm SD; Control mix printed with (c) 20 mm SD (d) 15 mm SD

In light of above results, it is thus confirmed that high yield stress materials can improve the buildability, but they may result weak interfaces for SD equals to nozzle width. The physical origin of bond strength is related to the structural build-up property of the substrate and keep on increasing with time gap and this could cause the interface too stiff (less moisture) and prevent intermixing with the subsequent layer. A decrease in SD can significantly improve the interface strength or alternatively, a rapid hardening low yield stress material can be used for 3DCP (see section 7.4).

6.3 Effect of printing parameters on properties of geopolymer mortar

In this section, directional property of one-part geopolymer mortar (F70G30A10) was investigated similar to the HVFA mortar. Since one-part geopolymer possess better rheological properties than both NC and SF modified mixtures, it was considered for strength investigations followed by large scale 3DCP. However, for interfacial bond test, a comparison between one-part and SF modified liquid silicate activated geopolymer was made due to uniqueness of 3DCP process.

6.3.1 Effect of print speed

The effect of print speed on filament width was investigated by varying the speed from 50 mm/sec to 100 mm/sec and based on visual observation (Figure 6.16) and filament width-to-nozzle width ratio, 90 mm/sec was selected the optimum printing speed for a constant pump flow rate.

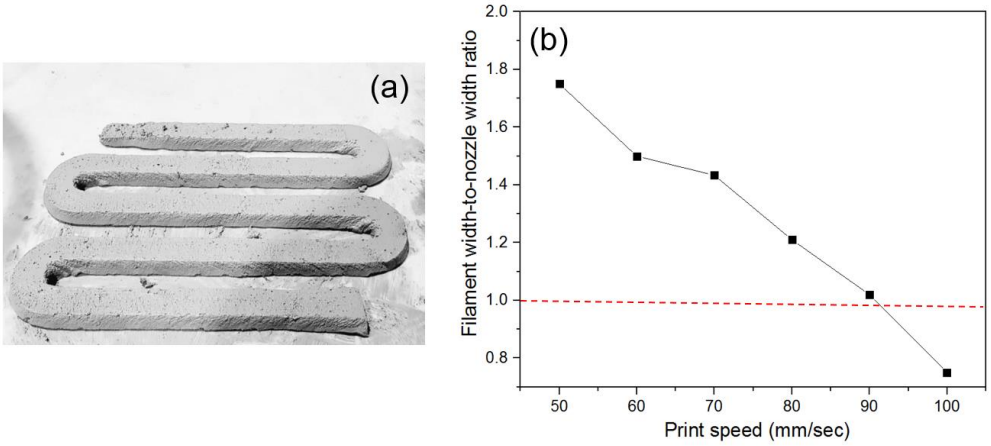

Figure 6.16 (a) Extrudability test and (b) effect of print speed on filament width of one-part geopolymer mortar

As described earlier, there exist a range of printing speed where the filament width can be almost same as nozzle width. There are no general guidelines for such mutual selection as it is subjected to the available pump type and maximum flow limit. Results shown in

Figure 6.16(b) demonstrated that 90 mm/sec is the optimum print speed for one-part geopolymer mortar as the filament and nozzle width are almost equal. The selection of print speed is highly dependent on material viscosity and it's effect is significantly visible in sharp corners of print path, if the print speed is not optimized as per material flow rate.

6.3.2 Effect of printing direction

The obtained result of directional compression test is shown in Figure 6.17 and compared with a mold casted one-part geopolymer mortar. It is apparent that the strength in F1 direction is approximately 5-8% stronger than the other two-layer directions which could be due to the way of motion of the material through the nozzle. It is not possible to state that this effect is due to the layer direction because the layer direction in test direction F2 and F3 are the same. The overall results indicate that the print directions have very less influence on the compressive strengths of the geopolymer mortars.

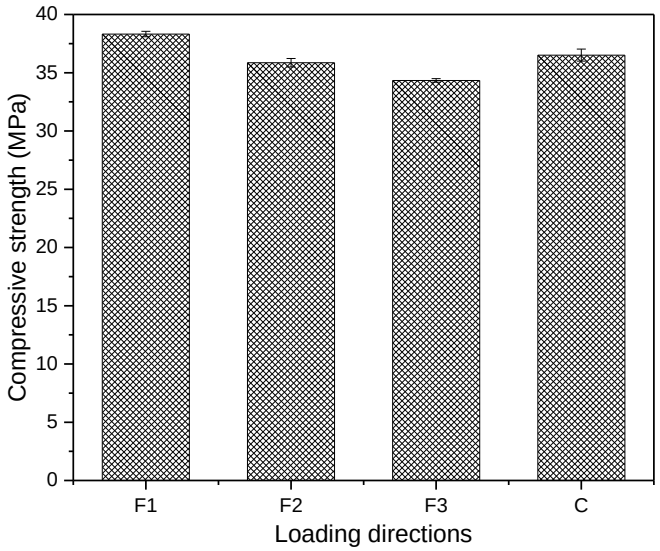

Figure 6.17 The effect of loading directions on compressive strength of geopolymer mortar

Le et al. [114] have also observed similar orthogonal mechanical properties while 3D printing high-performance concrete. The authors commented on effect of filament

compaction that not only affects the printed part density, but also the final strength properties. Figure 6.18 shows a comparison between good and bad printed geopolymer mortar, which also affects their hardened properties significantly.

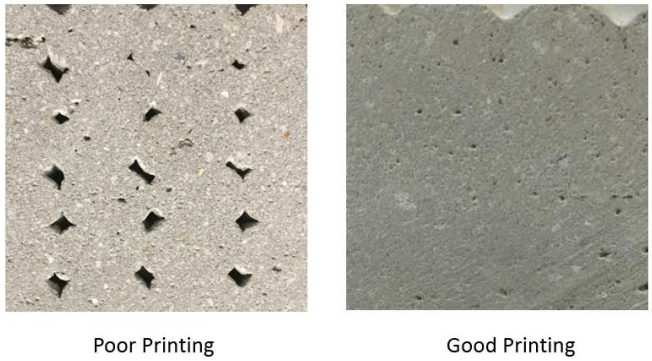

Figure 6.18 Illustration of good and poor 3D printing process

Figure 6.19 shows the average flexural strengths of 3D printed (one-part) geopolymer mortar and similar to HVFA, the weakest bending resistance was noticed in F1 loading direction. The anisotropic bending behaviour is in line with findings of Ma et. al. [159] and can be explained as follows, when the printed samples are subject to F1 direction, the tensile stress at the bottom of the prism is perpendicular to the weak joints between adjacent layers and this is where the material is weakest, so cracks are prone to initiate. Therefore, the samples exposed to F1 direction loadings performs the worst bending capacity. The fracture status of a printed sample is shown in Figure 6.20 , which indicate brittle failure of the layers and such fracture properties can be improved by adding micro fibers in the mixture design as demonstrated in [234].

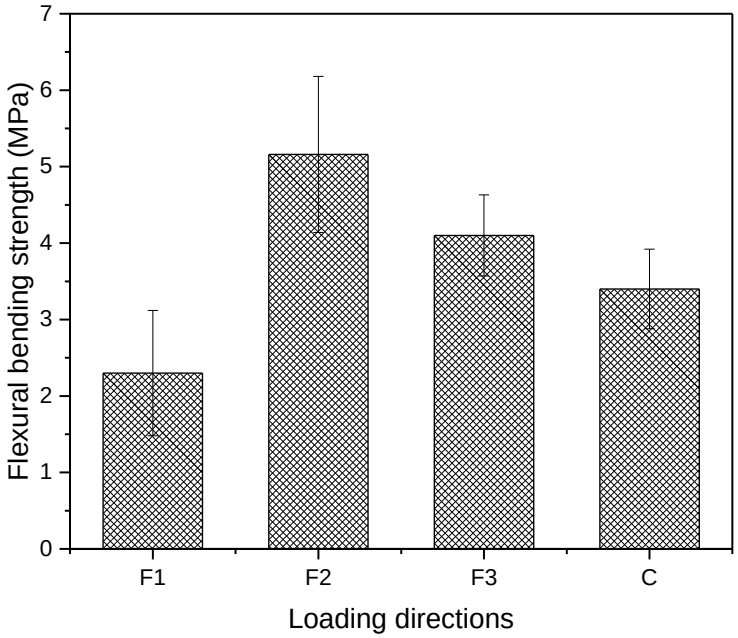

Figure 6.19 The effect of loading direction on flexural strength of geopolymer mortar

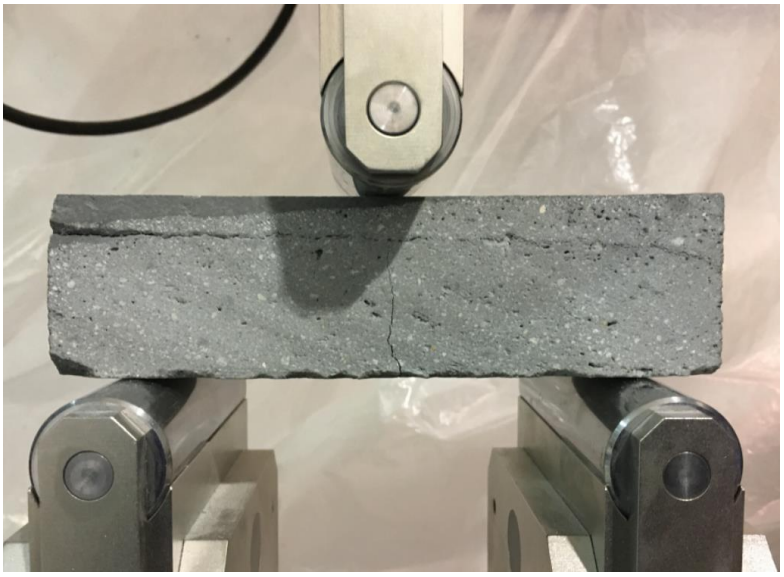

Figure 6.20 The failure status of geopolymer mortar

The results of directional tensile strengths of one-part geopolymer were averaged and shown in Figure 6.21. Unlike compression test, the layer direction has a significant effect

on the 28 days strength. Test direction F2 is the weakest among all since in this direction the layers are pulled off each other and depending on the inter-layer bond strength, the samples failed on the interface.

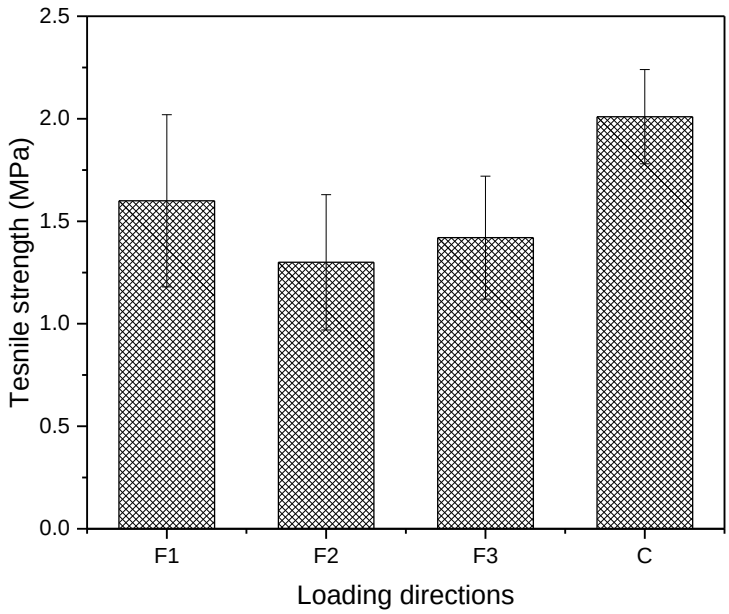

Figure 6.21 The effect of loading direction on tensile bond strength of geopolymer mortar

It is important to point out that few studies in the past have investigated directional mechanical strengths of 3D printed samples and these results are difficult to compare at this moment due to lack of standard measurement procedure. Some researchers used cylindrical shape instead of cube and most interestingly, due to change is sample size the complete process of 3D printing the sample changes. In some cases, 40 mm width layers were printed, and some reported the strength by extruding two 20 mm layers next to each other for producing the 40 mm width. Therefore, the standardization should be subject of research to determine the most appropriate approach of testing 3D printed concrete.

6.3.3 Effect of time gap between layers

Similar to the time gap study in section 6.2.3, one-part geopolymers were subjected to different time delay such as 0, 5,10 and 15 minutes before placing the second layer. The results obtained from the time interval test (Figure 6.22) indicate that the average bond strength decreases with increase in time gap and the standard deviation is quite variable, as expected for layered extrusion process.

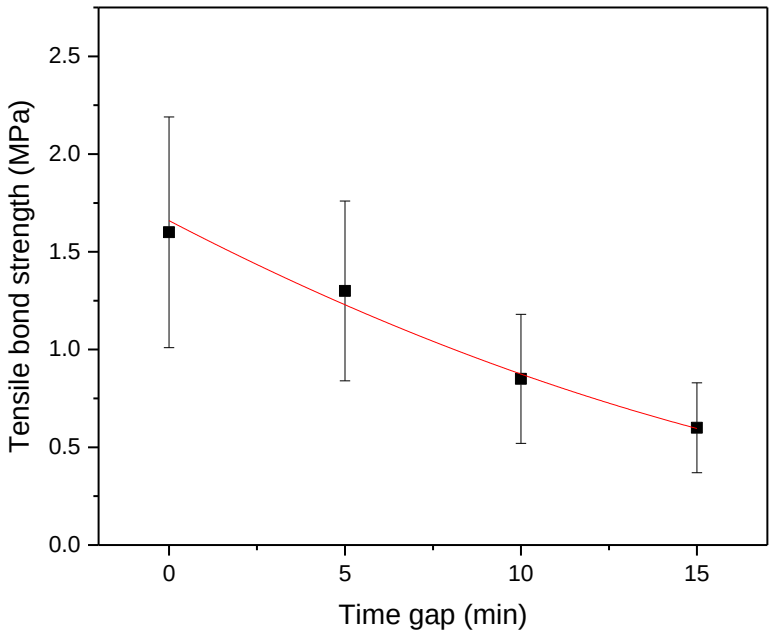

Figure 6.22 The effect of time gap on tensile bond strength of geopolymer mortar

All specimens with a time gap 15 minutes failed at the interface owing to lack of adhesion which can be explained by their structural build-up rates obtained from yield stress. The lack of adhesion was understood by adhesive failure, whereas the strong interface was dictated by a mixed (adhesion + cohesion) failure. Tay et al. [151] has recently reported increase in elastic modulus of first deposited layer is the origin of poor adhesion as increase in stiffness prohibits the inter mixing of the layers and sometimes, pressing of layers might be useful depending on extruded concrete rheological properties.

To envisage the effect of nozzle SD on inter layer bond strength of geopolymer, one-part geopolymer and (SF modified) liquid silicate activated geopolymer were printed as per the experimental plan shown in Figure 6.14. The main findings from the results confirms 37.5% increase in bond strength only for one-part geopolymer but SF modified geopolymer did not show any improvement when the second layer was added after 10 minutes time gap.

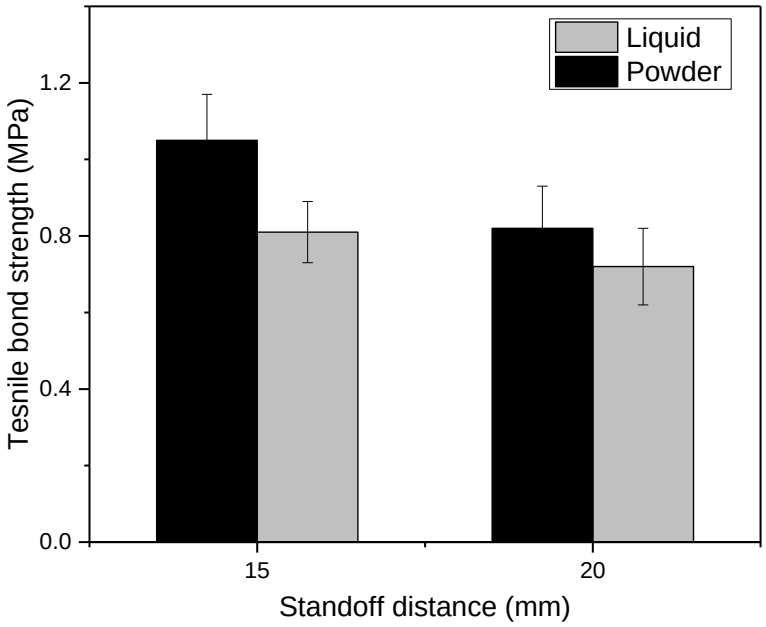

Figure 6.23 The effect of nozzle standoff distance on bond strength of geopolymer mortars

One-part geopolymer, as mentioned in the previous chapter has highest thixotropy among all modifications of the geopolymer and therefore pressing of layer by reducing the SD (20 to 15 mm) is improving the compaction and inter-mixing the layers, similar to distinct-layer casting of SCC [235]. However, in case of liquid silicate activated geopolymer negligible or almost no impact was observed except spreading of layer width due to viscous nature of liquid silicates. Usually geopolymers activated by liquid silicate behaves as soft material, which can be easily deform when extruded on the print bed. Therefore, effect of pressing has minimal impact on inter layer bond strength. Pressing

of layers or reducing the SD has another advantage which was recently addresses by Nerella et. al. [154]. The authors have claimed that the smaller interface pores can be easily filled with hydration products as shown in Figure 6.24. This self-healing is not always helpful, and it depends on the reactivity of the material that controls growth of the reaction products. Despite material property, the pores at the interface can be reduced by pressing the layer and the bond will be stronger with hydration products.

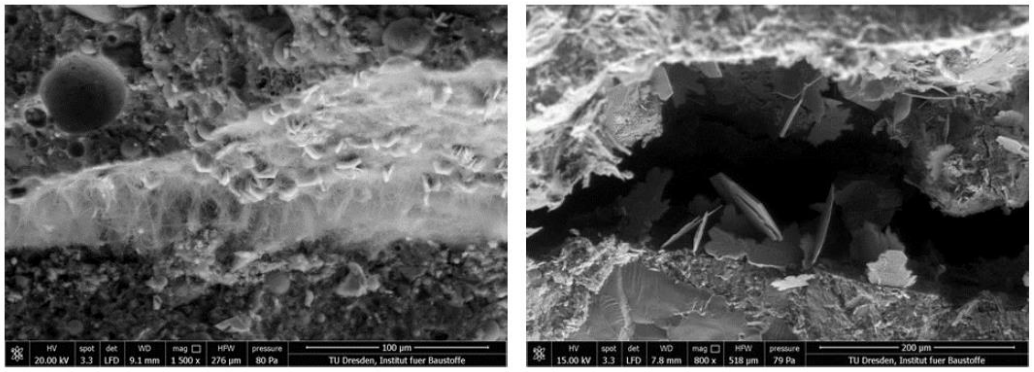

Figure 6.24 Examples of a) partial self-healing and b) only partial filling of large separation with hydration products [154]

6.4 Early age mechanical properties and large-scale printing of fly ash-cement mortar

In this section, a case study of large-scale 3DCP was demonstrated while understanding the effects both process parameters and material early age mechanical properties. Alternative to static yield stress, compressive green strength and young's modulus (stiffness) were used to study the deformation behaviour of fresh concrete and accordingly build height was limited. Based on maximum allowable height, the part design was splitted and later the printed parts are assembled together to form a larger object.

6.4.1 Material green strength evolution

In order to study the deformation behaviour of fresh concrete, compressive green strength test was carried out using the control HVFA mortar and subsequently, the material stiffness was compared with the developed SF and NC modified mix (5NC +2.5% SF). Figure 6.25 shows the force-displacement (F-d) curves for concrete age t = 5 to 150 mins. It is clearly noticed that the load initially increases approximately linearly as the vertical displacement increases. After this initial path, the increment of loading decreases as deformations grow. The younger specimens (i.e. t = 5, 30, and 60 min) show an increment in load with increasing deformations, up to a certain plateau. The older specimens (i.e. t = 120 and 150 min), on the other hand, show a load decrease after the initial peak, again to a certain limit. This difference in behaviour is attributed different material failure for e.g. a distinct failure plane is observed for older samples whereas younger samples fail by barrelling effect as shown in Figure 6.26 [148,236].

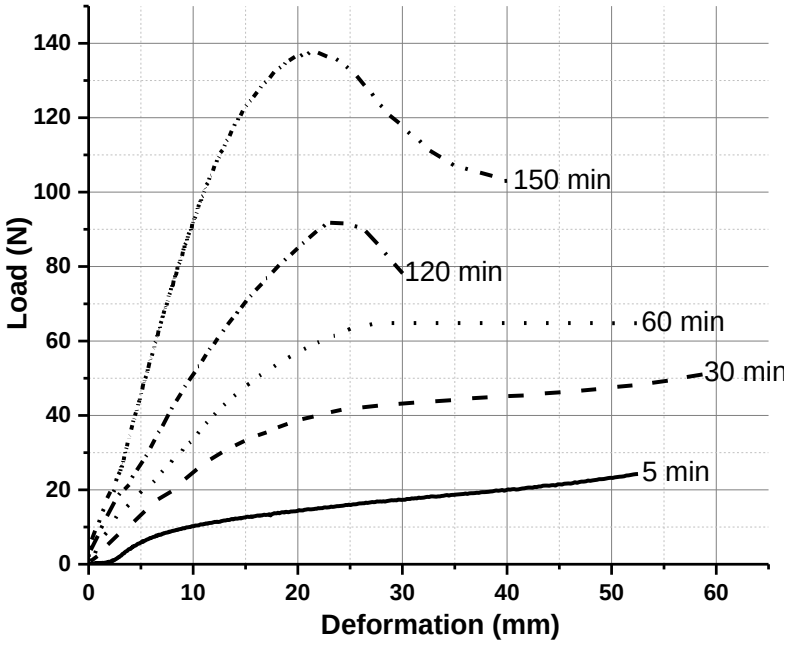

Figure 6.25 Load - deformation (F-d) diagram of fresh cement mortar age t=0 to 150 min

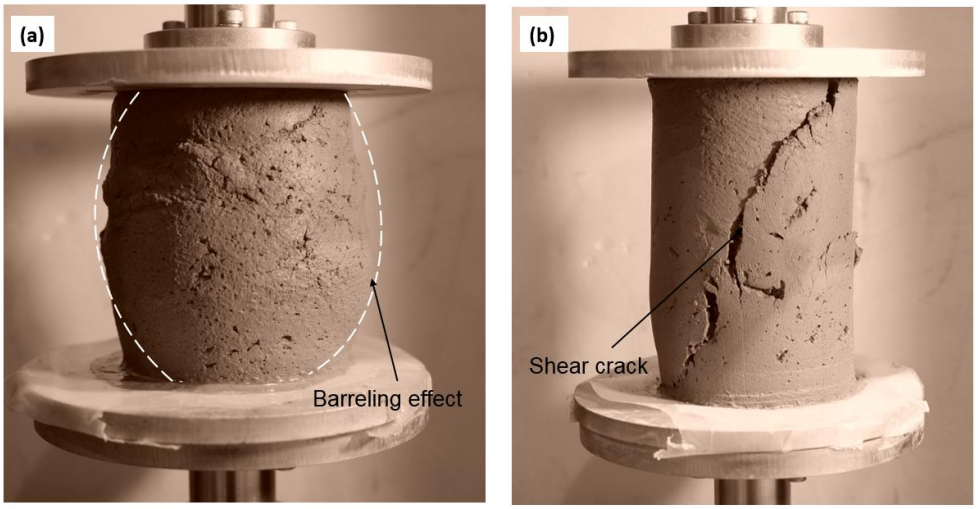

Figure 6.26 Typical failure modes of fresh cement mortar at (a) t = 30 min (b) 150 min

The compressive green strength was defined for each test as the maximum occurring stress after area correction and later, it was compared with yield stress of control mix obtained from the rheology test. Figure 6.27 shows the comparative results of green strength and static yield strength of control mix mortar at different time intervals ranging from 0-150 mins. It is clear that the yield stress evolution with time can be considered as linear for initial 30-40 mins and then it exponentially increases which can be explained based on Roussel linear model and Perrot et al. model [181]. In the early age (dormant period), yield stress of cementitious material increases linearly with time due to flocculation and C-S-H bridging [136], however after the dormant period, hydration occurs at faster rate due to ongoing chemical reaction which is reflected in terms of exponential rise of static yield stresses. Similar to yield strength evolution, green strength also increased with time, which was as expected for thixotropic fluids.

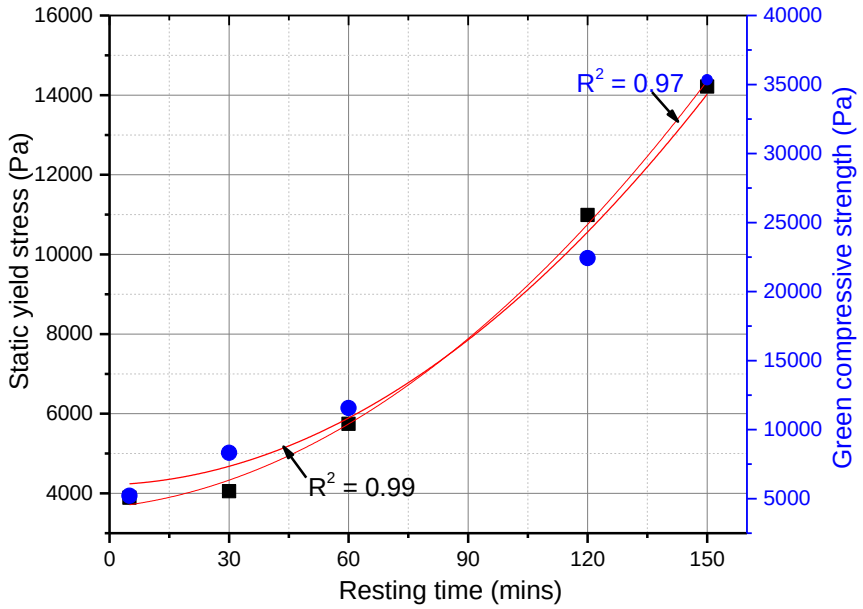

Figure 6.27 Co-relation between yield stress and green strength of the control mix

6.4.2 Strength based stability of the layers

Following the green strength measurement, the F-d curve was translated into stress-strain curve to obtain the young's modulus. An optics-based method was used to measure vertical and lateral deformation (See Chapter 3), since the fresh concrete was very sensitive to deformation by any kind of physical attachment of measuring devices. The newly measured deformation was used to calculate true stress and strain and the outcome is shown in Figure 6.28. Figure 6.28 (a) shows the load vs deformation curves for both control and modified HVFA mixes which were converted to stress-strain diagram in Figure 6.28(b) after cross section area correction as described in section 3.3.4. The slope of the curve represents stiffness (Young's modulus "E") of material, indicating the modified mix (E = 0.06 MPa) has higher stiffness compare to control mix (E = 0.03 MPa) and therefore, it is expected resist more deformation by the loads of layers on top of it.

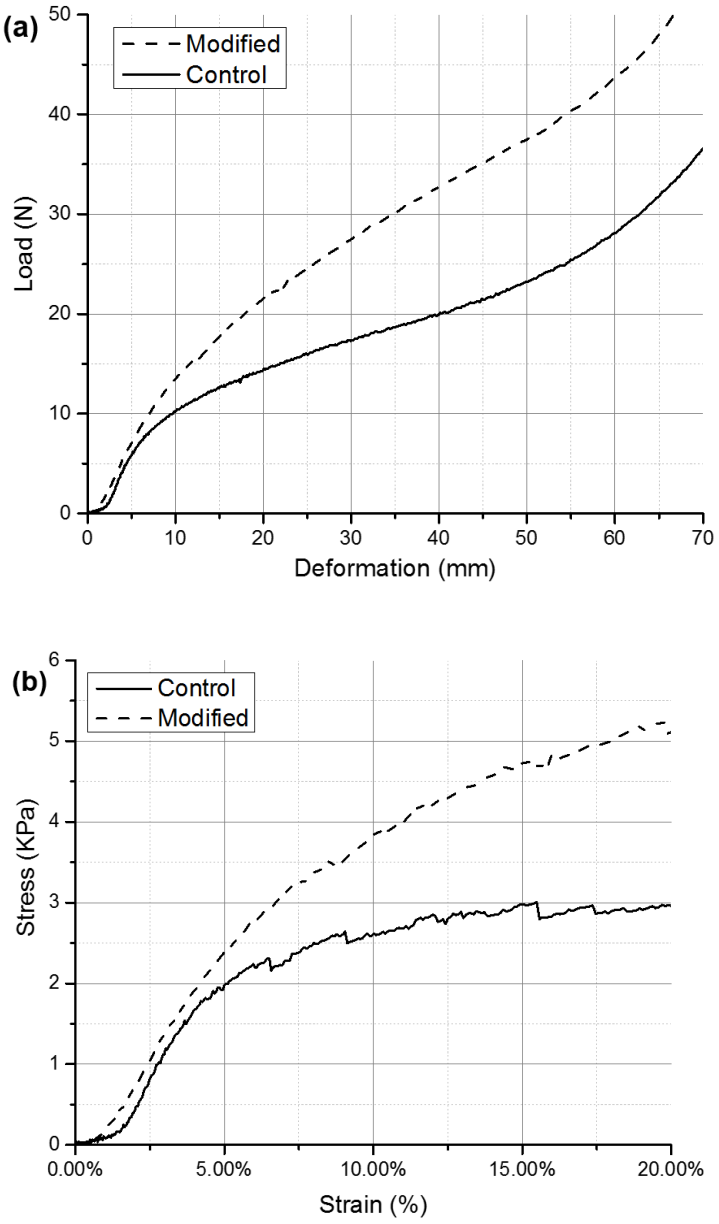

Figure 6.28 (a) Load-deformation (b) stress-strain curves of control and modified HVFA mixes

The effect of high stiffness property of modified mix is reflected in Figure 6.29, and it is very clear that the control mix material under goes elastic deformation after deposition of few layers and suddenly the bottom layer experienced plastic deformation which caused the entire structure to collapse before placing of the 10th layer. On the other hand,

the modified mix printed successfully up to 20 layers with very slow elastic deformation and on the placement of 21st layer, the whole structure started to collapse due to similar plastic deformation of the bottom layer.

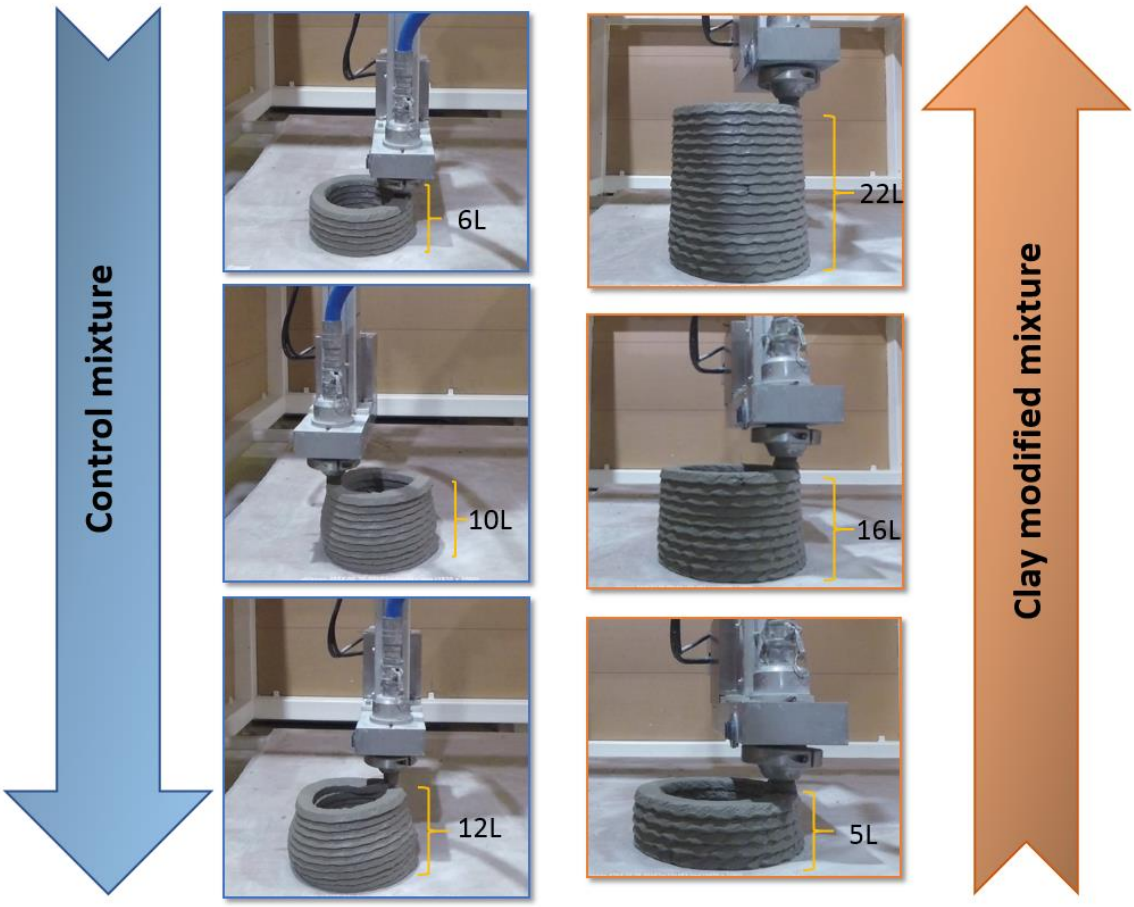

Figure 6.29 Progressive buildability performance of control (left) and modified HVFA mixes (right)

In light of above results, it is thus conformed that the layer deformation during concrete printing is an indication of low stiffness of material, which has been improved in this study by adding NC and SF to the control HVFA mortar. Two competing time dependent processes determine structural failure of a printed object: (1) the increasing green strength and (2) stiffness by thixotropy. The role of NC for improving the early age mechanical properties can be thought of due to flocculation or thixotropy effect, which has been already discussed in Chapter 4.

6.4.3 Design and demonstration of 3D printed portable toilet unit

In order to print 3DCP structure, a portable toilet was designed and manufactured in this study using the 3D printing facility of the NTU, Singapore. Despite the capability to print large scale structures, design of the toilet unit was challenging due to maximum height limit of the 3D printer. The first conceptual design of the toilet is shown in Figure 6.30, which spans 1030 mm long and 1800 mm tall. The total build height was out of the print box and therefore, it was decided to print the full structure in multiple sections that can be later assembled on the construction site.

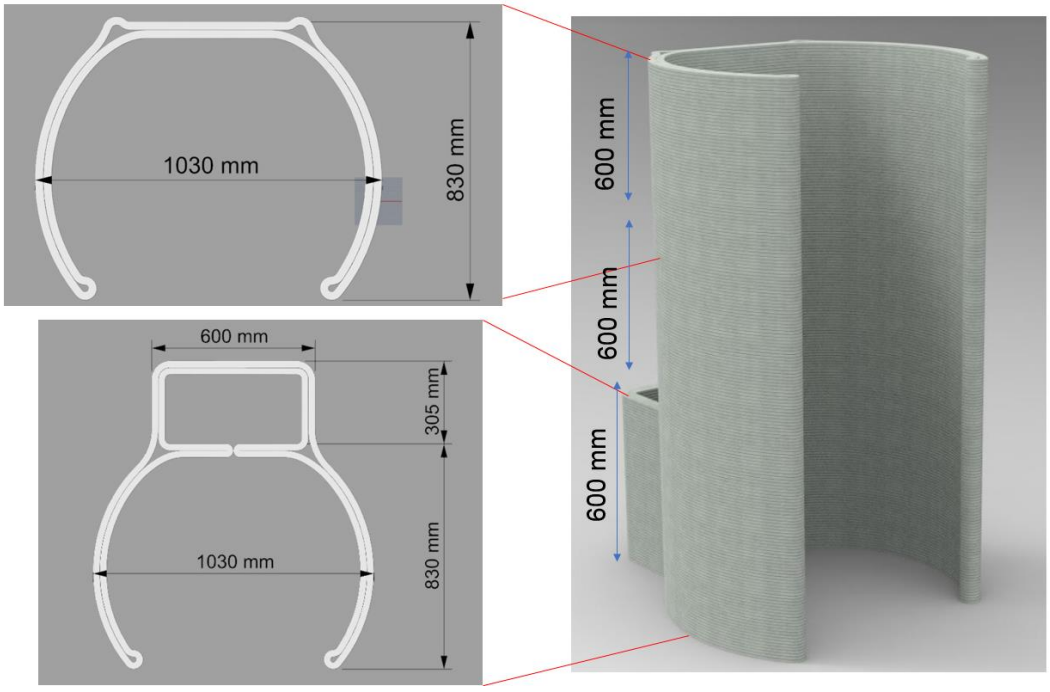

Figure 6.30 Initial design of portable toilet using modified HVFA mortar

The modified HVFA mortar was used to print the toilet and a small calculation was done using Eq. (3) to find the allowable buckling limit [136] the structure.

$$H_C = \sqrt[3]{\frac{2Ew^2}{3\rho g}} \quad (3)$$

where E is the elastic modulus of the material, ρ is the density of fresh mortar and w is the width of the extruded filament. To verify the estimated limit, the toilet was printed up to 22 layers, but unfortunately, no buckling effect was observed which underestimates the results reported in another study [136]. This observation can be explained because of geometry/shape effect of the toilet that allows higher inertia for same material volume. An example supporting this fact is shown in Figure 6.31, which was originally designed by contour crafting systems and now mostly used in 3D printing wall elements.

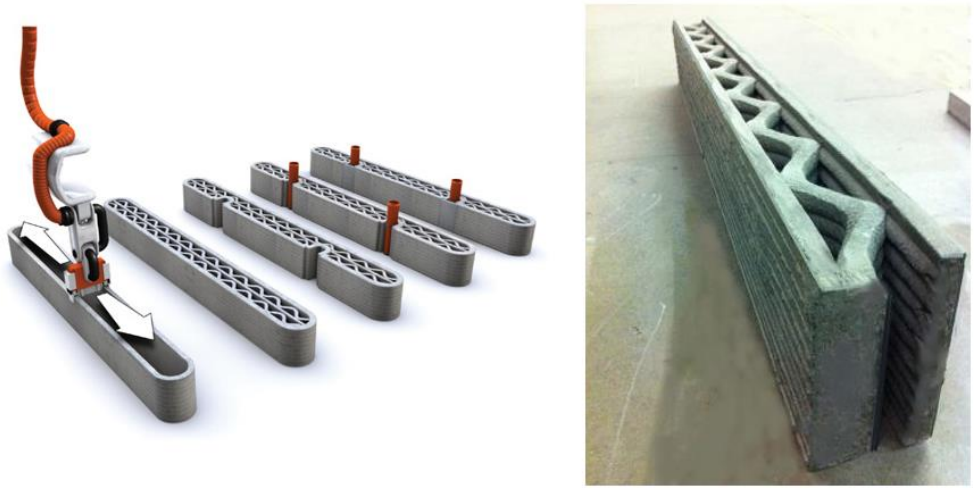

Figure 6.31 The shape adopted by (a) conprint3D and (b) contour crafting to enhance the buckling effect [154,7]

After deposition of 48 layers, the vertical wall found to be collapsed side wise and such failure was initially thought to be a structural failure. However, a close look at the bottom layer cross section area revealed small deformation (squeezed layer) which could be due to the insufficient green strength of the material. Due to lack of required strength, the bottom layer might have supressed causing instability in the structure and when more layers were deposited it collapsed in buckling. It was very difficult to identify the proper failure mechanism as the phenomena was instantaneous and was not recorded for

analysis. Therefore, the toilet was divided in to three parts, each consisting 48-50 layers (approx. 600 mm each) while understanding the maximum build height limit. The corner radius was maintained at 60 mm as it was found to be smooth and crack free in the previous section. Print speed and pump flow rate was maintained at 80 mm/sec and 0.83 lit/sec.

With these above settings, finally the three parts of the toilet were successfully printed and assembled as shown in Figure 6.32. However, for the ease of logistics, there was no material in the interface between the three parts for adhesion. Only after installation, cement grout was used to join it, with additional decoration features such as solar lamp, roof and the door. The cement grout was made by mixing PC with 40% tap water and injected into the joints using a grout gun. After 24 hours of ambient curing, steel frames carrying PVC roof system were inserted from top of the toilet. A semi flexible solar panel (30W,12V) was installed on the roof top by fastener and bolts for providing lighting facility in remote rural areas.

Figure 6.32 Snapshots of 3D concrete printed modular toilet unit

6.5 Early age mechanical properties and large-scale printing of geopolymer mortar

The early age mechanical strength of one-part geopolymer was analysed for concrete age t = 5 to 60 mins and results are shown in Figure 6.33(a). Due to rapid hardening properties, a distinct shear failure was noted to be around 60 minutes which is confirmed from the deformation image under uniaxial compression test (Figure 6.33(b)).

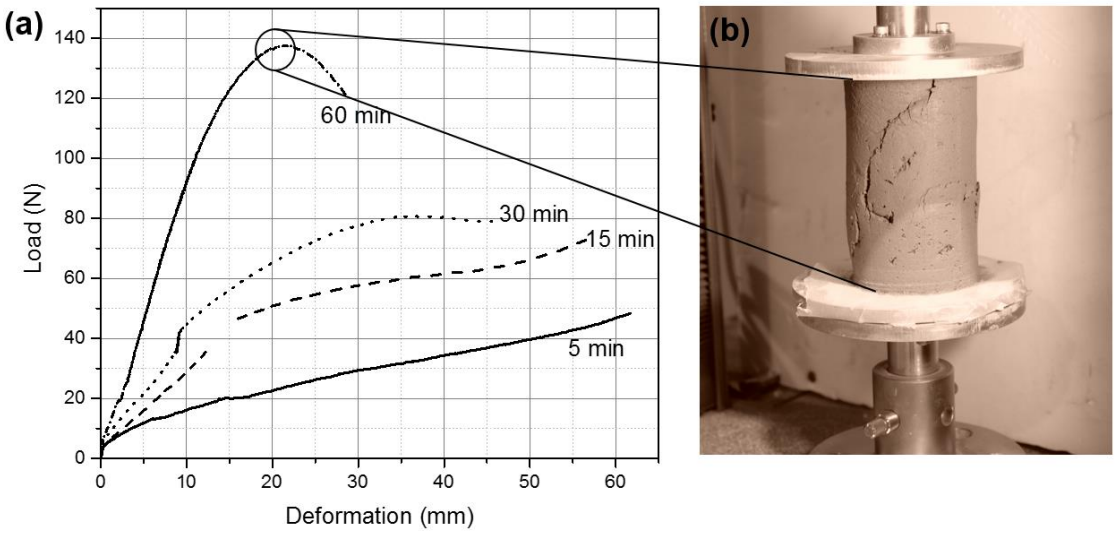

Figure 6.33 (a) Load - deformation relationship of fresh geopolymer mortar (b) Shear failure of fresh geopolymer mortar at age t= 60 mins

For stiffness (E) calculation, the 5-minutes load-deformation graph was first converted in to stress-strain plot (Figure 6.34) that indicates the material resistance to deformation in the fresh stage. The E-value of the one-part mix was found to be 1.06 MPa, which is 17 times higher than the modified HVFA mortar. Such significant increase in stiffness will allow more layers during 3DCP without deforming the bottom layers. Since one-part geopolymer contains higher amount of angular GGBS particles, it seems that internal friction or cohesion of the material mostly influences the green strength via interlocking of the particles. Similar phenomenon was also observed in another study by Hüsken and

Brouwers, where angular quartz flour lead to maximum green strength due to interlocking effect when compared with spherical FA particles. The study also concluded that the green-strength of a fresh concrete is a result of internal friction and adhesive forces, among which internal friction has a larger impact than adhesive forces.

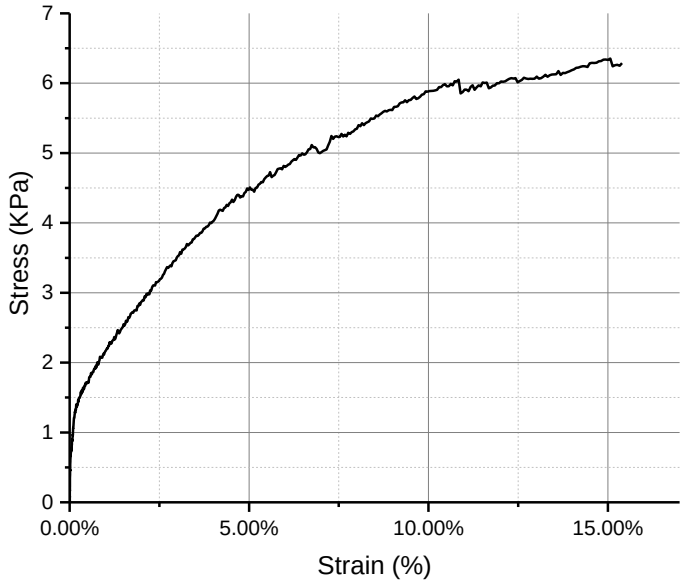

Figure 6.34 Stress-strain relationship of fresh geopolymer mortar for t = 5 mins

Despite higher E value, rapid structural build-up of geopolymer limited the material usages for large scale printing. The use of batch mixing leads us to re-design the part possible 3D printing within 60 minutes from mixing geopolymer with the activator. The modified part design is shown in Figure 6.35, where the total height remains same (i.e 1800 mm) except the changes in length and width of the part.

Unlike HVFA mortar, structural build-up of the geopolymer was noted to be much faster and therefore, the full height was divided into two parts only: each 900 mm length based on maximum height of the 3D printer. The decision of splitting was never based on material buildable limit since the one-part geopolymer exhibits much higher stiffens

compared to HVFA mortar and due to rapid chemical reaction, it can harden faster thus eliminating the fear of buckling (structural) failure as reported in few recent publications.

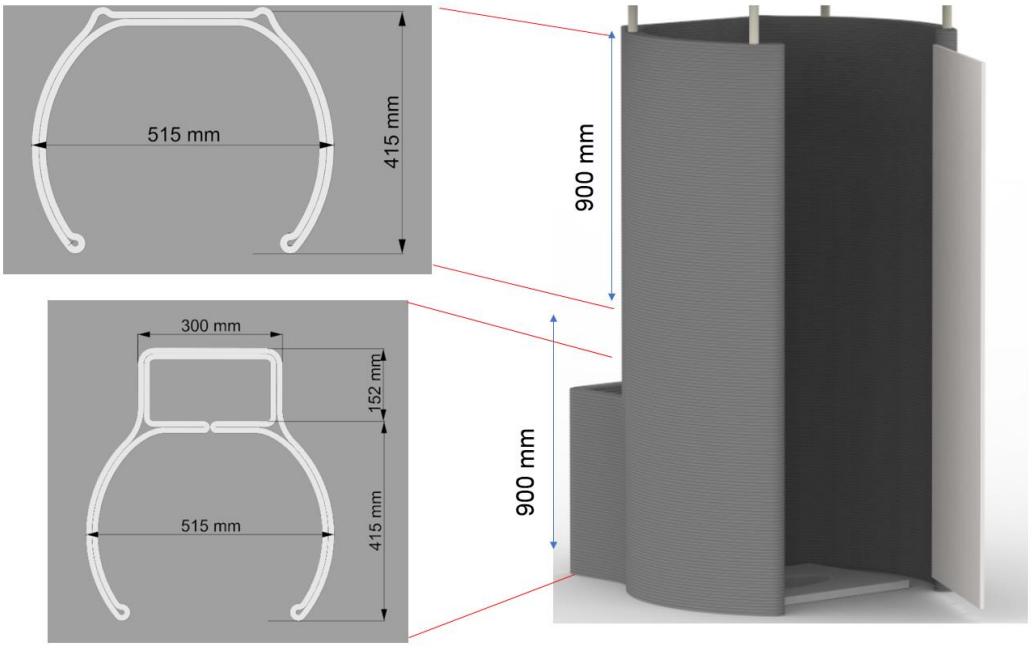

Figure 6.35 Re-design sketch of the toilet unit for geopolymer 3D printing

Finally, as a word of caution before generalizing the results of the present study, it is important to note that the suitability of the proposed part design for large-scale 3D printing and test methods to understand material early age behaviour are strongly dependent on the chemical composition of the mixture and equipment (material delivery system, 3D printer build volume) used to measure the properties. Any change in either of these may result in different conclusions and accordingly, material design can be benchmarked for the target application.

6.6 Conclusions

This study investigated the effects of process parameters and directional mechanical properties of 3D-printed mortars. The key findings are as follows:

- Although 3D printing seems to imply that any digital design can be produced independent of process planning, this does not apply for extrusion based 3DCP. There are several limitations in terms of manufacturing constraints (i.e. due to material behavior) that are not included in commercial CAD software. An interdependent relationship between process parameters, material and part design was found, which was even more pronounced for different material formulations.

- The filament thickness was influenced by the proper selection of print speed and flow rate, whereas there was a need for minimum radius of curvature with proper speed and layer height to avoid the outer edge cracking or excess material deposition at the corners.

- The 3D printed samples exhibited anisotropic mechanical properties due to the layer wise deposition of concrete filaments. This layering effect was found to be more significant in flexure and tension, however in compression, the final strength was almost equal to the strength of cast samples. The printed samples were also affected by the time gap allowed between each layer.

- Observations on the large scale 3DCP indicated that depending on material properties, the design of each part needs to be tailored for maximizing the benefits of 3D printing. A low viscous (thixotropic) and fast-setting printable concrete would be an ideal choice for large-scale concrete printing projects.

Chapter 7 Conclusions and suggestions for future work

7.1 Conclusions

The overall aim of this research was to design and evaluate 3D-printable fly ash (FA) based sustainable binders through a detailed investigation of rheological responses that are influential in ensuring extrudability and buildability. This was performed via formulating two different binders involving fly ash-cement and geopolymers; and investigating the effects of key parameters such as mix design, process parameter and part design. The conventional mix designs were amenable to extrusion-based 3D printing via the modification of their rheology through the use of viscosity modifying agent (VMA) or a combination of VMA and supplementary cementing materials (SCMs). The prepared mixtures were proportioned to improve the thixotropy (i.e. structural breakdown and recovery) and structural build-up rates essential for large scale 3D concrete printing (3DCP). The hydration process was analyzed via the use of isothermal calorimetry. The compressive, flexural and tensile strength measurements were executed to assess the mechanical performance of the modified mix designs. Additionally, microstructural analysis was performed via XRD and FESEM to study the changes in sample structure and composition.

The main conclusions drawn from the performed study are elaborated in the following sections:

7.1.1 Rheological requirements for 3D printable fly ash-cement mortar

(a) Based on experimental findings reported in the Chapter 4, the high-volume fly ash-cement (HVFA) mortar is a printable material. Due to thixotropic property of Portland cement (PC), the resultant mixture of FA and PC is easily extrudable with high shape retention property. In fact, the use of high-volume of FA makes the material more flowable without the need of any superplasticizer.

(b) The main challenge of the HVFA material was the slow (early-age) strength development that limits the buildability of the printed structures. Therefore, a very small amount (< 1%) of nanoclay (NC) was added to improve the early-age mechanical properties via enhancing the thixotropy at microstructure level. The effects of NC on thixotropy was tested for the first time with different shear rates and shearing time and it was found that compared to the control, the NC added mix has the potential to stabilize the viscosity recovery even after strong shearing for a longer time. Nevertheless, the effect of NC was not significant in increasing the strength gain rate (structural build-up), which is more controlled by the hydration reaction.

(c) To increase structural build up rate and avoid strength-based part failure, silica fume (SF) was further added to the NC modified mixture by replacing 0-5% of the FA while keeping the water-to-binder ratio constant. The addition of SF accelerates cement hydration attributed to the enhanced heterogeneous nucleation of the main hydration product, i.e. C−S−H, on the extra surfaces provided by SF. The synergetic effects of the NC and SF were found to be improve both early age mechanical properties and strength development rate, which is one of the required properties of 3D printable materials.

(d) In order to demonstrate the proposed criteria and mix design are suitable in practice, a large-scale printing was carried out using the final modified HVFA mortar. The mechanical property of the modified mix was found to be notably higher than the control mix, due to formation of pozzolanic C−S−H by SF reaction with portlandite present in the system.

7.1.2 Rheological requirements for 3D printable geopolymer mortar

(a) Unlike HVFA mortar, FA based geopolymer does not possess thixotropic behaviour due to lack to colloidal interactions and the rheological response was found to be very complex. Therefore, a series of mixtures that are amenable for 3D printing were developed through the use of SCMs and VMA including slag, SF and NC.

(b) When alkaline activators were used in lieu of water, the yield stress of the geopolymer mortar decreased, and the cohesiveness increased, similar to the use of a superplasticizer in conventional PC systems. The yield stress and viscosity was observed to increase with molar ratio (MR) following the change in activator viscosity with MR. Experiments on activator-to-solids ratio shows that the resultant viscosity of geopolymer is strongly influenced by the viscosity of activator solution whereas yield stress is more controlled by particle packing and in this regard, addition of SF was found to increase the yield stress which is reflected in the improved shape retention of the extruded filaments. SF can improve the flow properties by improving the particle packing of the constituents due to finer size and 10% SF was noted to be the optimum dosage to satisfy extrudability.

(c) Due to limited buildability of the SF modified geopolymer, NC was introduced in the mix design for the first time to improve the thixotropic property. The effect of clay addition changed significantly, based on water-to-solid ratio and activator-to-binder ratio used to produce geopolymer binders. Increasing the activator dosage was found to nullify the thixotropy effect of the clay, and in this regard, activator-to-binder ratio 0.35 and water-to-solid ratio 0.30 were found to be an optimum combination at 0.5% (mass of binder) clay addition.

(d) Powder-based activator was also used in this study for the first time to formulate printable geopolymer, so called one-part geopolymer. The rheological performance of one-part geopolymer was similar to HVFA mortar, which is completely different from conventional (liquid based) geopolymer. Therefore, this mix design was used in large scale printing with some modification in the part design. The modification was done in accordance with structural build rate of the geopolymer which is much faster than HVFA mortar. However, due to incomplete dissolution of silica from the powder silicate, the 28 days compressive strength was found to be reduced, which is further confirmed by FTIR analysis.

7.1.3 Mechanical properties of 3D printed mortars

(a) The mechanical property of the 3D printed mortar is not only an outcome of material used but also affected by the printing parameters. A well printed structure with proper *nozzle size*, *print speed* and *material selection* can result compressive strength similar to casted specimens. However, the influence of loading direction is more significant in flexural and tensile test.

(b) Inter-layer bond properties which is unique of 3DCP, was found to be notably affected by thixotropy of the material and the time gap between the layers. The average bond strength of printed samples was noted ~80% of the casted strength depending on the material build up rate and viscosity of interstitial fluid, that control the moisture loss from the surface. Due to viscous nature of liquid silicate, higher bond strength was observed in geopolymer compared to the HVFA mortar.

Finally, as a word of caution before generalizing the results of the present study, it is important to note that the suitability of the proposed test methods to characterize printable materials depend on the chemical composition of the mixture and equipment used to

measure the properties. Any change in either of these may result in different conclusions and accordingly, the material design can be tailored for 3DCP application.

7.2 Recommendations

The civil engineering is facing today a digital transformation linked to the implementation of different digital technologies including 3DCP. Despite the continuous progress, there are still no official standards for the assessment of 3D printed structures. This will certainly hinder the widespread application at a larger scale and hopefully; the findings and recommendations of this work will able to solve some of the important issues of 3DCP that need to be addressed in the future work.

(a) Many of the previous studies focuses on PC based binder while formulating printable mixtures and only a few recent journal articles involve the use of geopolymer in their mix compositions. The research direction of future studies should be towards the utilization of more sustainable materials (printable) in building applications. To maximize the benefit of rapid hardening like geopolymer, an in-line or continuous delivery system should be used instead of batch mixing, where the material can be mixed and deposit simultaneously. This will eliminate the difficulties in pumping due to change in material stiffness with time.

(b) Despite the need of high thixotropic material in 3DCP, pumping was found to be challenging for highly thixotropic NC and SF modified mix design. Therefore, the current mix design (blue line) can be further improved with addition of polycarboxylate ether superplasticizer (PCE), which will help in pumping via decreasing the dynamic yield stress and after deposition, the NC can effectively increase the yield stress by agglomerating the microstructure (flocculation). A schematic diagram for such material modification (red line) is shown in Figure

7.1. The thixotropy of such modified formulation can be analysis with "*characteristic time"* parameter, which is not considered in this thesis.

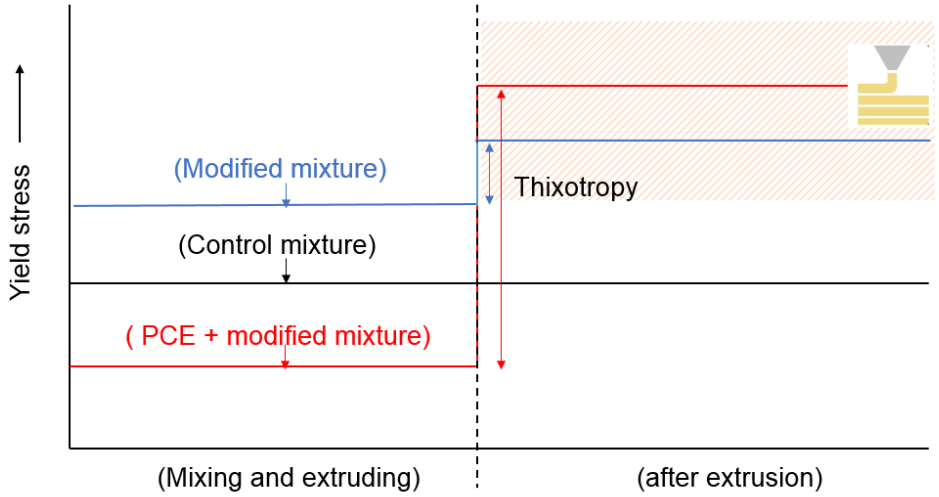

Figure 7.1 Schematic of material modification for extrusion-based 3DCP. Note that the shaded area is favorable for 3DCP after filament deposition.

(c) Since the time gap between the layers is a critical parameter in 3DCP process, there is a need of estimating a "critical time gap" considering thixotropy and thickness of the deposited layers. The critical time gap will allow to deposit the layers without causing cold joint problems which is reported in many published and unpublished literatures. Moreover, the effects of material compositions can be studied in future with different time gap and curing ages to reveal more information on the interface properties.

(d) Compared to the liquid activator, 3D printing of powder based geopolymer had reduced mechanical strength due to incomplete dissolution of silicate in ambient temperature. Future work can be carried out to enhance the solubility of powder activator by pre-heating it just before mixing with the binders. In addition, the anisotropic mechanical property of the printed concrete can be modelled to

understand the deformation and fracture properties under different loading conditions and able to optimize where necessary.

(e) The findings presented in this study have shown that the 3D printed mortars are not suitable for structural applications due to lack of ductile failure behaviour. Despite of recent approaches to increase the ductility of printed concrete by the use of microfiber, metal cable, post-tensioning rebars, the future application could be producing different fiber distribution in different layers, following the principle of functionally graded materials (FGM). 3D printing of FGMs would optimize the material usage and provide multi-functionally features for structural applications in building construction.

The obtained results so far have established a pathway towards understanding the 3D printability of fly ash based sustainable materials and continuation of this research in the directions listed above will enable the end users to adopt a new digital technology, so called 3D concrete printing, with lower environmental impacts and better productivity.

References

1. Pierre-Claude Aïtcin and Robert J. Flatt. (2016) Science and technology of concrete admixtures. Woodhead Publishing. Amsterdam. Hardcover ISBN: 9780081006931
2. De Schutter G., Bartos P., Domone P., Gibbs J. (2008) Self-Compacting Concrete, Whittles
3. Publishing, Caithness, UK, CRC Press, Taylor & Francis Group, Boca Raton, USA, ISBN 978-1904445-30-2, USA ISBN 978-1-4200-6833-7, pp. 296.
4. Clarkson H. Oglesby, Parker, H. W., & Howell, G. A. (1989). Productivity improvement in construction. McGraw-Hill.
5. Wu, P., Wang, J., & Wang, X. (2016). A critical review of the use of 3-D printing in the construction industry. Automation in Construction, 68, 21-31.
6. Chua, C. K., & Leong, K. F. (2014). 3D Printing and Additive Manufacturing: Principles and Applications of Rapid Prototyping. Fourth Edition. World Scientific Publishing Company.
7. [Online]. Available www.contourcrafting.com, Accessed date: 5 February 2019.
8. Panda, B., Tay, Y. W. D., Paul, S. C., & Tan, M. J. (2018). Current challenges and future potential of 3D concrete printing: Aktuelle Herausforderungen und Zukunftspotenziale des 3D-Druckens bei Beton. Materialwissenschaft und Werkstofftechnik, 49(5), 666-673.
9. De Schutter, G., Lesage, K., Mechtcherine, V., Nerella, V. N., Habert, G., & Agusti-Juan, I. (2018). Vision of 3D printing with concrete—technical, economic and environmental potentials. Cement and Concrete Research.
10. Rahul, A. V., Santhanam, M., Meena, H., & Ghani, Z. (2019). 3D printable concrete: Mixture design and test methods. Cement and Concrete Composites, 97, 13-23.
11. [Online]. Available www.apis-cor.com, Accessed date: 5 February 2019
12. [Online]. Available http://www.winsun3d.com, Accessed date: 5 February 2019
13. WBCSD, (2002). The cement sustainability initiative, our agenda for action. Geneva: World Business Council on Sustainable Development.
14. Duxson, P., & Van Deventer, J. S. J. (2009). Commercialization of geopolymers for construction–opportunities and obstacles. In Geopolymers (pp. 379-400). Woodhead Publishing.
15. Bakharev, T., Sanjayan, J. G., & Cheng, Y. B. (1999). Alkali activation of Australian slag cements. Cement and Concrete Research, 29(1), 113-120.
16. Rashad, A. M., Bai, Y., Basheer, P. A. M., Collier, N. C., & Milestone, N. B. (2012). Chemical and mechanical stability of sodium sulfate activated slag after exposure to elevated temperature. Cement and Concrete Research, 42(2), 333-343.
17. Mahaut, F., Mokeddem, S., Chateau, X., Roussel, N., & Ovarlez, G. (2008). Effect of coarse particle volume fraction on the yield stress and thixotropy of cementitious materials. Cement and concrete research, 38(11), 1276-1285.

18. Ravina, D., & Mehta, P. K. (1986). Properties of fresh concrete containing large amounts of fly ash. Cement and Concrete Research, 16(2), 227-238.
19. ASTM C618. (2003) Standard specification for coal fly ash and raw or calcined natural pozzolan for use in concrete. American society for testing and materials. West Conshohocken, PA, USA: ASTM International.
20. Malhotra, V. M. (1990). Durability of concrete incorporating high-volume of low-calcium (ASTM Class F) fly ash. Cement and Concrete Composites, 12(4), 271-277.
21. Griffin, C (2005). Sustainability, Performance and mix design of high-volume fly ash concrete', PhD Thesis, University of California, Berkeley.
22. Gjorv, O., & Sakai, K. (2014). Concrete technology for a sustainable development in the 21st century. CRC Press.
23. Meyer, C. (2009). The greening of the concrete industry. Cement and concrete composites, 31(8), 601-605.
24. Shannag, M. J., & Yeginobali, A. (1995). Properties of pastes, mortars and concretes containing natural pozzolan. Cement and Concrete Research, 25(3), 647-657.
25. Záleská, Martina, Milena Pavlíková, Zbyšek Pavlík, Ondřej Jankovský, Jaroslav Pokorný, Vratislav Tydlität, Petr Svora, and Robert Černý (2018). Physical and chemical characterization of technogenic pozzolans for the application in blended cements. Construction and Building Materials, 160, 106-116.
26. Targan, Ş., Olgun, A., Erdogan, Y., & Sevinc, V. (2003). Influence of natural pozzolan, colemanite ore waste, bottom ash, and fly ash on the properties of Portland cement. Cement and Concrete Research, 33(8), 1175-1182.
27. Naik, T. R., Singh, S. S., & Hossain, M. M. (1995). Properties of high-performance concrete systems incorporating large amounts of high-lime fly ash. Construction and Building Materials, 9(4), 195-204.
28. Xu, G., & Shi, X. (2018). Characteristics and applications of fly ash as a sustainable construction material: A state-of-the-art review. Resources, Conservation and Recycling, 136, 95-109.
29. Hemalatha, T., & Ramaswamy, A. (2017). A review on fly ash characteristics–Towards promoting high volume utilization in developing sustainable concrete. Journal of cleaner production, 147, 546-559.
30. Chindaprasirt, P., Jaturapitakkul, C., & Sinsiri, T. (2007). Effect of fly ash fineness on microstructure of blended cement paste. Construction and Building Materials, 21(7), 1534-1541.
31. Chindaprasirt, P., Homwuttiwong, S., & Sirivivatnanon, V. (2004). Influence of fly ash fineness on strength, drying shrinkage and sulfate resistance of blended cement mortar. Cement and Concrete Research, 34(7), 1087-1092.
32. Chindaprasirt, P., Chotithanorm, C., Cao, H. T., & Sirivivatnanon, V. (2007). Influence of fly ash fineness on the chloride penetration of concrete. Construction and Building Materials, 21(2), 356-361.
33. Bouzoubaa, N., Zhang, M. H., Bilodeau, A., & Malhotra, V. M. (1997). The effect of grinding on the physical properties of fly ashes and a Portland cement clinker. Cement and concrete research, 27(12), 1861-1874.

34. Bouzoubaa, N., Zhang, M. H., Malhotra, V. M., & Golden, D. M. (1999). Blended fly ash cements a review. Materials Journal, 96(6), 641-650.
35. Kumar, S., Kumar, R., Alex, T. C., Bandopadhyay, A., & Mehrotra, S. P. (2007). Influence of reactivity of fly ash on geopolymerisation. Advances in Applied Ceramics, 106(3), 120-127.
36. Bentz, D. P., Ferraris, C. F., Galler, M. A., Hansen, A. S., & Guynn, J. M. (2012). Influence of particle size distributions on yield stress and viscosity of cement–fly ash pastes. Cement and Concrete Research, 42(2), 404-409.
37. Bentz, D. P., Ferraris, C. F., De la Varga, I., Peltz, M. A., & Winpigler, J. A. (2010). Mixture proportioning options for improving high volume fly ash concretes. International Journal of Pavement Research and Technology, 3(5), 234-240.
38. Grzeszczyk, S., & Lipowski, G. (1997). Effect of content and particle size distribution of high-calcium fly ash on the rheological properties of cement pastes. Cement and concrete research, 27(6), 907-916.
39. Chancey, R., (2008) Characterization of Crystalline and Amorphous Phases and Respective Reactivities in a Class F Fly Ash. Ph.D. Dissertation. The University of Texas at Austin, TX, pp. 887e890
40. Yan, K., Guo, Y., Ma, Z., Zhao, Z., & Cheng, F. (2018). Quantitative analysis of crystalline and amorphous phases in pulverized coal fly ash based on the Rietveld method. Journal of Non-Crystalline Solids, 483, 37-42.
41. Sakai, E., Miyahara, S., Ohsawa, S., Lee, S. H., & Daimon, M. (2005). Hydration of fly ash cement. Cement and Concrete Research, 35(6), 1135-1140.
42. Palomo, A., Grutzeck, M. W., & Blanco, M. T. (1999). Alkali-activated fly ashes: a cement for the future. Cement and concrete research, 29(8), 1323-1329.
43. Fernandez-Jimenez, A. M., Palomo, A., & Lopez-Hombrados, C. (2006). Engineering properties of alkali-activated fly ash concrete. ACI Materials Journal, 103(2), 106.
44. Dakhane, A., Tweedley, S., Kailas, S., Marzke, R., & Neithalath, N. (2017). Mechanical and microstructural characterization of alkali sulfate activated high volume fly ash binders. Materials & Design, 122, 236-246.
45. EPRI, 1991. Mechanistic Basis for Cementing Action. EPRI GS-7122, Project 2708e4.
46. Shaikh, F. U., & Supit, S. W. (2014). Mechanical and durability properties of high-volume fly ash (HVFA) concrete containing calcium carbonate (CaCO3) nanoparticles. Construction and building materials, 70, 309-321.
47. Shaikh, F. U. A., Supit, S. W. M., & Sarker, P. K. (2014). A study on the effect of nano silica on compressive strength of high-volume fly ash mortars and concretes. Materials & Design, 60, 433-442.
48. Hou, P. K., Kawashima, S., Wang, K. J., Corr, D. J., Qian, J. S., & Shah, S. P. (2013). Effects of colloidal nanosilica on rheological and mechanical properties of fly ash–cement mortar. Cement and Concrete Composites, 35(1), 12-22.
49. Owens, K. J., Bai, Y., Cleland, D., Basheer, P. A. M., Kwasny, J., Sonebi, M., ... & Gupta, A. (2010). Activation of high-volume fly ash pastes using chemical

activators. In Proceedings of 2nd International Conference on Sustainable Construction Materials and Technologies, Ancona (Italy).
50. Boakye, K. A., Adjaottor, A. A., Tagbor, T. A., & Adjei, D. (2017). Influence of Na2SO4 on the Mechanical Properties of High-Volume Calcined Clay Pozzolan Cement. American Journal of Mechanical and Materials Engineering, 1(3), 78-82.
51. Velandia, D. F., Lynsdale, C. J., Provis, J. L., & Ramirez, F. (2018). Effect of mix design inputs, curing and compressive strength on the durability of Na2SO4-activated high volume fly ash concretes. Cement and Concrete Composites, 91, 11-20.
52. Hanehara, S., Tomosawa, F., Kobayakawa, M., & Hwang, K. (2001). Effects of water/powder ratio, mixing ratio of fly ash, and curing temperature on pozzolanic reaction of fly ash in cement paste. Cement and Concrete Research, 31(1), 31-39.
53. Lam, L., Wong, Y. L., & Poon, C. S. (2000). Degree of hydration and gel/space ratio of high-volume fly ash/cement systems. Cement and Concrete Research, 30(5), 747-756.
54. Poon, C. S., Kou, S. C., Lam, L., & Lin, Z. S. (2001). Activation of fly ash/cement systems using calcium sulfate anhydrite (CaSO4). Cement and Concrete Research, 31(6), 873-881.
55. Siddique, R. (2004). Performance characteristics of high-volume Class F fly ash concrete. Cement and Concrete Research, 34(3), 487-493.
56. Wang, A., Zhang, C., & Sun, W. (2004). Fly ash effects: III. The microaggregate effect of fly ash. Cement and concrete research, 34(11), 2061-2066.
57. ACI Committee 308, (2001) Guide to Curing Concrete (ACI 308R-01). American Concrete Institute, Farmington Hills.
58. Almusallam, A. A. (2001). Effect of environmental conditions on the properties of fresh and hardened concrete. Cement and Concrete Composites, 23(4-5), 353-361.
59. Xue, B., Pei, J., Sheng, Y., & Li, R. (2015). Effect of curing compounds on the properties and microstructure of cement concretes. Construction and Building Materials, 101, 410-416.
60. Maltais, Y., & Marchand, J. (1997). Influence of curing temperature on cement hydration and mechanical strength development of fly ash mortars. Cement and concrete research, 27(7), 1009-1020.
61. Davidovits, Joseph, (2005) Geopolymer, green chemistry and sustainable development solutions: proceedings of the world congress geopolymer 2005. Geopolymer Institute.
62. Weng, L., & Sagoe-Crentsil, K. (2007). Dissolution processes, hydrolysis and condensation reactions during geopolymer synthesis: Part I—Low Si/Al ratio systems. Journal of Materials Science, 42(9), 2997-3006.
63. Sagoe-Crentsil, K., & Weng, L. (2007). Dissolution processes, hydrolysis and condensation reactions during geopolymer synthesis: Part II. High Si/Al ratio systems. Journal of materials science, 42(9), 3007-3014.
64. Komnitsas, K., & Zaharaki, D. (2007). Geopolymerisation: A review and prospects for the minerals industry. Minerals engineering, 20(14), 1261-1277.

65. Duxson, P., Provis, J. L., Lukey, G. C., Mallicoat, S. W., Kriven, W. M., & Van Deventer, J. S. (2005). Understanding the relationship between geopolymer composition, microstructure and mechanical properties. Colloids and Surfaces A: Physicochemical and Engineering Aspects, 269(1-3), 47-58.
66. Steins, P., Poulesquen, A., Diat, O., & Frizon, F. (2012). Structural evolution during geopolymerization from an early age to consolidated material. Langmuir, 28(22), 8502-8510.
67. Nazari, A., & Sanjayan, J. G. (2015). Synthesis of geopolymer from industrial wastes. Journal of Cleaner Production, 99, 297-304.
68. Leong, H. Y., Ong, D. E. L., Sanjayan, J. G., & Nazari, A. (2016). The effect of different Na2O and K2O ratios of alkali activator on compressive strength of fly ash based-geopolymer. Construction and Building Materials, 106, 500-511.
69. Provis, J. L., Palomo, A., & Shi, C. (2015). Advances in understanding alkali-activated materials. Cement and Concrete Research, 78, 110-125.
70. Provis, J. L., & Van Deventer, J. S. J. (2007). Geopolymerisation kinetics. 2. Reaction kinetic modelling. Chemical Engineering Science, 62(9), 2318-2329.
71. Provis, J. L. (2006). Modelling the formation of geopolymer (Doctoral dissertation), Department of Chemical and Biomolecular Engineering, The University of Melbourne, Victoria, Australia.
72. Duxson, P., Fernández-Jiménez, A., Provis, J. L., Lukey, G. C., Palomo, A., & van Deventer, J. S. (2007). Geopolymer technology: the current state of the art. Journal of materials science, 42(9), 2917-2933.
73. Hardjito, D., & Rangan, B. V. (2005). Development and properties of low-calcium fly ash-based geopolymer concrete. PhD thesis. Curtin University of Technology. Australia.
74. Bajza, A., Rouseková, I., & Živica, V. (1998). Silica fume–sodium hydroxide binding systems. Cement and concrete research, 28(1), 13-18.
75. Ng, C., Alengaram, U. J., Wong, L. S., Mo, K. H., Jumaat, M. Z., & Ramesh, S. (2018). A review on microstructural study and compressive strength of geopolymer mortar, paste and concrete. Construction and Building Materials, 186, 550-576.
76. Zhang, P., Zheng, Y., Wang, K., & Zhang, J. (2018). A review on properties of fresh and hardened geopolymer mortar. Composites Part B: Engineering.
77. Part, W. K., Ramli, M., & Cheah, C. B. (2015). An overview on the influence of various factors on the properties of geopolymer concrete derived from industrial by-products. Construction and Building Materials, 77, 370-395.
78. Qing-Hua, C., & Sarkar, S. L. (1994). A study of rheological and mechanical properties of mixed alkali activated slag pastes. Advanced Cement Based Materials, 1(4), 178-184.
79. Poulesquen, A., Frizon, F., & Lambertin, D. (2011). Rheological behavior of alkali-activated metakaolin during geopolymerization. Journal of Non-Crystalline Solids, 357(21), 3565-3571.
80. Termkhajornkit, P., & Nawa, T. (2004). The fluidity of fly ash–cement paste containing naphthalene sulfonate superplasticizer. Cement and concrete research, 34(6), 1017-1024.

81. Criado, M., Palomo, A., Fernández-Jiménez, A., & Banfill, P. F. G. (2009). Alkali activated fly ash: effect of admixtures on paste rheology. Rheologica Acta, 48(4), 447-455.
82. Palacios, M., Houst, Y. F., Bowen, P., & Puertas, F. (2009). Adsorption of superplasticizer admixtures on alkali-activated slag pastes. Cement and Concrete Research, 39(8), 670-677.
83. Burgos-Montes, O., Palacios, M., Rivilla, P., & Puertas, F. (2012). Compatibility between superplasticizer admixtures and cements with mineral additions. Construction and Building Materials, 31, 300-309.
84. Vance, K., Dakhane, A., Sant, G., & Neithalath, N. (2014). Observations on the rheological response of alkali activated fly ash suspensions: the role of activator type and concentration. Rheologica Acta, 53(10-11), 843-855.
85. Zhang, D. W., Wang, D. M., Liu, Z., & Xie, F. Z. (2018). Rheology, agglomerate structure, and particle shape of fresh geopolymer pastes with different NaOH activators content. Construction and Building Materials, 187, 674-680.
86. Collins, F. G., & Sanjayan, J. G. (1999). Workability and mechanical properties of alkali activated slag concrete. Cement and concrete research, 29(3), 455-458.
87. Laskar, A. I., & Bhattacharjee, R. (2011). Rheology of Fly-Ash-Based Geopolymer Concrete. ACI Materials Journal, 108(5).
88. Sathonsaowaphak, A., Chindaprasirt, P., & Pimraksa, K. (2009). Workability and strength of lignite bottom ash geopolymer mortar. Journal of Hazardous Materials, 168(1), 44-50.
89. Chen, Z., Li, J. S., Zhan, B. J., Sharma, U., & Poon, C. S. (2018). Compressive strength and microstructural properties of dry-mixed geopolymer pastes synthesized from GGBS and sewage sludge ash. Construction and Building Materials, 182, 597-607.
90. Shaikh, F. U. A. (2018). Effects of slag content on the residual mechanical properties of ambient air-cured geopolymers exposed to elevated temperatures. Journal of Asian Ceramic Societies, 6(4), 342-358.
91. Huseien, G. F., Mirza, J., Ismail, M., & Hussin, M. W. (2016). Influence of different curing temperatures and alkali activators on properties of GBFS geopolymer mortars containing fly ash and palm-oil fuel ash. Construction and Building Materials, 125, 1229-1240.
92. Yan, S., & Sagoe-Crentsil, K. (2012). Properties of wastepaper sludge in geopolymer mortars for masonry applications. Journal of environmental management, 112, 27-32.
93. Arnoult, M., Perronnet, M., Autef, A., & Rossignol, S. (2018). How to control the geopolymer setting time with the alkaline silicate solution. Journal of Non-Crystalline Solids, 495, 59-66.
94. Chen, X., Sutrisno, A., Zhu, L., & Struble, L. J. (2017). Setting and nanostructural evolution of metakaolin geopolymer. Journal of the American Ceramic Society, 100(5), 2285-2295.
95. Favier, A., Habert, G., Roussel, N., & de Lacaillerie, J. B. D. E. (2015). A multinuclear static NMR study of geopolymerisation. Cement and concrete research, 75, 104-109.

96. Chen, X., Sutrisno, A., & Struble, L. J. (2018). Effects of calcium on setting mechanism of metakaolin-based geopolymer. Journal of the American Ceramic Society, 101(2), 957-968.
97. Part, W. K., Ramli, M., & Cheah, C. B. (2015). An overview on the influence of various factors on the properties of geopolymer concrete derived from industrial by-products. Construction and Building Materials, 77, 370-395.
98. Al-Majidi, M. H., Lampropoulos, A., Cundy, A., & Meikle, S. (2016). Development of geopolymer mortar under ambient temperature for in situ applications. Construction and Building Materials, 120, 198-211.
99. Ma, C. K., Awang, A. Z., & Omar, W. (2018). Structural and material performance of geopolymer concrete: A review. Construction and Building Materials, 186, 90-102.
100. Ling, Yifeng. (2018) Proportion and performance evaluation of fly ash-based geopolymer and its application in engineered composites." PhD Thesis. Iowa State University, USA
101. Singh, B., Ishwarya, G., Gupta, M., & Bhattacharyya, S. K. (2015). Geopolymer concrete: A review of some recent developments. Construction and building materials, 85, 78-90.
102. Chindaprasirt, P., Chareerat, T., & Sirivivatnanon, V. (2007). Workability and strength of coarse high calcium fly ash geopolymer. Cement and concrete composites, 29(3), 224-229.
103. Palacios, M., Banfill, P. F., & Puertas, F. (2008). Rheology and setting of alkali-activated slag pastes and mortars: effect of organic admixture. ACI Materials Journal, 105(2), 140.
104. Živica, V., Palou, M., Kuzielová, E., & Žemlička, M. (2016). Super high strength metabentonite based geopolymer. Procedia Engineering, 151, 133-140.
105. Hardjito, D., Wallah, S. E., Sumajouw, D. M., & Rangan, B. V. (2004). Factors influencing the compressive strength of fly ash-based geopolymer concrete. Civil engineering dimension, 6(2), 88-93.
106. Park, S., & Pour-Ghaz, M. (2018). What is the role of water in the geopolymerization of metakaolin? Construction and Building Materials, 182, 360-370.
107. Pouhet, R., Cyr, M., & Bucher, R. (2019). Influence of the initial water content in flash calcined metakaolin-based geopolymer. Construction and Building Materials, 201, 421-429.
108. Tay, Y. W. D., Panda, B., Paul, S. C., Noor Mohamed, N. A., Tan, M. J., & Leong, K. F. (2017). 3D printing trends in building and construction industry: a review. Virtual and Physical Prototyping, 12(3), 261-276.
109. Perkins, I., & Skitmore, M. (2015). Three-dimensional printing in the construction industry: A review. International Journal of Construction Management, 15(1), 1-9.
110. Khoshnevis, B., Hwang, D., Yao, K. T., & Yeh, Z. (2006). Mega-scale fabrication by contour crafting. International Journal of Industrial and Systems Engineering, 1(3), 301-320.

111. Dini, E., 2009. D-SHAPE – The 21st century revolution in building technology has a name. p. 1–16.
112. Buswell, R. A., de Silva, W. L., Jones, S. Z., & Dirrenberger, J. (2018). 3D printing using concrete extrusion: a roadmap for research. Cement and Concrete Research.
113. Khoshnevis, B. (2004). Automated construction by contour crafting—related robotics and information technologies. Automation in construction, 13(1), 5-19.
114. Le, T. T., Austin, S. A., Lim, S., Buswell, R. A., Gibb, A. G., & Thorpe, T. (2012). Mix design and fresh properties for high-performance printing concrete. Materials and structures, 45(8), 1221-1232.
115. [Online]. Available www. totalkustom.com Accessed date: 5 February 2019.
116. Gosselin, C., Duballet, R., Roux, P., Gaudillière, N., Dirrenberger, J., & Morel, P. (2016). Large-scale 3D printing of ultra-high-performance concrete–a new processing route for architects and builders. Materials & Design, 100, 102-109.
117. Bos, F., Wolfs, R., Ahmed, Z., & Salet, T. (2018). Large scale testing of digitally fabricated concrete (DFC) elements. In RILEM International Conference on Concrete and Digital Fabrication (pp. 129-147). Springer, Cham.
118. [Online]. Available www. cybe.eu Accessed date: 5 February 2019.
119. IAAC, 2014. Minibuilders. Accessed date: 5 February 2019.
120. Zhang, X., Li, M., Lim, J. H., Weng, Y., Tay, Y. W. D., Pham, H., & Pham, Q. C. (2018). Large-scale 3D printing by a team of mobile robots. Automation in Construction, 95, 98-106.
121. Bos, F., Wolfs, R., Ahmed, Z., & Salet, T. (2016). Additive manufacturing of concrete in construction: potentials and challenges of 3D concrete printing. Virtual and Physical Prototyping, 11(3), 209-225.
122. Costanzi, C. B., Ahmed, Z. Y., Schipper, H. R., Bos, F. P., Knaack, U., & Wolfs, R. J. M. (2018). 3D Printing concrete on temporary surfaces: The design and fabrication of a concrete shell structure. Automation in Construction, 94, 395-404.
123. Ma, G., Wang, L., & Ju, Y. (2018). State-of-the-art of 3D printing technology of cementitious material—an emerging technique for construction. Science China Technological Sciences, 61(4), 475-495.
124. Panda, B & Tan, M. J, (2018) Material properties of 3D printable high-volume slag cement. In Proceeding of First International Conference on 3D Construction Printing (3DcP), Swinburne University of Technology, Australia
125. Khalil, N., Aouad, G., El Cheikh, K., & Rémond, S. (2017). Use of calcium sulfoaluminate cements for setting control of 3D-printing mortars. Construction and Building Materials, 157, 382-391.
126. Ma, G., Li, Z., & Wang, L. (2018). Printable properties of cementitious material containing copper tailings for extrusion-based 3D printing. Construction and building materials, 162, 613-627.
127. Liu, Z., Li, M., Weng, Y., Wong, T. N., & Tan, M. J. (2019). Mixture Design Approach to optimize the rheological properties of the material used in 3D cementitious material printing. Construction and Building Materials, 198, 245-255.

128. Zhang, Y., Zhang, Y., Liu, G., Yang, Y., Wu, M., & Pang, B. (2018). Fresh properties of a novel 3D printing concrete ink. Construction and building materials, 174, 263-271.
129. Paul, S. C., van Zijl, G. P., Tan, M. J., & Gibson, I. (2018). A review of 3D concrete printing systems and materials properties: Current status and future research prospects. Rapid Prototyping Journal, 24(4), 784-798.
130. Bentz, D. P., Jones, S. Z., Bentz, I. R., & Peltz, M. A. (2018). Towards the formulation of robust and sustainable cementitious binders for 3-D additive construction by extrusion. Construction and Building Materials, 175, 215-224.
131. Alghamdi, H., Nair, S. A., & Neithalath, N. (2019). Insights into material design, extrusion rheology, and properties of 3D-printable alkali-activated fly ash-based binders. Materials & Design, 107634.
132. Nair, S. A., Alghamdi, H., Arora, A., Mehdipour, I., Sant, G., & Neithalath, N. (2018). Linking fresh paste microstructure, rheology and extrusion characteristics of cementitious binders for 3D printing. Journal of the American Ceramic Society.
133. Kazemian, A., Yuan, X., Cochran, E., & Khoshnevis, B. (2017). Cementitious materials for construction-scale 3D printing: Laboratory testing of fresh printing mixture. Construction and Building Materials, 145, 639-647.
134. Nerella, V. N., Näther, M., Iqbal, A., Butler, M., & Mechtcherine, V. (2019). Inline quantification of extrudability of cementitious materials for digital construction. Cement and Concrete Composites, 95, 260-270.
135. Ketel, S., Falzone, G., Wang, B., Washburn, N., & Sant, G. (2018). A printability index for linking slurry rheology to the geometrical attributes of 3D-printed components. Cement and Concrete Composites.
136. Roussel, N. (2018). Rheological requirements for printable concretes. Cement and Concrete Research.112, 76-85.
137. Roussel, N., Ovarlez, G., Garrault, S., & Brumaud, C. (2012). The origins of thixotropy of fresh cement pastes. Cement and Concrete Research, 42(1), 148-157.
138. Qian, Y., & Kawashima, S. (2018). Distinguishing dynamic and static yield stress of fresh cement mortars through thixotropy. Cement and Concrete Composites, 86, 288-296.
139. Jiao, D., Shi, C., Yuan, Q., An, X., Liu, Y., & Li, H. (2017). Effect of constituents on rheological properties of fresh concrete-A review. Cement and Concrete Composites, 83, 146-159.
140. Yuan, Q., Zhou, D., Khayat, K. H., Feys, D., & Shi, C. (2017). On the measurement of evolution of structural build-up of cement paste with time by static yield stress test vs. small amplitude oscillatory shear test. Cement and Concrete Research, 99, 183-189.
141. Nerella, V. N., Beigh, M. A. B., Fataei, S., & Mechtcherine, V. (2019). Strain-based approach for measuring structural build-up of cement pastes in the context of digital construction. Cement and Concrete Research, 115, 530-544.

142. Wallevik, J. E. (2009). Rheological properties of cement paste: thixotropic behavior and structural breakdown. Cement and Concrete Research, 39(1), 14-29.
143. Khayat, K. H., Omran, A., & Al Magdi, W. (2012, December). Evaluation of thixotropy of self-consolidating concrete and influence on concrete performance. In Proceedings 3rd Iberian Congress on Self Compacting Concrete, Madrid (pp. 3-16).
144. Jarny, S., Roussel, N., Roy, R. L., & Coussot, P. (2008). Thixotropic behavior of fresh cement pastes from inclined plane flow measurements. Applied Rheology, 18(1), 14251.
145. Jarny, S., Roussel, N., Le Roy, R., & Coussot, P. (2008). Modelling thixotropic behavior of fresh cement pastes from MRI measurements. Cement and Concrete Research, 38(5), 616-623.
146. Reiter, L., Wangler, T., Roussel, N., & Flatt, R. J. (2018). The role of early age structural build-up in digital fabrication with concrete. Cement and Concrete Research.
147. Marchon, D., Kawashima, S., Bessaies-Bey, H., Mantellato, S., & Ng, S. (2018). Hydration and rheology control of concrete for digital fabrication: Potential admixtures and cement chemistry. Cement and Concrete Research.
148. Wolfs, R. J. M., Bos, F. P., & Salet, T. A. M. (2018). Early age mechanical behaviour of 3D printed concrete: Numerical modelling and experimental testing. Cement and Concrete Research, 106, 103-116.
149. Le, T. T., Austin, S. A., Lim, S., Buswell, R. A., Law, R., Gibb, A. G., & Thorpe, T. (2012). Hardened properties of high-performance printing concrete. Cement and Concrete Research, 42(3), 558-566.
150. Feng, P., Meng, X., Chen, J. F., & Ye, L. (2015). Mechanical properties of structures 3D printed with cementitious powders. Construction and Building Materials, 93, 486-497.
151. Tay, Y. W. D., Ting, G. H. A., Qian, Y., Panda, B., He, L., & Tan, M. J. (2019). Time gap effect on bond strength of 3D-printed concrete. Virtual and Physical Prototyping, 14(1), 104-113.
152. Paul, S. C., Tay, Y. W. D., Panda, B., & Tan, M. J. (2018). Fresh and hardened properties of 3D printable cementitious materials for building and construction. Archives of Civil and Mechanical Engineering, 18(1), 311-319.
153. Sanjayan, J. G., Nematollahi, B., Xia, M., & Marchment, T. (2018). Effect of surface moisture on inter-layer strength of 3D printed concrete. Construction and Building Materials, 172, 468-475.
154. Nerella, V. N., Hempel, S., & Mechtcherine, V. (2019). Effects of layer-interface properties on mechanical performance of concrete elements produced by extrusion-based 3D-printing. Construction and Building Materials, 205, 586-601.
155. Panda B., Noor Mohamed N.A., Tay Y.W.D., Tan M.J. (2019) Bond Strength in 3D Printed Geopolymer Mortar. In: Wangler T., Flatt R. (eds) First RILEM International Conference on Concrete and Digital Fabrication – Digital Concrete 2018. DC 2018. RILEM Bookseries, vol 19. Springer, Cham

156. Marchment, T., & Sanjayan, J. (2018, September). Method of Enhancing Interlayer Bond Strength in 3D Concrete Printing. In RILEM International Conference on Concrete and Digital Fabrication (pp. 148-156). Springer, Cham.
157. Zareiyan, B., & Khoshnevis, B. (2017). Effects of interlocking on interlayer adhesion and strength of structures in 3D printing of concrete. Automation in Construction, 83, 212-221.
158. Hambach, M., & Volkmer, D. (2017). Properties of 3D-printed fiber-reinforced Portland cement paste. Cement and Concrete Composites, 79, 62-70.
159. Ma, G., Li, Z., Wang, L., Wang, F., & Sanjayan, J. (2019). Mechanical anisotropy of aligned fiber reinforced composite for extrusion-based 3D printing. Construction and Building Materials, 202, 770-783.
160. Ogura, H., Nerella, V., & Mechtcherine, V. (2018). Developing and testing of strain-hardening cement-based composites (SHCC) in the context of 3D-printing. Materials, 11(8), 1375.
161. Soltan, D. G., & Li, V. C. (2018). A self-reinforced cementitious composite for building-scale 3D printing. Cement and Concrete Composites, 90, 1-13.
162. Nematollahi, B., Xia, M., Sanjayan, J., & Vijay, P. (2018). Effect of type of fiber on inter-layer bond and flexural strengths of extrusion-based 3D printed geopolymer. In Materials Science Forum (Vol. 939, pp. 155-162). Trans Tech Publications.
163. Weng, Y., Li, M., Liu, Z., Lao, W., Lu, B., Zhang, D., & Tan, M. J. (2018). Printability and fire performance of a developed 3D printable fibre reinforced cementitious composites under elevated temperatures. Virtual and Physical Prototyping, 1-9.
164. Weng, Y., Lu, B., Li, M., Liu, Z., Tan, M. J., & Qian, S. (2018). Empirical models to predict rheological properties of fiber reinforced cementitious composites for 3D printing. Construction and Building Materials, 189, 676-685.
165. Nematollahi, B., Vijay, P., Sanjayan, J., Nazari, A., Xia, M., Naidu Nerella, V., & Mechtcherine, V. (2018). Effect of Polypropylene Fibre Addition on Properties of Geopolymers Made by 3D Printing for Digital Construction. Materials, 11(12), 2352.
166. Bos, F. P., Bosco, E., & Salet, T. A. M. (2018). Ductility of 3D printed concrete reinforced with short straight steel fibers. Virtual and Physical Prototyping, 1-15.
167. Bos, F., Ahmed, Z., Jutinov, E., & Salet, T. (2017). Experimental exploration of metal cable as reinforcement in 3D printed concrete. Materials, 10(11), 1314.
168. Lim, J. H., Panda, B., & Pham, Q. C. (2018). Improving flexural characteristics of 3D printed geopolymer composites with in-process steel cable reinforcement. Construction and Building Materials, 178, 32-41.
169. [Online]. Available www. xtreee.eu, Accessed date: 5 February 2019
170. Pilehvar, S., Cao, V. D., Szczotok, A. M., Carmona, M., Valentini, L., Lanzón, M., & Kjøniksen, A. L. (2018). Physical and mechanical properties of fly ash and slag geopolymer concrete containing different types of micro-encapsulated phase change materials. Construction and Building Materials, 173, 28-39.

171. Fauzi, A., Nuruddin, M. F., Malkawi, A. B., & Abdullah, M. M. A. B. (2016). Study of fly ash characterization as a cementitious material. Procedia engineering, 148, 487-493.
172. Bhagath Singh, G. V. P., & Subramaniam, K. V. (2016). Quantitative XRD analysis of binary blends of siliceous fly ash and hydrated cement. Journal of Materials in Civil Engineering, 28(8), 04016042.
173. Singh, G. B., & Subramaniam, K. V. (2016). Quantitative XRD study of amorphous phase in alkali activated low calcium siliceous fly ash. Construction and Building Materials, 124, 139-147.
174. Islam, A., Alengaram, U. J., Jumaat, M. Z., & Bashar, I. I. (2014). The development of compressive strength of ground granulated blast furnace slag-palm oil fuel ash-fly ash based geopolymer mortar. Materials & Design (1980-2015), 56, 833-841.
175. Deb, P. S., Nath, P., & Sarker, P. K. (2014). The effects of ground granulated blast-furnace slag blending with fly ash and activator content on the workability and strength properties of geopolymer concrete cured at ambient temperature. Materials & Design (1980-2015), 62, 32-39.
176. Brady, J. F. (1993). The rheological behavior of concentrated colloidal dispersions. The Journal of Chemical Physics, 99(1), 567-581.
177. Mehdipour, I., & Khayat, K. H. (2018). Understanding the role of particle packing characteristics in rheo-physical properties of cementitious suspensions: a literature review. Construction and Building Materials, 161, 340-353.
178. Panda, B., & Tan, M. J. (2019). Rheological behavior of high-volume fly ash mixtures containing micro silica for digital construction application. Materials Letters, 237, 348-351.
179. Ouyang, J., Tan, Y., Corr, D. J., & Shah, S. P. (2016). The thixotropic behavior of fresh cement asphalt emulsion paste. Construction and Building Materials, 114, 906-912.
180. Roussel, N. (2006). A thixotropy model for fresh fluid concretes: theory, validation and applications. Cement and Concrete Research, 36(10), 1797-1806.
181. Perrot, A., Rangeard, D., & Pierre, A. (2016). Structural built-up of cement-based materials used for 3D-printing extrusion techniques. Materials and Structures, 49(4), 1213-1220.
182. Lichti, D. D., Jamtsho, S., El-Halawany, S. I., Lahamy, H., Chow, J., Chan, T. O., & El-Badry, M. (2011). Structural deflection measurement with a range camera. Journal of Surveying Engineering, 138(2), 66-76.
183. ASTM C1702-15a, Standard Test Method for Measurement of Heat of Hydration of Hydraulic Cementitious Materials Using Isothermal Conduction Calorimetry, ASTM Committee C01, West Conshohocken, PA United States, 2015, p. 8 19428-2959
184. BS EN 196-1, Methods of Testing Cement – Part 1: Determination of Strength, British Standards Institution, 2016.
185. Panda, B., Paul, S. C., & Tan, M. J. (2017). Anisotropic mechanical performance of 3D printed fiber reinforced sustainable construction material. Materials Letters, 209, 146-149.

186. ASTM C1583/C1583M-13, 2013. Standard test method for tensile strength of concrete surfaces and the bond strength or tensile strength of concrete repair and overlay materials by direct tension (pull-off method). West Conshohocken, PA: ASTM International
187. Panda, B., Ruan, S., Unluer, C., & Tan, M. J. (2019). Improving the 3D printability of high-volume fly ash mixtures via the use of nano attapulgite clay. Composites Part B: Engineering, 165, 75-83.
188. De Schutter, G., & Feys, D. (2016). Pumping of fresh concrete: insights and challenges. RILEM Technical Letters, 1, 76-80.
189. Feys, D., Khayat, K. H., & Khatib, R. (2016). How do concrete rheology, tribology, flow rate and pipe radius influence pumping pressure?. Cement and Concrete Composites, 66, 38-46.
190. Secrieru, E., Fataei, S., Schröfl, C., & Mechtcherine, V. (2017). Study on concrete pumpability combining different laboratory tools and linkage to rheology. Construction and Building Materials, 144, 451-461.
191. Krieger, I. M., & Dougherty, T. J. (1959). A mechanism for non-Newtonian flow in suspensions of rigid spheres. Transactions of the Society of Rheology, 3(1), 137-152.
192. Hafid, H., Ovarlez, G., Toussaint, F., Jezequel, P. H., & Roussel, N. (2016). Effect of particle morphological parameters on sand grains packing properties and rheology of model mortars. Cement and Concrete Research, 80, 44-51.
193. Yammine, J., Chaouche, M., Guerinet, M., Moranville, M., & Roussel, N. (2008). From ordinary rhelogy concrete to self-compacting concrete: A transition between frictional and hydrodynamic interactions. Cement and Concrete Research, 38(7), 890-896.
194. Wang, Q., Cui, X., Wang, J., Li, S., Lv, C., & Dong, Y. (2017). Effect of fly ash on rheological properties of graphene oxide cement paste. Construction and Building Materials, 138, 35-44.
195. Wangler, T., Lloret, E., Reiter, L., Hack, N., Gramazio, F., Kohler, M., & Flatt, R. (2016). Digital concrete: opportunities and challenges. RILEM Technical Letters, 1, 67-75.
196. Mettler, L. K., Wittel, F. K., Flatt, R. J., & Herrmann, H. J. (2016). Evolution of strength and failure of SCC during early hydration. Cement and Concrete Research, 89, 288-296.
197. Jiao, D., Shi, C., Yuan, Q., Zhu, D., & De Schutter, G. (2019). Effects of rotational shearing on rheological behavior of fresh mortar with short glass fiber. Construction and Building Materials, 203, 314-321.
198. Quanji, Z., Lomboy, G. R., & Wang, K. (2014). Influence of nano-sized highly purified magnesium alumino silicate clay on thixotropic behavior of fresh cement pastes. Construction and Building Materials, 69, 295-300.
199. Kawashima, S., Kim, J. H., Corr, D. J., & Shah, S. P. (2012). Study of the mechanisms underlying the fresh-state response of cementitious materials modified with nanoclays. Construction and Building Materials, 36, 749-757.
200. Tregger, N. A., Pakula, M. E., & Shah, S. P. (2010). Influence of clays on the rheology of cement pastes. Cement and concrete research, 40(3), 384-391.

201. Qian, Y., & De Schutter, G. (2018). Enhancing thixotropy of fresh cement pastes with nanoclay in presence of polycarboxylate ether superplasticizer (PCE). Cement and Concrete Research, 111, 15-22.
202. Cheng, D. C. (1986). Yield stress: a time-dependent property and how to measure it. Rheologica Acta, 25(5), 542-554.
203. Wang, X., Wang, K., Tanesi, J., & Ardani, A. (2014). Effects of nanomaterials on the hydration kinetics and rheology of Portland cement pastes. Advances in Civil Engineering Materials, 3(2), 142-159.
204. Benaicha, M., Roguiez, X., Jalbaud, O., Burtschell, Y., & Alaoui, A. H. (2015). Influence of silica fume and viscosity modifying agent on the mechanical and rheological behavior of self-compacting concrete. Construction and Building Materials, 84, 103-110.
205. Lu, C., Yang, H., & Mei, G. (2015). Relationship between slump flow and rheological properties of self-compacting concrete with silica fume and its permeability. Construction and Building Materials, 75, 157-162.
206. Chung, D. D. L. (2002). Improving cement-based materials by using silica fume. Journal of Materials Science, 37(4), 673-682.
207. Ardalan, R. B., Joshaghani, A., & Hooton, R. D. (2017). Workability retention and compressive strength of self-compacting concrete incorporating pumice powder and silica fume. Construction and Building Materials, 134, 116-122.
208. Meng, W., Lunkad, P., Kumar, A., & Khayat, K. (2016). Influence of silica fume and polycarboxylate ether dispersant on hydration mechanisms of cement. The Journal of Physical Chemistry C, 120(47), 26814-26823.
209. Mazloom, M., Ramezanianpour, A. A., & Brooks, J. J. (2004). Effect of silica fume on mechanical properties of high-strength concrete. Cement and Concrete Composites, 26(4), 347-357.
210. Singh, L. P., Goel, A., Bhattacharyya, S. K., & Mishra, G. (2016). Quantification of hydration products in cementitious materials incorporating silica nanoparticles. Frontiers of Structural and Civil Engineering, 10(2), 162-167.
211. Panda, B., Unluer, C., & Tan, M. J. (2018). Investigation of the rheology and strength of geopolymer mixtures for extrusion-based 3D printing. Cement and Concrete Composites, 94, 307-314.
212. Alonso, M. M., Gismera, S., Blanco, M. T., Lanzón, M., & Puertas, F. (2017). Alkali-activated mortars: Workability and rheological behaviour. Construction and Building Materials, 145, 576-587.
213. Lemougna, P. N., Wang, K. T., Tang, Q., Kamseu, E., Billong, N., Melo, U. C., & Cui, X. M. (2017). Effect of slag and calcium carbonate addition on the development of geopolymer from indurated laterite. Applied Clay Science, 148, 109-117.
214. Chi, M. (2015). Effects of modulus ratio and dosage of alkali-activated solution on the properties and micro-structural characteristics of alkali-activated fly ash mortars. Construction and Building Materials, 99, 128-136.
215. Chang, S. H., Ryan, M. H., & Gupta, R. K. (1993). The effect of pH, ionic strength, and temperature on the rheology and stability of aqueous clay suspensions. Rheologica acta, 32(3), 263-269.

216. Favier, A., Hot, J., Habert, G., de Lacaillerie, J. D. E., & Roussel, N. (2014). Rheology of geopolymer: comparative study between Portland cement and metakaolin based geopolymer. In 1st RILEM International Conference on Rheology and Processing of Construction Materials, Paris (Vol. 1, p. 4794).
217. Assaedi, H., Shaikh, F. U. A., & Low, I. M. (2016). Characterizations of flax fabric reinforced nanoclay-geopolymer composites. Composites Part B: Engineering, 95, 412-422.
218. Joshi, A., Montes, C., Salehi, S., Allouche, E., & Lvov, Y. (2015). Optimization of geopolymer properties by coating of fly-ash microparticles with nanoclays. Journal of Inorganic and Organometallic Polymers and Materials, 25(2), 282-292.
219. Zuhua, Z., Xiao, Y., Huajun, Z., & Yue, C. (2009). Role of water in the synthesis of calcined kaolin-based geopolymer. Applied Clay Science, 43(2), 218-223.
220. Vance, K., Kumar, A., Sant, G., & Neithalath, N. (2013). The rheological properties of ternary binders containing Portland cement, limestone, and metakaolin or fly ash. Cement and Concrete Research, 52, 196-207.
221. Mehdipour, I., & Khayat, K. H. (2017). Effect of particle-size distribution and specific surface area of different binder systems on packing density and flow characteristics of cement paste. Cement and Concrete Composites, 78, 120-131.
222. Hou, P. K., Kawashima, S., Wang, K. J., Corr, D. J., Qian, J. S., & Shah, S. P. (2013). Effects of colloidal nanosilica on rheological and mechanical properties of fly ash–cement mortar. Cement and Concrete Composites, 35(1), 12-22.
223. Adesanya, E., Ohenoja, K., Luukkonen, T., Kinnunen, P., & Illikainen, M. (2018). One-part geopolymer cement from slag and pretreated paper sludge. Journal of Cleaner Production, 185, 168-175.
224. Kashani, A., Provis, J. L., Qiao, G. G., & van Deventer, J. S. (2014). The interrelationship between surface chemistry and rheology in alkali activated slag paste. Construction and Building Materials, 65, 583-591.
225. Puertas, F., Martínez-Ramírez, S., Alonso, S., & Vazquez, T. (2000). Alkali-activated fly ash/slag cements: strength behaviour and hydration products. Cement and concrete research, 30(10), 1625-1632.
226. Ibrahim, M., Johari, M. A. M., Rahman, M. K., & Maslehuddin, M. (2017). Effect of alkaline activators and binder content on the properties of natural pozzolan-based alkali activated concrete. Construction and Building Materials, 147, 648-660.
227. Ravikumar, D., & Neithalath, N. (2012). Effects of activator characteristics on the reaction product formation in slag binders activated using alkali silicate powder and NaOH. Cement and Concrete Composites, 34(7), 809-818.
228. García-Lodeiro, I., Fernández-Jiménez, A., Blanco, M. T., & Palomo, A. (2008). FTIR study of the sol–gel synthesis of cementitious gels: C–S–H and N–A–S–H. Journal of Sol-Gel Science and Technology, 45(1), 63-72.
229. Ravikumar, D., & Neithalath, N. (2012). Reaction kinetics in sodium silicate powder and liquid activated slag binders evaluated using isothermal calorimetry. Thermochimica Acta, 546, 32-43.

230. Hajimohammadi, A., & van Deventer, J. S. (2017). Characterisation of one-part geopolymer binders made from fly ash. Waste and biomass valorization, 8(1), 225-233.
231. Rao, G. A., & Prasad, B. R. (2002). Influence of the roughness of aggregate surface on the interface bond strength. Cement and Concrete Research, 32(2), 253-257.
232. Beushausen, H., Höhlig, B., & Talotti, M. (2017). The influence of substrate moisture preparation on bond strength of concrete overlays and the microstructure of the OTZ. Cement and Concrete Research, 92, 84-91.
233. He, Y., Zhang, X., Hooton, R. D., & Zhang, X. (2017). Effects of interface roughness and interface adhesion on new-to-old concrete bonding. Construction and Building Materials, 151, 582-590.
234. Panda, B., Paul, S. C., & Tan, M. J. (2017). Anisotropic mechanical performance of 3D printed fiber reinforced sustainable construction material. Materials Letters, 209, 146-149.
235. Roussel, N., & Cussigh, F. (2008). Distinct-layer casting of SCC: the mechanical consequences of thixotropy. Cement and Concrete Research, 38(5), 624-632.
236. Tang, L. S., Sang, H. T., Jing, S. O. N. G., Luo, Z. G., & Sun, Y. L. (2016). Mechanical model for failure modes of rock and soil under compression. Transactions of Nonferrous Metals Society of China, 26(10), 2711-2723.